



<http://researchspace.auckland.ac.nz>

### *ResearchSpace@Auckland*

#### **Copyright Statement**

The digital copy of this thesis is protected by the Copyright Act 1994 (New Zealand).

This thesis may be consulted by you, provided you comply with the provisions of the Act and the following conditions of use:

- Any use you make of these documents or images must be for research or private study purposes only, and you may not make them available to any other person.
- Authors control the copyright of their thesis. You will recognise the author's right to be identified as the author of this thesis, and due acknowledgement will be made to the author where appropriate.
- You will obtain the author's permission before publishing any material from their thesis.

To request permissions please use the Feedback form on our webpage.

<http://researchspace.auckland.ac.nz/feedback>

#### **General copyright and disclaimer**

In addition to the above conditions, authors give their consent for the digital copy of their work to be used subject to the conditions specified on the Library Thesis Consent Form.

# **Finite Element Solution of an Eikonal Equation for Excitation Wavefront Propagation in Ventricular Myocardium**

**Karl Antony Tomlinson**

**Supervised by Dr Andrew J. Pullan  
and Professor Peter J. Hunter**

A thesis submitted in partial fulfilment of the requirements  
for the degree of Doctor of Philosophy.



**Department of Engineering Science  
School of Engineering  
The University of Auckland  
New Zealand**

**March 2000**



# Abstract

An efficient finite element method is developed to model the spreading of excitation in ventricular myocardium by treating the thin region of rapidly depolarizing tissue as a propagating wavefront. The model is used to investigate the excitation sequence in the full canine ventricular myocardium.

The solution to an eikonal–curvature equation for excitation time is shown to satisfy a reaction–diffusion equation for the bidomain myocardial model at the wavefront, while the solution to an eikonal–diffusion equation approximately satisfies the reaction–diffusion equation in the vicinity of the wavefront. The features of these two eikonal equations are discussed.

A Petrov–Galerkin finite element method with cubic Hermite elements is developed to solve the eikonal–diffusion equation. The oscillatory errors seen when using the Galerkin weighted residual method with high mesh Péclet numbers are avoided by supplementing the Galerkin weights with  $C^0$  continuous functions based on derivatives of the interpolation functions. The ratio of the Galerkin and supplementary weights is a function of the Péclet number such that, for one-dimensional propagation, the error in the solution is within a small constant factor of the optimal error achievable in the trial space. An additional no-inflow boundary term is developed to prevent spurious excitation initiating on the boundary. The need for discretization in time is avoided by using a continuation method to gradually introduce the non-linear term of the governing equation. A small amount of artificial diffusion is sometimes necessary.

Simulations of excitation are performed using a model of the anisotropic canine ventricular myocardium with 2355 degrees of freedom for the dependent variable, and results are compared with reported experimental observations. When it was assumed that Purkinje fibres influence propagation only on the endocardial surface, excitation of the entire myocardium was completed in 56 ms. Altering material parameters to represent penetration of the Purkinje fibres beneath the left endocardial surface reduced the completion time to 48 ms. Modelling the effects of the laminar structure of myocardium by reducing the propagation speed by 40% in the direction normal to the layers delayed completion of excitation by only 4%.



# Acknowledgements

This work is in many ways a result of the efforts of a team of people, many of whom I have not even met. I am fortunate to have had the base of anatomical data and the foundations of CMISS from previous researchers in the Bioengineering Research Group, as well as the continued support and input of the more recent members of the group.

I have enjoyed working in the Department of Engineering Science and with the members of the Bioengineering Research Group from the Department of Physiology. The staff have always been available to help when I have requested their assistance. I am most grateful for the efforts of my supervisors, Andrew Pullan and Peter Hunter. They have provided guidance, motivation, inspiration, and friendship throughout the course of this work, and I look forward to working with them in the future.

The many graduate students I have had the pleasure of getting to know over the past few years have contributed to a cooperative and enjoyable work environment. Thanks in particular to Mark Trew and Nic Smith who have helped me even when under pressure themselves. Chris Bradley also has given his valuable time to help me when CMISS was not making sense. I am grateful to Adrian Croucher for sharing his understanding of the issues involved in numerical solution of the advection–diffusion equation. Carey Stevens and Martin Buist helped me considerably in my early days with CMISS and I have valued Leo Cheng’s understanding of programming issues.

I am appreciative of the work of Richard Christie, Shane Blackett, and David Bullivant on the graphics software that was used in analysis of results and in producing many of the figures included in this thesis.

I am grateful for the scholarship support provided at various stages of the program by the University of Auckland, Auckland UniServices Limited, IBM New Zealand Limited, and the William Georgetti Trust.

Thanks to my family and friends for believing in me, and for their love.

Finally, I would like to acknowledge the creator of our inexhaustibly explorable world. Without Jesus Christ sustaining the Universe this work would not have been possible.



# Contents

<i>List of Figures</i>	<b>xi</b>
<i>List of Tables</i>	<b>xiii</b>
<i>Glossary of Symbols</i>	<b>xv</b>
<i>Notation</i>	<b>xxi</b>
<b>Chapter 1 Introduction</b>	<b>1</b>
<b>Chapter 2 A Model of Myocardial Behaviour</b>	<b>5</b>
2.1 The Bidomain Model . . . . .	6
2.1.1 Governing Equations . . . . .	6
2.1.2 Dimensional Analysis . . . . .	9
2.1.3 One Dimensional Propagation . . . . .	12
2.1.4 Equal Anisotropy Approximation . . . . .	14
2.2 The Need for an Eikonal Approach . . . . .	16
2.3 Eikonal Equation Derivations . . . . .	18
2.3.1 Change of Variables . . . . .	18
2.3.2 Solution at the Wavefront . . . . .	20
2.3.3 Weighted Integral Solution . . . . .	21
2.4 Comparison of Eikonal Equations . . . . .	26
2.4.1 Ellipsoidal Wavefronts . . . . .	29
2.4.2 Boundary Effects . . . . .	31
2.4.3 Summary . . . . .	33
2.5 Numerical Solution of an Eikonal Equation . . . . .	34
2.5.1 Comparison with the Advection–Diffusion Equation . . . . .	35
2.5.2 Previous Approaches . . . . .	36

<b>Chapter 3</b>	<b>A Galerkin Finite Element Method</b>	<b>41</b>
3.1	Interpolation . . . . .	41
3.1.1	Lagrange Basis Functions . . . . .	42
3.1.2	Hermite Basis Functions . . . . .	44
3.2	Galerkin Weighted Residual Equations . . . . .	46
3.2.1	Poisson Equation . . . . .	46
3.2.2	Eikonal Equation . . . . .	48
3.3	Boundary Conditions for Wavefront Initiation . . . . .	49
3.3.1	Mesh Discretization . . . . .	49
3.3.2	Point Initiation . . . . .	50
3.4	Gaussian Quadrature . . . . .	53
3.5	Numerical Continuation . . . . .	54
3.5.1	Selecting a Continuum of Equations . . . . .	55
3.5.2	Implementation . . . . .	56
3.6	Quality of Numerical Results . . . . .	57
3.7	Error Norm Analysis . . . . .	59
3.7.1	Solution Spaces . . . . .	60
3.7.2	One-Dimensional Error Bound . . . . .	61
3.8	Difference Equation Analysis . . . . .	64
3.8.1	Convergence . . . . .	66
3.8.2	Error Transport . . . . .	69
<b>Chapter 4</b>	<b>Alternative Finite Element Methods</b>	<b>73</b>
4.1	The Least Squares Finite Element Method . . . . .	73
4.2	The Petrov–Galerkin Finite Element Method . . . . .	76
4.3	Stabilizing Terms . . . . .	79
4.3.1	Artificial Diffusion . . . . .	79
4.3.2	Higher Order Stabilizing Terms . . . . .	81
4.4	Summary . . . . .	87
<b>Chapter 5</b>	<b>A Petrov–Galerkin Finite Element Method</b>	<b>89</b>
5.1	Selection of Weighting Functions . . . . .	89
5.1.1	Approximate Symmetrization . . . . .	90
5.1.2	One-Dimensional Optimal Weighting Functions . . . . .	93
5.1.3	One-Dimensional Approximate Symmetrization . . . . .	99

5.1.4	Extension to Three Dimensions . . . . .	105
5.2	No-Inflow Boundary Condition . . . . .	112
5.2.1	Inflow Boundaries . . . . .	112
5.2.2	Evolution Without Diffusion . . . . .	114
5.2.3	A No-Inflow Boundary Term . . . . .	116
5.3	Summary of the Method . . . . .	121
 <b>Chapter 6 Myocardial Geometry, Structure, and Material Parameters</b>		<b>123</b>
6.1	A Model of Myocardial Geometry . . . . .	123
6.2	Myocardial Fibre and Sheet Structure . . . . .	126
6.3	Dependent Variable Discretization . . . . .	130
6.4	Material Parameters . . . . .	133
6.4.1	Resistivities . . . . .	134
6.4.2	Space Constants . . . . .	140
6.4.3	Time Constant . . . . .	141
6.4.4	Propagation Speeds . . . . .	144
6.4.5	Selection of Parameters . . . . .	145
 <b>Chapter 7 Simulations</b>		<b>147</b>
7.1	Epicardial Point Stimulation . . . . .	147
7.2	Stimulation from the Purkinje Network . . . . .	151
7.2.1	The Purkinje Network . . . . .	151
7.2.2	Numerical Stability . . . . .	153
7.2.3	Comparison with Experimental Observations . . . . .	159
7.3	Penetration of Purkinje Fibres . . . . .	162
7.4	Effects of Sheet Structures . . . . .	165
 <b>Chapter 8 Further Work</b>		<b>169</b>
8.1	Artificial Diffusion . . . . .	170
8.2	Improving Numerical Stability . . . . .	171
8.2.1	Treatment of the Evolution Term . . . . .	171
8.2.2	Existence of a Solution to the Non-Linear System . . . . .	172
8.3	Developing A Model of the Far-Field Potential . . . . .	173
8.4	Extensions to the Ventricular Model . . . . .	175

<i>Chapter 9</i>	<b>Conclusions</b>	<b>177</b>
<i>Appendix A</i>	Step-Function Point Current Source in a Passive Bidomain with Equal Anisotropy	<b>181</b>
<i>References</i>		<b>191</b>

# List of Figures

2.1	Planar wave propagation speeds predicted by the bidomain model and its monodomain approximation. . . . .	16
2.2	Comparison of magnitudes of $e^{-\alpha\tau^2}$ and $\tau e^{-\alpha\tau^2}$ with $\frac{dv_m}{d\tau}$ for $\alpha = 0.5$ . . . . .	24
2.3	Dimensionless propagation speeds of a small ellipsoidal wavefront, as specified by two eikonal equation variants. . . . .	30
2.4	Eikonal and reaction–diffusion equation solutions for excitation initiated at the left hand end of tissue four space constants in length. . . . .	32
3.1	One-dimensional linear Lagrange interpolation functions. . . . .	43
3.2	One-dimensional cubic Hermite interpolation functions. . . . .	45
3.3	Demonstration of the effect that modification of the diffusion term in the eikonal equation near a point initiation has on Galerkin solutions. . . . .	53
3.4	Excitation time solutions on an 8 mm square slice of tissue. . . . .	58
3.5	Galerkin solutions for excitation time on an annulus. . . . .	59
4.1	Numerical solution from a Galerkin method stabilized by a derivative discontinuity term for a length of tissue stimulated at both ends. . . . .	86
5.1	Optimal weighting functions $w_i^{0*}$ and $w_i^{1*}$ for $1 \leq i \leq N$ . . . . .	96
5.2	Optimal weighting function $w_0^{1*}$ near the Dirichlet boundary. . . . .	96
5.3	Localized optimal weighting functions $w_i^{0*}$ and $w_i^{1*}$ for $1 \leq i \leq N$ . . . . .	98
5.4	Localized optimal weighting function $w_0^{1*}$ near the Dirichlet boundary. . . . .	98
5.5	Comparison of estimated error factors with $\frac{A_\infty}{A_0}$ given by the simplified expression (5.34) and the optimal expression (5.29). . . . .	104
5.6	Comparison of estimated error factors with $\frac{A_\infty}{A_0}$ determined by the derivative-limited expressions (5.45) and the optimal expression (5.29). . . . .	111

5.7	Excitation contours calculated by the Petrov–Galerkin method for a slice of tissue stimulated unevenly at the left hand edge. . . . .	113
5.8	Excitation contours calculated by the Petrov–Galerkin method with $r_b$ defined by (5.61) in the additional boundary term (5.57). . . . .	120
5.9	Excitation contours calculated by the Petrov–Galerkin method with $r_b$ defined by (5.67) in the additional boundary term (5.57). . . . .	121
6.1	Fitted left ventricular endocardial surface. . . . .	125
6.2	Fitted right ventricular endocardial surface. . . . .	125
6.3	Fitted epicardial surface. . . . .	125
6.4	60-element geometric model of the ventricular myocardium. . . . .	127
6.5	Sample fibre and sheet orientations in the model of the ventricular myocardium. . . . .	129
6.6	Regions of the mesh where $C^1$ continuity in $U$ is not enforced. . . . .	131
7.1	Simulated epicardial excitation times after epicardial point stimulus. . . . .	148
7.2	Wavefront locations in simulation of propagation from an epicardial point stimulus. . . . .	149
7.3	Stimulation times on the portions of the endocardial surfaces that are stimulated by the Purkinje network. . . . .	153
7.4	Wavefront propagation for excitation initiated by the Purkinje network, from a simulation with $\alpha_c = 0.94$ . . . . .	154
7.5	Wavefront propagation for excitation initiated by the Purkinje network, from a simulation with $\alpha_c = 0.5$ . . . . .	157
7.6	Simulated epicardial excitation times for Purkinje fibre stimulation. . . . .	161
7.7	Wavefront propagation with penetration of Purkinje fibres. . . . .	164
7.8	Epicardial excitation times (ms) with different conductivities for the direction normal to sheets. . . . .	166
7.9	Wavefront propagation with reduced conductivity in the direction normal to sheets. . . . .	167

# List of Tables

2.1	Summary of the two eikonal equations proposed for modelling myocardial excitation wavefront propagation. . . . .	33
5.1	Comparison of calculated and estimated one-dimensional error factors. . . . .	102
6.1	Summary of ventricular surface fitting. . . . .	126



# Glossary of Symbols

- $A$  scalar constant.  
 $A$  set of possible vectors  $\mathbf{a}$  for the spread of excitation.  
 $A_0$  coefficient of  $w_{i0}$  in  $w_i$ .  
 $A_\infty$  coefficient of  $w_{i\infty}$  in  $w_i$ .  
 $A_b$  multiplier in no-inflow boundary term.  
 $\mathbf{a}$  vector for the spread of excitation or velocity field for advection.  
 $\mathbf{a}_k$  error transport eigenvector.  
 $\mathbf{a}_l$  fibre (or longitudinal) direction.  
 $\mathbf{a}_n$  direction normal to sheets.  
 $\mathbf{a}_t$  direction transverse to fibres within sheets.
- $B$  scalar constant.  
 $B(v, w)$  form representing the left hand side of the weighted residual equations.  
 $B_S(v, w)$  symmetric part of  $B(v, w)$ .
- $C_m$  membrane capacitance per unit area.  
 $c_m$  membrane capacitance per unit volume.  
 $c_0$  dimensionless propagation speed for a planar wavefront in homogeneous tissue.
- $D$  set of numbers for parameters that are known from Dirichlet boundary conditions.
- $e_p^r$  coefficient of  $h^p$  in the power series expansion of error in  $U_i^r$ .  
 $e_p^{r(n)}$   $n$ th derivative of  $e_p^r$ .  
 $e_p$  coefficient of  $h^p$  in the power series expansion of error in  $U_i$ .
- $f_{il}$  fraction of cross-sectional area normal to  $\mathbf{a}_l$  occupied by intracellular space.  
 $f_1, f_2$  unknown scalar functions.  
 $f_{ion}$  ionic activity function (dimension of voltage).

- $G^e$  extracellular effective conductivity tensor.  
 $G^i$  intracellular effective conductivity tensor.  
 $G^o$  conductivity tensor outside the myocardium.  
 $g_{el}, g_{et}, g_{en}$  principal extracellular effective conductivities for directions  $\mathbf{a}_l, \mathbf{a}_t,$  and  $\mathbf{a}_n$ .  
 $g_{il}, g_{it}, g_{in}$  principal intracellular effective conductivities for directions  $\mathbf{a}_l, \mathbf{a}_t,$  and  $\mathbf{a}_n$ .  
 $H^p(\Omega)$  space of functions for which the squares of derivatives up to order  $p$  may be integrated over  $\Omega$ .  
 $H_D^1$  space of functions in  $H^1(\Omega)$  satisfying the Dirichlet boundary conditions.  
 $H_{D_0}^1$  space of functions in  $H^1(\Omega)$  equal to zero on  $\Gamma_D$ .  
 $h$  element length.  
 $\mathbf{h}_1, \mathbf{h}_2, \mathbf{h}_3$  reference vectors for specification of  $\mathbf{a}_l, -\mathbf{a}_n,$  and  $\mathbf{a}_t$ .  
 $I$  total applied current.  
 $I_{ion}$  ionic membrane current per unit membrane area.  
 $i_{app}$  applied extracellular current per unit tissue volume.  
 $i_{ion}$  ionic membrane current per unit volume.  
 $i_m$  transmembrane current per unit tissue volume.  
 $\mathbf{j}_e$  extracellular current density.  
 $\mathbf{j}_i$  intracellular current density.  
 $\mathbf{j}_o$  current density outside the myocardium.  
 $K_{Gal}$  constant in Galerkin error bound.  
 $k_P$  constant in Poincaré bound.  
 $k_\zeta$  constant for  $\zeta$ .  
 $L$  domain length or characteristic distance.  
 $N$  number of nodes.  
 $\mathcal{N}$  set of parameter numbers not in  $D$ .  
 $\mathbf{n}$  normal to the boundary.  
 $\mathbf{n}^v$  normal to the boundary in the natural coordinate system.  
 $O(h^p)$  terms involving powers of  $h$  order  $p$  and higher.  
 $P_e$  mesh Péclet number.  
 $P_e^b$  mesh Péclet number at the boundary.

- $P_g$  global Péclet number.  
 $p_s$  piecewise polynomial function for modification of the diffusion term near a singularity.  
 $p_\zeta$  piecewise polynomial function for  $\zeta$ .  
 $\mathbf{p}$  direction of propagation (normal to the wavefront).  
 $R_m$  reciprocal of membrane conductance per unit area.  
 $R_S$  Riesz representer.  
 $r_{el}, r_{et}, r_{en}$  principal extracellular effective resistivities for directions  $\mathbf{a}_l$ ,  $\mathbf{a}_t$ , and  $\mathbf{a}_n$ .  
 $r_{il}, r_{it}, r_{in}$  principal intracellular effective resistivities for directions  $\mathbf{a}_l$ ,  $\mathbf{a}_t$ , and  $\mathbf{a}_n$ .  
 $r_l, r_t, r_n$  bulk tissue resistivities for directions  $\mathbf{a}_l$ ,  $\mathbf{a}_t$ , and  $\mathbf{a}_n$ .  
 $r_m$  reciprocal of membrane conductance per unit volume.  
 $\bar{r}_m$  spatially averaged value of  $r_m$ .  
 $r_b$  residual for no-inflow boundary term.  
 $S$   $(\frac{\partial T}{\partial \tau})^{-1}$ .  
 $S_D^h$  trial space.  
 $S_0^h$  space of possible variation within  $S_D^h$ .  
 $s$   $S(\boldsymbol{\xi}, 0)$ .  
 $T$  coordinate transformation function,  $T(\boldsymbol{\xi}, \tau) = t$ .  
 $T^h$  test space.  
 $T^{h*}$  optimal test space.  
 $t$  time.  
 $U$  numerical approximation of  $u$ .  
 $U^*$  optimal approximation to  $u$  in  $S_D^h$ .  
 $U_i$   $i$ th parameter determining  $U$ .  
 $U_i^{pqr}$  parameter at node  $j$  corresponding to  $U$  differentiated  $p$ ,  $q$ , and  $r$  times with respect to  $\xi_1$ ,  $\xi_2$ , and  $\xi_3$ , respectively.  
 $\mathbf{U}_i$  vector of parameters for  $U$  at node  $i$ .  
 $\tilde{U}_D$  sum of terms for  $U$  that are determined by Dirichlet boundary conditions.  
 $u$  excitation time.  
 $\tilde{u}_D$  Dirichlet boundary condition value.  
 $V_{el}$  jump in extracellular potential across a wavefront propagating along fibres.  
 $V_{et}$  jump in extracellular potential across a wavefront propagating transverse to fibres.

- $V_p$  plateau transmembrane potential.  
 $V_r$  resting transmembrane potential.  
 $V_m$  transmembrane potential.  
 $v_m$  transmembrane potential  $v_m(\tau)$ .
- $w_i$  finite element weighting function corresponding to parameter  $i$ .  
 $w_i^*$  optimal weighting function corresponding to parameter  $i$ .  
 $w_{i0}, w_{i\infty}$  weight terms based on  $w_i^*$  when  $P_e$  approaches 0 and  $\infty$ .  
 $w_i^p$  finite element weighting function corresponding to derivative  $p$  at node  $i$ .  
 $w_i^{p*}$  optimal weighting function corresponding to derivative  $p$  at node  $i$ .  
 $w_i^{p*}$  localized optimal weighting function corresponding to derivative  $p$  at node  $i$ .  
 $w_{i0}^p, w_{i\infty}^p$  weight terms based on  $w_i^{p*}$  when  $P_e$  approaches 0 and  $\infty$ .  
 $\hat{w}_i$  Petrov–Galerkin supplementary weighting function corresponding to parameter  $i$ .  
 $\hat{w}_i^p$  supplementary weighting function corresponding to derivative  $p$  at node  $i$ .
- $\mathbf{x}$  position in space.
- $\alpha$  a positive scalar.  
 $\alpha_\infty$  constant for smoothing  $w_{i\infty}$ .  
 $\alpha_b$  constant for smoothing  $r_b$ .  
 $\alpha_c$  continuation variable.  
 $\alpha_e$  ratio of  $M$  to  $M^e$  for equal anisotropy.  
 $\alpha_i$  ratio of  $M$  to  $M^i$  for equal anisotropy.  
 $\alpha_s$  multiplier in Petrov–Galerkin supplementary weighting functions.  
 $\alpha_s^p$  multiplier in supplementary weighting functions corresponding to derivative  $p$ .
- $\beta$  coefficient of artificial diffusion or stabilizing term.  
 $\beta^p$  coefficient of artificial diffusion term corresponding to derivative  $p$ .
- $\Gamma_D$  portion of the boundary on which Dirichlet boundary conditions are applied.  
 $\Gamma_N$   $\partial\Omega - \Gamma_D$ .  
 $\gamma$  ratio of first to second derivative coefficients in the one-dimensional eikonal equation.
- $\Delta_S$  constant determining test space performance.
- $\epsilon_k$  coefficients of error transport eigenfunctions.

- $\zeta$  multiplier in  $w_{i\infty}$  to ensure that  $w_i \in H_{D_0}^1$ .
- $\theta$  propagation speed.
- $\theta_1, \theta_t, \theta_n$  propagation speeds in directions  $\mathbf{a}_1$ ,  $\mathbf{a}_t$ , and  $\mathbf{a}_n$ .
- $\lambda$  space constant.
- $\lambda_k$  error transport eigenvalue.
- $\lambda_{el}, \lambda_{et}, \lambda_{en}$  singular values of  $M^e$  corresponding to eigenvectors  $\mathbf{a}_1$ ,  $\mathbf{a}_t$ , and  $\mathbf{a}_n$ .
- $\lambda_{il}, \lambda_{it}, \lambda_{in}$  singular values of  $M^i$  corresponding to eigenvectors  $\mathbf{a}_1$ ,  $\mathbf{a}_t$ , and  $\mathbf{a}_n$ .
- $\lambda_1, \lambda_t, \lambda_n$  space constants for directions  $\mathbf{a}_1$ ,  $\mathbf{a}_t$ , and  $\mathbf{a}_n$ .
- $M$  effective coupling tensor.
- $M^e$  extracellular coupling tensor.
- $M^i$  intracellular coupling tensor.
- $M^\xi$   $\xi$ -coordinate based coupling tensor.
- $\mu_{ij}$  component of  $M$ .
- $\mu_{mn}^\xi$  component of  $M^\xi$ .
- $\bar{\mu}^\xi$  average of the diagonal components of  $M^\xi$ .
- $\nu$  function mapping element-local parameter numbers to global parameter numbers.
- $\xi$  (Chapter 2) position in space.  $\xi = \mathbf{x}$  but  $\frac{\partial}{\partial \xi_i}$  is a derivative with  $\tau$  held constant.
- $\xi$  (Chapters 3,5,6) element-local coordinate system.
- $\xi_i$  component of  $\xi$ .
- $\sigma_{il}$  intracellular specific conductivity for the fibre direction.
- $\tau$  scalar function  $\tau(\mathbf{x}, t)$  defined such that  $V_m(\mathbf{x}, t) = v_m(\tau)$ .
- $\tau_f$  time constant of the early exponential rise in the foot of an action potential.
- $\tau_m$  membrane time constant.
- $\mathbf{v}$  local natural coordinate system.
- $v_p$  component of  $\mathbf{v}$ .
- $\phi_e$  extracellular potential.
- $\phi_i$  intracellular potential.
- $\phi_{\text{mono}}$  potential in a monodomain.
- $\phi_o$  potential outside the myocardium.
- $\varphi_e$  extracellular potential  $\varphi_e(\tau)$ .

- $\chi$  ratio of membrane surface area to volume of tissue.
- $\Psi$  element-local basis functions.
- $\psi_i$  interpolation function corresponding to parameter  $i$ .
- $\psi_i^p$  interpolation function corresponding to derivative  $p$  at node  $i$ .
- $\Omega$  domain of interest.
- $\partial\Omega$  boundary of  $\Omega$ .
- $\Omega_e$  domain of element  $e$ .
- $\partial\Omega_e$  boundary of element  $e$ .

# Notation

- The  $:=$  symbol denotes definition.
- Repeated indices imply summation over all values of the index unless explicitly stated:  
$$a_i b_i \equiv \sum_i a_i b_i.$$
- A following prime denotes differentiation: for  $u := u(x)$ ,  $u' \equiv \frac{du}{dx}$ .

Higher derivatives are denoted by multiple following primes or by a superscript in parentheses:  $u'''' \equiv u^{(4)} \equiv \frac{d^4 u}{dx^4}$ .

- A subscript on a differentiation operator indicates the coordinate system in which the differentiation is performed:  $\nabla_{\mathbf{v}} u$  is the gradient of  $u$  with respect to  $\mathbf{v}$  coordinates.
- Angle brackets indicate an inner product over the domain  $\Omega$ :  $\langle u, v \rangle$  is the inner product of  $u$  and  $v$ .



## *Chapter 1*

# **Introduction**

Cardiac disease is a leading cause of death in all regions of the world. The World Health Organization (1999) estimated cardiac disease to be the cause of 21.5 per cent of deaths in its member states during 1998. The development of more successful treatments for this problem depends heavily on improving the understanding of the general function of the heart and also on improving the methods for detection and diagnosis of each patient's condition. Both of these areas of research would benefit from a computational model of the function of the heart.

Experimental studies are necessary to improve the understanding of cardiac function but are limited to what can be observed. It will never be possible to observe every functional element at once. Computational models enable interpretation of data from experimental observations and representation of events that cannot be observed. In diagnosis, the amount of observable data is further restricted by the level of disruption to the patient that is reasonable. Computational models could provide predictions of the activity in regions where making experimental observations would be too invasive.

One area of application for computational models is in the study or determination of the electrical activation of the heart. The function of the cardiac muscle relies on the flux of ions across myocardial cell membranes, and this flux produces an electric field measurable on the torso surface. Data from non-invasive measurements of electrical potentials on the torso surface hold information about the electrical activity of the heart that could be extracted with the aid of a computational model.

This inverse problem of determining the activity and condition of the heart from electrical potentials on the torso surface requires some constraint on the solution space. This is because the set of electrical sources that produce a given potential field on a surface is not unique. The problem is often reduced therefore to that of determining only the electrical potentials on the surface of the heart, but is still ill-conditioned due to the smoothing effect of the torso on the potential distribution (Gulrajani, Roberge, and Savard, 1989). Regularization is necessary, which usually involves constraining epicardial potentials to be smooth, but these constraints are not physically realistic. Using instead a model of the activity of the heart would allow the application of physically realistic constraints and the determination of more physiologically important parameters such as tissue conduction velocities or initial excitation times.

The torso surface potentials are influenced most significantly by the electrical depolarization of cells in the ventricular myocardium, so this is the process about which information is going to be most easily extracted from surface measurements. In this thesis, a computational model is developed to represent the depolarization process in the ventricular myocardium.

The development of a computational model of biological processes is no easy task. Schmitt (1969) made the following statement:

We realize that no computer we are ever likely to lay our hands on will be big enough or versatile enough to imitate or represent cell by cell, molecule by molecule, hormone by hormone, nerve patterning by nerve patterning, the progress of a coordinated, biological, informational transaction even in the simplest organism. We must dissect by function, structure or organization all pertinent systems and then model representative elements, always using the largest feasible group of similar elements for lumping as one.

Although computers have advanced incredibly since 1969, the statement is most likely still true today. In Chapter 2, possible mathematical models for myocardial depolarization are reviewed. Following the advice of Schmitt, an eikonal equation model is selected to describe the propagation of an excitation wavefront representing the thin region of tissue in which the most intense electrical activity occurs.

A first attempt at a finite element computational method for obtaining a solution to the mathematical model is described in Chapter 3. The method performs reasonably well for simple problems, but oscillations corrupt the solutions to more complex problems. Investigation is

made into the reasons for the shortcomings of the method. Chapter 4 reviews possible alternative finite element methods from the field of solute transport in advecting fluids, and discusses the application of such methods to the eikonal equation. An improved finite element method for the eikonal equation is developed in Chapter 5.

Chapter 6 describes the geometry and structure of the model of the ventricular myocardium and reviews reported experimental values for the important model parameters. Simulations of the spreading of excitation in the full ventricular myocardium are presented and compared with experimental observations in Chapter 7.

Conclusions and suggestions for further improvements to the method are presented in Chapters 8 and 9.



## *Chapter 2*

# **A Model of Myocardial Behaviour**

In developing a model of the electrical behaviour of the ventricular myocardium, it would be unreasonable to expect to be able to model every microscopic biological process that occurs within and between each and every cell. Such detail in the model is also unnecessary. The ventricular function and the electrical fields induced in the torso are not so much affected by the activity of one ion or one ion channel or even one cell as by the collective activity of many cells. It is not necessary to resolve the small spatial detail of the microscopic processes, but sufficient to base the model on the collective macroscopic effect of these processes. Here, a model is sought to describe the electrical behaviour of myocardium at a spatial scale that is likely to influence the ventricular function or the electrical fields induced in the torso.

The most significant electrical activity is the depolarization of cells. It is this depolarization that leads to the activation of the mechanisms that cause the myocardium to contract and the heart to pump. This depolarization is also what causes the largest deflections in electrocardiographic recordings, the QRS interval. Depolarization occurs quickly and in only a narrow region of cells at a time, so this narrow region can be considered as a propagating *excitation wavefront*. If the spreading of depolarization can be modelled then it provides a very good indication of the function of the myocardium and a basis from which the expected QRS interval of the electrocardiograph can be calculated. A model is therefore sought to describe the propagation of the excitation wavefront.

## 2.1 The Bidomain Model

As a means for collecting together the microscopic functional elements of the myocardium to model their macroscopic effects, Schmitt (1969) suggested the concept of two interpenetrating domains. One domain was to represent the volume-averaged properties of the intracellular contents and their interconnections, and the other domain was to represent the volume-averaged properties of the surrounding extracellular tissue and fluid. These domains were to coexist spatially, and the behaviour of current flow between them was to be based on the volume-averaged properties of the cell membrane. This approach is now generally referred to as the *bidomain model* (Henriquez, 1993). The two domains are referred to as the *intracellular* and *extracellular* domains. Each is treated as a continuum.

### 2.1.1 Governing Equations

Assuming that capacitive, inductive, and electromagnetic propagative effects within the domains are negligible, the conservation of current equations are

$$\nabla \cdot \mathbf{j}_i = -i_m \quad \text{and} \quad \nabla \cdot \mathbf{j}_e = i_m + i_{\text{app}}, \quad (2.1)$$

where  $\mathbf{j}_i$  and  $\mathbf{j}_e$  represent the current densities in the intra- and extracellular domains,  $i_m$  represents the (outward) transmembrane current per unit tissue volume, and  $i_{\text{app}}$  represents any applied current per unit volume (assumed applied to the extracellular space).

Assuming the current in each domain obeys Ohm's Law, the current densities may be written as linear functions of the gradients of intra- and extracellular potentials,  $\phi_i$  and  $\phi_e$ :

$$\mathbf{j}_i = -G^i \nabla \phi_i \quad \text{and} \quad \mathbf{j}_e = -G^e \nabla \phi_e. \quad (2.2)$$

$G^i$  and  $G^e$  are intra- and extracellular *effective conductivity tensors*. They are symmetric and positive definite and it is assumed that they have the same principal axes. If  $\mathbf{a}_l$ ,  $\mathbf{a}_t$ , and  $\mathbf{a}_n$  are orthogonal unit vectors such that  $\mathbf{a}_l$  is parallel to the fibres (longitudinal),  $\mathbf{a}_t$  is transverse to the fibres but in the plane of the sheets, and  $\mathbf{a}_n$  is normal to the sheets (see Section 6.2 for

more detail on the definition of these directions), then  $G^i$  and  $G^e$  may be written as

$$G^i = \begin{bmatrix} \mathbf{a}_l & \mathbf{a}_t & \mathbf{a}_n \end{bmatrix} \begin{bmatrix} g_{il} & 0 & 0 \\ 0 & g_{it} & 0 \\ 0 & 0 & g_{in} \end{bmatrix} \begin{bmatrix} \mathbf{a}_l^T \\ \mathbf{a}_t^T \\ \mathbf{a}_n^T \end{bmatrix}$$

and

$$G^e = \begin{bmatrix} \mathbf{a}_l & \mathbf{a}_t & \mathbf{a}_n \end{bmatrix} \begin{bmatrix} g_{el} & 0 & 0 \\ 0 & g_{et} & 0 \\ 0 & 0 & g_{en} \end{bmatrix} \begin{bmatrix} \mathbf{a}_l^T \\ \mathbf{a}_t^T \\ \mathbf{a}_n^T \end{bmatrix}. \quad (2.3)$$

The principal effective conductivities  $g_{il}$ ,  $g_{it}$ ,  $g_{in}$ ,  $g_{el}$ ,  $g_{et}$ , and  $g_{en}$  represent averages of fractions of the *specific conductivities* of each space in each direction. For example, the effective conductivity  $g_{il}$  for the intracellular domain in the fibre direction  $\mathbf{a}_l$  represents a volume average of  $f_{il}\sigma_{il}$ , where  $f_{il}$  denotes the fraction of cross-sectional area occupied by intracellular space in the plane with normal  $\mathbf{a}_l$ , and  $\sigma_{il}$  denotes the specific conductivity of that space in that direction.

The transmembrane current  $i_m$  is usually divided into ionic and capacitive components:

$$i_m = \chi \left( I_{\text{ion}} + C_m \frac{\partial V_m}{\partial t} \right). \quad (2.4)$$

$\chi$  represents the ratio of membrane surface area to volume of tissue,  $I_{\text{ion}}$  represents the sum of the membrane ionic currents per unit area,  $C_m$  represents the membrane capacitance per unit area, and  $V_m$  is the transmembrane potential defined by

$$V_m := \phi_i - \phi_e. \quad (2.5)$$

(The symbol ‘:=’ denotes definition.) If it is only the depolarization phase of the action potential that is important, consideration of the large difference between the activation and inactivation time constants of the dominating fast sodium current leads to the approximation of  $I_{\text{ion}}$  as a time-independent function of the transmembrane voltage (Colli Franzone and Guerri, 1993a). That is  $I_{\text{ion}} = I_{\text{ion}}(V_m)$ . Defining

$$i_{\text{ion}} := \chi I_{\text{ion}} \quad \text{and} \quad c_m := \chi C_m, \quad (2.6)$$

so that  $i_{\text{ion}}$  is the membrane ionic current per unit volume and  $c_m$  is the membrane capacitance

per unit volume, the transmembrane current may be written as

$$i_m = i_{\text{ion}}(V_m) + c_m \frac{\partial V_m}{\partial t}, \quad (2.7)$$

Equations (2.1), (2.2), (2.7), and (2.5) may be combined to give a system of equations for  $V_m$  and  $\phi_e$  in the myocardial domain  $\Omega$ :

$$\begin{aligned} i_{\text{ion}}(V_m) + c_m \frac{\partial V_m}{\partial t} &= \nabla \cdot (G^i \nabla (\phi_e + V_m)), \\ -i_{\text{ion}}(V_m) - c_m \frac{\partial V_m}{\partial t} &= \nabla \cdot (G^e \nabla \phi_e) + i_{\text{app}}. \end{aligned} \quad (2.8)$$

This is a *reaction–diffusion system*. It may alternatively be written as

$$\begin{aligned} -\nabla \cdot (G^i \nabla V_m) &= \nabla \cdot ((G^i + G^e) \nabla \phi_e) + i_{\text{app}}, \\ -i_{\text{ion}}(V_m) - c_m \frac{\partial V_m}{\partial t} &= \nabla \cdot (G^e \nabla \phi_e) + i_{\text{app}}. \end{aligned} \quad (2.9)$$

This approach of using a macroscopic model for volume averages of microscopic properties is given some justification by the work of Neu and Krassowska (1993), who derived this system as the governing equations for volume-averaged potentials in a syncytium consisting of a periodic network of interconnected cells. Trayanova (1996a) developed a bidomain model with periodic intracellular conductivity to represent the difference between cytoplasmic conductivity and myocyte-to-myocyte junctional conductivity. Simulations of passive behaviour under applied currents showed that the transmembrane potential response was primarily determined by the macroscopic tissue properties but had a low-magnitude sawtooth component from microscopic discontinuities (Trayanova, 1996b).

The volumes outside the myocardial domain are usually assumed to be simple monodomain conductors satisfying Ohm's Law. It is also assumed that the extracellular space is in direct contact with the outside volume, so the extracellular potential  $\phi_e$  is continuous with the potential  $\phi_o$  in the outside volume. That is

$$\phi_e = \phi_o \quad \text{on } \partial\Omega. \quad (2.10)$$

Conservation of current between the volumes leads to the boundary condition,

$$\mathbf{n} \cdot (\mathbf{j}_i + \mathbf{j}_e) = \mathbf{n} \cdot \mathbf{j}_o \quad \text{on } \partial\Omega, \quad (2.11)$$

where  $\mathbf{n}$  is the unit normal the boundary, and  $\mathbf{j}_o$  is the current density in the outside volume. One more boundary condition is required to relate  $\mathbf{n} \cdot \mathbf{j}_i$  and  $\mathbf{n} \cdot \mathbf{j}_e$ . Krassowska and Neu (1994) showed by homogenization of a periodic microscopic structure that, if only the extra-cellular space is in direct contact with the outside volume, the appropriate other macroscopic boundary condition is

$$\mathbf{n} \cdot \mathbf{j}_i = 0 \quad \text{on } \partial\Omega. \quad (2.12)$$

Equations (2.12) and (2.11) lead to the following boundary conditions for  $V_m$  and  $\phi_e$ ,

$$\begin{aligned} \mathbf{n} \cdot G^i \nabla (\phi_e + V_m) &= 0 \\ \text{and} \quad \mathbf{n} \cdot G^e \nabla \phi_e &= \mathbf{n} \cdot G^o \nabla \phi_o \quad \text{on } \partial\Omega, \end{aligned} \quad (2.13)$$

where  $G^o$  is the conductivity tensor for the outside volume.

### 2.1.2 Dimensional Analysis

$V_m$  and  $\phi_e$  are functions of space and time. It is convenient to scale system (2.9) so that the parameters give indications of the important spatial and temporal scales. This can be done by dividing the terms in the system by a characteristic conductance per unit volume.

If the transmembrane potential  $V_m$  is near the resting potential  $V_r$ , the behaviour of the ionic membrane currents can be approximated by assuming the membrane has a passive resistance. That is

$$I_{\text{ion}}(V_m) \approx \frac{1}{R_m} (V_m - V_r), \quad (2.14)$$

where

$$\frac{1}{R_m} := \frac{dI_{\text{ion}}}{dV_m}(V_r) \quad (2.15)$$

is the apparent membrane conductance per unit area. A membrane conductance per unit

volume can therefore be obtained from

$$\frac{1}{r_m} := \chi \frac{1}{R_m}. \quad (2.16)$$

Multiplying the terms in system (2.9) by an average (space-independent) value  $\bar{r}_m$  of  $r_m$  gives

$$\begin{aligned} -\nabla \cdot (M^i \nabla V_m) &= \nabla \cdot ((M^i + M^e) \nabla \phi_e) + \bar{r}_m \dot{i}_{\text{app}}, \\ -f_{\text{ion}}(V_m) - \tau_m \frac{\partial V_m}{\partial t} &= \nabla \cdot (M^e \nabla \phi_e) + \bar{r}_m \dot{i}_{\text{app}}, \end{aligned} \quad (2.17)$$

where

$$M^i := \bar{r}_m G^i \quad \text{and} \quad M^e := \bar{r}_m G^e \quad (2.18)$$

are intra- and extracellular *coupling tensors* which have dimensions of space squared,

$$\tau_m := \bar{r}_m c_m \quad (2.19)$$

is the *membrane time constant* which has dimension of time, and

$$f_{\text{ion}}(V_m) := \bar{r}_m \dot{i}_{\text{ion}}(V_m) \quad (2.20)$$

is the *ionic activity function* which also has dimension of voltage. The boundary conditions (2.13) expressed in terms of these parameters are

$$\begin{aligned} \mathbf{n} \cdot M^i \nabla (\phi_e + V_m) &= 0 \\ \text{and} \quad \mathbf{n} \cdot M^e \nabla \phi_e &= \bar{r}_m \mathbf{n} \cdot G^o \nabla \phi_o \quad \text{on } \partial\Omega. \end{aligned} \quad (2.21)$$

The coupling tensors may be written as

$$M^i = \begin{bmatrix} \mathbf{a}_l & \mathbf{a}_t & \mathbf{a}_n \end{bmatrix} \begin{bmatrix} \lambda_{il}^2 & 0 & 0 \\ 0 & \lambda_{it}^2 & 0 \\ 0 & 0 & \lambda_{in}^2 \end{bmatrix} \begin{bmatrix} \mathbf{a}_l^T \\ \mathbf{a}_t^T \\ \mathbf{a}_n^T \end{bmatrix}$$

and

$$\mathbf{M}^e = \begin{bmatrix} \mathbf{a}_1 & \mathbf{a}_t & \mathbf{a}_n \end{bmatrix} \begin{bmatrix} \lambda_{el}^2 & 0 & 0 \\ 0 & \lambda_{et}^2 & 0 \\ 0 & 0 & \lambda_{en}^2 \end{bmatrix} \begin{bmatrix} \mathbf{a}_1^T \\ \mathbf{a}_t^T \\ \mathbf{a}_n^T \end{bmatrix}. \quad (2.22)$$

The singular values  $\lambda_{il}$ ,  $\lambda_{it}$ ,  $\lambda_{in}$ ,  $\lambda_{el}$ ,  $\lambda_{et}$ , and  $\lambda_{en}$  have dimension of space, and may be expressed in terms of conductivities using

$$\lambda_{il}^2 = \bar{r}_m g_{il}, \quad \text{etc.} \quad (2.23)$$

In each principal direction therefore, there are two parameters with dimension of space that can be derived from the important material properties. To obtain indicators of the important spatial dimensions from these parameters, the passive behaviour of the bidomain is analysed.

If the tissue is near resting potential, approximation (2.14) may be applied to system (2.17) to give

$$\begin{aligned} -\nabla \cdot (\mathbf{M}^i \nabla V_m) &= \nabla \cdot ((\mathbf{M}^i + \mathbf{M}^e) \nabla \phi_e) + \bar{r}_m \mathbf{i}_{app}, \\ -V_m + V_r - \tau_m \frac{\partial V_m}{\partial t} &= \nabla \cdot (\mathbf{M}^e \nabla \phi_e) + \bar{r}_m \mathbf{i}_{app}. \end{aligned} \quad (2.24)$$

If the tissue is homogeneous, the  $x$ -axis is aligned with the fibre direction  $\mathbf{a}_1$ , and there is no applied current, the functions,

$$V_m = V_r + \exp\left(\pm \frac{x}{\lambda_l}\right) \quad (2.25a)$$

$$\text{or} \quad V_m = V_r + \exp\left(\pm \frac{x}{\lambda_l}\right) \operatorname{erf}\left(\frac{x}{2\lambda_l} \sqrt{\frac{\tau_m}{t}} \pm \sqrt{\frac{t}{\tau_m}}\right), \quad (2.25b)$$

$$\text{with} \quad \phi_e = A + Bx - \left(\frac{\lambda_l}{\lambda_{el}}\right)^2 (V_m - V_r), \quad (2.25c)$$

are solutions to the system (2.24) when  $\lambda_l$  is defined such that

$$\frac{1}{\lambda_l^2} = \frac{1}{\lambda_{il}^2} + \frac{1}{\lambda_{el}^2}. \quad (2.26)$$

It is clear from solutions (2.25) that  $\tau_m$  is the appropriate time constant and  $\lambda_l$  is the appropriate space constant in direction  $\mathbf{a}_1$ . Space constants  $\lambda_t$  and  $\lambda_n$  can be defined similarly for directions  $\mathbf{a}_t$  and  $\mathbf{a}_n$ . Values for these constants can be obtained by fitting experimentally

measured potentials to the predicted potentials of model solutions such as those in (2.25) (see Section 6.4).

These space and time constants are appropriate when the behaviour of the tissue is largely passive such as in the early stages of the action potential. The behaviour in these stages is important for propagation as it initiates the change in transmembrane potential that leads to activation of the active currents. The time and space constants relevant in the fastest stage of depolarization, however, may be different. The magnitude of the maximum slope of  $i_{\text{ion}}(V_m)$  is much larger than the slope at  $V_m = V_r$  used to define  $R_m$  in equation (2.15). The appropriate multiplier for scaling the system of equations is then smaller than  $\bar{r}_m$  and so the appropriate space and time constants are probably also smaller. The space constants  $\lambda_l$ ,  $\lambda_t$ , and  $\lambda_n$  probably provide an indication of the region of influence that the excitation wavefront has, and, together with  $\tau_m$ , they provide an upper bound on the relevant spatial and temporal scales.

### 2.1.3 One Dimensional Propagation

The effect of anisotropy on propagation can be investigated analytically by considering planar waves travelling in various directions through homogeneous tissue.

A travelling wave solution is sought in the form

$$V_m(\mathbf{x}, t) = v_m(\tau) \quad \text{and} \quad \phi_e(\mathbf{x}, t) = \varphi_e(\tau) \quad (2.27)$$

with

$$\tau = t - \frac{1}{\theta} \mathbf{p} \cdot \mathbf{x}, \quad (2.28)$$

where  $\mathbf{p}$  is a vector of unit magnitude designating the direction of propagation and  $\theta$  is the propagation speed. The action potential profile is the same (except for a displacement in time) at all points in space.

Substituting into system (2.17) with  $\mathbf{i}_{\text{app}} = 0$  leads to

$$\begin{aligned} -\frac{1}{\theta^2} \mathbf{p} \cdot \mathbf{M}^i \mathbf{p} \frac{d^2 v_m}{d\tau^2} &= \frac{1}{\theta^2} \mathbf{p} \cdot (\mathbf{M}^i + \mathbf{M}^e) \mathbf{p} \frac{d^2 \varphi_e}{d\tau^2}, \\ -f_{\text{ion}}(v_m) - \tau_m \frac{dv_m}{d\tau} &= \frac{1}{\theta^2} \mathbf{p} \cdot \mathbf{M}^e \mathbf{p} \frac{d^2 \varphi_e}{d\tau^2}. \end{aligned}$$

The extracellular potential  $\varphi_e$  may be eliminated leaving

$$\begin{aligned} f_{\text{ion}}(v_m) + \tau_m \frac{dv_m}{d\tau} &= \frac{1}{\theta^2} \frac{(\mathbf{p} \cdot \mathbf{M}^i \mathbf{p})(\mathbf{p} \cdot \mathbf{M}^e \mathbf{p})}{\mathbf{p} \cdot (\mathbf{M}^i + \mathbf{M}^e) \mathbf{p}} \frac{d^2 v_m}{d\tau^2} \\ &= \frac{1}{\theta^2} \frac{(\mathbf{p} \cdot \mathbf{M}^i \mathbf{p})(\mathbf{p} \cdot \mathbf{M}^e \mathbf{p})}{\mathbf{p} \cdot \mathbf{M}^i \mathbf{p} + \mathbf{p} \cdot \mathbf{M}^e \mathbf{p}} \frac{d^2 v_m}{d\tau^2}. \end{aligned} \quad (2.29)$$

If there is only one mode of propagation in the direction  $\mathbf{p}_1$ , for example, there must be a unique solution for  $v_m(\tau)$  and  $\theta(\mathbf{p}_1)$ . In any other direction  $\mathbf{p}$  the solution for  $v_m(\tau)$  is still the same and  $\theta(\mathbf{p})$  satisfies

$$\frac{1}{\theta^2(\mathbf{p})} \frac{(\mathbf{p} \cdot \mathbf{M}^i \mathbf{p})(\mathbf{p} \cdot \mathbf{M}^e \mathbf{p})}{\mathbf{p} \cdot \mathbf{M}^i \mathbf{p} + \mathbf{p} \cdot \mathbf{M}^e \mathbf{p}} = \frac{1}{\theta^2(\mathbf{p}_1)} \frac{(\mathbf{p}_1 \cdot \mathbf{M}^i \mathbf{p}_1)(\mathbf{p}_1 \cdot \mathbf{M}^e \mathbf{p}_1)}{\mathbf{p}_1 \cdot \mathbf{M}^i \mathbf{p}_1 + \mathbf{p}_1 \cdot \mathbf{M}^e \mathbf{p}_1}.$$

This implies that

$$\theta^2 \propto \frac{(\mathbf{p} \cdot \mathbf{M}^i \mathbf{p})(\mathbf{p} \cdot \mathbf{M}^e \mathbf{p})}{\mathbf{p} \cdot \mathbf{M}^i \mathbf{p} + \mathbf{p} \cdot \mathbf{M}^e \mathbf{p}}$$

or equivalently

$$\frac{1}{\theta^2} \propto \frac{1}{\mathbf{p} \cdot \mathbf{M}^i \mathbf{p}} + \frac{1}{\mathbf{p} \cdot \mathbf{M}^e \mathbf{p}}. \quad (2.30)$$

The speed of propagation is therefore proportional to the square root of the effective coupling strength in the direction of propagation for the two domains in series.

### 2.1.4 Equal Anisotropy Approximation

If the anisotropy ratios of the coupling tensors were equal so that

$$\frac{1}{\lambda_{il}^2} M^i = \frac{1}{\lambda_{el}^2} M^e,$$

an *effective coupling tensor*  $M$  could be defined by

$$M := \alpha_i M^i = \alpha_e M^e, \quad (2.31)$$

where

$$\alpha_i := \left( \frac{\lambda_l}{\lambda_{il}} \right)^2 \quad \text{and} \quad \alpha_e := \left( \frac{\lambda_l}{\lambda_{el}} \right)^2, \quad (2.32)$$

so that

$$\alpha_i + \alpha_e = 1 \quad \text{and} \quad \frac{1}{\alpha_i} + \frac{1}{\alpha_e} = \frac{1}{\alpha_i \alpha_e}. \quad (2.33)$$

Using definition (2.31) and assuming that  $\alpha_i$  and  $\alpha_e$  are space-independent, system (2.17) could be expressed as

$$\begin{aligned} -\frac{1}{\alpha_i} \nabla \cdot (M \nabla V_m) &= \frac{1}{\alpha_i \alpha_e} \nabla \cdot (M \nabla \phi_e) + \bar{r}_m \mathbf{i}_{app}, \\ -f_{ion}(V_m) - \tau_m \frac{\partial V_m}{\partial t} &= \frac{1}{\alpha_e} \nabla \cdot (M \nabla \phi_e) + \bar{r}_m \mathbf{i}_{app}. \end{aligned} \quad (2.34)$$

The extracellular potential  $\phi_e$  can then be eliminated to give a simple *monodomain* reaction-diffusion equation in one variable:

$$f_{ion}(V_m) + \tau_m \frac{\partial V_m}{\partial t} = \nabla \cdot (M \nabla V_m) - \alpha_e \bar{r}_m \mathbf{i}_{app}. \quad (2.35)$$

Boundary conditions (2.21) could be expressed as

$$\begin{aligned} \frac{1}{\alpha_i} \mathbf{n} \cdot M \nabla (\phi_e + V_m) &= 0 \\ \text{and} \quad \frac{1}{\alpha_e} \mathbf{n} \cdot M \nabla \phi_e &= \bar{r}_m \mathbf{n} \cdot \mathbf{G}^o \nabla \phi_o \quad \text{on } \partial\Omega, \end{aligned}$$

which would imply that

$$\mathbf{n} \cdot \mathbf{M} \nabla V_m = -\alpha_e \bar{\Gamma}_m \mathbf{n} \cdot \mathbf{G}^o \nabla \phi_o \quad \text{on } \partial\Omega. \quad (2.36)$$

If the anisotropic ratios are not equal the monodomain equation (2.35) may still be used as an approximation of the bidomain system (2.17) if the effective coupling tensor is defined by

$$\mathbf{M} := \begin{bmatrix} \mathbf{a}_l & \mathbf{a}_t & \mathbf{a}_n \end{bmatrix} \begin{bmatrix} \lambda_l^2 & 0 & 0 \\ 0 & \lambda_t^2 & 0 \\ 0 & 0 & \lambda_n^2 \end{bmatrix} \begin{bmatrix} \mathbf{a}_l^T \\ \mathbf{a}_t^T \\ \mathbf{a}_n^T \end{bmatrix}. \quad (2.37)$$

To investigate the effect this approximation has on predicted propagation speeds consider the planar wave propagation speeds for homogeneous tissue.

For propagation in any of the three principal directions  $\mathbf{a}_l$ ,  $\mathbf{a}_t$ , or  $\mathbf{a}_n$ , both system (2.17) and equation (2.35) predict the same propagation speeds, but the speeds differ for intermediate directions  $\mathbf{p}$ . The bidomain model predicts that the speeds  $\theta(\mathbf{p})$  satisfy (2.30), but the monodomain model predicts that they satisfy

$$\theta^2 \propto \mathbf{p} \cdot \mathbf{M} \mathbf{p}. \quad (2.38)$$

The resulting predicted propagation speeds based on realistic material parameters (Section 6.4) are plotted in Figure 2.1 for directions between  $\mathbf{a}_l$  and  $\mathbf{a}_t$ . The maximum difference in the predicted speeds from the two models is about 5 per cent, which is significant but still small compared to the uncertainties in the material parameters. For simplicity, this work uses the monodomain approximation, but it is expected that it can be extended to the bidomain model.

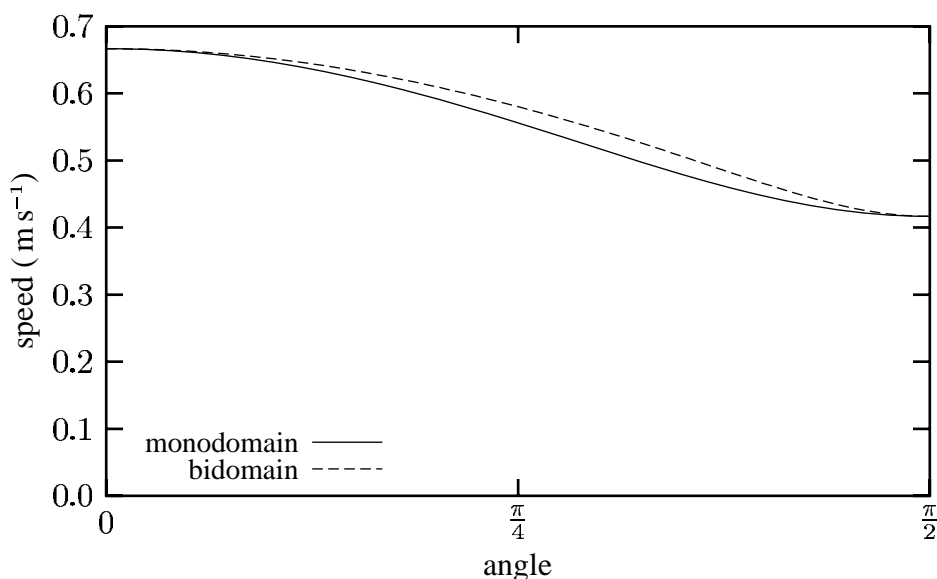


**Figure 2.1:** Planar wave propagation speeds predicted by the bidomain model (2.17) and its monodomain approximation (2.35) for directions in the sheet plane. Speeds are plotted against the angle between the propagation direction and the fibre direction. Material parameters are  $\lambda_{\parallel} = 1.59$  mm,  $\lambda_{it} = 0.66$  mm,  $\lambda_{el} = 0.92$  mm, and  $\lambda_{et} = 0.76$  mm.

## 2.2 The Need for an Eikonal Approach

Solution of the bidomain reaction–diffusion system (2.17) or its monodomain approximation (2.35) is very computationally demanding due to the important spatial scales being much smaller than the dimensions of the ventricles. As discussed in Section 6.4, the space constants for the passive behaviour of canine myocardium are probably  $\lambda_l \approx 0.8$  mm and  $\lambda_t \approx 0.5$  mm. The space constant  $\lambda_n$  for the direction normal to sheets is probably smaller, and, as discussed in Section 2.1.2, the relevant spatial scales in the steepest part of the depolarization upstroke are smaller than these values. Reasonable approximation of the potential would probably require at least 5 degrees of freedom to represent changes over the distance of a space constant. This implies that at least  $5^3$  degrees of freedom would be required to represent a volume of about  $0.8 \times 0.5 \times 0.5 = 0.2$  mm<sup>3</sup>. For the full canine ventricular myocardium with a volume of about  $0.2 \times 10^6$  mm<sup>3</sup>, at least  $10^8$  degrees of freedom would be needed. A time discretization would also be required, but an adaptive mesh could be used so that the number of time steps used to integrate at any point would be only a fraction of the total number of time steps.

Given the difficulty in numerically solving a reaction–diffusion equation for transmembrane potential, a governing equation is sought for the motion of the excitation wavefront. It is expected that the speed of propagation can be assumed to vary more slowly and over much larger spatial scales than the transmembrane potential. This assumption is probably reasonable most of the time but there are abrupt spatial changes in propagation speed where a wavefront collides with the boundary or another wavefront. The fine details of the wavefront shape in these small collision regions are not, however, expected to have much influence on either the overall ventricular function or the electrical fields induced in the torso.

If depolarization is initiated before the tissue has completely repolarized (by a re-entrant wavefront, for example), propagation is dependent on the degree of repolarization of the tissue. In normal propagation, however, the tissue may be assumed to be at rest, so repolarization processes do not need to be considered in modelling excitation wavefront propagation. Ignoring the details of repolarization means that some functional abnormalities such as fibrillation cannot be studied, but saves considerable computational work when modelling the spreading of excitation into quiescent tissue.

The geometric position of the excitation wavefront at any point in time could be described numerically by a set of parameters such as marker particles on the wavefront. However, because the wavefront is continually changing in size and shape and even topology, it would be necessary to continually update the number of marker particles according to the size and complexity of the wavefront at that point in time. It would also be necessary to continually check for wavefront collisions so that the description of the wavefront geometry could be updated appropriately.

The approach adopted here avoids these difficulties by determining the *excitation time* for each point in space (instead of the excitation location at each point in time). This excitation time  $u(\mathbf{x})$  is defined as the time at which the wavefront passes through the point  $\mathbf{x}$ , or more specifically the time at which the transmembrane potential at that point crosses the value midway between its resting and plateau potentials. This means that  $u(\mathbf{x})$  is defined such that

$$V_m(\mathbf{x}, u(\mathbf{x})) = \frac{1}{2} (V_r + V_p), \quad (2.39)$$

where  $V_r$  is the resting transmembrane potential and  $V_p$  is the plateau potential. Although there may not necessarily be a steady-state plateau potential, the value of the potential when

its rate of change significantly reduces after the rapid changes in the upstroke may be considered a plateau.

The position of the wavefront at any time  $t$  is then given by the surface along which  $u(\mathbf{x}) = t$ . The excitation time can be described numerically on a stationary mesh, and, as there is only one excitation time for each point in space, collisions are handled automatically.

Such an approach suggests the use of an *eikonal equation* as the governing equation for the excitation time. The standard eikonal equation,

$$|\nabla u| = 1 \quad (2.40)$$

is used in optics to determine ‘eikonals’  $u(\mathbf{x})$ , which are the path lengths of rays from a source to each point  $\mathbf{x}$  (Klein, 1970, for example). A similar equation can be used to determine the time taken for a myocardial excitation wavefront to reach each point  $\mathbf{x}$ .

## 2.3 Eikonal Equation Derivations

Eikonal equations for myocardial excitation time  $u(\mathbf{x})$  are derived in this section from the reaction–diffusion equation (2.35).

### 2.3.1 Change of Variables

In a normally-functioning heart, although there are variations in the temporal action potential profile through the ventricular myocardium (Anyukhovsky, Sosunov, and Rosen, 1996; Rodriguez-Sinovas, Cinca, Tapias, Armadans, Tresanchez, and Soler-Soler, 1997; Yan, Shimizu, and Antzelevitch, 1998), the depolarization upstroke is similar at each point in the tissue. This suggests that a variable  $\tau$  can be found such that the transmembrane potential

during depolarization is a function only of  $\tau$ . That is

$$V_m(\mathbf{x}, t) = v_m(\tau). \quad (2.41)$$

It is therefore convenient to use a change of variables,

$$\mathbf{x} = \boldsymbol{\xi} \quad \text{and} \quad t = T(\boldsymbol{\xi}, \tau), \quad (2.42)$$

and to choose the transformation function  $T$  such that (2.41) is satisfied. In addition  $\tau = 0$  is defined to be the instant when the transmembrane potential is midway between resting and plateau potentials, so

$$\begin{aligned} V_m(\mathbf{x}, u(\mathbf{x})) &= v_m(0) \\ \Rightarrow u(\mathbf{x}) &= T(\boldsymbol{\xi}, 0). \end{aligned} \quad (2.43)$$

Under this change of variables,

$$\begin{aligned} \frac{\partial}{\partial \xi_i} &= \frac{\partial}{\partial x_i} + \frac{\partial T}{\partial \xi_i} \frac{\partial}{\partial t}, \\ \text{and} \quad \frac{\partial}{\partial \tau} &= \frac{\partial T}{\partial \tau} \frac{\partial}{\partial t}. \end{aligned}$$

Defining  $S(\boldsymbol{\xi}, \tau)$  by

$$S := \left( \frac{\partial T}{\partial \tau} \right)^{-1}, \quad (2.44)$$

it follows that

$$\begin{aligned} \frac{\partial}{\partial t} &= S \frac{\partial}{\partial \tau}, \\ \text{and} \quad \frac{\partial}{\partial x_i} &= \frac{\partial}{\partial \xi_i} - \frac{\partial T}{\partial \xi_i} S \frac{\partial}{\partial \tau}. \end{aligned}$$

As the transmembrane potential is independent of  $\boldsymbol{\xi}$ , and the components  $\mu_{ij}$  of the coupling tensor  $\mathbb{M}$  are independent of  $\tau$ , the spatial derivatives of transmembrane potential can be

written as

$$\begin{aligned}
\frac{\partial V_m}{\partial x_j} &= -S \frac{\partial T}{\partial \xi_j} \frac{dv_m}{d\tau}, \\
\frac{\partial}{\partial x_i} \left( \mu_{ij} \frac{\partial V_m}{\partial x_j} \right) &= \left( S \frac{\partial T}{\partial \xi_i} \frac{\partial}{\partial \tau} - \frac{\partial}{\partial \xi_i} \right) \left( \mu_{ij} S \frac{\partial T}{\partial \xi_j} \frac{dv_m}{d\tau} \right) \\
&= S^2 \frac{\partial T}{\partial \xi_i} \mu_{ij} \frac{\partial T}{\partial \xi_j} \frac{d^2 v_m}{d\tau^2} + S \frac{\partial T}{\partial \xi_i} \frac{\partial}{\partial \tau} \left( S \mu_{ij} \frac{\partial T}{\partial \xi_j} \right) \frac{dv_m}{d\tau} - \frac{\partial}{\partial \xi_i} \left( S \mu_{ij} \frac{\partial T}{\partial \xi_j} \right) \frac{dv_m}{d\tau} \\
&= S^2 \frac{\partial T}{\partial \xi_i} \mu_{ij} \frac{\partial T}{\partial \xi_j} \frac{d^2 v_m}{d\tau^2} + \frac{1}{2} \frac{\partial}{\partial \tau} \left( S^2 \frac{\partial T}{\partial \xi_i} \mu_{ij} \frac{\partial T}{\partial \xi_j} \right) \frac{dv_m}{d\tau} - \frac{\partial}{\partial \xi_i} \left( S \mu_{ij} \frac{\partial T}{\partial \xi_j} \right) \frac{dv_m}{d\tau}.
\end{aligned}$$

The reaction–diffusion equation (2.35) for the transmembrane potential then becomes (assuming no applied current)

$$f_{\text{ion}}(v_m) + \left( \tau_m S + \frac{\partial}{\partial \xi_i} \left( S \mu_{ij} \frac{\partial T}{\partial \xi_j} \right) - \frac{1}{2} \frac{\partial}{\partial \tau} \left( S^2 \frac{\partial T}{\partial \xi_i} \mu_{ij} \frac{\partial T}{\partial \xi_j} \right) \right) \frac{dv_m}{d\tau} = S^2 \frac{\partial T}{\partial \xi_i} \mu_{ij} \frac{\partial T}{\partial \xi_j} \frac{d^2 v_m}{d\tau^2}. \quad (2.45)$$

This equation in  $T(\boldsymbol{\xi}, \tau)$  and  $v_m(\tau)$  now looks more complicated than the reaction–diffusion equation (2.35) in  $V_m(\mathbf{x}, t)$ , but may actually require less computational work to solve. Unlike  $V_m(\mathbf{x}, t)$ , the dependent variable  $T(\boldsymbol{\xi}, \tau)$  is not expected to change rapidly on small spatial scales, so such a fine mesh is probably not required.

Since it is  $u(\mathbf{x}) = T(\boldsymbol{\xi}, 0)$  that is important, it is not necessary to determine  $T(\boldsymbol{\xi}, \tau)$  and  $v_m(\tau)$  for all  $\tau$ . The approach used here is to find an approximate solution of (2.45) that gives an expression for  $u(\mathbf{x})$ . Two methods of finding this approximate solution are now discussed.

### 2.3.2 Solution at the Wavefront

If the function  $T(\boldsymbol{\xi}, 0)$  (which defines the change of variables) could be found to ensure that the coefficients of derivatives of  $v_m$  in (2.45) are functions of  $\tau$  only, then this would guarantee that  $v_m$  is a function of  $\tau$  only. Equating the coefficients of  $\frac{d^2 v_m}{d\tau^2}$  and  $\frac{dv_m}{d\tau}$  to functions of  $\tau$

gives the system,

$$\begin{aligned} S^2 \frac{\partial T}{\partial \xi_i} \mu_{ij} \frac{\partial T}{\partial \xi_j} &= f_1(\tau), \\ \tau_m S + \frac{\partial}{\partial \xi_i} \left( S \mu_{ij} \frac{\partial T}{\partial \xi_j} \right) &= f_2(\tau), \end{aligned} \quad (2.46)$$

where  $f_1$  and  $f_2$  are unknown functions. This system now over-determines the function  $T$ , but an expression for  $u(\mathbf{x})$  can be obtained by solving the equations at  $\tau = 0$ , assuming that they could be approximately satisfied for  $\tau \neq 0$ .

With  $s(\mathbf{x}) := S(\boldsymbol{\xi}, 0)$  chosen to be positive so that  $T$  increases as  $\tau$  increases, system (2.46) at  $\tau = 0$  becomes

$$\begin{aligned} s \sqrt{\frac{\partial u}{\partial x_i} \mu_{ij} \frac{\partial u}{\partial x_j}} &= c_1, \\ \tau_m s + \frac{\partial}{\partial x_i} \left( s \mu_{ij} \frac{\partial u}{\partial x_j} \right) &= c_2, \end{aligned} \quad (2.47)$$

where  $c_1$  and  $c_2$  are constants.

This system of equations is equivalent to that derived by Keener (1991) using a similar process but with the change of variables instead chosen such that  $v_m$  is a function only of a spatial variable normal to the wavefront. The system is parabolic with propagation effectively being determined only by information at the wavefront. The boundary has no effect on propagation until the wavefront actually reaches it. Similarly the propagation of a wavefront is unaffected by another approaching wavefront until a collision occurs.

### 2.3.3 Weighted Integral Solution

System (2.46) does not need to be satisfied in order to satisfy equation (2.45). Here an approximate solution is sought directly for (2.45). The approach is to determine a first order approximation of  $T$  that satisfies the equation as closely as possible. The first order approximation assumes that the shape of the upstroke of the temporal action potential profile is the

same at every point in space except for a translation and a linear stretch in time. That is

$$T(\boldsymbol{\xi}, \tau) := u(\boldsymbol{\xi}) + \frac{\tau}{s(\boldsymbol{\xi})}. \quad (2.48)$$

The residual in equation (2.45) is then

$$f_{\text{ion}}(v_m) + \left( \tau_m s + s \frac{\partial}{\partial \xi_i} \left( \mu_{ij} \frac{\partial T}{\partial \xi_j} \right) + \frac{\partial s}{\partial \xi_i} \mu_{ij} \frac{\partial T}{\partial \xi_j} - \frac{1}{2} \frac{\partial}{\partial \tau} \left( s^2 \frac{\partial T}{\partial \xi_i} \mu_{ij} \frac{\partial T}{\partial \xi_j} \right) \right) \frac{dv_m}{d\tau} - s^2 \frac{\partial T}{\partial \xi_i} \mu_{ij} \frac{\partial T}{\partial \xi_j} \frac{d^2 v_m}{d\tau^2}, \quad (2.49)$$

but

$$\begin{aligned} \frac{\partial s}{\partial \xi_i} \mu_{ij} \frac{\partial T}{\partial \xi_j} &= -s^2 \frac{\partial}{\partial \xi_i} \left( \frac{1}{s} \right) \mu_{ij} \frac{\partial T}{\partial \xi_j} \\ &= -s^2 \frac{\partial^2 T}{\partial \xi_i \partial \tau} \mu_{ij} \frac{\partial T}{\partial \xi_j} \\ &= -\frac{1}{2} \frac{\partial}{\partial \tau} \left( s^2 \frac{\partial T}{\partial \xi_i} \mu_{ij} \frac{\partial T}{\partial \xi_j} \right) \end{aligned} \quad (2.50)$$

and

$$\frac{\partial}{\partial \tau} \left( s^2 \frac{\partial T}{\partial \xi_i} \mu_{ij} \frac{\partial T}{\partial \xi_j} \right) \frac{dv_m}{d\tau} + s^2 \frac{\partial T}{\partial \xi_i} \mu_{ij} \frac{\partial T}{\partial \xi_j} \frac{d^2 v_m}{d\tau^2} = \frac{\partial}{\partial \tau} \left( s^2 \frac{\partial T}{\partial \xi_i} \mu_{ij} \frac{\partial T}{\partial \xi_j} \frac{dv_m}{d\tau} \right), \quad (2.51)$$

so applying (2.50) and (2.51) to (2.49) allows the residual to be written as

$$f_{\text{ion}}(v_m) + \left( \tau_m s + s \frac{\partial}{\partial \xi_i} \left( \mu_{ij} \frac{\partial T}{\partial \xi_j} \right) \right) \frac{dv_m}{d\tau} - \frac{\partial}{\partial \tau} \left( s^2 \frac{\partial T}{\partial \xi_i} \mu_{ij} \frac{\partial T}{\partial \xi_j} \frac{dv_m}{d\tau} \right). \quad (2.52)$$

The aim is now to make this residual as close to zero as is possible over all  $\tau$  under the restriction of the first order approximation (2.48). There are two parameters to find so two weighted integrals over  $\tau$  are set to zero. The propagation of the wavefront is expected to be almost unaffected by features far from the wavefront, so a Gaussian in  $\tau$  is included as a multiplier in both weights to emphasize the interval near the wavefront. The weights are chosen to be

$$w_1 = e^{-\alpha\tau^2} \quad \text{and} \quad w_2 = \tau e^{-\alpha\tau^2}. \quad (2.53)$$

The weighted integral of residual (2.52) with weight  $w_1$  asks that (2.45) is satisfied in an average sense. The weights approach zero at  $\pm\infty$  and  $w_2$  is essentially a derivative of  $w_1$ , so Green's theorem can be applied to show that the integral with weight  $w_2$  is equivalent to a weighted integral with  $w_1$  of the derivative of (2.52) with respect to  $\tau$ .

Multiplying (2.52) by  $w_1$ , integrating over  $\tau$ , and setting the result to zero gives

$$\begin{aligned} \int_{-\infty}^{\infty} f_{\text{ion}}(v_m) w_1 \, d\tau + \int_{-\infty}^{\infty} \left( \tau_m s + s \frac{\partial}{\partial \xi_i} \left( \mu_{ij} \frac{\partial T}{\partial \xi_j} \right) \right) \frac{dv_m}{d\tau} w_1 \, d\tau \\ = \int_{-\infty}^{\infty} \frac{\partial}{\partial \tau} \left( s^2 \frac{\partial T}{\partial \xi_i} \mu_{ij} \frac{\partial T}{\partial \xi_j} \frac{dv_m}{d\tau} \right) w_1 \, d\tau \\ = - \int_{-\infty}^{\infty} s^2 \frac{\partial T}{\partial \xi_i} \mu_{ij} \frac{\partial T}{\partial \xi_j} \frac{dv_m}{d\tau} \frac{\partial w_1}{\partial \tau} \, d\tau. \quad (2.54) \end{aligned}$$

The change to the right hand side is an application of Green's theorem using the fact that  $w_1 \rightarrow 0$  as  $\tau \rightarrow \pm\infty$ . Substituting expressions (2.48) for  $T$  and (2.53) for  $w_1$  gives

$$\begin{aligned} \int_{-\infty}^{\infty} f_{\text{ion}}(v_m) e^{-\alpha\tau^2} \, d\tau + \left( \tau_m s + s \frac{\partial}{\partial \xi_i} \left( \mu_{ij} \frac{\partial u}{\partial \xi_j} \right) \right) \int_{-\infty}^{\infty} \frac{dv_m}{d\tau} e^{-\alpha\tau^2} \, d\tau \\ + s \frac{\partial}{\partial \xi_i} \left( \mu_{ij} \frac{\partial}{\partial \xi_j} \left( \frac{1}{s} \right) \right) \int_{-\infty}^{\infty} \frac{dv_m}{d\tau} \tau e^{-\alpha\tau^2} \, d\tau \\ = 2\alpha s^2 \frac{\partial u}{\partial \xi_i} \mu_{ij} \frac{\partial u}{\partial \xi_j} \int_{-\infty}^{\infty} \frac{dv_m}{d\tau} \tau e^{-\alpha\tau^2} \, d\tau \\ + 4\alpha s^2 \frac{\partial}{\partial \xi_i} \left( \frac{1}{s} \right) \mu_{ij} \frac{\partial u}{\partial \xi_j} \int_{-\infty}^{\infty} \frac{dv_m}{d\tau} \tau^2 e^{-\alpha\tau^2} \, d\tau \\ + 2\alpha s^2 \frac{\partial}{\partial \xi_i} \left( \frac{1}{s} \right) \mu_{ij} \frac{\partial}{\partial \xi_j} \left( \frac{1}{s} \right) \int_{-\infty}^{\infty} \frac{dv_m}{d\tau} \tau^3 e^{-\alpha\tau^2} \, d\tau. \quad (2.55) \end{aligned}$$

All of the integrands now depend only on  $\tau$ , so all the integrals are constant, therefore giving an equation in  $u$  and  $s$ . The equation can be simplified considerably, however, by removing the small terms. No scale has yet been defined for  $\tau$ , so its scale can be chosen such that most of the variation in  $v_m$  across the wavefront occurs over a unit change in  $\tau$ . Dimensional

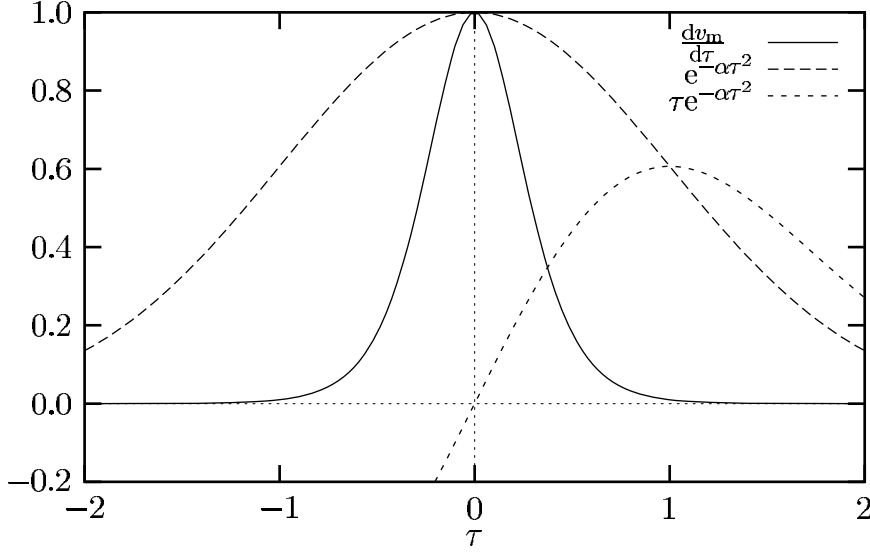


Figure 2.2: Comparison of magnitudes of  $e^{-\alpha\tau^2}$  and  $\tau e^{-\alpha\tau^2}$  with  $\frac{dv_m}{d\tau}$  for  $\alpha = 0.5$ .

analysis then suggests that the following terms are of similar size:

$$\begin{aligned} \left| s \frac{\partial}{\partial \xi_i} \left( \mu_{ij} \frac{\partial u}{\partial \xi_j} \right) \right| &\sim \left| s \frac{\partial}{\partial \xi_i} \left( \mu_{ij} \frac{\partial}{\partial \xi_j} \left( \frac{1}{s} \right) \right) \right| \\ &\sim \left| s^2 \frac{\partial u}{\partial \xi_i} \mu_{ij} \frac{\partial u}{\partial \xi_j} \right| \sim \left| s^2 \frac{\partial}{\partial \xi_i} \left( \frac{1}{s} \right) \mu_{ij} \frac{\partial u}{\partial \xi_j} \right| \sim \left| s^2 \frac{\partial}{\partial \xi_i} \left( \frac{1}{s} \right) \mu_{ij} \frac{\partial}{\partial \xi_j} \left( \frac{1}{s} \right) \right|. \end{aligned} \quad (2.56)$$

The coefficients of these terms in (2.55) are all integrals of  $\frac{dv_m}{d\tau}$  multiplied by  $e^{-\alpha\tau^2}$  and various powers of  $\tau$ . Figure 2.2 shows a profile for  $\frac{dv_m}{d\tau}$  illustrating the expected dominating features during the depolarization upstroke together with plots of  $e^{-\alpha\tau^2}$  and  $\tau e^{-\alpha\tau^2}$  for  $\alpha = 0.5$ . It can be seen that, in the ranges of  $\tau$  where  $\frac{dv_m}{d\tau}$  has a significant magnitude,  $e^{-\alpha\tau^2}$  is large but  $\tau e^{-\alpha\tau^2}$  is small, implying that

$$\left| \int_{-\infty}^{\infty} \frac{dv_m}{d\tau} e^{-\alpha\tau^2} d\tau \right| \gg \left| \int_{-\infty}^{\infty} \frac{dv_m}{d\tau} \tau e^{-\alpha\tau^2} d\tau \right|.$$

It can similarly be argued that integrals containing higher powers of  $\tau$  are even smaller. So provided  $\alpha \lesssim 0.5$  (i.e. the Gaussian is wide enough), the terms on the right hand side of (2.55) and the last term on the left hand side are all small compared to the second to last term

on the left hand side. Removing these small terms leaves

$$\tau_m s + s \frac{\partial}{\partial \xi_i} \left( \mu_{ij} \frac{\partial u}{\partial \xi_j} \right) \approx c_2. \quad (2.57)$$

Multiplying residual (2.52) by  $w_2$  and setting the integral over  $\tau$  to zero yields a second equation in  $u$  and  $s$ :

$$\begin{aligned} & \int_{-\infty}^{\infty} f_{\text{ion}}(v_m) \tau e^{-\alpha \tau^2} d\tau + \left( \tau_m s + s \frac{\partial}{\partial \xi_i} \left( \mu_{ij} \frac{\partial u}{\partial \xi_j} \right) \right) \int_{-\infty}^{\infty} \frac{dv_m}{d\tau} \tau e^{-\alpha \tau^2} d\tau \\ & \quad + s \frac{\partial}{\partial \xi_i} \left( \mu_{ij} \frac{\partial}{\partial \xi_j} \left( \frac{1}{s} \right) \right) \int_{-\infty}^{\infty} \frac{dv_m}{d\tau} \tau^2 e^{-\alpha \tau^2} d\tau \\ & = -s^2 \frac{\partial u}{\partial \xi_i} \mu_{ij} \frac{\partial u}{\partial \xi_j} \int_{-\infty}^{\infty} \frac{dv_m}{d\tau} e^{-\alpha \tau^2} d\tau - 2s^2 \frac{\partial}{\partial \xi_i} \left( \frac{1}{s} \right) \mu_{ij} \frac{\partial u}{\partial \xi_j} \int_{-\infty}^{\infty} \frac{dv_m}{d\tau} \tau e^{-\alpha \tau^2} d\tau \\ & \quad - s^2 \frac{\partial}{\partial \xi_i} \left( \frac{1}{s} \right) \mu_{ij} \frac{\partial}{\partial \xi_j} \left( \frac{1}{s} \right) \int_{-\infty}^{\infty} \frac{dv_m}{d\tau} \tau^2 e^{-\alpha \tau^2} d\tau + 2\alpha s^2 \frac{\partial u}{\partial \xi_i} \mu_{ij} \frac{\partial u}{\partial \xi_j} \int_{-\infty}^{\infty} \frac{dv_m}{d\tau} \tau^2 e^{-\alpha \tau^2} d\tau \\ & \quad + 4\alpha s^2 \frac{\partial}{\partial \xi_i} \left( \frac{1}{s} \right) \mu_{ij} \frac{\partial u}{\partial \xi_j} \int_{-\infty}^{\infty} \frac{dv_m}{d\tau} \tau^3 e^{-\alpha \tau^2} d\tau + 2\alpha s^2 \frac{\partial}{\partial \xi_i} \left( \frac{1}{s} \right) \mu_{ij} \frac{\partial}{\partial \xi_j} \left( \frac{1}{s} \right) \int_{-\infty}^{\infty} \frac{dv_m}{d\tau} \tau^4 e^{-\alpha \tau^2} d\tau. \end{aligned} \quad (2.58)$$

The first term on the left hand side is constant and (2.57) implies that the second term is effectively constant. From (2.56) and consideration of the magnitudes of the integrals, the first term on the right hand dominates the remaining terms, so removing the small terms leaves

$$s^2 \frac{\partial u}{\partial \xi_i} \mu_{ij} \frac{\partial u}{\partial \xi_j} \approx c_1^2. \quad (2.59)$$

Reverting back to the original coordinate system and choosing  $s$  to be positive, (2.57) and (2.59) provide the following governing system of equations:

$$\begin{aligned} & s \sqrt{\frac{\partial u}{\partial x_i} \mu_{ij} \frac{\partial u}{\partial x_j}} = c_1, \\ & \tau_m s + s \frac{\partial}{\partial x_i} \left( \mu_{ij} \frac{\partial u}{\partial x_j} \right) = c_2. \end{aligned} \quad (2.60)$$

This system is equivalent to the first order equation derived by Colli Franzone, Guerri, and Rovida (1990) and Colli Franzone, Guerri, and Tentoni (1990) using singular perturbation techniques if the intra- and extracellular conductivities have equal anisotropy ratios. The system is elliptic so wavefront propagation depends on the properties of the whole domain.

The elliptic system demands a boundary condition. Without a model of the surrounding tissue, it is not possible to predict the current flux from the outside domain so the boundary condition (2.36) for the reaction–diffusion system is not helpful. However, experimental evidence suggests that epicardial isochrones are unaffected by surrounding conducting volumes (Green, Taccardi, Ershler, and Lux, 1991). Without a surrounding volume, boundary condition (2.36) reduces to the simple no-flux boundary condition,

$$\frac{\partial V_m}{\partial x_i} \mu_{ij} n_j = 0 \quad \text{on } \partial\Omega. \quad (2.61)$$

Applying coordinate transformation (2.42) leads to

$$\begin{aligned} -\frac{\partial T}{\partial \xi_i} S \frac{dv_m}{d\tau} \mu_{ij} n_j &= 0 \\ \Rightarrow \frac{\partial T}{\partial \xi_i} \mu_{ij} n_j &= 0, \end{aligned} \quad (2.62)$$

so at  $\tau = 0$ ,

$$\frac{\partial u}{\partial \xi_i} \mu_{ij} n_j = \frac{\partial u}{\partial x_i} \mu_{ij} n_j = 0 \quad \text{on } \partial\Omega. \quad (2.63)$$

This boundary condition may not be entirely appropriate when there is a surrounding conductor. However, the observation that surrounding conductors do not affect epicardial isochrones suggests that the effect of inaccuracies in this boundary condition on the excitation sequence must be small.

## 2.4 Comparison of Eikonal Equations

In each of the two systems of equations, (2.47) and (2.60), the unknown  $s$  can be eliminated to give single equations in excitation time  $u$  only. There are then two possible governing equations for the wavefront propagation. With  $c_0$  defined as  $\frac{c_2}{c_1}$ , system (2.47) reduces to the

parabolic equation,

$$c_0 \sqrt{\nabla u \cdot M \nabla u} - \sqrt{\nabla u \cdot M \nabla u} \nabla \cdot \left( \frac{M \nabla u}{\sqrt{\nabla u \cdot M \nabla u}} \right) = \tau_m, \quad (2.64)$$

and system (2.60) reduces to the elliptic equation,

$$c_0 \sqrt{\nabla u \cdot M \nabla u} - \nabla \cdot (M \nabla u) = \tau_m, \quad (2.65)$$

with the boundary condition,

$$\mathbf{n} \cdot M \nabla u = 0, \quad (2.66)$$

where  $\mathbf{n}$  is the unit normal to the boundary. Interpretations of the governing equations can be made from each of the terms involved.

The contours of  $u$  give the positions of the wavefront at time,  $t = u$ . The gradient of  $u$  at any point along one of these contours is therefore normal to that wavefront surface and has magnitude equal to the reciprocal of the speed of that point on the wavefront. That is

$$\nabla u = \frac{1}{\theta} \mathbf{p}, \quad (2.67)$$

where  $\theta$  is the local wavefront speed and  $\mathbf{p}$  is the unit normal to the wavefront pointing away from depolarized tissue. A space constant  $\rho$  in the direction of propagation  $\mathbf{p}$  may be calculated from the square root of the component of the coupling tensor in that direction:

$$\rho := \sqrt{\mathbf{p} \cdot M \mathbf{p}}. \quad (2.68)$$

Both governing equations, (2.64) and (2.65) have the same first term, which may be written as

$$c_0 \sqrt{\nabla u \cdot M \nabla u} = c_0 \frac{\rho}{\theta}. \quad (2.69)$$

This term is an anisotropic generalization of the left hand side of the standard eikonal equation (2.40). It is a function of the local speed of the wavefront surface and is called the *evolution* term.

The second term in the parabolic equation (2.64) may be written as,

$$\sqrt{\nabla u \cdot M \nabla u} \nabla \cdot \left( \frac{M \nabla u}{\sqrt{\nabla u \cdot M \nabla u}} \right) = \frac{\rho}{\theta} \nabla \cdot \left( \frac{1}{\rho} M \mathbf{p} \right) = \frac{\rho}{\theta} \kappa, \quad (2.70)$$

where  $\kappa$  is an anisotropic generalization of mean curvature. It is positive when the wavefront is convex if viewed from ahead of the wavefront. The parabolic equation is therefore called an *eikonal–curvature equation*.

Using expressions (2.69) and (2.70) in the eikonal–curvature equation (2.64) gives

$$\frac{\tau_m}{\rho} \theta = c_0 - \kappa. \quad (2.71)$$

For a given propagation direction, this equation states that the speed of the wavefront is a linear function of its anisotropic mean curvature. Propagation is faster when the wavefront is concave, and slower when it is convex. This makes sense physically as the depolarization of tissue depends upon diffusion of charge from already depolarized tissue. If there is more depolarized tissue in close proximity to a region of quiescent tissue then that region will be depolarized faster.

Propagation is also a function of the spatial variation in the coupling tensor through the anisotropic mean curvature term  $\kappa$ . For example, if the coupling is increasing in the direction of propagation, then a greater proportion of the current supplied to depolarizing tissue on the wavefront is drawn away ahead of the wavefront, so the tissue depolarization and wavefront propagation are slower.

If  $\kappa = 0$ , the speed of propagation is  $c_0$  space constants per time constant. The constant  $c_0$  is therefore the dimensionless propagation speed for a planar wavefront in homogeneous tissue.

The second term in the elliptic eikonal equation (2.65) is a generalized Laplacian representing anisotropic diffusion of  $u$ . The equation is therefore called an *eikonal–diffusion equation*. Although it is difficult to comprehend diffusion of excitation time, it is not too surprising that there is a Laplacian in the governing equation as the propagation process depends heavily on the diffusion of charge.

Note that the eikonal–curvature equation (2.64) may be written as

$$c_0 \sqrt{\nabla u \cdot M \nabla u} - \nabla \cdot (M \nabla u) + \nabla \sqrt{\nabla u \cdot M \nabla u} \cdot \frac{M \nabla u}{\sqrt{\nabla u \cdot M \nabla u}} = \tau_m, \quad (2.72)$$

and differs from the eikonal–diffusion equation (2.65) only in the additional third term. This additional term is effectively the component of the generalized Laplacian normal to the wavefront surface, so the eikonal–curvature equation may be considered as equivalent to the eikonal–diffusion equation except that it lacks the component of the Laplacian in the direction of propagation.

The eikonal–diffusion equation (2.65) may be written as

$$c_0 \frac{\rho}{\theta} + \nabla \cdot \left( \frac{1}{\theta} M \mathbf{p} \right) = \tau_m, \quad (2.73)$$

which is equivalent to

$$\frac{\tau_m}{\rho} \theta = c_0 - \kappa + \frac{1}{\theta} \nabla \cdot \left( \frac{\theta}{\rho} \right) M \mathbf{p}. \quad (2.74)$$

The last term, which is not in the eikonal–curvature equation (2.71), is what makes this equation elliptic. Under this equation, propagation speed depends not only on information at the wavefront, but also on the activity of the surrounding tissue. The constant  $c_0$  is still the dimensionless speed of steady wavefront propagation in infinite homogeneous tissue.

### 2.4.1 Ellipsoidal Wavefronts

It is interesting to investigate three-dimensional analytic solutions to these two governing equations for a wavefront spreading out from the origin in an infinite homogeneous domain. There exist solutions that may be written as functions of only the dimensionless distance from the origin,

$$r := \sqrt{\mathbf{x} \cdot M^{-1} \mathbf{x}}. \quad (2.75)$$

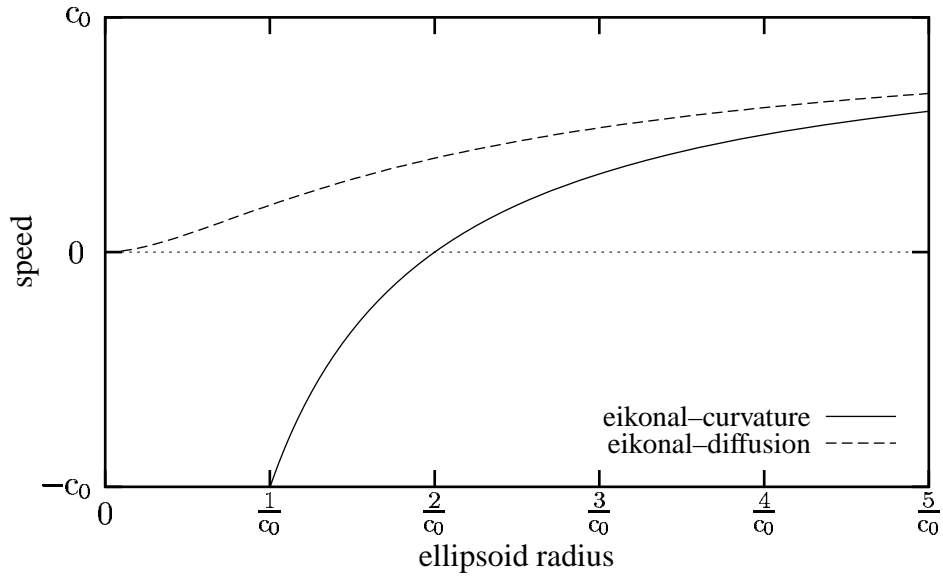


**Figure 2.3:** Dimensionless propagation speeds of a small ellipsoidal wavefront, as specified by two eikonal equation variants. The ellipsoid radius is the dimensionless distance  $r$ , which is the number of space constants from the origin. The dimensionless propagation speed is measured in the direction away from the origin with units of space constants per time constant.

The eikonal–curvature equation (2.64) has the solution

$$\frac{u}{\tau_m} = \frac{r}{c_0} + \frac{2}{c_0^2} \ln |c_0 r - 2|, \quad (2.76)$$

and the eikonal–diffusion equation (2.65) has the solution

$$\frac{u}{\tau_m} = \frac{r}{c_0} + \frac{2}{c_0^2} \ln(c_0 r) - \frac{2}{c_0^3 r}. \quad (2.77)$$

The solutions describe ellipsoidal wavefronts having the same principal axes as the coupling tensor. Both eikonal equations predict that an initial wavefront of this shape will retain the same shape as it spreads outwards. Figure 2.3 plots the speed of these ellipsoidal wavefronts against their size for each of the equations. The speed plotted is a dimensionless speed defined as the reciprocal of  $\frac{1}{\tau_m} \frac{du}{dr}$ . Under the eikonal–curvature equation, this is

$$\frac{\tau_m}{\frac{du}{dr}} = c_0 \frac{r - \frac{2}{c_0}}{r}, \quad (2.78)$$

and under the eikonal–diffusion equation, it is

$$\frac{\tau_m}{\frac{du}{dr}} = c_0 \frac{r^2}{r^2 + \frac{2}{c_0}r + \frac{2}{c_0^2}}. \quad (2.79)$$

For very large  $r$ , both equations predict that the ellipsoid grows at the same constant speed, but for small  $r$ , the equations differ in the way they predict propagation under large curvature.

The eikonal–curvature equation has a singularity at  $r = \frac{2}{c_0}$ . The equation suggests that the initially depolarized region must have a radius of at least  $\frac{2}{c_0}$  space constants in order for the region to be able to supply enough current to surrounding tissue for propagation to proceed. If the initially depolarized region is smaller than this threshold size, then the equation predicts that the wavefront will retreat, and the region will repolarize.

The eikonal–diffusion equation only has a singularity at the origin. The equation suggests that if enough current has been injected into the tissue to depolarize a region of tissue, then propagation will proceed however small this region may be. Initial propagation may, however, be very slow.

## 2.4.2 Boundary Effects

Analytic one-dimensional solutions to the eikonal–curvature equation (2.64) and the eikonal–diffusion equation (2.65) are compared in Figure 2.4 with a numerical solution to the reaction–diffusion equation (2.35) obtained using an explicit finite difference scheme. Excitation is initiated at the left hand end and the no-flux boundary condition (2.61) is specified at the right hand end. For the reaction–diffusion equation, the cubic current/voltage law,

$$f_{\text{ion}}(V_m) = V_m(1 - V_m)(1 - 10V_m) \quad (2.80)$$

was used to model ionic current. For the eikonal equations, the parameter  $c_0$  was set to 1.789, which is the analytic steady-state dimensionless propagation speed for the reaction–diffusion equation with this ionic current model (Hunter, McNaughton, and Noble, 1975).

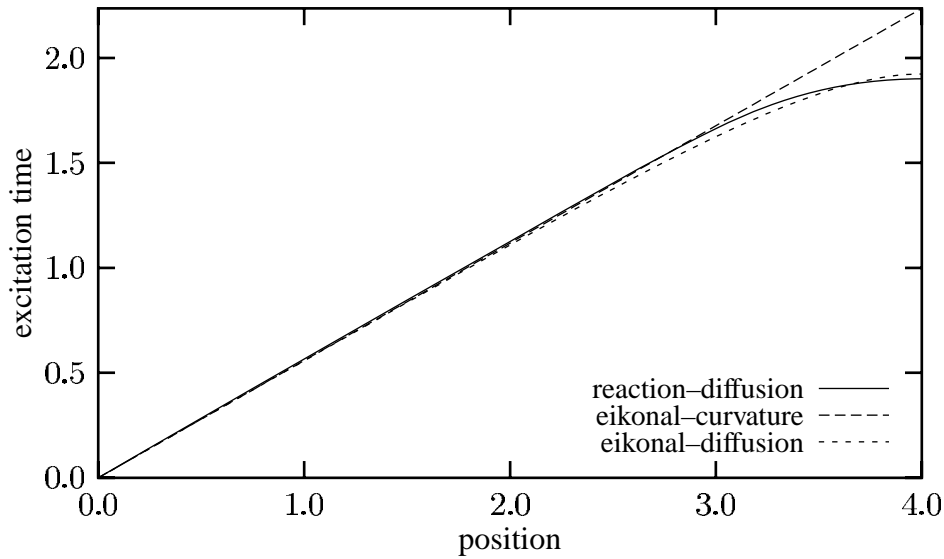


**Figure 2.4:** Eikonal and reaction–diffusion equation solutions for excitation initiated at the left hand end of tissue four space constants in length. The labels for position indicate the number of space constants and labels for activation time indicate the number of time constants.

The problem represented in Figure 2.4 is equivalent to a planar wavefront colliding with a parallel boundary. As mentioned in Section 2.3.3, the no-flux boundary condition may not be appropriate if the boundary is in contact with another conducting volume, but this simple problem allows us to consider the behaviour of two planar wavefronts colliding. If two wavefronts are colliding at the right hand end of Figure 2.4, symmetry leads to the no-flux boundary condition.

As a wavefront approaches a no-flux boundary or another approaching wavefront, there is less quiescent tissue to drain current from the depolarizing tissue at the wavefront, so depolarization is faster. The effect this has on propagation can be seen in the solution to the reaction–diffusion system, which shows faster propagation near the boundary. Notice, however, that the eikonal–curvature equation does not include any effects of the boundary or collision on wavefront propagation. The solution to the eikonal–diffusion equation, on the other hand, satisfies the boundary condition (2.66).

The eikonal–diffusion equation much more accurately models the variations in propagation speed due to another approaching wavefront. Although it is uncertain what the correct be-

haviour near a boundary with a surrounding volume should be, the eikonal–diffusion equation at least more accurately approximates the reaction–diffusion equation in this case. The region over which solutions disagree is small, but the eikonal–diffusion equation (2.65) certainly provides a better approximation of the reaction–diffusion equation.

In more than one dimension, the boundary condition (2.66) for eikonal equation (2.65) gives a relationship between propagation direction and the boundary surface. If one of the principal directions of the coupling tensor is perpendicular to the boundary (for example, if fibre sheets are parallel to the boundary), then (2.66) states that the wavefront must be orthogonal to the boundary. Otherwise the relationship is more complex.

### 2.4.3 Summary

The two eikonal equations proposed for modelling propagation are summarized in Table 2.1.

Equation	Eikonal–Diffusion (2.65)	Eikonal–Curvature (2.64)
Reference	Colli Franzone, Guerri, and Rovida, 1990; Colli Franzone, Guerri, and Tentoni, 1990.	Keener, 1991.
Nature	elliptic.	parabolic.
Terms	evolution, curvature, diffusion normal to the wavefront.	evolution, curvature.
Direction of wavefront motion	The wavefront always moves towards resting tissue.	The wavefront retreats if its curvature is greater than a threshold (or if the region of excited tissue is smaller than a threshold).
Boundary effects	The wavefront accelerates when approaching a boundary or another wavefront.	Boundaries and other wavefronts have no influence.

**Table 2.1:** Summary of the two eikonal equations proposed for modelling myocardial excitation wavefront propagation.

The eikonal–diffusion equation (2.65) seems to better approximate the reaction–diffusion equation near wavefront collisions. It is also more numerically appealing with its one-directional wavefront motion and its elliptic nature (2.65). The eikonal–diffusion equation is selected as the governing eikonal equation and shall be referred to simply as the eikonal equation.

## 2.5 Numerical Solution of an Eikonal Equation

The governing eikonal equation (2.65) has the advantages over the reaction–diffusion equation (2.35) that the domain is reduced by one dimension (because the dependent variable is no longer a function of time) and that the important spatial scales are much larger. In order to make use of these advantages, a numerical method needs to be found that requires only a spatial discretization and will work effectively when this discretization is reasonably coarse.

Numerical solution of an elliptic differential equation usually involves two main stages. The first of these is discretization, in which the dependent variable is described by a finite number of parameters and the governing equation is reduced to a system of a finite number of equations. The second stage is solving these equations. The discrete system of equations determines what the numerical solution should satisfy, and so determines the solution itself. The first stage therefore determines what the numerical solution is and the second merely finds this solution.

The two stages are not unrelated, however, as the choice of a method for solving the discrete system of equations and the ease or difficulty with which they can be solved depends on their nature. This needs to be taken into consideration when selecting the discretization of the governing equation. The non-linear nature of the eikonal equation means that solving the discrete system may be difficult and the solution may not even be unique.

### 2.5.1 Comparison with the Advection–Diffusion Equation

If the eikonal equation (2.65) is written in the form,

$$c_0 \frac{M \nabla u}{\sqrt{\nabla u \cdot M \nabla u}} \cdot \nabla u - \nabla \cdot (M \nabla u) = \tau_m, \quad (2.81)$$

then its similarity to the generalized classic steady-state *advection–diffusion equation*,

$$\mathbf{a} \cdot \nabla u - \nabla \cdot (M \nabla u) = \tau_m \quad (2.82)$$

can be seen. This linear advection–diffusion equation is used to model transport of solutes ( $u$  is solute concentration) or heat ( $u$  is temperature) in a fluid with velocity field  $\mathbf{a}$ , diffusion tensor  $M$ , and source field  $\tau_m$ . The first term is called the *advection* term and represents transport due to fluid motion, while the second term is called the *diffusion* term and represents diffusive transport. These correspond to the evolution and diffusion terms in the eikonal equation.

The evolution term in the eikonal equation (2.81) is like an advection term except that the velocity field  $\mathbf{a}$  depends on the gradient of the solution. It does not depend on the magnitude of the gradient but only on its direction. In an isotropic domain, the coefficient vector has constant magnitude and is in the direction of wavefront propagation. The eikonal equation can therefore be considered a non-linear advection–diffusion equation where the direction of the velocity field depends on the direction of wavefront propagation.

As the space constants for the coupling tensor  $M$  are several times smaller than the spatial dimensions of the tissue, the magnitude of the evolution term tends to be significantly larger than that of the diffusion term. The process of wavefront propagation is therefore said to be evolution dominated.

The similarity between these two equations suggests that the discretization techniques used for numerical solution of the advection–diffusion equation may also be effective for the eikonal equation. The non-linearity of the eikonal equation, however, necessitates the use of a different procedure for solving the resulting discrete system.

### 2.5.2 Previous Approaches

Myocardial excitation models that are based on Huygens' principle are effectively approximating an eikonal equation. More accurate numerical solutions to eikonal equations for excitation wavefront propagation have been obtained by two approaches that use related time-dependent parabolic equations.

#### *Huygens' Principle*

Many myocardial excitation models have been based on Huygens' principle (reviewed by Plonsey and Barr, 1987). In such models, the heart is represented by a matrix of cells or grid points. At fixed time intervals after any cell is excited, its quiescent neighbouring cells are excited. The time interval before excitation of each neighbouring cell depends on the distance to the cell and the propagation speed for that direction.

The speed of propagation  $\theta$  can be calculated from an ellipsoidal function of the propagation direction  $\mathbf{p}$ ,

$$\theta = \sqrt{\mathbf{p} \cdot \mathbf{H} \mathbf{p}}, \quad (2.83)$$

where  $\mathbf{H}$  is a symmetric positive definite tensor. From the relation of propagation speed and direction to the gradient of activation time (2.67), the speed function suggests that

$$\sqrt{\nabla u \cdot \mathbf{H} \nabla u} = 1, \quad (2.84)$$

which is an anisotropic generalization of the standard eikonal equation (2.40). Although this eikonal equation does not include the effects of curvature on propagation, it probably provides a reasonable approximation of the large scale features of the overall excitation sequence.

This method has the advantage that it requires little computational effort. The disadvantage is that the numerical treatment of the eikonal equation is very low order and propagation can only occur in a finite number of directions. The result is that the wavefronts generated are polyhedral instead of ellipsoidal.

*Relaxation*

In their numerical solution of the eikonal equation, Colli Franzone and Guerri (1993b) added a time derivative term to give a related parabolic equation in space and time. For the eikonal equation (2.65), the related time-dependent equation is

$$\frac{\partial \varphi}{\partial t} + c_0 \sqrt{\nabla \varphi \cdot M \nabla \varphi} - \nabla \cdot (M \nabla \varphi) = \tau_m. \quad (2.85)$$

Note that this equation becomes equivalent to (2.65) when  $\frac{\partial \varphi}{\partial t} = 0$ , so the steady-state solution for  $\varphi(\mathbf{x}, t)$  is the excitation time  $u(\mathbf{x})$ . To find this steady-state solution, spatial discretization was performed using finite-element-like integrals of quantities calculated by finite differences, and a finite difference scheme was used to step through time until an initial guess for  $u$  approached its limiting value. The spatial discretization was later modified by Colli Franzone, Guerri, Pennacchio, and Taccardi (1998) so that traditional finite element integrals were used for most terms but a first-order upwind finite difference was used in the evolution term.

Each time step is linear if the evolution term is treated explicitly, and using a purely explicit finite difference scheme in time gave a method that was similar to Jacobi successive over-relaxation. In order to avoid instability, the time step (or relaxation parameter) had to be small, so convergence was very slow. Treating the diffusion term implicitly may give a larger possible time step and an improved relaxation scheme, but, because the diffusion term tends to be small, convergence would still be slow.

*Level Sets*

Another method is that used by Keener (1991). Instead of finding excitation time, a parabolic time-dependent equation was solved for the function  $\varphi(\mathbf{x}, t)$  defined so that, at any time  $t$ , the level set of points  $\mathbf{x}$  such that  $\varphi(\mathbf{x}, t) = 0$  gives the position of the wavefront at that time. An equation for  $\varphi$  corresponding to the eikonal equation (2.65) is

$$c_0 \sqrt{\nabla \varphi \cdot M \nabla \varphi} + \nabla \cdot (M \nabla \varphi) = \tau_m \frac{\partial \varphi}{\partial t}. \quad (2.86)$$

The numerical solution for  $\varphi(\mathbf{x}, t)$  was found using finite difference discretizations in space and time. The solution procedure differed from the relaxation approach in that, instead of finding the solution as  $t \rightarrow \infty$ , the equation is solved for  $\varphi(\mathbf{x}, t)$  over the interval of time that it takes the wavefront to cross the domain. This probably gives the method the advantage that it does not require as many iterations, but also gives the method the disadvantage that the solution needs to be stored for all  $t$  in that interval, thus demanding much more storage space. The value of  $\varphi$ , however, is only important in the neighbourhood of  $\varphi = 0$ , so an adaptive mesh could be used to solve (2.86) accurately only in this neighbourhood, reducing both the amount of work performed in each iteration and the amount of information stored.

Second order central differences were initially used for the spatial discretization (Keener, 1991), but Keener and Panfilov (1995) later replaced these with first order upwind differences to stabilize the numerical solution.

If  $\varphi(\mathbf{x}, t)$  is chosen to be  $t - u(\mathbf{x})$  then (2.86) reduces to the eikonal equation (2.65) for excitation time, but leaving  $\varphi$  general means that it doesn't have any physical interpretation away from its zero contour. This makes the selection of initial conditions unclear.

### *Discussion*

Both the relaxation and level set methods discussed above fail to take advantage of the fact that excitation time depends only on spatial position. The use of either of the time dependent equations (2.85) or (2.86) increases the size of the domain by one dimension. For this reason, the method investigated here uses a solver based on Newton's method applied directly to a spatial discretization of the eikonal equation (2.65), to converge from an initial guess to the solution. Each Newton iteration does not require much more work than that required in an iteration of an implicit time stepping scheme for either (2.85) or (2.86), yet makes a considerably better attempt to go directly to the required solution. If wavefront propagation directions in the initial guess are well-orientated, then the derivatives for Newton's method are almost constant and the method converges very quickly.

As well as providing a review of level set methods for wavefront propagation problems, Sethian (1996) also presents a fast marching method for simple monotonically advancing wavefronts. The method systematically sweeps through a grid of points, evaluating  $u$  at each

of the points in a narrow band that traverses the mesh in a similar manner to the wavefront. The method relies on the discretization of the governing equation being such that the value of  $u$  at each grid point can be evaluated only from smaller neighbouring grid point values of  $u$ . This requirement means that the method is only effective if the governing equation in  $u$  is parabolic, and the numerical discretization of the equation must be purely *upwind*. Extensions to the method for irregular grids and higher than first order discretization still need to be developed. Myocardial excitation wavefront propagation depends on diffusion of charge so, as was seen in Section 2.4.2, the excitation time cannot be evaluated solely from the excitation time of upwind tissue. This marching method discussed is therefore not directly applicable to the solution of eikonal equation (2.65). However, the fact that excitation time is heavily dependent on upwind activity means that a preconditioner based on this marching method would probably be very effective for iterative solution of the Newton equations.



of the points in a narrow band that traverses the mesh in a similar manner to the wavefront. The method relies on the discretization of the governing equation being such that the value of  $u$  at each grid point can be evaluated only from smaller neighbouring grid point values of  $u$ . This requirement means that the method is only effective if the governing equation in  $u$  is parabolic, and the numerical discretization of the equation must be purely *upwind*. Extensions to the method for irregular grids and higher than first order discretization still need to be developed. Myocardial excitation wavefront propagation depends on diffusion of charge so, as was seen in Section 2.4.2, the excitation time cannot be evaluated solely from the excitation time of upwind tissue. This marching method discussed is therefore not directly applicable to the solution of eikonal equation (2.65). However, the fact that excitation time is heavily dependent on upwind activity means that a preconditioner based on this marching method would probably be very effective for iterative solution of the Newton equations.



## Chapter 3

# A Galerkin Finite Element Method

Wavefront locations are found from contours of excitation time so the numerical discretization technique used in solving the eikonal equation should provide a solution for excitation time  $u(\mathbf{x})$  over the entire domain continuum. This requirement and the complexity of the geometry of the heart suggest that the finite element method should be used. One of the most commonly used finite element methods is the *Galerkin* finite element method.

### 3.1 Interpolation

The domain is assumed to be a continuum containing an infinite number of points at which the value of the unknown dependent variable  $u(\mathbf{x})$  is required. For numerical solution to be feasible,  $u(\mathbf{x})$  must be approximated by a function  $U(\mathbf{x})$  having only a discrete number of unknown parameters  $U_i$ . This approximating function is most useful if it is linear such that the parameters are coefficients of known *interpolation functions*  $\psi_i(\mathbf{x})$ :

$$U(\mathbf{x}) := U_i \psi_i(\mathbf{x}). \quad (3.1)$$

In the finite element method, the domain is divided into a number of *elements* so that within each element  $U$  depends on only a subset of the parameters. The collection of elements

forming the domain is called the *mesh*. For each element, a local coordinate system  $\boldsymbol{\xi}$  is defined, so within that element,

$$U(\boldsymbol{x}(\boldsymbol{\xi})) := U_{\nu(e,j)}\Psi_j(\boldsymbol{\xi}), \quad (3.2)$$

where  $\Psi_j(\boldsymbol{\xi})$  are the element's local *basis functions*, and  $\nu(e, j)$  is a known function mapping the local parameter  $j$  in element  $e$  to its corresponding global parameter. The interpolation functions  $\psi_i(\boldsymbol{x}(\boldsymbol{\xi}))$  are therefore equal to corresponding basis functions  $\Psi_j(\boldsymbol{\xi})$  in elements influenced by  $U_i$  and zero elsewhere.

### 3.1.1 Lagrange Basis Functions

The most commonly used basis functions for finite element methods are *linear Lagrange* basis functions. With this form of interpolation, the parameters  $U_i$  are simply the values of  $U$  at points called *nodes* lying on the vertices of the elements. Within each element, the basis functions then perform a linear interpolation of the values at these nodes.

In one dimension, each element is surrounded by two nodes. The local coordinate  $\xi$  is defined such that  $\xi = 0$  at one node and monotonically increases across the element until  $\xi = 1$  at the other node. The basis functions are

$$\Psi_0(\xi) := 1 - \xi \quad \text{and} \quad \Psi_1(\xi) := \xi, \quad (3.3)$$

and the mapping  $\nu(e, j)$  is defined such that  $\nu(e, 0)$  indexes the node at  $\xi = 0$  in element  $e$  and  $\nu(e, 1)$  indexes the node at  $\xi = 1$  in the same element. The global interpolation functions that derive from these basis functions are plotted in Figure 3.1.

For higher dimensions, basis functions can be constructed from the tensor product of one-dimensional basis functions. For example, two-dimensional quadrilateral bi-linear Lagrange elements interpolate the four nodal values at the corners using,

$$U(\boldsymbol{x}(\boldsymbol{\xi})) := U_{\nu(e,i,j)}\Psi_{ij}(\boldsymbol{\xi}), \quad (3.4)$$

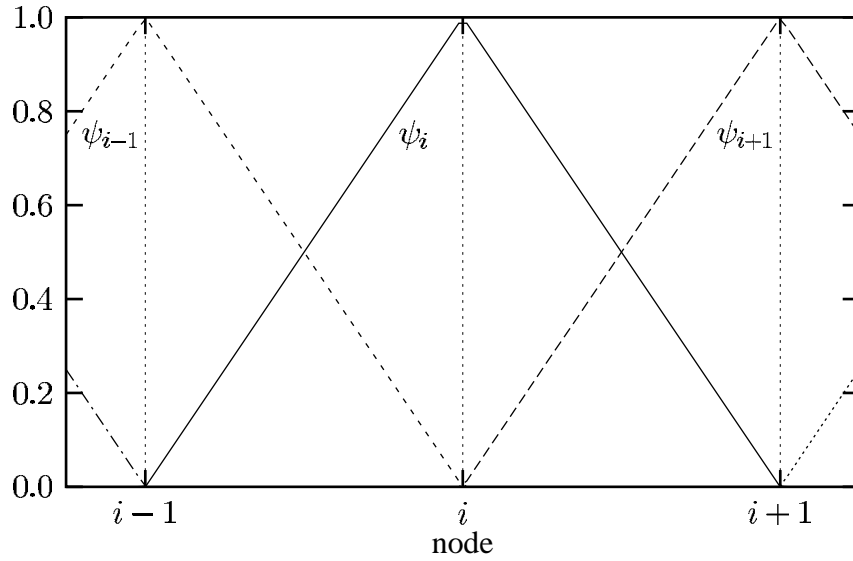


**Figure 3.1:** One-dimensional linear Lagrange interpolation functions.

where the basis functions are defined by

$$\Psi_{ij}(\boldsymbol{\xi}) := \Psi_i(\xi_1) \Psi_j(\xi_2), \quad (3.5)$$

so that  $i$  indicates the  $\xi_1$  position of the corresponding node and  $j$  indicates the  $\xi_2$  position.

Linear Lagrange elements are simple to use but their low order approximation means that a very large number of elements is needed to represent a complex function accurately. In order to improve on this, one approach would be to use higher order Lagrange elements, which have higher order polynomial basis functions.

When using linear elements, because all of the nodes lie on the vertices of elements, each node is shared by surrounding elements. This ensures that there is  $C^0$  continuity between elements. It also means that, for any number of dimensions, there is about the same number of parameters as elements. (Because the boundary nodes are shared by fewer elements, there are slightly more parameters than elements.) Higher order Lagrange elements have additional nodes throughout the element. In  $m$  dimensions, a Lagrange element of order  $n$  is influenced by  $(n+1)^m$  nodes and has the same number of basis functions. As some of these nodes are shared by surrounding elements, the number of parameters is approximately  $n^m$  times the number of elements.

### 3.1.2 Hermite Basis Functions

In contrast to the higher order Lagrange basis functions, *Hermite* basis functions interpolate parameters at nodes lying only on the vertices of the elements. Higher order interpolation is achieved by having more than one parameter at each node, with the parameters now including derivatives of  $U$ . The result is that there is a higher degree of continuity between elements, but perhaps the greater advantage is that all the parameters can be shared by the elements surrounding a vertex, so a high order interpolation is achieved with fewer parameters.

For one-dimensional Hermite interpolation, the notation  $U_i^p$  is used to indicate the parameter supplying the  $p$ th order derivative at node  $i$ . Within each element, the interpolation is

$$U(x(\xi)) := U_{\nu(e,j)}^p \Psi_j^p(\xi). \quad (3.6)$$

For cubic Hermite interpolation, the value and first derivative of  $U$  are supplied at each node, and the scheme ensures  $C^1$  continuity. The basis functions are given by:

$$\begin{aligned} \Psi_0^0(\xi) &:= (1 - \xi)^2(1 + 2\xi) & \Psi_1^0(\xi) &:= \xi^2(3 - 2\xi) \\ \Psi_0^1(\xi) &:= (1 - \xi)^2\xi & \Psi_1^1(\xi) &:= \xi^2(1 - \xi). \end{aligned} \quad (3.7)$$

Global interpolation functions  $\psi_i^p(x)$  corresponding to each parameter  $U_i^p$  can be derived from these basis functions and are plotted in Figure 3.2.

In higher dimensions, higher order *cross* derivatives need to be supplied at the nodes to retain the  $C^1$  continuity. For example, the quadrilateral-like bi-cubic Hermite elements provide an interpolation of nodal values of  $U$ ,  $\frac{\partial U}{\partial \xi_1}$ ,  $\frac{\partial U}{\partial \xi_2}$ , and  $\frac{\partial^2 U}{\partial \xi_1 \partial \xi_2}$ ,

$$U(\mathbf{x}(\boldsymbol{\xi})) := U_{\nu(e,i,j)}^{pq} \Psi_{ij}^{pq}(\boldsymbol{\xi}), \quad (3.8)$$

where  $p$  and  $q$  now indicate the order of derivative in the  $\xi_1$ - and  $\xi_2$ -directions respectively, and the basis functions are obtained from the tensor product of the one-dimensional basis functions:

$$\Psi_{ij}^{pq}(\boldsymbol{\xi}) := \Psi_i^p(\xi_1) \Psi_j^q(\xi_2). \quad (3.9)$$

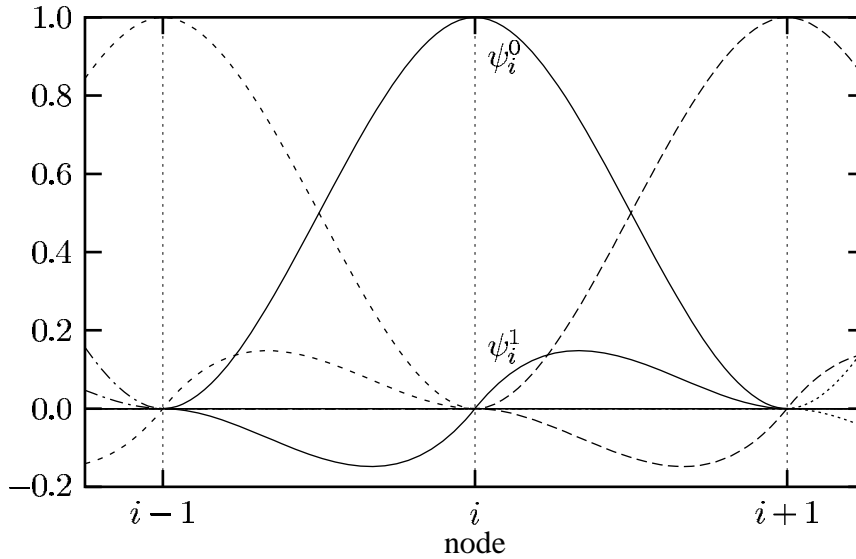


*Figure 3.2:* One-dimensional cubic Hermite interpolation functions.

Hermite elements providing interpolation of order  $n$  require derivatives up to order  $\frac{n-1}{2}$  to be supplied at each node. (The interpolation order of Hermite elements is always odd.) For  $m$  dimensions, there are  $\left(\frac{n+1}{2}\right)^m$  parameters per node. As the nodes lie only on the element vertices, there are about the same number of nodes as elements, implying that the number of parameters is approximately  $\left(\frac{n+1}{2}\right)^m$  times the number of elements.

A mesh of Hermite elements of order  $n$  therefore requires about the same number of parameters as would be required by the same number of Lagrange elements of order  $\frac{n+1}{2}$ . This feature makes Hermite elements attractive but care needs to be taken in their use. The higher order interpolation is achieved by assuming a higher degree of continuity. If the exact value of the function being approximated does not have this continuity, then the assumption breaks down and the Hermite elements do not provide a very good approximation. Even if the function is sufficiently continuous with respect to the global coordinate  $\boldsymbol{x}$ , it will only be sufficiently continuous with respect to the local coordinate  $\boldsymbol{\xi}$  if that coordinate system has the necessary continuity.

Cubic Hermite elements are used here for discretization of the dependent variable as these provide a sufficiently high order interpolation while demanding only a reasonable level of continuity and remaining reasonably simple. Because the exact solution  $u$  satisfies an elliptic

differential equation with predominantly smooth space-dependent coefficients and boundary conditions, it is expected to be sufficiently smooth. Across any surface where the coefficients of the equation are not sufficiently smooth, similar interpolation can be used but with the elements on opposing sides of the surface using separate derivative parameters. In order to ensure that continuity with respect to  $\boldsymbol{x}$  implies enough continuity with respect to  $\boldsymbol{\xi}$ , the same mesh of cubic Hermite elements is used to describe each of the components of  $\boldsymbol{x}$  in terms of  $\boldsymbol{\xi}$ .

## 3.2 Galerkin Weighted Residual Equations

For numerical solution of the Poisson equation, the Galerkin finite element method is well founded and has optimal convergence properties. For more general equations, such as the eikonal equation, however, the method is more difficult to justify.

### 3.2.1 Poisson Equation

Without its evolution term, the eikonal equation reduces to the simple generalized Poisson equation,

$$-\nabla \cdot (M\nabla u) = \tau_m. \quad (3.10a)$$

By recognizing the variational form of this problem, the *Rayleigh-Ritz* finite element method can be used to solve the equation numerically. This equation and its *Neumann* boundary condition,

$$\boldsymbol{n} \cdot M\nabla u = 0, \quad (3.10b)$$

are the Euler–Lagrange equation and natural boundary condition for the solution to the min-

imization of the energy functional,

$$\frac{1}{2} \int_{\Omega} \nabla u \cdot M \nabla u \, d\Omega - \int_{\Omega} \tau_m u \, d\Omega, \quad (3.11)$$

where  $\Omega$  is the domain.

The Rayleigh-Ritz approach is to find the discrete parameters  $U_j$  to minimize the same energy term for the numerical approximation (3.1) of the solution. The numerical solution is then the best possible solution (within the constraints of the interpolation scheme) in the sense that the error,  $u - U$  has minimum energy,

$$\int_{\Omega} \nabla(u - U) \cdot M \nabla(u - U) \, d\Omega. \quad (3.12)$$

The solution to the discrete minimization problem satisfies

$$U_j \int_{\Omega} \nabla \psi_j \cdot M \nabla \psi_i \, d\Omega = \int_{\Omega} \tau_m \psi_i \, d\Omega, \quad (3.13)$$

providing a symmetric positive definite system of equations to solve for  $U_j$ . Application of Green's theorem within each element puts the system of equations into the Galerkin weighted residual form,

$$-\sum_e \int_{\Omega_e} (\nabla \cdot (M \nabla U) + \tau_m) \psi_i \, d\Omega + \sum_e \int_{\partial\Omega_e} \mathbf{n} \cdot M \nabla u \, \psi_i \, d\Gamma = 0, \quad (3.14)$$

where  $\partial\Omega_e$  are the boundaries of the elements  $\Omega_e$  making up the domain  $\Omega$ . The numerical solution therefore satisfies the condition that the sums of integrals of the residual in the original equation (3.10a) and the residual in the flux across the element and domain boundaries, weighted with each of the interpolation functions in turn, are required to be zero.

### 3.2.2 Eikonal Equation

Although the eikonal equation (2.65) does not result from the minimization of any energy functional, a similar Galerkin weighted residual approach can be used:

$$\sum_e \int_{\Omega_e} \left( c_0 \sqrt{\nabla U \cdot M \nabla U} - \nabla \cdot (M \nabla U) - \tau_m \right) \psi_i \, d\Omega + \sum_e \int_{\partial\Omega_e} \mathbf{n} \cdot M \nabla u \psi_i \, d\Gamma = 0. \quad (3.15)$$

If the interpolation scheme for  $U$  provides  $C^1$  continuity and material constants have  $C^0$  continuity, then the fluxes are continuous across inter-element boundaries. The integrals on coincident element boundaries then cancel leaving only those on the domain boundary. The weighted residual equation simplifies to

$$\int_{\Omega} \left( c_0 \sqrt{\nabla U \cdot M \nabla U} - \nabla \cdot (M \nabla U) - \tau_m \right) \psi_i \, d\Omega + \int_{\partial\Omega} \mathbf{n} \cdot M \nabla u \psi_i \, d\Gamma = 0, \quad (3.16)$$

where  $\partial\Omega$  is the boundary of the domain. The equation is now a weighted residual of the original equation (2.65) and its Neumann boundary condition (2.66).

A possibly more computationally appealing form of (3.15) results from applying Green's theorem within each element:

$$\int_{\Omega} \left( c_0 \sqrt{\nabla U \cdot M \nabla U} \psi_i + \nabla U \cdot M \nabla \psi_i \right) \, d\Omega = \int_{\Omega} \tau_m \psi_i \, d\Omega. \quad (3.17)$$

This has the advantage that there are no second derivatives or boundary integrals to be evaluated.  $C^1$  continuity is not required in  $U$ .

The Galerkin approach provides a system of the same number of equations as unknowns but, as it is no longer a minimization process, there is no longer any symmetry or positive definiteness in the system. There is also no guarantee that the error is minimized, but it seems reasonable to assume that, if the weighted integral of the residual is zero for a great enough number of weighting functions, then the error must be small. The system of equations is

non-linear so an iterative method is required for its solution.

### 3.3 Boundary Conditions for Wavefront Initiation

The time and location of excitation wavefront initiation is specified by *Dirichlet* boundary conditions for excitation time  $u$  on  $\Gamma_D$ , where  $\Gamma_D$  denotes the portion of the boundary where  $u$  is known from the initiation process. In the finite element method, these boundary conditions are enforced by specifying the values of the parameters  $U_j$  that describe  $U$  on  $\Gamma_D$ . The set  $D$  is defined as the list of indices  $j$  for these parameters  $U_j$  and their corresponding interpolation functions  $\psi_j$ . The set  $N$  is defined as the list of indices  $j$  of the remaining parameters, which are unknown and do not influence the value of  $U$  on  $\Gamma_D$ . Equations (3.17) are generated for each  $i \in N$  to provide the same number of equations as unknown parameters.

The Neumann boundary condition (3.10b), derived from the requirement that no current flows across the boundary, is weakly enforced by the boundary integral in (3.15) on any section of the boundary where an interpolation function  $\psi_i$  with  $i \in N$  is non-zero.  $\Gamma_N$  is used to denote the portion of the boundary on which the Neumann boundary condition is applied. Initiation of excitation requires an injection of charge into the domain, so the no-current condition is not enforced on any portion of the boundary where  $U$  is defined by Dirichlet boundary conditions.

#### 3.3.1 Mesh Discretization

When selecting a mesh for the discretization, care must be taken in the regions surrounding excitation initiation, as this is where Dirichlet and Neumann portions of the boundary meet.

Consider first either a Lagrange or Hermite element and fixing all the parameters that determine the value of  $U$  on one side. As the value of  $U$  is fixed over the entire side, a Dirichlet boundary condition is enforced on the entire side. The interpolation functions corresponding to the remaining parameters are all zero on this side, so the portion of the boundary integral in (3.15) corresponding to this element side is zero for all  $i \in N$  and the Neumann boundary

condition is not enforced.

Second, consider the same element side but with one or more of the parameters determining  $U$  on the side allowed to be free. Now, although certain features of the  $U$  on this side may be fixed, the value itself is not determined, so a Dirichlet boundary condition is not enforced. Also, as there is now an interpolation function  $\psi_i$  with  $i \in N$  that is non-zero along this side, the boundary integral does not vanish, and the Neumann boundary condition is enforced (weakly) on the entire side.

In a domain mesh, therefore, each element side lying on the boundary has either a Neumann or Dirichlet boundary condition applied along the entire side. This means that the discretization mesh must be chosen such that borders between no current flow and wavefront initiation portions of the boundary must coincide with borders between elements.

### 3.3.2 Point Initiation

In the case of excitation initiated by injection of current at a point, the boundary condition can be applied by fixing the parameter  $U_j$  corresponding to a node positioned on that point. If the point lies on the boundary of the domain, then, because there exist interpolation functions  $\psi_i$  with  $i \in N$  that are non-zero on the adjacent element edges on the boundary, the Neumann boundary condition is enforced on these edges. At the point of current injection, however, all these  $\psi_i$  vanish so the point forms an infinitesimal portion of the boundary where charge can be injected to initiate excitation and a Dirichlet boundary condition is applied. If the point lies within the domain, then the point forms a similar infinitesimal Dirichlet boundary for wavefront initiation.

In the neighbourhood of the point of excitation initiation, the exact solution to the eikonal equation (2.65) is similar to the ellipsoidal solution (2.77), and has the same singularity at the initiation point. The eikonal equation solution states that the wavefront is initially travelling infinitely slowly and therefore takes an infinite period of time to reach any tissue a finite distance away from the point initiation. This is not physically realistic, the reason being that the boundary conditions are not physically realistic. Myocardial tissue excitation is never initiated from an infinitesimal point, but the applied current initiates the excitation of cells in

a small but finite region of tissue. Once the cells in this region are excited, they then produce currents that cause propagation of excitation into surrounding cells. The dimensions of the initial region of excitation are probably in the order of the space constants  $\lambda_l$ ,  $\lambda_t$ , and  $\lambda_n$ .

In order to accurately model physically realistic boundary conditions, it would be necessary for the domain mesh to represent the boundary of the finite region of initial excitation as a finite boundary. The shape of this region depends on the details of the microscopic structure so its exact shape is not known. Even if it were known, the small size of the region would mean that a very fine mesh would be required. If only the large scale effects of excitation are important then it is sufficient to approximate the behaviour in this small region.

If the element is large compared to the space constants, then representing the region of initial excitation as an infinitesimal point does provide successful solutions. The singularity in solution (2.77) results from the diffusion term, but the effects of this term are only great near the point of initiation. All the interpolation functions vanish at this point, so the weighted residual equations (3.15) do not put much emphasis on attempting to satisfy the eikonal equation where the exact solution is singular. The numerical solution instead aims to satisfy the governing equation further away from the initiation point, and simply provides a smooth continuation into the small region where diffusion is important.

If, however, the element dimensions are of similar magnitude to the space constants, the effects of diffusion are great in a larger portion of the element. In this portion, the exact solution cannot be at all well approximated by the polynomial basis functions. The weighted residual equations attempt to reduce the large eikonal equation residual in this region, but the result is that the solution is corrupted in other areas.

In most problems analysed here the elements are much larger than the space constants, so representing the region of initial excitation as a point is sufficient. However, as will be discussed in Section 3.5, obtaining the numerical solution to these problems requires the numerical solution of similar problems with more significant diffusion terms. The numerical solutions of these similar problems would be corrupted by the singularities. If the nature of numerical solutions for diffusion-dominated problems could be improved, they would provide better starting points for the solution of evolution-dominated problems.

The singularity in solution to the eikonal equation (2.65) can be removed by modifying the

diffusion term. Note that, if the diffusion term is changed so that the governing equation is

$$c_0 \sqrt{\nabla u \cdot M \nabla u} - r^2 \nabla \cdot \left( \frac{1}{r^2} M \nabla u \right) = \tau_m, \quad (3.18)$$

the solution for the spreading of ellipsoidal wavefronts from the origin of an infinite homogeneous domain is

$$\frac{u}{\tau_m} = \frac{r}{c_0}, \quad (3.19)$$

where  $r$  is the dimensionless distance from the origin defined by equation (2.75). This solution is similar to the ellipsoidal solution (2.77) for eikonal equation (2.65) far from the point of initial excitation but does not have the singularity at the initiation point.

The governing equation can be modified only near the point of initial excitation by using

$$c_0 \sqrt{\nabla u \cdot M \nabla u} - p_s \nabla \cdot \left( \frac{1}{p_s} M \nabla u \right) = \tau_m, \quad (3.20)$$

where  $p_s$  is a simple non-negative  $C^0$  continuous piecewise polynomial function that is one over most of the domain but approaches zero with order  $r^2$  at point initiations. In this way, the singularity is removed from the solution, while the equation is changed as little as possible. If the elements are large compared to the space constants, the modification has little effect on the numerical solution, but, if the elements are small, the absence of any singularity in the exact solution to the modified equation means that it can be represented much more closely by polynomial basis functions.

The function  $p_s$  is described by cubic Hermite interpolation of nodal quantities in elements that are adjacent to a point initiation, and is set to one in other elements. The nodal values of  $p_s$  are zero if there is a point initiation at that node and one otherwise. Nodal derivatives are all zero. For two-dimensional problems,  $p_s$  should approach zero with order  $r$  at point initiations, so nodal derivatives at corresponding nodes should be non-zero. The slope of  $p_s$  decreases monotonically with respect to distance from the initiation point if nodal derivatives are chosen so that, at the node, the rate of increase of  $p_s$  with respect to unit magnitude change in  $\xi$  is 3.

The effect that this modification has on numerical solutions for point initiation in the corner of an element with dimensions equal to the space constant are shown in Figure 3.3. The

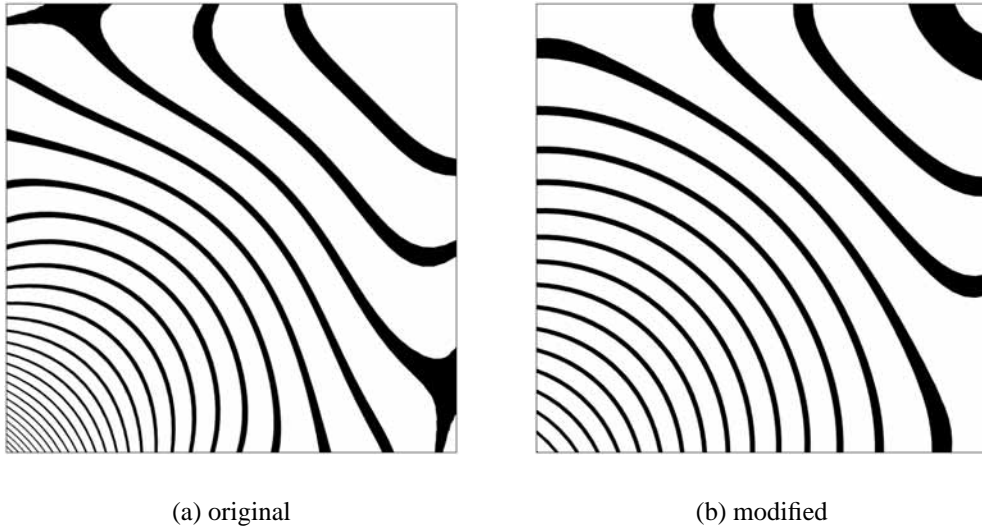


**Figure 3.3:** Demonstration of the effect that modification of the diffusion term in the eikonal equation near a point initiation has on Galerkin solutions. The domain is a square of size  $\lambda$  represented by a single bi-cubic Hermite element, and excitation is initiated at the bottom-left corner.  $M = \lambda^2 I$  and  $c_0 = 2.5$ . Contours are at intervals of  $0.02\tau_m$ .

solution to the modified equation does not have the slow propagation near the initiation point but satisfies the eikonal equation much more closely in other regions.

### 3.4 Gaussian Quadrature

The integrals in equations (3.17) are evaluated using Gauss–Legendre quadrature schemes within each element. For an  $m$ -dimensional one-element domain with interpolation for  $U$  that is cubic Hermite in each direction, there are  $4^m$  parameters  $U_i$ . If fewer than  $4^m$  quadrature points were used to evaluate the integrals, the resulting equations would be linearly dependent. In order to generate enough independent equations to determine each  $U_i$ , at least  $4^m$  quadrature points are needed in the element. This suggests using a grid of quadrature points with 4 points in each direction. The components of the  $\xi$  positions for the quadrature points are the corresponding abscissas for one-dimensional quadrature schemes in each direction, and the weights are the products of the corresponding weights for the one-dimensional

schemes.

With more than one element, nodal parameters are shared between elements but quadrature points are not. This means that, for a mesh with enough elements in each direction, a grid of  $3^m$  quadrature points per element would provide enough independent equations. Even on regular meshes, however, if  $m > 1$ , the integrands include terms that are 6th order polynomials in some directions. Exact integration of a 6th order polynomial requires 4 Gauss–Legendre quadrature points, so it seems appropriate to use a grid of  $4^m$  points in each element.

### 3.5 Numerical Continuation

The discrete system of equations (3.17) is solved using Newton’s method. This method requires a good enough initial guess for the solution on which it can iteratively improve. If the diffusion term dominates, the equation is close to linear, so almost any initial guess will lead to rapid convergence. An initial guess of  $U_j = 0 \forall j \in N$  is sufficient. If the evolution term dominates, however, the significant non-linearities may prevent the method from converging if the initial guess is not good enough.

The components of the Jacobian matrix for Newton’s method are the derivatives of equations (3.17) with respect to each unknown parameter  $U_j$ , which are

$$\int_{\Omega} \left( \frac{c_0 \nabla U \cdot M \nabla \psi_j}{\sqrt{\nabla U \cdot M \nabla U}} \psi_i + \nabla \psi_j \cdot M \nabla \psi_i \right) d\Omega. \quad (3.21)$$

Note that these depend on the orientation of  $\nabla U$  but are independent of its magnitude. The Jacobian therefore remains constant if the propagation directions in the solution estimates remain constant. If an initial guess provides a good enough estimate of the propagation directions, Newton’s method can be expected to converge very quickly.

A suitable initial guess for solution of the governing eikonal equation can be obtained from the approximate solution of another equation that is similar but easier to solve. Removing the evolution term from the eikonal equation provides a simple diffusion equation that requires only one Newton iteration to obtain the exact solution. The solution is not similar to that of

an evolution-dominated eikonal equation, but it is similar to that of a diffusion-dominated eikonal equation. The solution from the diffusion equation can be used as an initial guess for the solution of a diffusion-dominated eikonal equation, which can be used for the initial guess for the solution of an eikonal equation with a more influential evolution term. In this way, Newton's method can be applied to a series of equations starting from a diffusion equation and finishing at the desired eikonal equation. Such a scheme, that transforms the solution of one equation into the solution of another, is called a *numerical continuation method* (Allgower and Georg, 1990).

### 3.5.1 Selecting a Continuum of Equations

There are two simple continua of equations that could be used to find the solution of an eikonal equation by gradually introducing the non-linearities into an initially linear equation. One continuum starts by removing the evolution term and then gradually introduces it. That is

$$\alpha_c c_0 \sqrt{\nabla u \cdot M \nabla u} - \nabla \cdot (M \nabla u) = \tau_m, \quad (3.22a)$$

where  $\alpha_c$  is the *continuation variable*, which increases from 0 to 1. The other continuum gradually introduces the source term  $\tau_m$  also:

$$\alpha_c c_0 \sqrt{\nabla u \cdot M \nabla u} - \nabla \cdot (M \nabla u) = \alpha_c \tau_m. \quad (3.22b)$$

This gradual introduction of the evolution and source terms is equivalent to a gradual reduction in the diffusion term. To determine which continuum of equations to use, consider the behaviour of the solutions as  $\alpha_c$  traverses the interval  $[0, 1]$ .

With the first continuum (3.22a), when  $\alpha_c$  is small enough so that the diffusion term is more significant than the evolution term, increasing  $\alpha_c$  has only a small effect on the solution because the dominating diffusion and source terms remain the same. On the other hand, when  $\alpha_c$  becomes large enough so that the evolution term is more significant, the solution depends predominantly on the evolution and source terms. The evolution term is changing but the source term is not, so the solution depends heavily on the value of  $\alpha_c$ . If excitation is initiated at only one point, then the solution is essentially scaled by  $\frac{1}{\alpha_c}$ , the Jacobian for

Newton iterations remains essentially constant, and the method should perform reasonably well. If excitation is initiated at more than one point, however, and initiation times differ, the effect  $\alpha_c$  has on the solution is more complex. The directions of propagation change with  $\alpha_c$  so the Jacobian changes and Newton's method does not converge so quickly. Increments in  $\alpha_c$  would need to be small so that the initial guess for Newton's method would be good enough for convergence.

With the second continuum (3.22b), when diffusion dominates the solution is essentially scaled by  $\alpha_c$ . When evolution dominates, changes in  $\alpha_c$  affect the evolution and source terms consistently so changes in the solution are small.

Continuum (3.22a) therefore has the more appealing behaviour when diffusion dominates but continuum (3.22b) has the more appealing behaviour when evolution dominates. It would be possible to design a hybrid continuum that combined both advantages but this is unnecessary. When diffusion dominates, the equation is almost linear and the Jacobian is almost constant, so large changes in the solution do not present any problem. Continuum (3.22b) is therefore chosen for its more appealing behaviour when evolution dominates. The superiority of this continuum over (3.22a) was also observed experimentally.

### 3.5.2 Implementation

The sizes of the increments in  $\alpha_c$  are based on the performance of Newton's method at each step. Each increment should be small enough so that the change in the Jacobian is small and one iteration of Newton's method significantly reduces the residual in the system of equations. If the reduction in residual is poor, the solution estimate is reverted to that for the previous value of  $\alpha_c$  and a smaller increment is taken. If the reduction in the residual is very good, it is not necessary to find the exact solution for each value of  $\alpha_c$ , so the next step is performed with a larger increment in  $\alpha_c$ . If the reduction is not so good more Newton iterations may be performed with the same value of  $\alpha_c$  and a smaller increment is used for the next step. When  $\alpha_c$  reaches 1, Newton iterations are performed until the desired accuracy is obtained in the solution. This process can be automated but was performed manually for the solution of most problems presented here.

Each Newton iteration requires solution of a system of linear equations. There exist quasi-Newton methods that use an update such as that of Broyden (1965) at each iteration to build up an approximation to the Jacobian or its inverse. The methods have the advantages that the Jacobian does not need to be explicitly evaluated and there may be no need for a matrix factorization. With the finite element method, however, the cost of evaluating the Jacobian is not so much more than the cost of evaluating of the residual that it is worth performing the extra iterations required to build up a good approximation. It is also difficult to design these quasi-Newton methods to take advantage of the sparsity of the Jacobian. The Jacobian is therefore explicitly evaluated at each iteration.

For small enough problem sizes, the system of linear equations for each Newton iteration was solved using the unsymmetric-pattern multifrontal (UMFPACK) direct sparse matrix solver of Davis and Duff (1997). For larger problem sizes, using instead the generalized minimum residual (GMRES) iterative solver (Saad and Schultz, 1986) required less computation time and much less memory. No restarts were used. A simple diagonal preconditioner was used but, as mentioned in Section 2.5.2, a marching preconditioner could be designed to take advantage of the predominantly one-directional dependence of excitation times. The level of accuracy demanded in each iterative solution of a linear system can be varied according the error expected in the residuals of the non-linear system (Eisenstat and Walker, 1994), but this was not investigated here.

### 3.6 Quality of Numerical Results

Figure 3.4 compares the contours of excitation times obtained from a Galerkin finite element solution to the eikonal equation (2.65) with those from a finite difference solution to the reaction–diffusion equation (2.35) for excitation initiated in the corner of a square slice of anisotropic tissue. In the finite element solution, an  $8 \times 8$  bi-cubic Hermite element mesh is used, and, in order to avoid errors due to the singularity at the initiation point, the excitation time obtained from the reaction–diffusion equation is specified as a Dirichlet boundary condition on the boundary edges of the corner element. The cubic ionic current model (2.80) was used in the reaction–diffusion solution.

The comparison shows how accurately the eikonal equation approximates the effects of

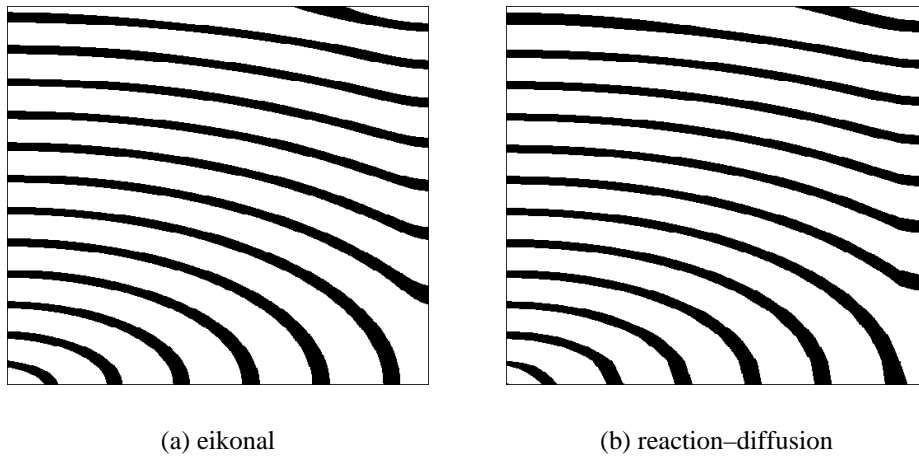


**Figure 3.4:** Excitation time solutions on an 8mm square slice of tissue stimulated at the bottom-left corner. Contours are at 2ms intervals.  $\mathbf{M}$  is a diagonal tensor with components  $0.126$  and  $0.0316 \text{ mm}^2$  for the horizontal and vertical directions respectively,  $\tau_m = 0.907 \text{ ms}$  and  $c_0 = 1.763$ .

anisotropy and wavefront curvature on the solution to the reaction–diffusion equation. The accuracy of the eikonal equation is also demonstrated in the results of Colli Franzone, Guerri, and Rovida (1990) and Colli Franzone and Guerri (1993b).

The Galerkin finite element method provides good solutions for reasonably simple excitation sequences such as in Figure 3.4, but for more complex excitation sequences performance is much less satisfactory. Results from the Galerkin weighted residual equations (3.17) for excitation time on a two-dimensional annular domain are shown in Figure 3.5. The fibre directions are orientated circumferentially and the annulus has similar spatial dimensions to those involved in the ventricular myocardium.

The solution on the coarse mesh with 3 elements radially and 8 elements circumferentially (Figure 3.5(a)) shows undesirable oscillations in wavefront velocity that have a wavelength equal to the circumferential element length. Circumferential refinement of the mesh to 64 elements (Figure 3.5(b)) reduces the magnitude of the oscillations a great deal but does not remove them completely. Oscillations can still be seen in the enlarged region from near the collision.

These oscillations are only seen in solutions where wavefront–wavefront collisions occur.

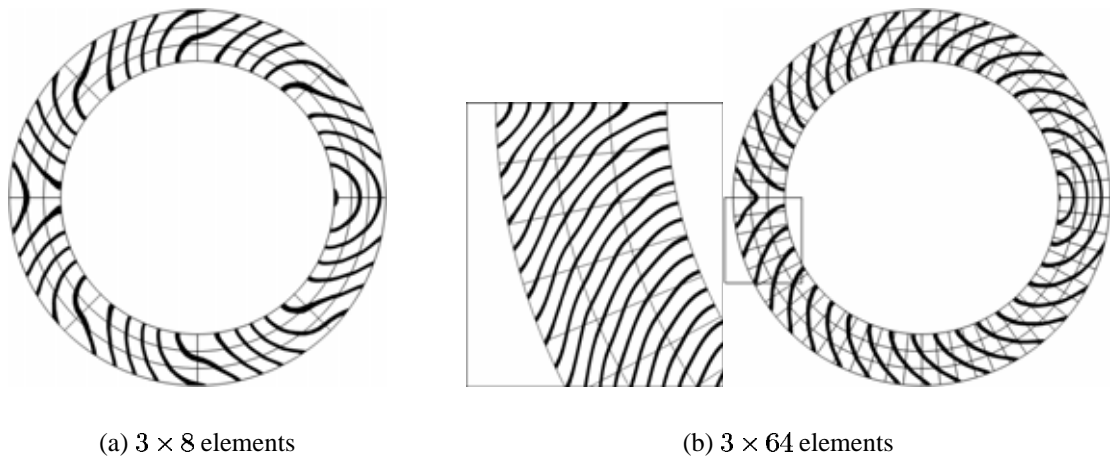


**Figure 3.5:** Galerkin solutions for excitation time on an annulus of external diameter 110 mm and thickness 15 mm using two different meshes. The wavefront is initiated at a point on the inside of the right wall and a collision occurs in the left wall. For the finer mesh, a region near the collision is enlarged to show the existence of oscillations. The contour intervals are 10 ms in the diagrams of the complete annulus and 2.5 ms in the enlargement. Material parameters are  $\lambda_l = 0.8$  mm and  $\lambda_t = 0.5$  mm for the circumferential and radial directions respectively,  $\tau_m = 3$  ms, and  $c_0 = 2.5$ .

If the wavefront simply dies out on the boundary, then a coarse mesh provides an adequate solution. In modelling the excitation of the heart, however, the numerical solution scheme needs to be able to handle these collisions.

The  $3 \times 64$  element mesh in Figure 3.5(b) has an element length of about 5 mm. This implies that, in order to obtain reasonable solutions, the required mesh size is only a few times larger than the wavefront-thickness mesh size that would be required in a solution of the reaction–diffusion system. In order to use the eikonal equation to its best advantage, it is necessary to develop a finite element scheme that does not require such a fine mesh.

### 3.7 Error Norm Analysis

Although the Galerkin finite element solution to the eikonal equation is not guaranteed to minimize any energy function of the error, it is possible to derive a bound on a norm of the

error for simple one-dimensional problems.

### 3.7.1 Solution Spaces

In analysis of the convergence properties of finite element methods, it is convenient to define the *trial space*  $S_D^h$  as the space of possible approximations to  $u$  provided by the discretization scheme. The approximation is determined by the parameters  $U_j$  but the subset of these parameters corresponding to  $j \in D$  are fixed to match the Dirichlet boundary conditions. The remaining parameters are free to be determined by the finite element method. The function  $\tilde{U}_D(\mathbf{x})$  is defined on  $\Omega$  as the component of the approximation  $U$  determined by Dirichlet boundary conditions,

$$\tilde{U}_D := \sum_{j \in D} U_j \psi_j, \quad (3.23a)$$

and the space  $S_0^h$  is defined as the space of possible variations in the approximation,

$$S_0^h := \left\{ V : \exists v_j \in \mathbb{R} \text{ s.t. } V = \sum_{j \in N} v_j \psi_j \right\}. \quad (3.23b)$$

The trial space is a linear combination of these:

$$S_D^h := \left\{ V : \exists v_j \in \mathbb{R} \text{ s.t. } V = \tilde{U}_D + \sum_{j \in N} v_j \psi_j \right\}. \quad (3.23c)$$

The *test space* is the space of weighting functions for which the weighted residual equation is satisfied. For the Galerkin method, the test space is simply  $S_0^h$ . This method can be formulated as finding  $U \in S_D^h$  such that

$$B(U, V) = \langle \tau_m, V \rangle \quad \forall V \in S_0^h, \quad (3.24)$$

where

$$B(v, w) := \langle c_0 \sqrt{\nabla v \cdot M \nabla v}, w \rangle + \langle M \nabla v, \nabla w \rangle \quad (3.25)$$

and  $\langle \cdot, \cdot \rangle$  denotes the inner product over the domain  $\Omega$ .

The exact solution  $u$  is expected to lie in the Sobolev space  $H^1(\Omega)$  (defined as the space of functions for which the squares of the function and its first derivatives can be integrated over  $\Omega$ ). It is also known that, on the Dirichlet portion of the boundary  $\Gamma_D$ ,  $u$  is equal to the boundary conditions  $\tilde{u}_D$ . The spaces  $H_D^1$  and  $H_{D_0}^1$  are defined for the exact solution in a similar manner to  $S_D^h$  and  $S_0^h$  for the approximate solution:

$$H_D^1 := \{v \in H^1(\Omega) : v = \tilde{u}_D \text{ on } \Gamma_D\}, \quad (3.26a)$$

$$\text{and } H_{D_0}^1 := \{v \in H^1(\Omega) : v = 0 \text{ on } \Gamma_D\}. \quad (3.26b)$$

Note that for either Lagrange or Hermite interpolation  $S_0^h \subset H_{D_0}^1$ , and, assuming  $\tilde{U}_D = \tilde{u}_D$  on  $\Gamma_D$ ,  $S_D^h \subset H_D^1$ . Under these conditions we also have  $u - U \in H_{D_0}^1$ .

### 3.7.2 One-Dimensional Error Bound

It is easiest to analyse the behaviour of the Galerkin finite element method in one dimension. Although the results of this analysis may not necessarily apply in higher dimensions, they do show important characteristics of the method and provide an insight into what might be expected on more complex geometries.

Consider a one-dimensional problem on a domain of length  $L$  with a Dirichlet boundary condition at  $x = 0$  and a Neumann boundary condition at  $x = L$  so that wavefront propagation is only in the direction of increasing  $x$ . The excitation time  $u(x)$  is required to satisfy

$$c_0\sqrt{M}u' - Mu'' = \tau_m \quad \text{on } (0, L), \quad (3.27a)$$

$$u(0) = 0, \quad \text{and} \quad Mu'(L) = 0, \quad (3.27b)$$

where  $c_0$  and  $M$  are positive constants and  $'$  denotes the derivative with respect to  $x$ .

With propagation in only one direction the form  $B(\cdot, \cdot)$  is bilinear. For constant  $c_0$  and  $M$ , it simplifies to

$$B(v, w) := c_0\sqrt{M}\langle v', w \rangle + M\langle v', w' \rangle. \quad (3.28)$$

The second inner product is symmetric and can be used as a norm for error analysis. Denoting

this part of the form as

$$B_S(v, w) := M\langle v', w' \rangle, \quad (3.29)$$

an associated norm can be defined:

$$\|v\|_{B_S}^2 := B_S(v, v). \quad (3.30)$$

Strictly,  $\|\cdot\|_{B_S}$  is a semi-norm as it only involves derivatives of the function. Adding a constant to the function does not change the value of the semi-norm, so it is only positive semi-definite. If, however, the function is restricted to  $H_{D_0}^1$  then a constant perturbation is not possible.  $\|v\|_{B_S}$  is positive definite for  $v \in H_{D_0}^1$  and behaves like a norm.

Investigating the convergence properties of the method relies on determining a lower bound for  $B(v, v)$  in terms of a norm of  $v$ . Such a bound can be found using  $\|v\|_{B_S}$  as follows:

$$\begin{aligned} B(v, v) &= c_0\sqrt{M}\langle v', v \rangle + M\langle v', v' \rangle \\ &= \frac{1}{2}c_0\sqrt{M} [v^2|_{x=L} - v^2|_{x=0}] + B_S(v, v) \\ &= \frac{1}{2}c_0\sqrt{M} v^2|_{x=L} + \|v\|_{B_S}^2 \quad \forall v \in H_{D_0}^1 \\ &\geq \|v\|_{B_S}^2. \end{aligned} \quad (3.31)$$

The exact solution  $u$  satisfies the same weighted residual equations (3.24) as does the approximate solution  $U$ :

$$B(u, V) = \langle \tau_m, V \rangle \quad \forall V \in S_0^h.$$

Subtracting (3.24) from this provides an orthogonality property for the error  $u - U$ :

$$B(u - U, V) = 0 \quad \forall V \in S_0^h. \quad (3.32)$$

From the results (3.31) and (3.32) we have

$$\|u - U\|_{B_S}^2 \leq B(u - U, u - U) + B(u - U, V) \quad \forall V \in S_0^h.$$

Putting  $W = U - V$  allows this to be written as

$$\begin{aligned}
\|u - U\|_{B_S}^2 &\leq B(u - U, u - W) && \forall W \in S_D^h \\
&= c_0 \sqrt{M} \langle u' - U', u - W \rangle + M \langle u' - U', u' - W' \rangle \\
&\leq \|u - U\|_{B_S} [c_0 \|u - W\|_{L_2} + \|u - W\|_{B_S}] \\
\Rightarrow \|u - U\|_{B_S} &\leq c_0 \|u - W\|_{L_2} + \|u - W\|_{B_S}. && (3.33)
\end{aligned}$$

As  $u - W \in H_{D_0}^1$  the  $\|\cdot\|_{L_2}$  norm can be bounded by the  $\|\cdot\|_{B_S}$  norm using the *Poincaré inequality*,

$$c_0 \|u - W\|_{L_2} \leq k_P \|u - W\|_{B_S}. \quad (3.34)$$

Substituting this into bound (3.33) implies

$$\begin{aligned}
\|u - U\|_{B_S} &\leq K_{\text{Gal}} \|u - W\|_{B_S} && \forall W \in S_D^h \\
\Rightarrow \|u - U\|_{B_S} &\leq K_{\text{Gal}} \inf_{W \in S_D^h} \|u - W\|_{B_S}, && (3.35)
\end{aligned}$$

where  $K_{\text{Gal}} = k_P + 1$ . This indicates that the  $\|\cdot\|_{B_S}$  norm of the error is always less than a constant factor times the best possible value obtainable using the approximation space  $S_D^h$ . The order of convergence is the best possible order but the factor may be very large.

A better value can probably be found for the constant  $K_{\text{Gal}}$  than that of  $k_P + 1$  derived using the Poincaré inequality (3.34). In inequality (3.33), the norm of the error is bounded by the sum of two different norms. The  $\|\cdot\|_{L_2}$  norm is based on the values of the function  $u - W$  while the  $\|\cdot\|_{B_S}$  norm is based on first derivatives, so, for most approximation spaces, the best possible value obtainable for the  $\|\cdot\|_{L_2}$  norm is usually an order better than for the  $\|\cdot\|_{B_S}$  norm. If elements are of equal length  $h$ ,

$$\inf_{W \in S_D^h} c_0 \|u - W\|_{L_2} \sim P_e \inf_{W \in S_D^h} \|u - W\|_{B_S} \quad (3.36)$$

where

$$P_e = \frac{c_0 h}{\sqrt{M}} \quad (3.37)$$

is the *mesh Péclet number*. Bound (3.35) is probably satisfied for  $K_{\text{Gal}} \sim P_e + 1$ . Morton (1996) provides a more detailed analysis.

The right hand side of the error bound (3.35) derives from an upper bound for  $B(v, w)$  that includes both the evolution and diffusion terms, but the left hand side comes from the lower bound (3.31) for  $B(v, v)$  that relies solely on the diffusion term. If diffusion dominates ( $P_e$  is small) then  $K_{\text{Gal}}$  is close to 1 and the solution is very close to optimal in the sense of the  $\|\cdot\|_{B_S}$  norm. As the effect of diffusion becomes small, however,  $K_{\text{Gal}}$  becomes arbitrarily large and the bound on error becomes very poor.

### 3.8 Difference Equation Analysis

The nature of the error that appears when diffusion is small can be understood by studying the equations produced in the discretization. Consider the one-dimensional problem (3.27) with propagation only in the direction of increasing  $x$ . The domain is discretized into  $N$  cubic Hermite elements of equal length  $h$  with the nodes labelled in the direction of increasing  $x$  so that node 0 is at  $x = 0$  and node  $N$  is at  $x = L$ .

For one-dimensional cubic Hermite elements, there are two weighted residual equations (3.17) for each node except for those where Dirichlet boundary conditions are applied. These equations correspond to the two interpolation functions per node, which are used as weighting functions. For nodes not lying on the boundary, the equations are

$$\int_{\Omega} \left( c_0 \sqrt{M} \left| U_j^q \frac{d\psi_j^q}{dx} \right| - M U_j^q \frac{d^2 \psi_j^q}{dx^2} - \tau_m \right) \psi_i^p d\Omega = 0, \quad i = 1, \dots, N-1, p = 0, 1. \quad (3.38)$$

As the wavefront is travelling only in the direction of increasing  $x$ ,  $\frac{du}{dx}$  is always positive, so these equations are linear:

$$U_j^q \int_{\Omega} \left( c_0 \sqrt{M} \frac{d\psi_j^q}{dx} - M \frac{d^2 \psi_j^q}{dx^2} \right) \psi_i^p d\Omega = \int_{\Omega} \tau_m \psi_i^p d\Omega, \quad i = 1, \dots, N-1, p = 0, 1. \quad (3.39)$$

As  $\psi_j^q$  and  $\psi_i^p$  are both non-zero in the same region only when  $i$  and  $j$  refer to either the same or adjacent nodes, the integrals can be evaluated to provide a set of simple *difference equations* relating the parameters at each node  $i$  to those at its surrounding nodes. For constant  $c_0$ ,  $M$ , and  $\tau_m$ , the difference equations for  $0 < i < N$  are

$$c_0\sqrt{M} \left( \begin{bmatrix} -\frac{1}{2} & -\frac{1}{10} \\ \frac{1}{10} & \frac{1}{60} \end{bmatrix} \mathbf{U}_{i-1} + \begin{bmatrix} 0 & \frac{1}{5} \\ -\frac{1}{5} & 0 \end{bmatrix} \mathbf{U}_i + \begin{bmatrix} \frac{1}{2} & -\frac{1}{10} \\ \frac{1}{10} & -\frac{1}{60} \end{bmatrix} \mathbf{U}_{i+1} \right) \\ - \frac{M}{h} \left( \begin{bmatrix} \frac{6}{5} & \frac{1}{10} \\ -\frac{1}{10} & \frac{1}{30} \end{bmatrix} \mathbf{U}_{i-1} + \begin{bmatrix} -\frac{12}{5} & 0 \\ 0 & -\frac{4}{15} \end{bmatrix} \mathbf{U}_i + \begin{bmatrix} \frac{6}{5} & -\frac{1}{10} \\ \frac{1}{10} & \frac{1}{30} \end{bmatrix} \mathbf{U}_{i+1} \right) = \tau_m h \begin{bmatrix} 1 \\ 0 \end{bmatrix}, \quad (3.40)$$

where the components of the vector  $\mathbf{U}_i$  are the nodal parameters,  $U_i^0$  and  $U_i^1$ .

The weighted residual equations corresponding to the interpolation functions at node  $N$  provide the difference equations,

$$c_0\sqrt{M} \left( \begin{bmatrix} -\frac{1}{2} & -\frac{1}{10} \\ \frac{1}{10} & \frac{1}{60} \end{bmatrix} \mathbf{U}_{N-1} + \begin{bmatrix} \frac{1}{2} & \frac{1}{10} \\ -\frac{1}{10} & 0 \end{bmatrix} \mathbf{U}_N \right) \\ - \frac{M}{h} \left( \begin{bmatrix} \frac{6}{5} & \frac{1}{10} \\ -\frac{1}{10} & \frac{1}{30} \end{bmatrix} \mathbf{U}_{N-1} + \begin{bmatrix} -\frac{12}{5} & \frac{1}{10} \\ \frac{1}{10} & -\frac{2}{15} \end{bmatrix} \mathbf{U}_N \right) = \tau_m h \begin{bmatrix} \frac{1}{2} \\ -\frac{1}{12} \end{bmatrix}. \quad (3.41)$$

At node 0, the Dirichlet boundary condition provides the equation,

$$\begin{bmatrix} 1 & 0 \end{bmatrix} \mathbf{U}_0 = 0, \quad (3.42a)$$

and the weighted residual equation corresponding to the derivative interpolation function at that node provides

$$c_0\sqrt{M} \left( \begin{bmatrix} -\frac{1}{10} & 0 \end{bmatrix} \mathbf{U}_0 + \begin{bmatrix} \frac{1}{10} & -\frac{1}{60} \end{bmatrix} \mathbf{U}_1 \right) \\ - \frac{M}{h} \left( \begin{bmatrix} -\frac{1}{10} & -\frac{2}{15} \end{bmatrix} \mathbf{U}_0 + \begin{bmatrix} \frac{1}{10} & \frac{1}{30} \end{bmatrix} \mathbf{U}_1 \right) = \tau_m h \frac{1}{12}. \quad (3.42b)$$

### 3.8.1 Convergence

If a Taylor series expansion of the exact solution about each node is substituted into the corresponding set of difference equations then equality does not hold. The differences between the left and right hand sides are the *truncation errors*. From these the expected rate of convergence for the numerical error in the nodal parameters can be determined. However, the numerical error arising from truncation errors at the boundaries is of a different nature to that arising from truncation errors at nodes not on the boundary. The error is therefore considered in two parts.

It is assumed that the numerical solution for nodal parameters  $U_i$  and the exact solution  $u(x)$  can be related by

$$U_i = \begin{bmatrix} u(ih) \\ h \frac{du}{dx}(ih) \end{bmatrix} + \sum_{p=0}^{\infty} h^p e_p(ih) + \sum_{k=1}^4 \epsilon_k \mathbf{a}_k \lambda_k^i. \quad (3.43)$$

The error due to truncation errors away from the boundaries is expressed in terms of a power series in  $h$ , where the vector coefficients  $e_p(x)$  are continuous functions having components  $e_p^0(x)$  and  $e_p^1(x)$ . The components  $e_p^0(x)$  satisfy the homogeneous boundary conditions,

$$e_p^0(0) = \frac{de_p^0}{dx}(L) = 0. \quad (3.44)$$

The error due to truncation errors at the boundaries is expressed in terms of a linear combination of the four eigenfunctions  $\mathbf{a}_k \lambda_k^i$  of the difference equation,

$$\begin{aligned} c_0 \sqrt{M} & \left( \begin{bmatrix} -\frac{1}{2} & -\frac{1}{10} \\ \frac{1}{10} & \frac{1}{60} \end{bmatrix} \mathbf{a}_k \lambda_k^{i-1} + \begin{bmatrix} 0 & \frac{1}{5} \\ -\frac{1}{5} & 0 \end{bmatrix} \mathbf{a}_k \lambda_k^i + \begin{bmatrix} \frac{1}{2} & -\frac{1}{10} \\ \frac{1}{10} & -\frac{1}{60} \end{bmatrix} \mathbf{a}_k \lambda_k^{i+1} \right) \\ & - \frac{M}{h} \left( \begin{bmatrix} \frac{6}{5} & \frac{1}{10} \\ -\frac{1}{10} & \frac{1}{30} \end{bmatrix} \mathbf{a}_k \lambda_k^{i-1} + \begin{bmatrix} -\frac{12}{5} & 0 \\ 0 & -\frac{4}{15} \end{bmatrix} \mathbf{a}_k \lambda_k^i + \begin{bmatrix} \frac{6}{5} & -\frac{1}{10} \\ \frac{1}{10} & \frac{1}{30} \end{bmatrix} \mathbf{a}_k \lambda_k^{i+1} \right) = \mathbf{0}. \quad (3.45) \end{aligned}$$

The eigenvalues  $\lambda_k$  can be found from the four roots of the quartic characteristic equation,

$$\left| c_0 \sqrt{M} \left( \begin{bmatrix} -\frac{1}{2} & -\frac{1}{10} \\ \frac{1}{10} & \frac{1}{60} \end{bmatrix} + \begin{bmatrix} 0 & \frac{1}{5} \\ -\frac{1}{5} & 0 \end{bmatrix} \lambda_k + \begin{bmatrix} \frac{1}{2} & -\frac{1}{10} \\ \frac{1}{10} & -\frac{1}{60} \end{bmatrix} \lambda_k^2 \right) - \frac{M}{h} \left( \begin{bmatrix} \frac{6}{5} & \frac{1}{10} \\ -\frac{1}{10} & \frac{1}{30} \end{bmatrix} + \begin{bmatrix} -\frac{12}{5} & 0 \\ 0 & -\frac{4}{15} \end{bmatrix} \lambda_k + \begin{bmatrix} \frac{6}{5} & -\frac{1}{10} \\ \frac{1}{10} & \frac{1}{30} \end{bmatrix} \lambda_k^2 \right) \right| = 0, \quad (3.46)$$

where  $|\cdot|$  indicates the determinant of the matrix. If there are no repeated roots then the vectors  $\mathbf{a}_k$  are constant and can be found (up to a multiplicative scalar) after substituting the corresponding  $\lambda_k$  into the difference equation (3.45). If a root is repeated  $n$  times, then the  $n$  corresponding  $\mathbf{a}_k$  may be polynomials in  $i$  of order up to  $n - 1$ . The coefficients in the polynomials can be found by substituting into (3.45) and equating powers of  $i$ .

Substituting expression (3.43) for  $\mathbf{U}_i$  into the difference equations (3.40), using (3.45), and writing  $u(x)$ ,  $e_p^0(x)$ , and  $e_p^1(x)$  as Taylor series expansions (assuming the solution is smooth enough) about node  $i$  gives the equations,

$$\begin{aligned} & c_0 \sqrt{M} \left( hu^{(1)} + \frac{h^3}{15} u^{(3)} \right) - M \left( hu^{(2)} + \frac{h^3}{15} u^{(4)} \right) \\ & + c_0 \sqrt{M} \left( h^{p+1} e_p^{0(1)} + \frac{h^{p+3}}{6} e_p^{0(3)} - \frac{h^{p+2}}{10} e_p^{1(2)} \right) \\ & - M \left( \frac{6h^{p+1}}{5} e_p^{0(2)} - \frac{h^p}{5} e_p^{1(1)} + \frac{h^{p+3}}{10} e_p^{0(4)} - \frac{h^{p+2}}{30} e_p^{1(3)} \right) = h\tau_m + O(h^5) \end{aligned} \quad (3.47a)$$

and

$$\begin{aligned} & c_0 \sqrt{M} \frac{h^2}{15} u^{(2)} - M \frac{h^2}{15} u^{(3)} \\ & + c_0 \sqrt{M} \left( \frac{h^{p+2}}{10} e_p^{0(2)} - \frac{h^{p+1}}{30} e_p^{1(1)} \right) \\ & - M \left( \frac{h^p}{5} e_p^{0(1)} - \frac{h^{p-1}}{5} e_p^{1(0)} + \frac{h^{p+2}}{30} e_p^{0(3)} + \frac{h^{p+1}}{30} e_p^{1(2)} \right) = O(h^4), \end{aligned} \quad (3.47b)$$

where there is an implied sum over the repeated index  $p$  and the superscripts in parentheses indicate a derivative of the specified order at node  $i$ . Because  $u$  satisfies  $c_0 \sqrt{M} u^{(n+1)} - M u^{(n+2)} = \tau_m^{(n)}$ , all the terms involving  $u$  and  $\tau_m$  cancel except those contained in the  $O(h^5)$  and  $O(h^4)$  truncation terms.

Equating the remaining terms involving like powers of  $h$  provides equations for the error coefficients  $e_p^0(x)$  and  $e_p^1(x)$ . Equating the terms involving the lowest powers of  $h$  (assuming  $M \neq 0$ ) first gives the equations,

$$e_0^{1(1)} = 0 \quad \text{and} \quad e_0^{1(0)} = 0,$$

thus eliminating the first derivative error term  $e_0^1$ . Further terms can be eliminated by noting that, if

$$e_p^0 = 0 \quad \forall p < q \quad \text{and} \quad e_p^1 = 0 \quad \forall p < q + 1,$$

and  $q < 4$ , then equating the terms involving the lowest remaining powers of  $h$  gives the system,

$$\begin{aligned} c_0 \sqrt{M} e_q^{0(1)} - M e_q^{0(2)} - \frac{1}{5} M \left( e_q^{0(2)} - e_{q+1}^{1(1)} \right) &= 0, \\ -\frac{1}{5} M \left( e_q^{0(1)} - e_{q+1}^{1(0)} \right) &= 0. \end{aligned}$$

This system and the boundary conditions (3.44) have the unique solution,  $e_q^0 = e_{q+1}^1 = 0$ . Recursive application of this process for  $q = 0, 1, 2, 3$  gives the results,

$$e_p^0 = 0 \quad \forall p < 4 \quad \text{and} \quad e_p^1 = 0 \quad \forall p < 5. \quad (3.48)$$

Substituting the remaining non-zero terms in expression (3.43) into the difference equations (3.41) generated at node  $N$ , using Taylor series expansions about that node, then using the fact that  $u$  satisfies the original equation and the Neumann boundary condition gives the following two linear equations for the error coefficients  $\epsilon_k$ :

$$\begin{aligned} \sum_k \left( c_0 \sqrt{M} \left( \begin{bmatrix} -\frac{1}{2} & -\frac{1}{10} \\ \frac{1}{10} & \frac{1}{60} \end{bmatrix} \mathbf{a}_k \lambda_k^{N-1} + \begin{bmatrix} \frac{1}{2} & \frac{1}{10} \\ -\frac{1}{10} & 0 \end{bmatrix} \mathbf{a}_k \lambda_k^N \right) \right. \\ \left. - \frac{M}{h} \left( \begin{bmatrix} \frac{6}{5} & \frac{1}{10} \\ -\frac{1}{10} & \frac{1}{30} \end{bmatrix} \mathbf{a}_k \lambda_k^{N-1} + \begin{bmatrix} -\frac{12}{5} & \frac{1}{10} \\ \frac{1}{10} & -\frac{2}{15} \end{bmatrix} \mathbf{a}_k \lambda_k^N \right) \right) \epsilon_k = \begin{bmatrix} O(h^4) \\ O(h^3) \end{bmatrix}. \quad (3.49a) \end{aligned}$$

The difference equations (3.42) at node 0 provide two further equations:

$$\sum_k \begin{bmatrix} 1 & 0 \end{bmatrix} \mathbf{a}_k \epsilon_k = 0,$$

$$\sum_k \left( c_0 \sqrt{M} \left( \begin{bmatrix} -\frac{1}{10} & 0 \end{bmatrix} \mathbf{a}_k + \begin{bmatrix} \frac{1}{10} & -\frac{1}{60} \end{bmatrix} \mathbf{a}_k \lambda_k \right) - \frac{M}{h} \left( \begin{bmatrix} -\frac{1}{10} & -\frac{2}{15} \end{bmatrix} \mathbf{a}_k + \begin{bmatrix} \frac{1}{10} & \frac{1}{30} \end{bmatrix} \mathbf{a}_k \lambda_k \right) \right) \epsilon_k = O(h^3). \quad (3.49b)$$

Provided the numerical scheme is stable, the error terms due to truncation errors at the boundaries  $\mathbf{a}_k \lambda_k \epsilon_k$  will be largest near the boundaries. Unless the system of the four linear equations above is singular, it determines  $\epsilon_k$  and the order of the error at the boundary. As  $h$  becomes small the coefficients associated with the diffusion term dominate, so these error terms approach  $O(h^4)$ .

For small enough  $h$ , therefore, the largest terms in the error expansions (3.43) are  $O(h^4)$ , and so fourth order convergence can be expected in the nodal parameters. The Hermite elements also provide cubic interpolation for the numerical solution between the nodes. The error in this interpolation is also  $O(h^4)$ , so fourth order convergence can be expected in the solution for excitation time at any point in the domain.

### 3.8.2 Error Transport

The above convergence analysis confirms that a high order of convergence can be expected when using the Galerkin finite element method with sufficiently small elements. However, it is necessary for the numerical method to also perform well for reasonably large elements.

It was observed in numerical experiments (Section 3.6) that, for large  $h$ , the Galerkin method provided good solutions when there were no collisions between wavefronts. If wavefronts collided, however, the solution deteriorated not only in the region of the collision, but over the whole domain.

The gradient of the exact solution for excitation time varies very rapidly near a wavefront collision. If the elements are much larger than the region of rapid change then they are not able to represent the solution accurately. This on its own would not be of great concern as deviations in the position of a small part of the wavefront are not expected to greatly affect either the overall function of the heart or the far-field potentials. The problem is that, although the truncation errors due to the inability of the interpolation to represent the collision accurately are local, they corrupt the solution in all regions in the domain.

In one dimension, the transport of error from a region of inaccuracy to the rest of the domain is determined by the solutions to the difference equation (3.45). If the elements are large, the evolution terms dominate. The error in the nodal parameters over any region of the domain resulting from truncation errors outside that region then resembles

$$\epsilon_1 \begin{bmatrix} 1 \\ 0 \end{bmatrix} + \epsilon_2 \begin{bmatrix} 0 \\ 1 \end{bmatrix} + \epsilon_3 \begin{bmatrix} 1 \\ \sqrt{30} \end{bmatrix} (11 + 2\sqrt{30})^i + \epsilon_4 \begin{bmatrix} 1 \\ -\sqrt{30} \end{bmatrix} (11 + 2\sqrt{30})^{-i}, \quad (3.50)$$

where the coefficients  $\epsilon_k$  are constants determined by the errors at the ends of the region under consideration. The first term is a result of the fact that residual in the governing equation is unaffected by an additive constant in the solution. The last two terms are each large only at opposite ends of the region and decay exponentially within the region. Their coefficients are effectively determined by the error at the end at which they are largest. The decay rate of these terms means that the error they carry is attenuated rapidly and is therefore not transported across the whole region. The second term, however, does not decay at all. It transports any error in the derivative parameters across the entire domain.

It is reasonable to assume that this process of error transport in the nodal derivative parameters also occurs in higher dimensions. This explains the element size wavelength oscillations seen in Figure 3.5. The inability of the large element interpolation to represent the wavefront collision accurately results in errors in the circumferential derivative parameters that are transported throughout the entire domain.

One way to avoid these oscillatory errors is to ensure that the elements are small enough to represent the solution accurately. The elements need to be very small to accurately approximate the solution in the region of a wavefront collision, but, if the whole domain mesh is made up of elements of the same size, the numerical solution process would be too computa-

tionally demanding. Instead a mesh could be made up of much larger elements over most of the domain where the solution is smooth and small elements only in the regions of collisions. It is not known before-hand, however, where the wavefront collisions are going to occur, so an adaptive mesh refinement algorithm would be required.

Similar problems with transport of error in the form of oscillations throughout the domain have been observed when using the Galerkin finite element method with linear Lagrange elements to solve the advection–diffusion equation (2.82) (Zienkiewicz and Taylor, 1994, for example). With linear elements, instead of a constant error term being transported through the domain, the error alternates in sign from node to node. Various alternative finite element methods have been suggested to prevent the formation of these oscillatory errors without the need for an adaptive mesh refinement algorithm. These are discussed in the next chapter.



## Chapter 4

# Alternative Finite Element Methods

A finite element method for the eikonal equation (2.65) that deals with the problem of error transport better than the Galerkin finite element method is sought by considering the approaches that have been used to deal with oscillatory errors in the steady-state advection–diffusion equation (2.82). Many of these approaches involve using an alternative weighted residual finite element method where the weights are asymmetric about nodes and depend on the direction of advection. There are additional considerations when applying these approaches to the non-linear eikonal equation and when using cubic Hermite interpolation.

## 4.1 The Least Squares Finite Element Method

Probably the finite element method that at first glance seems the most appropriate is the *least squares finite element method*. This method minimizes a functional involving integrals of the squares of the residuals in the governing equation and in the Neumann boundary condition. For the eikonal equation (2.65) the functional is

$$\int_{\Omega} \left( c_0 \sqrt{\nabla U \cdot M \nabla U} - \nabla \cdot (M \nabla U) - \tau_m \right)^2 d\Omega + k_b \int_{\Gamma_N} (\mathbf{n} \cdot M \nabla U)^2 d\Gamma, \quad (4.1)$$

where  $\Gamma_N$  indicates the area of the boundary over which the Neumann boundary condition (2.66) is applied. Dirichlet boundary conditions are applied in the same way as for the

Galerkin method by specifying the values of parameters describing  $u$  in the appropriate regions. Choice of the coefficient  $k_b$  for the boundary integral controls the amount of emphasis put on satisfying the Neumann boundary condition or the governing equation.

For a given finite element discretization, provided the above functional is smooth enough with respect to the nodal parameters, the derivatives of the functional with respect to each parameter must be zero at the minimum. That is

$$\int_{\Omega} \left( c_0 \sqrt{\nabla U \cdot M \nabla U} - \nabla \cdot (M \nabla U) - \tau_m \right) \left( \frac{c_0 \nabla U \cdot M \nabla \psi_i}{\sqrt{\nabla U \cdot M \nabla U}} - \nabla \cdot (M \nabla \psi_i) \right) d\Omega + k_b \int_{\Gamma_N} (\mathbf{n} \cdot M \nabla U) (\mathbf{n} \cdot M \nabla \psi_i) d\Gamma = 0 \quad (4.2)$$

for each  $i \in N$ . These equations form a symmetric system. It can now be seen that this is a weighted residual method where the weights are derivatives of the interpolation functions.

Like the Galerkin weighted residual equations, these become linear and equivalent to those for the advection–diffusion equation on a one-dimensional domain with the wavefront travelling in one direction only. For a cubic Hermite discretization of a simple problem such as that described in Section 3.8, the difference equations corresponding to nodes not on the boundary are

$$c_0^2 M \left( \begin{bmatrix} -\frac{6}{5} & -\frac{1}{10} \\ \frac{1}{10} & -\frac{1}{30} \end{bmatrix} \mathbf{U}_{i-1} + \begin{bmatrix} \frac{12}{5} & 0 \\ 0 & \frac{4}{15} \end{bmatrix} \mathbf{U}_i + \begin{bmatrix} -\frac{6}{5} & \frac{1}{10} \\ -\frac{1}{10} & -\frac{1}{30} \end{bmatrix} \mathbf{U}_{i+1} \right) + \frac{M^2}{h^2} \left( \begin{bmatrix} -12 & -6 \\ 6 & 2 \end{bmatrix} \mathbf{U}_{i-1} + \begin{bmatrix} 24 & 0 \\ 0 & 8 \end{bmatrix} \mathbf{U}_i + \begin{bmatrix} -12 & 6 \\ -6 & 2 \end{bmatrix} \mathbf{U}_{i+1} \right) = \mathbf{0}. \quad (4.3)$$

It is concerning that these difference equations do not include the driving source term  $\tau_m$ . The influence of this source term is only included through the difference equations at the boundary. This could mean that the effect of  $\tau_m$  on the solution throughout the domain is heavily dependent on the accuracy of the difference equations at the boundaries.

If the elements are large so that evolution dominates, the error within a region due to exterior

truncation error resembles

$$\epsilon_1 \begin{bmatrix} 1 \\ 0 \end{bmatrix} + \epsilon_2 \left( i \begin{bmatrix} 1 \\ 0 \end{bmatrix} + \begin{bmatrix} 0 \\ 1 \end{bmatrix} \right) + \epsilon_3 \begin{bmatrix} 1 \\ 3\sqrt{8} \end{bmatrix} (3 + \sqrt{8})^i + \epsilon_4 \begin{bmatrix} 1 \\ -3\sqrt{8} \end{bmatrix} (3 + \sqrt{8})^{-i}. \quad (4.4)$$

As with expression (3.50) for the error transport in the Galerkin method, the first term is expected due to the nature of the governing equation, and the last two terms decay reasonably rapidly. The second term does not decay exponentially but it is different in nature to the second term of (3.50) in that it is smooth and non-oscillatory.

Although the difference equations may not immediately seem appealing, the fact that the method minimizes a functional guarantees that there is a sense in which the solution is optimal. This optimal solution may not, however, behave as expected. For a two- or three-dimensional domain where the geometry and boundary conditions are functions of one element-local coordinate  $\xi_k$  only, the solution should be a function only of  $\xi_k$ . The numerical solution from the least squares finite element method, however, generally varies over the other coordinates also. This is due to the fact that the weights are not simply tensor products of one dimensional functions. A one-dimensional solution satisfying the weighted residual equations for weights corresponding to one-dimensional interpolation functions may not satisfy the weighted residual equations for the multi-dimensional weighting functions.

The convergence properties of this method require  $C^1$  continuity in the interpolation functions for  $U$  (Zienkiewicz and Taylor, 1994). Cubic Hermite elements can provide this level of continuity but, as discussed in Section 6.3, there are places in the ventricular myocardium where the exact solution  $u$  is not expected to be  $C^1$  continuous. If the first derivatives of  $u$  are not continuous, the first derivatives of  $U$  should not be forced to be continuous. The need for  $C^1$  continuous interpolation functions can be avoided by reformulating the eikonal equation (2.65) as a system of first order equations for variables that are first derivatives of  $u$ . The interpolation functions for these derivative variables, however, must still be  $C^0$  continuous, so a numerical scheme based on such a first order system would still be attempting to approximate a  $C^1$  continuous solution  $u$ . Use of such a scheme would also multiply the number of degrees of freedom in the problem by the number of dimensions.

There are also disadvantages with the least squares method that occur when using the method to solve the non-linear eikonal equation. Notice that as well as the residual of the govern-

ing equation being non-linear, the weights in the weighted residual equations (4.2) are also non-linear. This produces additional difficulties in solving the discrete system of equations, increasing the risk of the solver finding a local minimum instead of the global minimum.

Another disadvantage is that the weights may be discontinuous. Whenever two approaching wavefronts collide, a singularity occurs at the collision. This demands a complicated integration scheme to make a reasonable approximation of the integrals. If the integrals are calculated exactly then the integrals are smooth functions of the nodal parameters. If, however, the integrals are evaluated numerically by a sampling method such as Gaussian quadrature, then a discontinuity in the calculated integral occurs when the estimate of the solution is altered in such a way that the location of a collision crosses a sample point. This discontinuity further complicates solution of the discrete system of non-linear equations. There may not even be a solution. A possible remedy for this is to change the residual from the eikonal equation (2.65) to

$$\sqrt{c_0^2(1 - \alpha)\nabla U \cdot M\nabla U + \alpha(\nabla \cdot (M\nabla U) + \tau_m)^2} - \nabla \cdot (M\nabla U) - \tau_m, \quad (4.5)$$

where  $\alpha \in (0, 1)$ . This residual term is zero if and only if the eikonal equation is satisfied but behaves more smoothly than the residual in (2.65). The derivative is discontinuous when both  $\sqrt{\nabla U \cdot M\nabla U}$  and  $\nabla \cdot (M\nabla U) + \tau_m$  are zero, but in this situation the residual is zero, so the derivative of the square of the residual is continuous.

## 4.2 The Petrov–Galerkin Finite Element Method

Probably the most popular remedy to the problem of oscillatory error transport in the numerical solution of the steady-state advection–diffusion equation is a modification of the Galerkin weighted residual equations. Instead of just using the interpolation functions as weighting functions, they are supplemented with asymmetric functions  $\hat{w}_i$ . The weighted residual equations for the advection–diffusion equation (2.82) are then

$$\sum_e \int_{\Omega_e} (\mathbf{a} \cdot \nabla U - \nabla \cdot (M\nabla U) - \tau_m) w_i \, d\Omega + \sum_e \int_{\partial\Omega_e} \mathbf{n} \cdot M\nabla U w_i \, d\Gamma = 0, \quad (4.6)$$

where

$$w_i := \psi_i + \hat{w}_i. \quad (4.7)$$

The supplementary weighting functions  $\hat{w}_i$  are non-zero only in the elements where the corresponding  $\psi_i$  are non-zero, and are usually zero on inter-element boundaries so that the integrals on these boundaries are unaltered. These methods are called *Petrov–Galerkin* finite element methods.

Christie, Griffiths, Mitchell, and Zienkiewicz (1976) applied this method to the one-dimensional advection–diffusion equation using linear elements. For constant coefficients and equal-length elements, equivalent sets of difference equations were obtained when  $\hat{w}_i$  were either piecewise linear or quadratic  $C^0$  continuous functions satisfying  $\int \hat{w}_i dx = 0$ . By including in the supplementary functions  $\hat{w}_i$  the carefully selected coefficient

$$\alpha_s := \frac{1}{2} \coth \frac{P_e}{2} - \frac{1}{P_e}, \quad (4.8)$$

where the mesh Péclet number  $P_e$  is defined by

$$P_e := \frac{ah}{M}, \quad (4.9)$$

the truncation error in the difference equations vanished and the method gave the exact solution at the nodes.

When extending the method to the multi-dimensional advection–diffusion equation, the selection of  $\hat{w}_i$  is more difficult. Heinrich, Huyakorn, and Zienkiewicz (1977) suggested an extension of the above method to two dimensions using weighting functions that were tensor products of the quadratic-supplemented one-dimensional weights mentioned above. An improved and easier to implement scheme suggested by Brooks and Hughes (1982) used supplementary functions that were discontinuous derivatives of the interpolation functions:

$$\hat{w}_i(\mathbf{x}) = \begin{cases} \alpha_s h^* \frac{\mathbf{a}}{|\mathbf{a}|} \cdot \nabla \psi_i & \text{if } \mathbf{x} \text{ lies within an element,} \\ 0 & \text{if } \mathbf{x} \text{ lies on an element boundary,} \end{cases} \quad (4.10)$$

where  $h^*$  is a generalization of the element length for the direction  $\mathbf{a}$ . Although cancellation of truncation error is unlikely for general two-dimensional problems, a generalization of

expression (4.8) was suggested for  $\alpha_s$ . It was argued that the exact choice of  $\alpha_s$  is not as important as the nature of the supplementary functions  $\hat{w}_i$ . Morton (1996) gives alternative suggestions for  $\alpha_s$  that are based on norms of the error over the domain instead of nodally exact solutions for one-dimensional problems.

Application of a Petrov–Galerkin method to the eikonal equation (2.65) using  $C^1$  continuous cubic Hermite interpolation would provide weighted residual equations of the form,

$$\int_{\Omega} \left( c_0 \sqrt{\nabla U \cdot M \nabla U} - \nabla \cdot (M \nabla U) - \tau_m \right) w_i \, d\Omega + \int_{\partial\Omega} \mathbf{n} \cdot M \nabla U w_i \, d\Gamma = 0. \quad (4.11)$$

There are, however, difficulties in this extension both due to the cubic Hermite interpolation and due to the non-linear nature of the governing equation.

When using cubic Hermite interpolation even for one-dimensional geometries, there are two interpolation functions corresponding to each node  $i$ , so there are two different weighting functions, which are denoted by

$$w_i^p = \psi_i^p + \hat{w}_i^p \quad (4.12)$$

for derivative order  $p = 0, 1$ . There are therefore two potentially different parameters  $\alpha_s^p$  to determine. For supplementary weighting functions of the form,

$$\hat{w}_i^p = \alpha_s^p h \frac{\frac{du}{dx}}{\left| \frac{du}{dx} \right|} \frac{d\psi_i^p}{dx}, \quad (4.13)$$

the truncation errors in the difference equations vanish when

$$\alpha_s^0 := \frac{6 \sinh P_e - (12P_e^{-1} + P_e) (\cosh P_e - 1)}{2 (\cosh P_e - 1) - P_e \sinh P_e}$$

and

$$\alpha_s^1 := \frac{4 (\cosh P_e - 1) - (6P_e^{-1} + P_e) \sinh P_e + 6}{24 \sinh P_e + (60P_e^{-1} + 2P_e) (\cosh P_e - 1) - 6P_e}, \quad (4.14)$$

where  $P_e$  is defined by (3.37). It is not clear how this method should be extended to higher dimensions, because there are then many weighting functions at each node. The values of the various  $\alpha_s$  need to depend on the direction of propagation as well as the magnitude of the Péclet number.

The dependence of the supplementary functions  $\hat{w}_i$  on the direction of propagation means that they are non-linear and they are probably discontinuous at wavefront collisions. This method therefore suffers some of the same difficulties as the least squares method.

Donea, Belytschko, and Smolinski (1985) suggested an alternative formulation for the advection–diffusion equation that, instead of supplementing the weights with their derivatives, involved supplementing the residual in the governing equation with its derivative. This formulation was suggested for the extension of the Petrov–Galerkin approach to quadratic Lagrange elements, but it suffers the same difficulties in its extension to high order elements as the traditional Petrov–Galerkin method. Furthermore, as the derivative of the residual in the eikonal equation is discontinuous, it also suffers similar difficulties in its extension to this non-linear governing equation.

## 4.3 Stabilizing Terms

The problem of oscillatory errors in finite difference solutions to the advection-dominated advection–diffusion equation has long been recognized. The exact solution to the governing equation is usually smooth over most of the domain but it may be rapidly changing over small boundary layers in downstream regions of the domain. If the grid is not fine enough to represent the boundary layers accurately then the solution over the whole domain can be corrupted by oscillatory errors. One method to avoid this problem is to replace the standard central difference schemes for the advection term with *upwind* difference schemes. Use of these upwind differences means that only upstream information is ever used in calculating the value of the advection term at a grid point. This prevents the transport of error from downstream regions of the solution throughout the domain. Finite element methods can be given similar upwind properties by adding stabilizing terms to the weighted residual equations.

### 4.3.1 Artificial Diffusion

The simplest upwind finite difference schemes for the advection term are first order. In one dimension, if the coefficients in the governing equation are constant and the grid is regular,

the first-order upwind difference schemes are equivalent to adding *artificial diffusion* to the second-order central difference schemes. The amount of artificial diffusion can be carefully chosen to eliminate truncation error and provide exact solutions at the nodes. The error introduced by the artificial diffusion cancels the error in the numerical differencing, so the added diffusion is often called ‘balancing’ diffusion. Artificial diffusion is easily extended to general multidimensional problems, but the elimination of error is no longer expected.

The process of adding artificial diffusion has also been suggested for finite element solution of the advection–diffusion equation with linear elements (Kelly, Nakazawa, Zienkiewicz, and Heinrich, 1980). If the source term is constant, the resulting scheme is equivalent to the Petrov–Galerkin finite element method (Brooks and Hughes, 1982). For higher order elements, however, the methods are not equivalent.

When using cubic Hermite elements of equal length  $h$  for the solution of a one-dimensional eikonal equation with constant coefficients, artificial diffusion can be added by replacing the Galerkin weighted residual equations with

$$\int_{\Omega} \left( c_0 \sqrt{M} \left| \frac{du}{dx} \right| - \left( M + \beta^p h c_0 \sqrt{M} \right) \frac{d^2 u}{dx^2} - \tau_m \right) \psi_i^p d\Omega + \int_{\partial\Omega} M \frac{du}{dn} \psi_i^p d\Gamma = 0, \quad (4.15)$$

where the parameters  $\beta^p$  determine the amount of artificial diffusion added. There is no sum over the index  $p$  indicating the order of the derivative to which  $\psi_i^p$  and  $\beta^p$  correspond. If the values of the parameters  $\beta^p$  are defined by

$$\beta^0 := \frac{6 \sinh P_e - (12 P_e^{-1} + P_e) (\cosh P_e - 1)}{12 (\cosh P_e - 1) - P_e \sinh P_e}$$

and

$$\beta^1 := \frac{4 (\cosh P_e - 1) - (6 P_e^{-1} + P_e) \sinh P_e + 6}{6 \sinh P_e + 2 P_e (\cosh P_e - 1)}, \quad (4.16)$$

then, for a wavefront propagating in one direction only, the error in the resulting difference equations is eliminated.

The fact that the value of  $\beta^p$  is different for each of the two types of weighting functions means that this procedure is not the same as adding diffusion to the original equation. The procedure simply eliminates the error in the difference equations by adding a calculated amount of a modifying term. There is in fact no reason why the modifying term needs to be

a diffusion term.

This method has the appealing advantage over the Petrov–Galerkin methods that, if it is applied to a situation where there are wavefront collisions, then it does not produce any discontinuities or additional nonlinearities in the numerical equations. It does, however, suffer from similar problems to Petrov–Galerkin methods in its extension to higher dimensions. The values of  $\beta^p$  are easily selected in one dimension because the exact solution is simple and is known (although care needs to be taken as the denominator of  $\beta^0$  in (4.16) passes through zero near  $P_e = 12$ ). In higher dimensions there are many values of  $\beta^p$  to select and the solution can be very complicated. It is no longer reasonable to expect a numerical scheme to provide exact answers at the nodes. What is expected from the scheme is that it does not propagate the error in a small region throughout the rest of the domain. Values of  $\beta^p$  could probably be chosen so that error is damped quickly, but the modifying terms introduce their own error.

If the parameters in the governing equation are not constant or if the mesh is not regular or if the solution is not one-dimensional, then the added diffusion terms do not cancel the error in the difference equations but introduce a second order error. This means that instead of the fourth order convergence expected from the Galerkin finite element method, a numerical scheme including artificial diffusion will show only first order convergence. In order to avoid this severe reduction of the convergence rate, alternative modifying terms were investigated.

### 4.3.2 Higher Order Stabilizing Terms

When the second order artificial diffusion terms are added to the governing equation the convergence of the numerical method is reduced to first order. This may be the best approach for linear elements, as the diffusion term is the highest order term that can be reasonably easily obtained within the scope of the finite element method and provides stability when added to the governing equation. For cubic elements, however, higher order stabilizing terms can be used.

When the artificial diffusion term is added to the Galerkin weighted residual equations for linear elements, it is not applied in the same way as in equation (4.15) because the discretiza-

tion cannot represent second derivatives. For a one-dimensional regular mesh, the modified equations are instead of the form,

$$\int_{\Omega} \left( c_0 \sqrt{M} \left| \frac{du}{dx} \right| \psi_i + (M + \beta h c_0 \sqrt{M}) \frac{du}{dx} \frac{d\psi_i}{dx} - \tau_m \psi_i \right) d\Omega - \int_{\partial\Omega} \beta h c_0 \sqrt{M} \frac{du}{dn} \psi_i d\Gamma = 0. \quad (4.17)$$

The modifying terms can be converted to an integral solely over the inter-element boundaries by using Green's theorem on each element:

$$\begin{aligned} & \int_{\Omega} \beta h c_0 \sqrt{M} \frac{du}{dx} \frac{d\psi_i}{dx} d\Omega - \int_{\partial\Omega} \beta h c_0 \sqrt{M} \frac{du}{dn} \psi_i d\Gamma \\ &= - \sum_e \int_{\Omega_e} \beta h c_0 \sqrt{M} \frac{d^2 u}{dx^2} \psi_i d\Omega + \sum_e \int_{\partial\Omega_e} \beta h c_0 \sqrt{M} \frac{du}{dn} \psi_i d\Gamma - \int_{\partial\Omega} \beta h c_0 \sqrt{M} \frac{du}{dn} \psi_i d\Gamma. \end{aligned} \quad (4.18)$$

The domain integral on the right hand side is zero because the second derivative of the linear interpolation of  $u$  is zero. The integrals over the element edges that lie on the domain boundary cancel with the domain boundary integral. The only remaining terms on the right hand side are integrals over inter-element boundaries. The modifying term is therefore a function of the differences in first derivatives across inter-element boundaries, and the scheme can be imagined to stabilize the numerical solution by restricting the discontinuities present in the first derivatives.

With higher order elements, there is a higher order of accuracy in the derivatives so inter-element derivative discontinuity terms are of higher order. With cubic Hermite interpolation, however, the first derivative is usually continuous between elements. Using the discontinuities in higher order derivatives to generate stabilizing terms was investigated, but an approach that seems more appealing is to relax the first-derivative continuity constraint.

For one-dimensional cubic Hermite interpolation using separate derivative parameters in each element, the vector  $\mathbf{U}_i$  of parameters corresponding to node  $i$  at  $x = x_i$  is defined by

$$\mathbf{U}_i := \begin{bmatrix} U(x_i) \\ \lim_{x \nearrow x_i} U'(x) \\ \lim_{x \searrow x_i} U'(x) \end{bmatrix}. \quad (4.19)$$

The first component of  $\mathbf{U}_i$  is the value of  $U$  at the node and is used by both adjacent elements, the second component is the derivative parameter used by the adjacent element in the direction of decreasing  $x$ , and the third component is the derivative parameter used by the adjacent element in the other direction.

When using this interpolation for the simple one-directional propagation problem described in Section 3.8, the contribution from the evolution term to the Galerkin difference equations at interior nodes is

$$c_0 \sqrt{M} \left( \begin{bmatrix} -\frac{1}{2} & 0 & -\frac{1}{10} \\ \frac{1}{10} & 0 & \frac{1}{60} \\ 0 & 0 & 0 \end{bmatrix} \mathbf{U}_{i-1} + \begin{bmatrix} 0 & \frac{1}{10} & \frac{1}{10} \\ -\frac{1}{10} & 0 & 0 \\ -\frac{1}{10} & 0 & 0 \end{bmatrix} \mathbf{U}_i + \begin{bmatrix} \frac{1}{2} & -\frac{1}{10} & 0 \\ 0 & 0 & 0 \\ \frac{1}{10} & -\frac{1}{60} & 0 \end{bmatrix} \mathbf{U}_{i+1} \right). \quad (4.20)$$

When the diffusion term is negligible, the roots of the corresponding characteristic equation for the eigenvalues  $\lambda_k$  are 0, 0, 1,  $-1$ ,  $\infty$ , and  $\infty$ . The eigenfunctions corresponding to the eigenvalues 1 and  $-1$  are

$$\begin{bmatrix} 1 \\ 0 \\ 0 \end{bmatrix} \quad \text{and} \quad \begin{bmatrix} \frac{1}{12} \\ 1 \\ -1 \end{bmatrix} (-1)^i. \quad (4.21)$$

The first term reflects the fact that the solution depends on the boundary condition for  $U$  at the upstream end of the domain, while the second term is oscillatory and is a mode by which error can be transported unattenuated from downstream regions. The repeated eigenvalues

0 and  $\infty$  represent rapidly decaying modes. One of the 0 eigenvalues results from the non-existence of the second component of  $\mathbf{U}_0$  and the other corresponds to the mode

$$\left\{ \left[ \begin{array}{c} -1 \\ \cdot \\ 6 \end{array} \right] \text{ at node } 0, \left[ \begin{array}{c} 0 \\ 1 \\ 0 \end{array} \right] \text{ at node } 1, \mathbf{0} \text{ elsewhere} \right\}, \quad (4.22)$$

which affects only the most upstream element. The  $\infty$  eigenvalues correspond to the non-existence of the third component of  $\mathbf{U}_N$  and the mode

$$\left\{ \left[ \begin{array}{c} 1 \\ 6 \\ \cdot \end{array} \right] \text{ at node } N, \left[ \begin{array}{c} 0 \\ 0 \\ 1 \end{array} \right] \text{ at node } (N - 1), \mathbf{0} \text{ elsewhere} \right\}, \quad (4.23)$$

which affects only the most downstream element.

When using cubic Hermite elements with separate derivative parameters in each element, therefore, the undesirable mode corresponds to an eigenvalue of  $-1$ . When the derivative parameters are shared between elements the undesirable mode corresponds to an eigenvalue of 1 (equation (3.50)). A derivative discontinuity term is therefore included to loosely couple the derivatives at each node so as to obtain a more favourable eigenvalue.

A derivative discontinuity term of the form

$$\sum_e \int_{\partial\Omega_e} \beta h c_0 \sqrt{M} \frac{du}{dn} \psi_i d\Gamma - \int_{\partial\Omega} \beta h c_0 \sqrt{M} \frac{du}{dn} \psi_i d\Gamma \quad (4.24)$$

contributes the term,

$$\beta c_0 \sqrt{M} \begin{bmatrix} 0 & 1 & -1 \\ 0 & 0 & 0 \\ 0 & 0 & 0 \end{bmatrix} \mathbf{U}_i \quad (4.25)$$

to the difference equations for the nodal parameters. When diffusion is negligible, the eigen-

functions  $\mathbf{a}_k \lambda_k^i$  determining the available modes for error transport satisfy

$$\begin{bmatrix} -\frac{1}{2} & 0 & -\frac{1}{10} \\ \frac{1}{10} & 0 & \frac{1}{60} \\ 0 & 0 & 0 \end{bmatrix} \mathbf{a}_k \lambda_k^{i-1} + \begin{bmatrix} 0 & \frac{1}{10} + \beta & \frac{1}{10} - \beta \\ -\frac{1}{10} & 0 & 0 \\ -\frac{1}{10} & 0 & 0 \end{bmatrix} \mathbf{a}_k \lambda_k^i + \begin{bmatrix} \frac{1}{2} & -\frac{1}{10} & 0 \\ 0 & 0 & 0 \\ \frac{1}{10} & -\frac{1}{60} & 0 \end{bmatrix} \mathbf{a}_k \lambda_k^{i+1} = \mathbf{0} \quad (4.26)$$

(cf. expression (4.20)). The eigenvalues  $\lambda_k$  are therefore

$$0, 0, 1, \frac{12\beta + 1}{12\beta - 1}, \infty, \text{ and } \infty. \quad (4.27)$$

To minimize the transport of error from downstream regions a value of  $\frac{1}{12}$  is selected for  $\beta$ , giving three infinite eigenvalues.

With  $\beta = \frac{1}{12}$ , the eigenfunction corresponding to the unit eigenvalue is the same as that for the Galerkin method and reflects the dependence of the solution on the excitation time of upstream regions. The other mode representing transport of information from upstream regions (corresponding to the zero eigenvalues) is

$$\left\{ \begin{bmatrix} -11 \\ \cdot \\ 66 \end{bmatrix} \text{ at node } 0, \begin{bmatrix} 0 \\ 6 \\ 0 \end{bmatrix} \text{ at node } 1, \mathbf{0} \text{ elsewhere} \right\}. \quad (4.28)$$

The modes permitting transport of information from downstream regions (corresponding to the infinite eigenvalues) are

$$\left\{ \begin{bmatrix} 1 \\ 6 \\ \cdot \end{bmatrix} \text{ at node } N, \begin{bmatrix} 0 \\ 0 \\ 6 \end{bmatrix} \text{ at node } (N-1), \mathbf{0} \text{ elsewhere} \right\}, \quad (4.29)$$

$$\text{and } \left\{ \begin{bmatrix} 11 \\ 60 \\ \cdot \end{bmatrix} \text{ at node } N, \begin{bmatrix} 1 \\ 6 \\ 0 \end{bmatrix} \text{ at node } (N-1), \begin{bmatrix} 0 \\ 0 \\ 6 \end{bmatrix} \text{ at node } (N-2), \mathbf{0} \text{ elsewhere} \right\}. \quad (4.30)$$

The error in any element therefore does not influence the upstream solution any further than the nearest two elements.

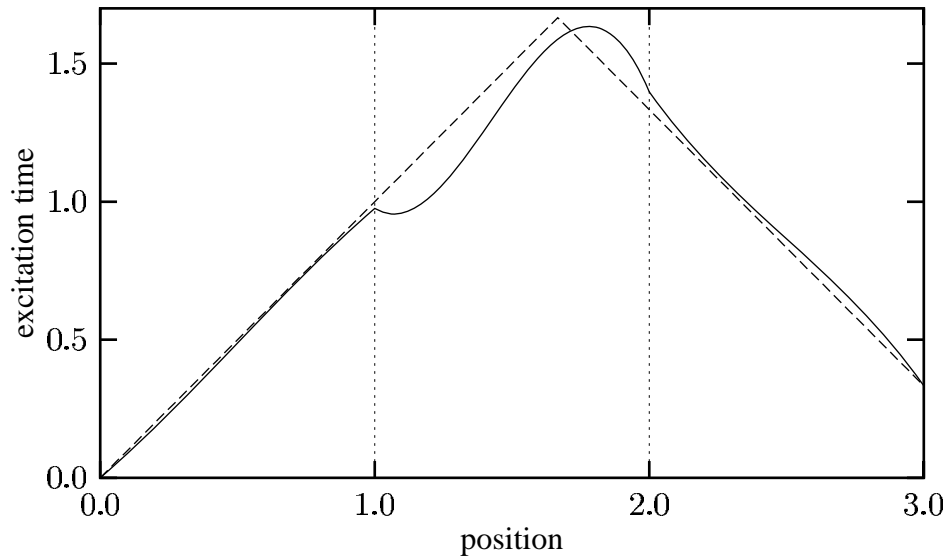


**Figure 4.1:** Numerical solution from a Galerkin method stabilized by a derivative discontinuity term for a 3-element length of tissue stimulated at both ends. There is no diffusion. The right hand end is stimulated later than the left hand end so that the collision occurs off-centre in the middle element. The dashed line shows the exact solution.

The upwind nature of the method is demonstrated in Figure 4.1 on a 3-element mesh with a collision in the middle element. In the elements upstream from the collision, the solution is affected little by the inability to represent the exact solution near the collision. In the element containing the collision, although a perfect solution cannot be expected, the method provides an undesirably oscillatory solution. It may be acceptable to have an inaccurate solution in a few elements of the mesh when solving a linear advection–diffusion equation, but with the non-linear eikonal equation, the reversal in the direction of propagation can lead to completely unreasonable solutions or there may be no solution to the discrete system of equations. The method easily extends to multi-dimensional problems but solutions are more complex in such problems and an inaccurate direction of propagation may seriously corrupt the solution.

## 4.4 Summary

The least squares finite element method is appealing because there is a sense in which the method is minimizing the error. The non-one-dimensional solutions to one dimensional problems, however, may suggest that the sense in which error is minimized may not be the most appropriate. The method also has the significant disadvantage that it requires  $C^1$  continuity in the solution, and there may be problems with the non-linearities in the governing equation.

The upwind nature of the method with the stabilizing derivative discontinuity term is appealing. The method has only been investigated on a regular grid so whether or not the method is still strongly upwind for irregular grids is uncertain. The poor performance of the method within an element containing a collision makes the method unattractive. This results from the lack of any sense in which the solution is optimal. The stabilizing term is essentially a balancing term selected from a simple one-dimensional problem where the solution was known. When the solution is more complex, as in an element with a collision and possibly when irregular meshes are used, the level of balancing may no longer be appropriate.

Petrov–Galerkin methods do not guarantee any optimality of the solution but they have the advantage over the least squares method that they do not require  $C^1$  continuity. They also provide one-dimensional solutions to one-dimensional problems. In the next chapter it is shown that, for one-dimensional propagation at least, the error in the solution from a Petrov–Galerkin method is within a constant factor of the optimal error. The bound does not require a regular mesh. There is freedom to select weighting functions that do not contain any disruptive discontinuities, and the values of the multipliers  $\alpha_s$  in the supplementary weights do not need to depend on the derivative index  $p$ . The non-linear nature of the weighting functions is a disadvantage but it seems that this may be necessary to obtain a reasonable bound on the error. A Petrov–Galerkin method for the multi-dimensional eikonal equation is developed in the next chapter.



## Chapter 5

# A Petrov–Galerkin Finite Element Method

The general Petrov–Galerkin finite element method for determining an approximation  $U$  for  $u$  may be formulated as finding  $U \in S_D^h$  such that

$$B(U, W) = \langle \tau_m, W \rangle \quad \forall W \in T^h, \quad (5.1)$$

where  $B(\cdot, \cdot)$  is defined as in (3.25) and  $T^h$  is the test space. In contrast to the Galerkin method,  $T^h \neq S_0^h$ . The performance of a Petrov–Galerkin method depends on the choice of the test space  $T^h$ .

## 5.1 Selection of Weighting Functions

In this section, a means for estimating the quality of a test space  $T^h$  is described, and a set of weighting functions, which form a basis for  $T^h$ , is selected on the grounds of keeping the expected error in the solution to a minimum and facilitating numerical solution of the resulting weighted residual equations.

### 5.1.1 Approximate Symmetrization

The poor performance of the Galerkin finite element method when diffusion is small results from the asymmetric nature of  $B(\cdot, \cdot)$ . The small symmetric component gives only a small lower bound (3.31) for  $B(v, v)$ . The object of selecting a Petrov–Galerkin scheme is to choose a mapping from  $S_0^h$  to  $T^h$  so that it compensates for this asymmetry. Barrett and Morton (1984) showed how an error bound can be derived for a test space  $T^h$  if  $B(\cdot, \cdot)$  is bilinear. A summary of the key points follows.

If  $T^h \subset H_{D_0}^1$  then the exact solution  $u$  satisfies the same weighted residual equations (5.1) as the numerical solution  $U$ . Therefore, if  $B(\cdot, \cdot)$  is bilinear, the error  $u - U$  satisfies the orthogonality property,

$$B(u - U, W) = 0 \quad \forall W \in T^h. \quad (5.2)$$

The convergence properties implied by this orthogonality property depend on  $T^h$ .

If  $B_S(\cdot, \cdot)$  is any symmetric continuous coercive bilinear form on  $H_{D_0}^1 \times H_{D_0}^1$ , then, from the Riesz representation theorem, there exists a *representer*  $R_S: H_{D_0}^1 \rightarrow H_{D_0}^1$  such that

$$B(v, w) = B_S(v, R_S w) \quad \forall v, w \in H_{D_0}^1. \quad (5.3)$$

Assuming  $u - U \in H_{D_0}^1$ , this means that the orthogonality property (5.2) may be written as

$$B_S(u - U, R_S W) = 0 \quad \forall W \in T^h. \quad (5.4)$$

If the test space  $T^h$  is chosen to be equal to  $T^{h*} \subset H_{D_0}^1$  defined such that

$$R_S T^{h*} = S_0^h, \quad (5.5)$$

then the orthogonality property (5.4) for the error in the corresponding Petrov–Galerkin ap-

proximation  $U^*$  is equivalent to

$$B_S(u - U^*, V) = 0 \quad \forall V \in S_0^h \quad (5.6)$$

$$\Rightarrow \|u - U^*\|_{B_S} = \inf_{Z \in S_D^h} \|u - Z\|_{B_S}. \quad (5.7)$$

In the sense of the  $\|\cdot\|_{B_S}$  norm, therefore,  $U^*$  is the best possible approximation available in  $S_D^h$ . Unfortunately, finding the optimal test space  $T^{h*}$  is usually at least as difficult as solving the original problem.

For non-optimal test spaces, the performance of the method depends on how closely  $S_0^h$  can be approximated by  $R_S T^h$ . If  $T^h \subset H_{D_0}^1$  and there exists a constant  $\Delta_S \in [0, 1)$  such that

$$\inf_{W \in T^h} \|V - R_S W\|_{B_S} \leq \Delta_S \|V\|_{B_S} \quad \forall V \in S_0^h, \quad (5.8)$$

then it is possible to determine a bound for the error in terms of the optimal error and the constant  $\Delta_S$ .

The orthogonality equation (5.6) for the optimal solution  $U^*$  may be used to write

$$\|u - U\|_{B_S}^2 = \|u - U^*\|_{B_S}^2 + \|U^* - U\|_{B_S}^2. \quad (5.9)$$

The first term on the right hand side is the best possible value for the left hand side and the second term can be bounded using (5.6), (5.4), and (5.8):

$$\begin{aligned} \|U^* - U\|_{B_S}^2 &\equiv B_S(U^* - U, U^* - U) \\ &= B_S(u - U, U^* - U) \\ &= B_S(u - U, U^* - U - R_S W) \quad \forall W \in T^h \\ &\leq \|u - U\|_{B_S} \|U^* - U - R_S W\|_{B_S} \quad \forall W \in T^h \\ \Rightarrow \|U^* - U\|_{B_S}^2 &\leq \Delta_S \|u - U\|_{B_S} \|U^* - U\|_{B_S} \\ \Rightarrow \|U^* - U\|_{B_S} &\leq \Delta_S \|u - U\|_{B_S}. \end{aligned} \quad (5.10)$$

Substituting this into (5.9) and using (5.7) gives the bound,

$$\|u - U\|_{B_S} \leq \frac{1}{\sqrt{1 - \Delta_S^2}} \inf_{Z \in S_B^h} \|u - Z\|_{B_S}. \quad (5.11)$$

The ratio of this bound on the error to the optimal solution error is therefore described by the *error factor*  $(1 - \Delta_S^2)^{-\frac{1}{2}}$ .

If the representer  $R_S$  is known then the constant  $\Delta_S$  may be calculated for given  $S_0^h$  and  $T^h$ . The approximation property (5.8) is satisfied for

$$\Delta_S^2 = \sup_{V \in S_0^h} \frac{\inf_{W \in T^h} \|V - R_S W\|_{B_S}^2}{\|V\|_{B_S}^2}. \quad (5.12)$$

In the Petrov–Galerkin finite element method,  $T^h$  and  $S_0^h$  are both of dimension  $N$ , and the vectors  $V \in S_0^h$  and  $W \in T^h$  may be written as

$$V(\mathbf{x}) = V_i \psi_i(\mathbf{x}) \quad \text{and} \quad W(\mathbf{x}) = W_i w_i(\mathbf{x}). \quad (5.13)$$

Defining the  $N$ -vectors  $\mathbf{V}$  and  $\mathbf{W}$  with components  $V_i$  and  $W_i$ , and the  $N \times N$  matrices  $A$ ,  $B$ , and  $C$  with entries

$$\begin{aligned} A_{ij} &:= B_S(R_S w_i, R_S w_j), \\ B_{ij} &:= B_S(R_S w_i, \psi_j) = B(\psi_j, w_i), \\ \text{and} \quad C_{ij} &:= B_S(\psi_i, \psi_j), \end{aligned} \quad (5.14)$$

equation (5.12) may be written as

$$\Delta_S^2 = \sup_{\mathbf{V}} \frac{\inf_{\mathbf{W}} \{\mathbf{V}^T C \mathbf{V} - 2\mathbf{W}^T B \mathbf{V} + \mathbf{W}^T A \mathbf{W}\}}{\mathbf{V}^T C \mathbf{V}}.$$

The infimum over  $\mathbf{W}$  is reached when  $A\mathbf{W} = B\mathbf{V}$  so

$$\Delta_S^2 = \sup_{\mathbf{V}} \frac{\mathbf{V}^T C \mathbf{V} - \mathbf{V}^T B^T A^{-1} B \mathbf{V}}{\mathbf{V}^T C \mathbf{V}},$$

which means

$$1 - \Delta_S^2 = \inf_{\mathbf{V}} \frac{\mathbf{V}^T B^T A^{-1} B \mathbf{V}}{\mathbf{V}^T C \mathbf{V}}. \quad (5.15)$$

It is therefore possible to calculate the error factor  $(1 - \Delta_S^2)^{-\frac{1}{2}}$  as the reciprocal of the square root of the smallest eigenvalue  $\lambda$  of the generalized eigenvalue problem

$$B^T A^{-1} B \mathbf{V} = \lambda C \mathbf{V}. \quad (5.16a)$$

Provided  $B$  is non-singular, putting  $\mathbf{V} = C^{-1} B^T \mathbf{W}$  indicates that the problem

$$B C^{-1} B^T \mathbf{W} = \lambda A \mathbf{W} \quad (5.16b)$$

has the same eigenvalues, and can also be used for calculating the error factor.

### 5.1.2 One-Dimensional Optimal Weighting Functions

The above analysis applies only when  $B(\cdot, \cdot)$  is bilinear. This form is bilinear for the eikonal equation if and only if propagation is in one direction only. Weighting functions are first selected for this simple case before extension to more complex cases is considered.

Consider then the one-dimensional problem (3.27). For this problem the Riesz representer  $R_S$  may be easily found. From its defining relation (5.3) and definitions of  $B(\cdot, \cdot)$  (3.28) and  $B_S(\cdot, \cdot)$  (3.29),

$$\begin{aligned} c_0 \sqrt{M} \langle v', w \rangle + M \langle v', w' \rangle &= M \langle v', (R_S w)' \rangle \\ \Rightarrow \langle M v', \frac{c_0}{\sqrt{M}} w + w' - (R_S w)' \rangle &= 0 \quad \forall v, w \in H_{D_0}^1. \end{aligned}$$

With the Neumann boundary condition at  $x = L$ ,  $v$  is only confined to be zero at  $x = 0$  so

$$(R_S w)' = \gamma w + w' \quad \forall w \in H_{D_0}^1, \quad (5.17)$$

where  $\gamma = \frac{c_0}{\sqrt{M}}$ . This and the boundary condition  $(R_S w)(0) = 0$  due to  $R_S w \in H_{D_0}^1$  uniquely determine  $R_S w$  for any given  $w$ .

If each of the weighting functions  $w_i^*$  were chosen such that  $R_S w_i^* = \psi_i$ , they would form a basis for the optimal test space  $T^{h*}$ . Substituting  $w_i^*$  for  $w$  and  $\psi_i$  for  $R_S w$  in (5.17), then

solving for  $w_i^*$  gives

$$w_i^*(x) = \int_0^x \psi_i'(t) e^{\gamma(t-x)} dt. \quad (5.18)$$

Note that this approaches  $\psi_i(x)$  when  $\gamma \rightarrow 0$  (as  $\psi_i(0) = 0 \forall i \in N$ ).

The integral may be evaluated for general  $\gamma$  by considering each element in turn. For an element spanning nodes  $j$  and  $j + 1$  (numbered in the direction of increasing  $x$ ),

$$w_i^*(x) = w_i^*(x_j) e^{-\gamma(x-x_j)} + \int_{x_j}^x \psi_i'(t) e^{\gamma(t-x)} dt \quad \forall x \in [x_j, x_{j+1}]$$

If  $\frac{dx}{d\xi} = h$  is constant (i.e. equally spaced elements) and the basis functions are order  $N$ , the  $(N + 1)$ th derivative of  $\psi(x)$  is 0, so integrating by parts  $N$  times leads to

$$w_i^*(x) = w_i^*(x_j) e^{-\gamma(x-x_j)} + \sum_{k=1}^N (-\gamma)^{-k} \left( \psi_i^{(k)}(x_j) e^{-\gamma(x-x_j)} - \psi_i^{(k)}(x) \right) dt$$

$$\forall x \in [x_j, x_{j+1}] \quad (5.19)$$

where the  $k$ th derivatives  $\psi_i^{(k)}(x_j)$  and  $\psi_i^{(k)}(x_{j+1})$  are defined as the limits of  $\psi_i^{(k)}(x)$  as  $x$  approaches  $x_j$  and  $x_{j+1}$  from within  $(x_j, x_{j+1})$ . It can now be seen that  $w_i^*(x) \rightarrow \frac{1}{\gamma} \psi_i'(x)$  when  $\gamma \rightarrow \infty$ .

For  $N$  cubic Hermite elements, the optimal weighting functions  $w_i^{p*}(x)$  calculated in this way from  $\psi_i^p(x)$  are

$$w_i^{0*} = \begin{cases} 0 & \text{on } [0, x_{i-1}], \\ \gamma^{-1} \psi_i^{0'} - \gamma^{-2} \psi_i^{0''} + \gamma^{-3} \psi_i^{0'''} + [6(\gamma h)^{-2} + 12(\gamma h)^{-3}] e^{-\gamma(x-x_{i-1})} & \text{on } (x_{i-1}, x_i], \\ \gamma^{-1} \psi_i^{0'} - \gamma^{-2} \psi_i^{0''} + \gamma^{-3} \psi_i^{0'''} - 24(\gamma h)^{-3} e^{-\gamma(x-x_i)} + [6(\gamma h)^{-2} + 12(\gamma h)^{-3}] e^{-\gamma(x-x_{i-1})} & \text{on } (x_i, x_{i+1}], \\ -6(\gamma h)^{-2} (1 - e^{-2\gamma h}) + 12(\gamma h)^{-3} (1 - e^{-\gamma h})^2 & \text{on } (x_{i+1}, L], \end{cases} \quad (5.20a)$$

and

$$w_i^{1*} = \begin{cases} 0 & \text{on } [0, x_{i-1}], \\ \gamma^{-1}\psi_i^{1'} - \gamma^{-2}\psi_i^{1''} + \gamma^{-3}\psi_i^{1'''} - [2(\gamma h)^{-2} + 6(\gamma h)^{-3}]e^{-\gamma(x-x_{i-1})} & \text{on } (x_{i-1}, x_i], \\ \gamma^{-1}\psi_i^{1'} - \gamma^{-2}\psi_i^{1''} + \gamma^{-3}\psi_i^{1'''} - 8(\gamma h)^{-2}e^{-\gamma(x-x_i)} - [2(\gamma h)^{-2} + 6(\gamma h)^{-3}]e^{-\gamma(x-x_{i-1})} & \text{on } (x_i, x_{i+1}], \\ -2(\gamma h)^{-2}(1 + 4e^{-\gamma h} + e^{-2\gamma h}) + 6(\gamma h)^{-3}(1 - e^{-2\gamma h}) & \text{on } (x_{i+1}, L], \end{cases} \quad (5.20b)$$

for  $1 \leq i \leq N$ , and

$$w_0^{1*} = \begin{cases} \gamma^{-1}\psi_0^{1'} - \gamma^{-2}\psi_0^{1''} + \gamma^{-3}\psi_0^{1'''} - [(\gamma h)^{-1} + 4(\gamma h)^{-2} + 6(\gamma h)^{-3}]e^{-\gamma x} & \text{on } [0, x_1], \\ -(\gamma h)^{-1}e^{-\gamma h} - (\gamma h)^{-2}(2 + 4e^{-\gamma h}) + 6(\gamma h)^{-3}(1 - e^{-\gamma h}) & \text{on } (x_1, L]. \end{cases} \quad (5.20c)$$

The weighting functions (5.20a) and (5.20b) corresponding to internal nodes are plotted in Figure 5.1 for various values of  $P_e = \gamma h$ , and the weighting function (5.20c) corresponding to node 0 is plotted in Figure 5.2. These functions are not local to the neighbouring elements but are non-zero over much of the domain.

The same optimal test space  $T^{h*}$  can be generated using local weighting functions. Note that a basis for  $S_0^h$  can be constructed from the functions

$$v_i^p(x) := \psi_i^p + k_i^p \sum_{j=i+1}^N \psi_j^0, \quad (5.21)$$

where  $k_i^p$  are any constants. If the weighting functions  $w_i^{p*}$  are chosen to satisfy  $R_S w_i^{p*} = v_i^p$ ,

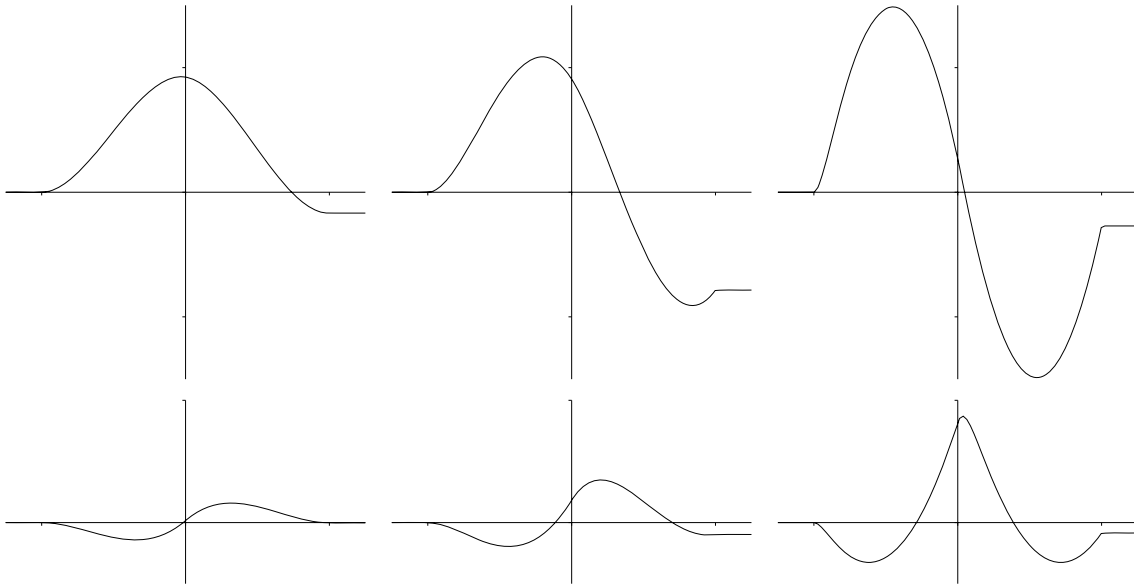


**Figure 5.1:** Optimal weighting functions  $w_i^{0*}$  (top) and  $w_i^{1*}$  (bottom) for  $1 \leq i \leq N$  from equations (5.20) when  $P_e = 0.2$  (left), 2 (centre), and 20 (right). Plots are centred on node  $i$  and ticks on the  $x$ -axis indicate neighbouring nodes. Functions are scaled by  $\sqrt{1 + P_e^2}$  for consistency in magnitudes.

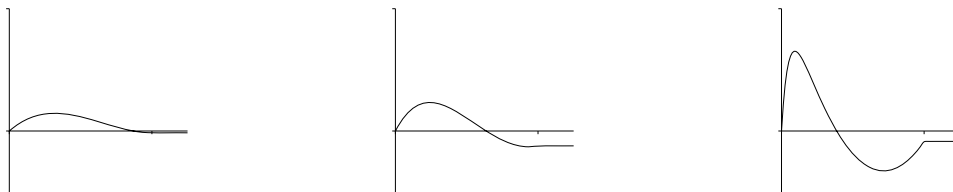


**Figure 5.2:** Optimal weighting function  $w_0^{1*}$  near the Dirichlet boundary from equations (5.20) when  $P_e = 0.2$  (left), 2 (centre), and 20 (right).

they are optimal. This is achieved with

$$w_i^{0*} = \begin{cases} 0 & \text{on } [0, x_{i-1}], \\ \gamma^{-1}\psi_i^{0'} - \gamma^{-2}\psi_i^{0''} + \gamma^{-3}\psi_i^{0'''} \\ \quad + [6(\gamma h)^{-2} + 12(\gamma h)^{-3}]e^{-\gamma(x-x_{i-1})} & \text{on } (x_{i-1}, x_i], \\ \gamma^{-1}\psi_i^{0'} - \gamma^{-2}\psi_i^{0''} + \gamma^{-3}\psi_i^{0'''} - 24(\gamma h)^{-3}e^{-\gamma(x-x_i)} \\ \quad + [6(\gamma h)^{-2} + 12(\gamma h)^{-3}]e^{-\gamma(x-x_{i-1})} \\ \quad + k_i^0 \{ \gamma^{-1}\psi_{i+1}^{0'} - \gamma^{-2}\psi_{i+1}^{0''} + \gamma^{-3}\psi_{i+1}^{0'''} \\ \quad + [6(\gamma h)^{-2} + 12(\gamma h)^{-3}]e^{-\gamma(x-x_i)} \} & \text{on } (x_i, x_{i+1}], \\ -6(\gamma h)^{-2}(1 - e^{-2\gamma h}) + 12(\gamma h)^{-3}(1 - e^{-\gamma h})^2 \\ \quad + k_i^0 \{ 6(\gamma h)^{-2}(1 + e^{-\gamma h}) - 12(\gamma h)^{-3}(1 - e^{-\gamma h}) \} & \text{on } (x_{i+1}, L], \end{cases} \quad (5.22a)$$

and

$$w_i^{1*} = \begin{cases} 0 & \text{on } [0, x_{i-1}], \\ \gamma^{-1}\psi_i^{1'} - \gamma^{-2}\psi_i^{1''} + \gamma^{-3}\psi_i^{1'''} \\ \quad - [2(\gamma h)^{-2} + 6(\gamma h)^{-3}]e^{-\gamma(x-x_{i-1})} & \text{on } (x_{i-1}, x_i], \\ \gamma^{-1}\psi_i^{1'} - \gamma^{-2}\psi_i^{1''} + \gamma^{-3}\psi_i^{1'''} - 8(\gamma h)^{-2}e^{-\gamma(x-x_i)} \\ \quad - [2(\gamma h)^{-2} + 6(\gamma h)^{-3}]e^{-\gamma(x-x_{i-1})} \\ \quad + k_i^1 \{ \gamma^{-1}\psi_{i+1}^{0'} - \gamma^{-2}\psi_{i+1}^{0''} + \gamma^{-3}\psi_{i+1}^{0'''} \\ \quad + [6(\gamma h)^{-2} + 12(\gamma h)^{-3}]e^{-\gamma(x-x_i)} \} & \text{on } (x_i, x_{i+1}], \\ -2(\gamma h)^{-2}(1 + 4e^{-\gamma h} + e^{-2\gamma h}) + 6(\gamma h)^{-3}(1 - e^{-2\gamma h}) \\ \quad + k_i^1 \{ 6(\gamma h)^{-2}(1 + e^{-\gamma h}) - 12(\gamma h)^{-3}(1 - e^{-\gamma h}) \} & \text{on } (x_{i+1}, L], \end{cases} \quad (5.22b)$$

for  $1 \leq i \leq N$ , and

$$w_0^{1*} = \begin{cases} \gamma^{-1}\psi_0^{1'} - \gamma^{-2}\psi_0^{1''} + \gamma^{-3}\psi_0^{1'''} \\ \quad - [(\gamma h)^{-1} + 2(\gamma h)^{-2} + 6(\gamma h)^{-3}]e^{-\gamma x} \\ \quad + k_i^1 \{ \gamma^{-1}\psi_{i+1}^{0'} - \gamma^{-2}\psi_{i+1}^{0''} + \gamma^{-3}\psi_{i+1}^{0'''} \\ \quad + [6(\gamma h)^{-2} + 12(\gamma h)^{-3}]e^{-\gamma(x-x_i)} \} & \text{on } [0, x_1], \\ -(\gamma h)^{-1}e^{-\gamma h} - (\gamma h)^{-2}(2 + 4e^{-\gamma h}) + 6(\gamma h)^{-3}(1 - e^{-\gamma h}) \\ \quad + k_i^1 \{ 6(\gamma h)^{-2}(1 + e^{-\gamma h}) - 12(\gamma h)^{-3}(1 - e^{-\gamma h}) \} & \text{on } (x_1, L]. \end{cases} \quad (5.22c)$$

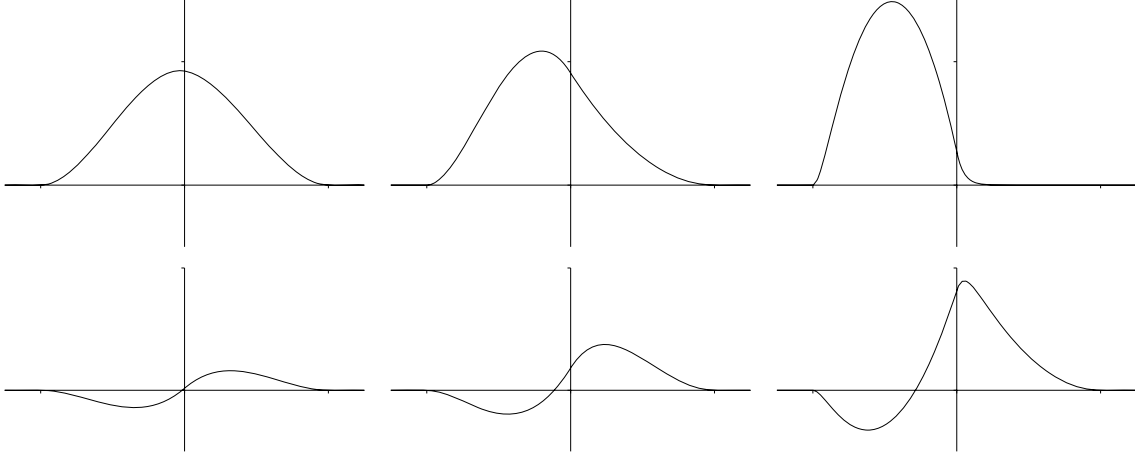


**Figure 5.3:** Localized optimal weighting functions  $w_i^{0*}$  (top) and  $w_i^{1*}$  (bottom) for  $1 \leq i \leq N$  from equations (5.22) when  $P_e = 0.2$  (left), 2 (centre), and 20 (right).

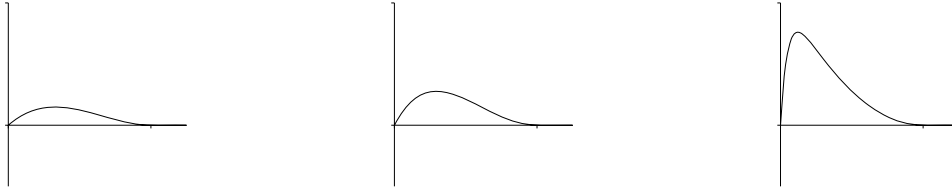


**Figure 5.4:** Localized optimal weighting function  $w_0^{1*}$  near the Dirichlet boundary from equations (5.22) when  $P_e = 0.2$  (left), 2 (centre), and 20 (right).

Each  $w_i^{p*}$  is zero on  $[x_{i+1}, L]$  and therefore local to neighbouring elements if

$$k_i^p = \begin{cases} \frac{(\gamma h)^2 e^{-\gamma h} + \gamma h(2 + 4e^{-\gamma h}) - 6(1 - e^{-\gamma h})}{6\gamma h(1 + e^{-\gamma h}) - 12(1 - e^{-\gamma h})} & \text{if } i = 0, p = 1, \\ 1 - e^{-\gamma h} & \text{if } 1 \leq i \leq N, p = 0, \\ \frac{2\gamma h(1 + 4e^{-\gamma h} + e^{-2\gamma h}) - 6(1 - e^{-2\gamma h})}{6\gamma h(1 + e^{-\gamma h}) - 12(1 - e^{-\gamma h})} & \text{if } 1 \leq i \leq N, p = 1. \end{cases} \quad (5.22d)$$

These weighting functions are plotted for various values of  $P_e$  in Figures 5.3 and 5.4.

### 5.1.3 One-Dimensional Approximate Symmetrization

The formulae (5.20) and (5.22) for optimal one-dimensional weighting functions  $w_i^{p*}$  and  $w_i^{p*}$  are rather complicated and become even more complicated for irregular meshes or variable coefficients. Extension to more than one dimension and to the non-linear eikonal equation does not seem feasible.

Instead, therefore, the weighting functions are chosen to be simple combinations of the optimal functions when  $P_e$  approaches 0 and  $\infty$ . For one-dimensional problem (3.27) the weighting functions are

$$w_i^p := A_0 w_{i0}^p + A_\infty w_{i\infty}^p, \quad (5.23)$$

where

$$w_{i0}^p := \psi_i^p \quad \text{and} \quad w_{i\infty}^p := \gamma^{-1} \psi_i^{p'}. \quad (5.24)$$

These are local and easily evaluated. With the  $C^1$  continuity of cubic Hermite interpolation, they all lie in  $H_{D_0}^1$  except  $w_0^1$ . The exception will be discussed and corrected later in this section.

#### *Selection of Coefficients*

The proportionality coefficients  $A_0$  and  $A_\infty$  in the combination are chosen with the intention of making the factor in the error bound (5.11) as small as possible. This error factor depends on the closeness with which  $R_S T^h$  approximates  $S_0^h$  as measured by the constant  $\Delta_S$  in bound (5.8).  $(R_S W)'$  is given by expression (5.17), so bound (5.8) is equivalent to

$$\inf_{W \in T^h} \|V' - \gamma W - W'\|_{L_2} \leq \Delta_S \|V'\|_{L_2} \quad \forall V \in S_0^h. \quad (5.25)$$

Bounds for error factors in terms of  $P_e$  and  $N$  have been obtained for meshes of equal-length one-dimensional linear elements using eigenvalue problem (5.16b) (Morton, 1996), but extension to cubic Hermite elements is difficult. Analysis is therefore simplified by considering only the function in  $S_0^h$  that is expected to be most poorly approximated by functions in  $R_S T^h$ .

With cubic Hermite interpolation, each  $V'$  for  $V \in S_0^h$  is piecewise quadratic with  $C^0$  continuity.  $V'$  may have discontinuities in derivatives at element boundaries. If evolution dominates ( $\gamma$  is large), each  $V'$  must be approximated by a  $W \in T^h$ . With Galerkin weights  $\psi_i^p$ , each  $W$  is piecewise cubic with  $C^1$  continuity and cannot approximate discontinuities in first derivatives. If elements are equally spaced, the function  $V \in S_0^h$  with the largest discontinuities in first derivatives of  $V'$  relative to  $\|V\|_{L_2}$  is

$$\hat{V} := \sum_{j=0}^N \psi_j^1. \quad (5.26)$$

$\hat{V}'$  is orthogonal to every  $\psi_i^p$  except  $\psi_0^1$  and  $\psi_N^1$  (in the elements at the boundaries). This explains the poor performance of the Galerkin method in evolution-dominated problems. Of course on the other hand, the space spanned by derivative weights  $\psi_i^{p'}$  allows any  $V'$  for  $V \in S_0^h$  to be represented exactly. If diffusion dominates ( $\gamma$  is small), each  $V'$  must be approximated by a  $W'$  such that  $W \in T^h$ . Galerkin weights achieve this exactly because  $T^h = S_0^h$ . With derivative weights, however, each  $W'$  is piecewise linear. These  $W'$  are therefore orthogonal to the highest frequency (piecewise-quadratic) function  $V'$  such that  $V \in S_0^h$ . The function that cannot be approximated is again  $\hat{V}'$ .

Here  $A_0$  and  $A_\infty$  are selected so that  $\hat{V}'$  is approximated as closely as possible by  $\gamma\hat{W} + \hat{W}'$ , where  $\hat{W}$  is a simple combination of the  $W$ s that provide an exact representation when  $P_e$  approaches 0 and  $\infty$ :

$$\hat{W} := A_0\hat{V} + A_\infty\gamma^{-1}\hat{V}'. \quad (5.27)$$

The smallest eigenvalue in eigenvalue problem (5.16) is estimated by considering only  $\hat{V}$  and  $\hat{W}$ . This leads to an estimate of the error factor in bound (5.11),

$$\frac{1}{\sqrt{1 - \Delta_S^2}} \approx \frac{\|\hat{V}\|_{B_S} \|R_S \hat{W}\|_{B_S}}{B(\hat{V}, \hat{W})} = \frac{\|\hat{V}'\|_{L_2} \|(R_S \hat{W})'\|_{L_2}}{\langle \hat{V}', (R_S \hat{W})' \rangle},$$

where, from (5.17) and (5.27),

$$(R_S \hat{W})' = \gamma A_0 \hat{V}' + (A_0 + A_\infty) \hat{V}' + \gamma^{-1} A_\infty \hat{V}''.$$

If elements are of equal length  $h$  and boundary effects are ignored, the integrals may be

evaluated to give

$$\begin{aligned}\|\hat{V}'\|_{L_2}^2 &= \frac{N}{5h}, \\ \|(R_S \hat{W})'\|_{L_2}^2 &= \frac{NP_e^2}{210h} A_0^2 + \frac{N}{5h} (A_0^2 + A_\infty^2) + \frac{12N}{hP_e^2} A_\infty^2, \\ \langle \hat{V}', (R_S \hat{W})' \rangle &= \frac{N}{5h} (A_0 + A_\infty),\end{aligned}$$

so

$$\frac{1}{\sqrt{1 - \Delta_S^2}} \approx \frac{\sqrt{(\frac{P_e^2}{42} + 1)A_0^2 + (1 + \frac{60}{P_e^2})A_\infty^2}}{A_0 + A_\infty}. \quad (5.28)$$

This estimate is minimized when

$$\frac{A_\infty}{A_0} = \frac{P_e^2 + 42}{42(P_e^2 + 60)} P_e^2. \quad (5.29)$$

With coefficients in this optimum ratio,

$$\frac{1}{\sqrt{1 - \Delta_S^2}} \approx \sqrt{\frac{P_e^4 + 102P_e^2 + 2520}{P_e^4 + 84P_e^2 + 2520}}. \quad (5.30)$$

As expected, the estimate of the error factor approaches 1 as  $P_e$  approaches  $\infty$  or 0. Its maximum value is  $\sqrt{\frac{2\sqrt{70}+17}{2\sqrt{70}+14}} \approx 1.05$  which is predicted at  $P_e = \sqrt{6\sqrt{70}} \approx 7.1$ .

### *Dirichlet Boundaries*

The undesirable feature of the set of weighting functions defined in (5.23) is that  $w_0^1$  is non-zero at  $x = 0$ , where the Dirichlet boundary condition is applied. This means that the weighted residual equations (5.1) are not satisfied if the exact solution  $u$  is substituted for  $U$ , and so the error orthogonality property (5.2) does not hold. This is corrected by changing the definition of the derivative term  $w_{0\infty}^1$  to include a multiplier  $\zeta \in H_{D_0}^1$  so that  $w_0^1 \in H_{D_0}^1$ :

$$w_{0\infty}^1 := \zeta \gamma^{-1} \psi_0^{1'}. \quad (5.31)$$

The multiplier is chosen to be an exponential ramp,

$$\zeta := \frac{1 - e^{-\gamma x}}{1 - e^{-\gamma h}}, \quad (5.32)$$

so that for large  $\gamma$  the behaviour of  $w_{0\infty}^1$  near  $x = 0$  is similar to that of the optimal weighting functions  $w_0^{1*}$  in (5.20) and  $w_0^{1*}$  in (5.22). The term still becomes an optimal weighting function when  $\gamma \rightarrow \infty$ .

### Verification of Error Estimates

The estimates of the optimal ratio of  $A_\infty$  to  $A_0$  (5.29) and of the error factor (5.30) rely on the assumption that  $\hat{V}$  is the function in  $S_0^h$  that is most poorly approximated by functions in  $R_S T^h$ . To investigate the validity of this assumption, error factors were calculated for various  $N$  and  $P_e$  from the smallest eigenvalues of problem (5.16) with the full trial and test spaces. The weighting functions  $w_i^p$  in (5.23) were defined using (5.31) for  $w_{0\infty}^1$  and (5.24) for the other  $w_{i\infty}^p$  and all  $w_{i0}^p$ .  $\frac{A_\infty}{A_0}$  was given by equation (5.29). The resulting error factors are compared with estimates from equation (5.30) in Table 5.1.

N	error factor $(1 - \Delta_S^2)^{-\frac{1}{2}}$		
	$P_e = 2$	$P_e = 7.1$	$P_e = 20$
1	1.010305	1.028631	1.009653
2	1.011456	1.039068	1.013869
5	1.012121	1.045161	1.016868
10	1.012322	1.046765	1.017733
20	1.012407	1.047366	1.018050
50	1.012445	1.047607	1.018165
100	1.012453	1.047653	1.018184
200	1.012456	1.047666	1.018189
$\infty$ (est.)	1.012457	1.047671	1.018191

**Table 5.1:** Comparison of calculated and estimated ( $N = \infty$ ) one-dimensional error factors.

In all cases investigated the calculated error factors approached the estimate (5.30) as  $N$  became large. The eigenvector of (5.16a) corresponding to the smallest eigenvalue was, in each case, dominated by components corresponding to  $w_j^1$  that were almost constant in the

middle of the domain but smaller nearer the boundaries. This affirms that without boundary effects  $\hat{V}$  is indeed the most poorly approximated function in  $S_0^h$ . Near boundaries  $\hat{V}$  can be approximated better, but the estimate (5.30) based on  $\hat{V}$  and ignoring boundary effects appears to provide a good upper bound on the error factor.

### *Variable Lengths and Coefficients*

The terms in the approximately optimal weighting function (5.23) are optimal weights when  $P_e$  approaches 0 and  $\infty$  even with unequally spaced elements and variable equation coefficients, but the ratio  $\frac{A_\infty}{A_0}$  given in (5.29) is based on constant element lengths and coefficients. With variable lengths or coefficients, the best choices of  $A_0$  and  $A_\infty$  are no longer constant. It is assumed that weighting functions (5.23) are still close to optimal if the ratio in (5.29) is used with a local mesh Péclet number defined by

$$P_e := \frac{c_0}{\sqrt{M}} \frac{dx}{d\xi}. \quad (5.33)$$

There seems little point in evaluating (5.29) exactly, however, if it is not even known to be the best choice. Instead the simplified expression,

$$\frac{A_\infty}{A_0} := \frac{P_e^2}{6\sqrt{70}} \quad (5.34)$$

is used. To investigate the expected effect this has on error bounds, estimates of the error factors from (5.28) based on constant element lengths and coefficients are compared in Figure 5.5 for ratios (5.29) and (5.34). The two expressions for  $\frac{A_\infty}{A_0}$  are equal at the point  $P_e = \sqrt{6\sqrt{70}}$  where the error factor is at its maximum. Elsewhere, the difference is small and is therefore expected to be unimportant for variable lengths and coefficients also.

Equation (5.34) specifies a ratio for  $A_0$  and  $A_\infty$ , but the variation in their total magnitude over  $x$  is yet to be determined. Note that with weighting functions (5.23) and propagation only in the direction of increasing  $x$ , if boundary effects are ignored, the error orthogonality

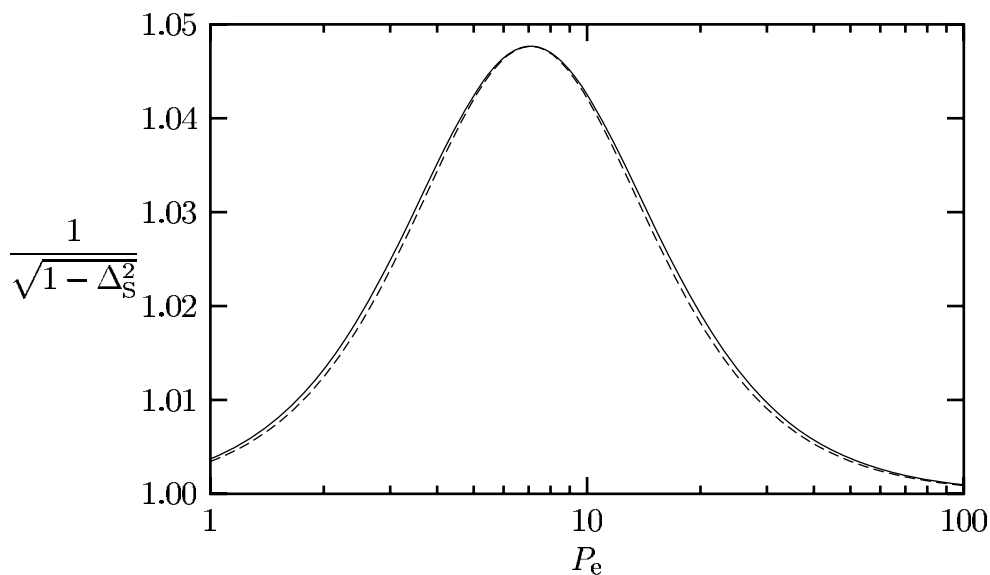


**Figure 5.5:** Comparison of estimated error factors from (5.28) with  $\frac{A_\infty}{A_0}$  given by the simplified expression (5.34) (solid line) and the optimal expression (5.29) (dashed line).

property (5.2) may be written as

$$\langle u' - U', A_0 \gamma M V \rangle + \langle u' - U', (A_0 + A_\infty) M V' \rangle + \langle u' - U', A_\infty \gamma^{-1} M V'' \rangle = 0 \quad \forall V \in S_0^h.$$

If we aim for a small error in the sense of the  $\|\cdot\|_{B_S}$  norm then the left hand side should resemble  $B_S(u - U, V)$ . The second term is therefore the desirable term and its dominance is achieved by appropriate selection of  $\frac{A_\infty}{A_0}$  in (5.34). The second term is equivalent to  $B_S(u - U, V)$  if

$$A_0 + A_\infty := 1. \quad (5.35)$$

Combining this with the ratio specified by (5.34) gives

$$A_0 = \frac{6\sqrt{70}}{6\sqrt{70} + P_e^2} \quad \text{and} \quad A_\infty = \frac{P_e^2}{6\sqrt{70} + P_e^2}. \quad (5.36)$$

### 5.1.4 Extension to Three Dimensions

For modelling the excitation of the heart, the definitions of the terms in the weighting functions need to be extended to the three-dimensional case with wavefronts travelling in any direction. Weighting functions are still based on the simple combination (5.23) of terms selected for their performance when  $P_e$  approaches 0 and  $\infty$ , but the Riesz representer theory of Section 5.1.1 can no longer be applied because the form  $B(\cdot, \cdot)$  defined in (3.25) is no longer bilinear.

#### *Selection of Weight Terms*

When  $P_e \rightarrow 0$ ,  $B(\cdot, \cdot)$  becomes bilinear so  $w_{i0}$  are defined as the optimal weights in the sense of  $\|\cdot\|_{B_S}$ , which are still  $\psi_i$ .

When the evolution term is present, its non-linearity means that the techniques used in Section 5.1.2 can no longer be used to find a weight that guarantees minimum error in the sense of the  $\|\cdot\|_{B_S}$  norm. However, when  $P_e \rightarrow \infty$ , the least squares weight,

$$\frac{\nabla U \cdot M \nabla \psi_i}{c_0 \sqrt{\nabla U \cdot M \nabla U}}$$

minimizes the integral of the square of the residual in the governing equation and therefore ensures that

$$\left\| \sqrt{\nabla u \cdot M \nabla u} - \sqrt{\nabla U \cdot M \nabla U} \right\|_{L_2}$$

is minimized.

The least squares term is discontinuous at wavefront collisions. If it were used in the weights, the test functions  $W$  in the discretized equations (5.1) would not be members of  $H^1(\Omega)$ . That would mean that, when the diffusion term is present, the equations may not be satisfied by the exact solution  $u$ . This, however, is not the concern, because, when  $u$  is substituted for  $U$  in the expressions for each  $W$ , the resulting discretized equations are satisfied by  $u$  (due to the discontinuities in  $W$  occurring at the points where the gradient of the solution is zero). In this sense, therefore, equations (5.1) are still weighted residual equations.

The main concern with such a discontinuous weight is, as discussed in Section 4.1, the difficulty in designing an integration scheme to ensure that the residuals in the resulting discrete system of non-linear equations are continuous with respect to the nodal parameters  $U_j$ . In order to keep the integration scheme simple, the smooth term,

$$w_{i\infty} := \frac{\nabla U \cdot M \nabla \psi_i}{\sqrt{(1 - \alpha_\infty) c_0^2 \nabla U \cdot M \nabla U + \alpha_\infty \tau_m^2}}, \quad (5.37)$$

is used instead with the constant  $\alpha_\infty \in (0, 1)$ . This term is close to the least squares term when evolution dominates and  $U$  is close to  $u$ . At a collision, however, the denominator remains greater than zero so the term vanishes. As well as ensuring a smooth weight, the reduction in the magnitude of the term near a collision also means that less emphasis is put on making the residual small in regions where the interpolation scheme cannot accurately approximate  $u$ . The best value for  $\alpha_\infty$  has not been thoroughly investigated but  $\alpha_\infty = \frac{1}{4}$  seems to work well.

The coefficients  $A_0$  and  $A_\infty$  in the simple combination (5.23) of  $w_{i0}$  and  $w_{i\infty}$  can be similar to the one-dimensional selections (5.36), but a more general expression needs to be found for  $P_e$ . The type of combination that performed well for just one dimension is expected to still perform well for more than one dimension because the evolution term in the eikonal equation (2.65) is effectively a derivative of the solution in the direction of propagation. As expression (5.37) for  $w_{i\infty}$  is based on a derivative of the interpolation function in the direction of propagation, the variation in the weight in this direction is of similar nature to that of the one dimensional weight. The weight does not include any derivatives in the other directions because changes in derivatives of the solution in these directions have only second order effects on the evolution term.

### *Mesh Péclet Number*

The one-dimensional expression for  $P_e$  (5.33) included the equation space constant  $\sqrt{M}$  and an element spatial scale  $\frac{dx}{d\xi}$ . In more than one dimension, these quantities are not scalar so the intention is to base  $P_e$  on suitable space constants in the direction of propagation.

It is convenient to define a dimensionless *natural coordinate system*  $\mathbf{v}$  at each point in space

so that the components of  $M$  may be written as

$$\mu_{ij} = \frac{\partial x_i}{\partial v_p} \frac{\partial x_j}{\partial v_p}. \quad (5.38)$$

Note that there does not necessarily exist a single function  $\mathbf{v}(\mathbf{x})$  that satisfies this for all  $\mathbf{x}$ . However, because  $M(\mathbf{x})$  is symmetric and positive definite, there exist real matrices  $X(\mathbf{x})$  such that  $M = XX^T$ . Here, it is not necessary to actually evaluate  $X$  but the obvious choice would be to use the material direction vectors ( $\mathbf{a}_1$ ,  $\mathbf{a}_t$ , and  $\mathbf{a}_n$  of Section 2.1.1) multiplied by the corresponding space constants ( $\lambda_1$ ,  $\lambda_t$ , and  $\lambda_n$ ) for the columns of  $X$ . For each point  $\mathbf{x}^*$  a natural coordinate system can be defined with constant base vectors  $\frac{\partial \mathbf{x}}{\partial v_p}$  equal to the columns of  $X(\mathbf{x}^*)$  so that (5.38) is satisfied at  $\mathbf{x}^*$ .

In this natural coordinate system, the coupling tensor  $M$  transforms to the identity matrix and the evolution term becomes isotropic:

$$c_0 \sqrt{\nabla U \cdot M \nabla U} \equiv c_0 |\nabla_{\mathbf{v}} U|,$$

where  $\nabla_{\mathbf{v}}$  denotes the gradient operator with respect to  $\mathbf{v}$  coordinates. It therefore seems appropriate to use this coordinate system in determining the direction of propagation,

$$\frac{\nabla_{\mathbf{v}} U}{|\nabla_{\mathbf{v}} U|}.$$

In this coordinate system, the least squares weights when  $P_e \rightarrow \infty$ ,

$$\frac{\nabla U \cdot M \nabla \psi_i}{c_0 \sqrt{\nabla U \cdot M \nabla U}} \equiv \frac{1}{c_0} \frac{\nabla_{\mathbf{v}} U}{|\nabla_{\mathbf{v}} U|} \cdot \nabla_{\mathbf{v}} \psi_i$$

are simply scaled derivatives of the interpolation functions in the direction of propagation.

The one-dimensional scalar ratio of  $\sqrt{M}$  to  $\frac{dx}{d\xi}$  corresponds to a multi-dimensional tensor having components  $\frac{\partial \xi_m}{\partial v_p}$ . To obtain a scalar quantity from this, the rate of change of  $\xi$  arc length with respect to  $\mathbf{v}$  arc length in the direction of propagation,

$$\left| \frac{\frac{\partial U}{\partial v_p} \frac{\partial \xi}{\partial v_p}}{\sqrt{\frac{\partial U}{\partial v_r} \frac{\partial U}{\partial v_r}}} \right| = \frac{\sqrt{\frac{\partial U}{\partial v_p} \frac{\partial \xi_m}{\partial v_p} \frac{\partial \xi_m}{\partial v_q} \frac{\partial U}{\partial v_q}}}{\sqrt{\frac{\partial U}{\partial v_r} \frac{\partial U}{\partial v_r}}} \quad (5.39)$$

is used. The natural coordinate system  $\boldsymbol{v}$  does not need to be determined if a local element coordinate based symmetric tensor  $M^\xi$  is defined with components,

$$\mu_{mn}^\xi := \frac{\partial \xi_m}{\partial x_i} \mu_{ij} \frac{\partial \xi_m}{\partial x_i} = \frac{\partial \xi_m}{\partial v_p} \frac{\partial \xi_m}{\partial v_p}, \quad (5.40)$$

so that expression (5.39) may be written as

$$\frac{\sqrt{\frac{\partial U}{\partial \xi_p} \mu_{pr}^\xi \mu_{rq}^\xi \frac{\partial U}{\partial \xi_q}}}{\sqrt{\frac{\partial U}{\partial \xi_m} \mu_{mn}^\xi \frac{\partial U}{\partial \xi_n}}} = \frac{\sqrt{\nabla_\xi U \cdot M^\xi M^\xi \nabla_\xi U}}{\sqrt{\nabla_\xi U \cdot M^\xi \nabla_\xi U}}.$$

$P_e$  could therefore be defined by

$$P_e := \frac{c_0 \sqrt{\nabla_\xi U \cdot M^\xi \nabla_\xi U}}{\sqrt{\nabla_\xi U \cdot M^\xi M^\xi \nabla_\xi U}},$$

but this expression may have discontinuities at wavefront collisions, so it is modified to give the smooth expression,

$$P_e := \frac{c_0 \sqrt{(1 - \alpha_\infty) c_0^2 \nabla_\xi U \cdot M^\xi \nabla_\xi U + \alpha_\infty \tau_m^2}}{\sqrt{(1 - \alpha_\infty) c_0^2 \nabla_\xi U \cdot M^\xi M^\xi \nabla_\xi U + \alpha_\infty \tau_m^2 \bar{\mu}^\xi}}, \quad (5.41)$$

where

$$\bar{\mu}^\xi := \frac{1}{3} \mu_{mm}^\xi \quad (5.42)$$

is an average of the diagonal elements of  $M^\xi$ .

### Dirichlet Boundaries

Some of the weighting functions are not zero on Dirichlet portions of the boundary due to the derivative term  $w_{i\infty}$  defined in (5.37). As in the one-dimensional case, this is corrected by multiplying the term by a function  $\zeta \in H_{D_0}^1$  giving

$$w_{i\infty} := \zeta \frac{\nabla_\xi U \cdot M^\xi \nabla_\xi \psi_i}{\sqrt{(1 - \alpha_\infty) c_0^2 \nabla_\xi U \cdot M^\xi \nabla_\xi U + \alpha_\infty \tau_m^2}}. \quad (5.43)$$

(The term is written using derivatives with respect to local element coordinates  $\xi$  as these are easiest to evaluate computationally.) Instead of determining which weights need to have the multiplier  $\zeta$  applied, the same expression is used for all weights.  $\zeta$  is based on the one-dimensional expression for the function (5.32), and is defined by

$$\zeta := \frac{1 - e^{-\frac{Pe p_\zeta}{k_\zeta}}}{1 - e^{-\frac{Pe}{k_\zeta}}}, \quad (5.44)$$

where  $k_\zeta$  is a constant and  $p_\zeta$  is a simple non-negative function in  $H_{D_0}^1$ . In elements adjacent to Dirichlet boundaries,  $p_\zeta$  is a polynomial function of  $\xi$ ; in other elements,  $p_\zeta = 1$ . Over most of the domain therefore,  $\zeta$  is equal to one, so most weights are unaffected by the multiplier.

Near Dirichlet boundaries, the weights have similar behaviour to one-dimensional optimal weighting functions for large  $Pe$  if  $p_\zeta$  increases from zero at the boundary with slope  $|\nabla_\xi p_\zeta| = k_\zeta$ . The most simple choice would be to set  $k_\zeta = 1$  and to make  $p_\zeta$  a linear interpolation of nodal values that are 0 on Dirichlet boundaries and 1 elsewhere. Such an interpolation, however, gives small values for  $p_\zeta$  over most or all of an element if more than one of its borders lies on a Dirichlet boundary. A cubic interpolation is therefore used for  $p_\zeta$  and  $k_\zeta$  is set to 3. Away from Dirichlet boundaries, nodal values of  $p_\zeta$  are set to 1 and derivatives to 0. On Dirichlet boundaries nodal values are 1 and derivatives are set so that the slope of  $p_\zeta$  at the boundary is as close to 3 as possible.

### *Discontinuous Derivatives of $U$*

Expressions (5.36) for the coefficients  $A_0$  and  $A_\infty$  are only useful if  $U$  is  $C^1$  continuous. As discussed in Section 6.3, however, there are places in the ventricular myocardium where  $u$  is not expected to be  $C^1$  continuous. The coefficients in (5.36) and  $w_{i\infty}$  in (5.43) depend on first derivatives of  $U$ , so, with only  $C^0$  continuity in  $U$ , the weighting functions (5.23) may be discontinuous. To retain continuity in the weights,  $A_0$  is made constant and  $p_\zeta$  is set to zero on inter-element boundaries where  $C^1$  continuity in  $U$  is not expected. The nodal values of  $p_\zeta$  on inter-element boundaries without  $C^1$  continuity are set in the same manner as if they were on Dirichlet boundaries. In this way,  $A_0 w_{i0}$  retains the  $C^0$  continuity of the interpolation functions and  $A_\infty w_{i\infty}$  approaches zero at inter-element boundaries where derivatives of  $U$  are not expected to be continuous.

With constant  $A_0$ , keeping the ratio of  $A_\infty$  to  $A_0$  similar to the one-dimensional optimal ratio (5.29) would mean that for large  $P_e$  the weights would resemble

$$\frac{1}{42} A_0 \zeta \frac{\sqrt{(1 - \alpha_\infty) c_0^2 \nabla_\xi U \cdot M^\xi \nabla_\xi U + \alpha_\infty \tau_m^2 \nabla_\xi U \cdot M^\xi \nabla_\xi \psi_i}}{(1 - \alpha_\infty) c_0^2 \nabla_\xi U \cdot M^\xi M^\xi \nabla_\xi U + \alpha_\infty \tau_m^2 \bar{\mu}^\xi}.$$

The magnitude of this weight is heavily dependent on the direction of propagation, which makes the weighted residual equations very non-linear. In trying to solve the resulting system of equations, the solver attempts to improve the quality of the solution by reducing the magnitude of the weight instead of reducing the residual in the governing equation.

A possible remedy might be to define  $P_e$  to be some function independent of  $U$ . It might approximate some average of expression (5.41) over all propagation directions. Expressions (5.36) could then be used for  $A_0$  and  $A_\infty$ . Alternatively,  $P_e$  could be defined so that it was only independent of  $U$  where  $C^1$  continuity in  $U$  is not expected but closely resembled (5.41) elsewhere. Neither of these approaches have been investigated.

The approach used here is to make the ratio of  $A_\infty$  to  $A_0$  similar to (5.29) for small  $P_e$  but to limit the magnitude of the derivative term in (5.43) for large  $P_e$ . Using expression (5.41) for  $P_e$ ,  $A_0$  and  $A_\infty$  are defined by

$$A_0 := 1 \quad \text{and} \quad A_\infty := \frac{P_e^2}{k_{\text{lim}} P_e + 50}, \quad (5.45)$$

where the constant  $k_{\text{lim}}$  determines the maximum magnitude of the derivative term. It is chosen to be 2 (discussed below). The weighting functions are therefore given by the sum of Galerkin and supplementary weighting functions,

$$w_i = \psi_i + \hat{w}_i, \quad (5.46)$$

where the supplementary weighting functions are defined by

$$\hat{w}_i := \zeta \frac{P_e}{2P_e + 50} \frac{c_0 \nabla_\xi U \cdot M^\xi \nabla_\xi \psi_i}{\sqrt{(1 - \alpha_\infty) c_0^2 \nabla_\xi U \cdot M^\xi M^\xi \nabla_\xi U + \alpha_\infty \tau_m^2 \bar{\mu}^\xi}}. \quad (5.47)$$

For large  $P_e$ , the magnitude of the supplementary weighting functions, which are dependent on  $U$ , is similar to that of the Galerkin weighting functions, which are independent of  $U$ . This reduces the effects of non-linearity in the weighted residual equations, facilitating their

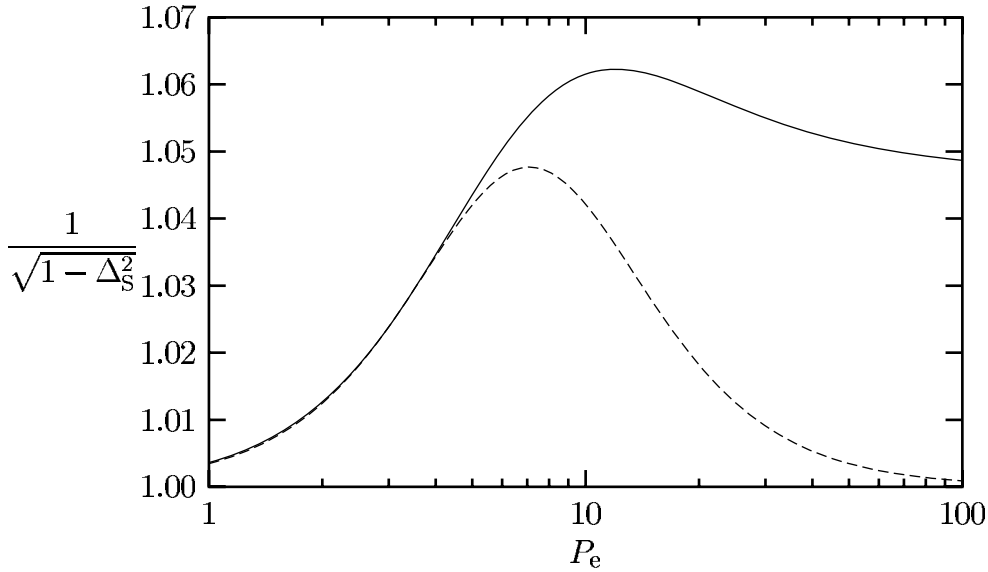


**Figure 5.6:** Comparison of one-dimensional error factor estimates from (5.28) with  $\frac{A_\infty}{A_0}$  determined by the derivative-limited expressions (5.45) (solid line) and the optimal expression (5.29) (dashed line).

solution.

To estimate the error introduced by not using the optimal ratio of  $A_\infty$  to  $A_0$  (5.29), one-dimensional error factor estimates for ratios from (5.45) and (5.29) are compared in Figure 5.6. These error factors are calculated from expression (5.28), which is based on constant equation coefficients and assumes a large number of equal length one-dimensional elements. The maximum predicted error factor with (5.45) is less than 2 per cent greater than the maximum with the optimal ratio (5.29). The constant  $k_{\text{lim}}$  in (5.45) was set to 2 so as to keep the non-linear term in the weight as small as possible while not significantly increasing the expected error factor.

When evaluating the weighted residual equations numerically, transferring the divergence in the diffusion term to a gradient of the weight, as in form (3.17) of the Galerkin equations, would have the advantage that there would be no boundary integrals to evaluate. The Petrov–Galerkin weights, however, are much more complicated than Galerkin weights, and the gradients of the supplementary terms  $\hat{w}_i$  would be expensive to calculate. The weighted

residual equations are therefore evaluated from the form,

$$\int_{\Omega} \left( (c_0 \sqrt{\nabla U \cdot M \nabla U} - \tau_m)(\psi_i + \hat{w}_i) + \nabla U \cdot M \nabla \psi_i - \nabla \cdot (M \nabla U) \hat{w}_i \right) d\Omega + \int_{\partial\Omega} \mathbf{n} \cdot M \nabla U \hat{w}_i d\Gamma = 0, \quad (5.48)$$

using Gaussian quadrature for each of the integrals. There are no integrals over inter-element boundaries, because  $\hat{w}_i$  is zero on any of these boundaries where continuity of  $M \nabla U$  is not assured. The divergence in the diffusion term is transferred to a gradient of the Galerkin weight  $\psi_i$  because the resulting expression retains its symmetric and positive definite properties even under the approximations introduced by Gaussian quadrature. It also avoids the evaluation of integrals over inter-element boundaries with discontinuous  $M \nabla U$  (which would be required as  $\psi_i$  is non-zero).

## 5.2 No-Inflow Boundary Condition

For large Péclet numbers, the no-flux boundary condition derived from the diffusion of charge is not necessarily enough to sufficiently constrain the solution.

### 5.2.1 Inflow Boundaries

The stability under large Péclet numbers of the Petrov–Galerkin method developed in the previous section is tested in the situation shown in Figure 5.7. The tissue is stimulated in such a way that the wavefront is initially concave (when viewed from inactive tissue). Note that for  $P_e = 10$  the curvature of the wavefront reduces as it propagates across the tissue, but for  $P_e = 100$  the curvature increases.

The nature of the solution for  $P_e = 100$  is in some ways quite reasonable. The residual in the eikonal equation (2.65) is very small. An inwardly propagating circular wavefront becomes

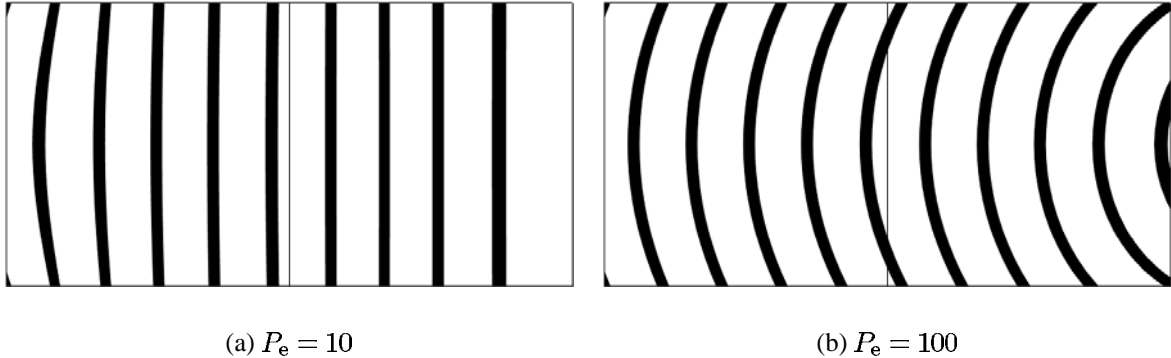


**Figure 5.7:** Excitation contours calculated by the Petrov–Galerkin method for a slice of tissue stimulated unevenly at the left hand edge. Stimulus times are specified by a quadratic function so that the corners are stimulated first and the centre of the edge last. The tissue is represented by two unit-square cubic Hermite elements. Equation parameters are selected for unit plane wave speed in any direction. Results are shown for Péclet numbers of 10 and 100. Contours are at intervals of 0.2.

a smaller circle, so an initially concave wavefront becomes more concave. The problem with the solution is that the no-flux boundary condition (2.66) is not satisfied.

The no-flux boundary condition is not very well satisfied on the boundary at the right hand end of the tissue in the solution for  $P_e = 10$  either. Such boundaries where the wavefront extinguishes shall be referred to as *outflow* boundaries. The boundary condition at these boundaries only affects a small *boundary layer* of tissue, so failure to satisfy the boundary condition does not introduce much error into the solution (see Section 2.4.2). The boundaries where the wavefronts enter the domain shall be called *inflow* boundaries. The boundary at the left hand end of the tissue is an inflow boundary because tissue is stimulated on this boundary. In the  $P_e = 10$  solution the no-flux boundary condition on the other boundaries is satisfied very well.

In the  $P_e = 100$  solution the no-flux boundary condition on the boundaries at the top and bottom of the domain is not satisfied. The boundary condition (2.66) is derived from the prevention of diffusion of charge across the boundary. For large Péclet numbers, diffusion effects are small and so the emphasis on satisfying the boundary condition is small. Because the coarse discretization does not allow  $U$  to exactly represent  $u$ , the numerical method selects a solution that closely satisfies the eikonal equation but almost ignores the boundary

condition.

As the effects of diffusion are small, the propagation speed should be almost unaffected by curvature and should be almost equal to the unit plane wave speed. This is reflected in the solution through the magnitude of the gradient of activation time which is close to one over the entire domain. Note, however, that the average propagation speed along the top and bottom edges of the domain is about 1.1. This is due to the fact the method does not recognize that tissue needs to be excited by other excited tissue. It is assumed that the propagation direction is normal to the wavefront, but, because the boundary condition is not strongly enforced, the wavefront normal is not parallel to the boundary. The wavefront is propagating from outside the boundary into the domain, and the boundary is an inflow boundary. Tissue is being excited by non-existent imaginary tissue outside the boundary.

Without a mechanism to prevent wavefronts entering the domain through unwanted inflow boundaries, excitation can initiate at arbitrary points on the boundary and totally corrupt the numerical solution. This problem occurs when the diffusion term becomes insignificant, so the nature of evolution without diffusion is now investigated to determine a prevention mechanism.

## 5.2.2 Evolution Without Diffusion

For large Péclet numbers the numerical scheme behaves as if it is solving the eikonal equation without a diffusion term and without the associated no-flux boundary condition. Without these the solution to the eikonal equation (2.65) is not unique. To reflect the fact that tissue must be excited by neighbouring tissue, the governing equation should instead be

$$\sup_{\mathbf{a} \in A(\mathbf{x})} \left\{ \lim_{\alpha \searrow 0} \frac{u(\mathbf{x}) - u(\mathbf{x} - \alpha \mathbf{a})}{\alpha} \right\} = \tau_m(\mathbf{x}) \quad \forall \mathbf{x} \in \Omega - \Gamma_D, \quad (5.49)$$

where, for  $m$  dimensions,

$$A(\mathbf{x}) := \{ \mathbf{a} \in \mathbb{R}^m : \mathbf{a} \cdot \mathbf{M}^{-1} \mathbf{a} = c_0^2; \exists \alpha \in \mathbb{R} \text{ s.t. } \alpha > 0, \mathbf{x} - \alpha \mathbf{a} \in \Omega \}. \quad (5.50)$$

Restricting the vectors  $\mathbf{a}$  to the set  $A(\mathbf{x})$  determines the directions in which propagation can occur at the point  $\mathbf{x}$  and the propagation speeds for these directions. Propagation is constrained to only spread from tissue that is already excited.

In regions where the solution is smooth enough this governing equation is equivalent to

$$\sup_{\mathbf{a} \in A} \{\mathbf{a} \cdot \nabla u\} = \tau_m. \quad (5.51)$$

(If  $A$  is replaced with  $A_{\Omega^0}$  defined in (5.52) below, this equation is a special case of that used by Falcone, Giorgi, and Loreti (1994) in their analysis of front propagation problems.) For a point not on the boundary, the definition of  $A$  simplifies to

$$A_{\Omega^0} := \{\mathbf{a} \in \mathbb{R}^m : \mathbf{a} \cdot M^{-1}\mathbf{a} = c_0^2\}. \quad (5.52)$$

and the supremum in (5.51) occurs when

$$\mathbf{a} = c_0 \frac{M\nabla u}{\sqrt{\nabla u \cdot M\nabla u}}.$$

Away from the boundaries, therefore, equation (5.51) is equivalent to the eikonal equation (2.65) without a diffusion term.

Without diffusion, there is no Neumann boundary condition but the notation  $\Gamma_N$  shall be used for  $\partial\Omega - \Gamma_D$ , the portion of the boundary where there is no Dirichlet boundary condition applied. For a point on this portion of the boundary, the definition of  $A$  may be changed to

$$A_{\partial\Omega} := \{\mathbf{a} \in \mathbb{R}^m : \mathbf{a} \cdot M^{-1}\mathbf{a} = c_0^2, \mathbf{n} \cdot \mathbf{a} \geq 0\}, \quad (5.53)$$

where  $\mathbf{n}$  is the unit outward-pointing normal to the boundary.

In order to investigate the nature of the solution to (5.51) near boundaries, consider two points,  $\mathbf{x}_{\partial\Omega} \in \Gamma_N$  and  $\mathbf{x}_{\Omega^0} \in \Omega - \partial\Omega$  such that  $\mathbf{x}_{\Omega^0}$  is an infinitesimal distance from  $\mathbf{x}_{\partial\Omega}$ . As discussed above, the solution at  $\mathbf{x}_{\Omega^0}$  satisfies

$$c_0 \frac{M\nabla u}{\sqrt{\nabla u \cdot M\nabla u}} \cdot \nabla u = \tau_m.$$

If the solution is smooth enough in the vicinity of the points one would expect that  $\nabla u(\mathbf{x}_{\partial\Omega})$

is equal to  $\nabla u(\mathbf{x}_{\Omega^0})$  and should satisfy the same equation. This is only consistent with (5.51) if

$$c_0 \frac{M\nabla u}{\sqrt{\nabla u \cdot M\nabla u}} \in A_{\partial\Omega},$$

so the direction of propagation on  $\Gamma_N$  is restricted by

$$\mathbf{n} \cdot M\nabla u \geq 0. \quad (5.54)$$

$\Gamma_D$  is therefore the only inflow boundary.

If some diffusion is included, it can be assumed that  $u$  is smooth enough so that the governing equation becomes

$$\sup_{\mathbf{a} \in A} \{\mathbf{a} \cdot \nabla u\} - \nabla \cdot (M\nabla u) = \tau_m. \quad (5.55)$$

The limit of the solution to this equation as the diffusion term vanishes is the solution to equation (5.49).

The no-flux boundary condition on  $\Gamma_N$  ensures that  $M\nabla u$  is either parallel to the boundary or zero. The supremum in (5.55) therefore occurs when  $\mathbf{a} = \frac{M\nabla u}{\sqrt{\nabla u \cdot M\nabla u}}$  and (5.55) is equivalent to the eikonal equation (2.65). The limit of the solution to the eikonal equation (2.65) and its no-flux boundary condition (2.66) as the diffusion term vanishes is the solution to the evolution governing equation (5.49).

### 5.2.3 A No-Inflow Boundary Term

Although the exact solution of the eikonal equation (2.65) approaches the solution of the evolution equation (5.49), the same is not necessarily true for the numerical solution. Unfortunately, with the Petrov–Galerkin method for numerical solution of the eikonal equation, when diffusion effects become small they are swamped by discretization errors. The method behaves as if it is solving an eikonal equation without a diffusion term and without the no-flux boundary condition. Without these the solution is not unique so the scheme becomes unstable. To prevent this, the numerical treatment of the evolution term needs to more closely represent its form in equation (5.49).

With a finite difference method this is easily done by using an upwind difference scheme (Osher and Sethian, 1988). Such schemes can select the grid points used in the difference expressions for the evolution term so that at each grid point the expression depends only on grid points with lower excitation times. In this way the excitation time of each grid point is calculated as the expected time for a wavefront to arrive from neighbouring grid points. As there are only grid points in the domain, the wavefront can only arrive from points in the domain, and there are no unwanted inflow boundaries.

None of the so-called ‘upwind’ finite element methods for steady-state problems provide the same restrictions on the solution. Finite element methods only evaluate the evolution term at Gauss points in the domain, so the boundaries have no influence on propagation.

The approach used here to stabilize the Petrov–Galerkin solution of the eikonal equation is to add to the weighted residual equations a boundary integral term that encourages the solution to satisfy the boundary inequality (5.54). If this is satisfied, the supremum in (5.51) occurs when  $\mathbf{a} = \frac{M\nabla u}{\sqrt{\nabla u \cdot M\nabla u}}$ , so the residual in the eikonal equation (2.65) is equivalent to the residual in (5.51).

The satisfaction of boundary inequality (5.54) is encouraged by including a penalty term when it is not satisfied. This penalty term is constructed from minimization of an integral over  $\Gamma_N$  of the square of a residual in (5.54),

$$\int_{\Gamma_N} A_b r_b^2 d\Gamma, \quad (5.56)$$

where  $r_b$  is a residual that is zero if and only if (5.54) is satisfied and  $A_b$  is a coefficient independent of  $U$ . The minimum occurs when the derivatives with respect to each parameter  $U_i$ ,

$$\int_{\Gamma_N} A_b r_b \frac{\partial r_b}{\partial U_i} d\Gamma \quad (5.57)$$

are zero. If these integrals are added to the left hand side the Petrov–Galerkin discrete equations (5.48), the numerical solution  $U$  is encouraged to satisfy the boundary inequality (5.54).

It is again convenient to work with the natural coordinate system  $\mathbf{v}$  introduced in Section

5.1.4. Under this coordinate system the inequality is simply

$$\mathbf{n}^v \cdot \nabla_v u \geq 0, \quad (5.58)$$

where  $\mathbf{n}^v$  is the unit outward-pointing normal to the boundary in the natural coordinate system. In three dimensions,  $\mathbf{n}^v$  may be calculated from

$$\mathbf{n}^v = \frac{\iota}{J_2^v} \frac{\partial \mathbf{v}}{\partial \xi_s} \times \frac{\partial \mathbf{v}}{\partial \xi_t}, \quad (5.59)$$

where

$$J_2^v := \left| \frac{\partial \mathbf{v}}{\partial \xi_s} \times \frac{\partial \mathbf{v}}{\partial \xi_t} \right|, \quad (5.60)$$

$\xi_s$  and  $\xi_t$  are the local element coordinates that vary over the boundary, and  $\iota$  is either 1 or  $-1$  so that  $\mathbf{n}^v$  is outward-pointing.

The residual in inequality (5.58) may be used in the boundary term (5.57):

$$r_b := \min(\mathbf{n}^v \cdot \nabla_v U, 0). \quad (5.61)$$

If  $r_b \neq 0$  its derivative is given by

$$\frac{\partial r_b}{\partial U_i} = \mathbf{n}^v \cdot \nabla_v \psi_i. \quad (5.62)$$

If  $r_b = 0$  its derivative does not need to be evaluated.

If the Petrov–Galerkin weights  $w_{i0} = \psi_i$  and  $w_{i\infty}$  given by (5.43) were used for the eikonal equation residual in combination (5.23) with coefficients  $A_0$  and  $A_\infty$  given by (5.36), then, for large Péclet numbers, the products of the evolution term and the weights,  $c_0 |\nabla_v U| w_i$  would be of similar magnitude to the boundary integrands,  $r_b \frac{\partial r_b}{\partial U_i}$ . With the coefficients given by (5.45), however, the boundary integrands need to be multiplied by the mesh Péclet number. For consistency of magnitudes over all Péclet numbers, they are multiplied by

$$P_e^b \left( 1 + \frac{P_e^b}{2P_e^b + 50} \right)$$

(cf. equations (5.46) and (5.47)). To retain the symmetric and positive semi-definite nature

of the boundary terms (5.57), an expression that is independent of  $U$  is used for the Péclet number:

$$P_e^b := c_0 \left| \mathbf{n}^v \cdot \frac{\partial \mathbf{v}}{\partial \xi_n} \right|, \quad (5.63)$$

where  $\xi_n$  is the local element coordinate that does not vary over the boundary. The expression is based on the spatial properties in the direction normal to the boundary instead of in the direction of propagation used in (5.41).

Although the integrands are dimensionally consistent, there is still a difference in the order of one spatial dimension between the dimensions of the boundary and domain integrals. An appropriate multiplier needs to be found for the boundary term so as to balance the emphasis on satisfaction of the eikonal equation and of the boundary inequality. This should reflect the depth of the region of influence that the boundary terms should have. The parameters  $U_j$  that are included in the boundary terms have a significant direct influence on the solution over about half an element. If the boundary terms are given a multiplier that resembles half the width of the element, then the equations involving these parameters should put even emphasis on satisfaction of domain equation and boundary inequality. The multiplier is chosen to be

$$\frac{1}{2} \left| \mathbf{n} \cdot \frac{\partial \mathbf{x}}{\partial \xi_n} \right|,$$

so that the width of the element is estimated from information at the boundary.

The coefficient  $A_b$  in the boundary terms (5.57) is therefore chosen to be

$$A_b := \frac{P_e^b}{2} \left( 1 + \frac{P_e^b}{2P_e^b + 50} \right) \left| \mathbf{n} \cdot \frac{\partial \mathbf{x}}{\partial \xi_n} \right|. \quad (5.64)$$

The numerical solutions obtained by this modified scheme in solving the test problem of Section 5.2.1 are shown in Figure 5.8. The solution shows no unwanted inflow boundaries, but the propagation speeds are inaccurate, particularly in the middle-left region of the tissue. The initially concave wavefront rapidly distorts and becomes convex. It seems that the eikonal equation is being ignored so as to ensure that the boundary inequality is accurately satisfied everywhere. Too much emphasis is put on the boundary inequality.

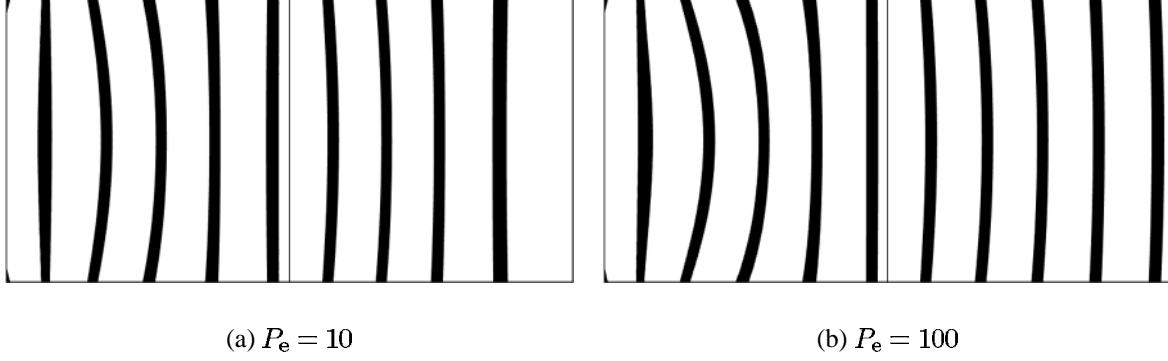


**Figure 5.8:** Excitation contours calculated by the Petrov–Galerkin method with  $r_b$  defined by (5.61) in the additional boundary term (5.57). The slice of tissue is described in Figure 5.7.

The emphasis on the boundary inequality (5.58) can be reduced by using a residual that is more closely associated with the evolution term. Instead of using the residual in (5.58), the following residual may be used:

$$r_b := |\nabla_{\mathbf{v}}U| - \sqrt{|\nabla_{\mathbf{v}}U|^2 - \min(\mathbf{n}^{\mathbf{v}} \cdot \nabla_{\mathbf{v}}U, 0)^2}. \quad (5.65)$$

If (5.58) is satisfied, this expression is zero. If (5.58) is not satisfied, the expression is essentially the difference between the evolution term and what it would be if it were calculated from only the components of  $\nabla_{\mathbf{v}}U$  in the surface of the boundary. The magnitude of this residual is similar to that of the residual in (5.61) when propagation is predominantly normal to the boundary but is much smaller when propagation is almost parallel to the boundary.

When this residual is non-zero its derivative is given by

$$\frac{\partial r_b}{\partial U_i} = \frac{\nabla_{\mathbf{v}}U \cdot \nabla_{\mathbf{v}}\psi_i}{|\nabla_{\mathbf{v}}U|} - \frac{\nabla_{\mathbf{v}}U \cdot \nabla_{\mathbf{v}}\psi_i - (\mathbf{n}^{\mathbf{v}} \cdot \nabla_{\mathbf{v}}U)(\mathbf{n}^{\mathbf{v}} \cdot \nabla_{\mathbf{v}}\psi_i)}{\sqrt{|\nabla_{\mathbf{v}}U|^2 - (\mathbf{n}^{\mathbf{v}} \cdot \nabla_{\mathbf{v}}U)^2}}. \quad (5.66)$$

The expression  $r_b \frac{\partial r_b}{\partial U_i}$  has a discontinuity when  $|\nabla_{\mathbf{v}}U| = \mathbf{n}^{\mathbf{v}} \cdot \nabla_{\mathbf{v}}U$ , which corresponds to propagation into the domain normal to the boundary. It is not likely that this will occur, but, to ensure that the discrete equations are smooth enough for solution by Newton’s method,

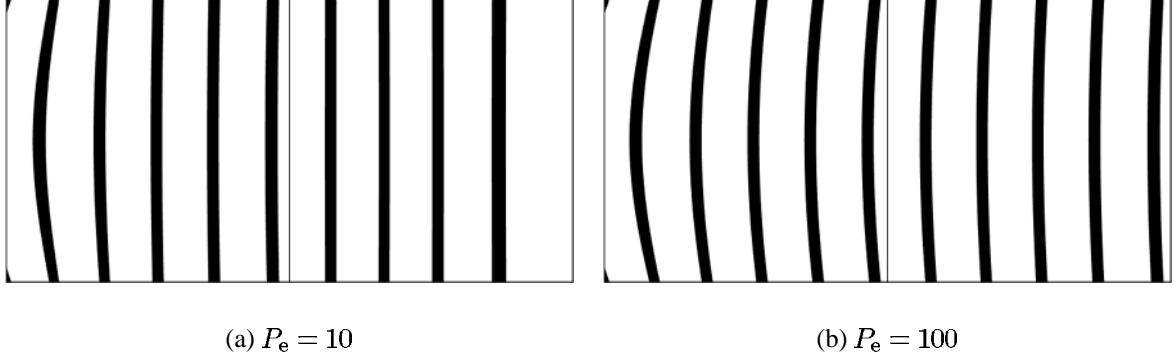


**Figure 5.9:** Excitation contours calculated by the Petrov–Galerkin method with  $r_b$  defined by (5.67) in the additional boundary term (5.57). The slice of tissue is described in Figure 5.7.

the modified residual,

$$r_b := \sqrt{|\nabla_{\mathbf{v}} U|^2 + \alpha_b \frac{\tau_m^2}{c_0^2}} - \sqrt{|\nabla_{\mathbf{v}} U|^2 - \min(\mathbf{n}^{\mathbf{v}} \cdot \nabla_{\mathbf{v}} U, 0)^2 + \alpha_b \frac{\tau_m^2}{c_0^2}} \quad (5.67)$$

is used. Its derivative is

$$\frac{\partial r_b}{\partial U_i} = \frac{\nabla_{\mathbf{v}} U \cdot \nabla_{\mathbf{v}} \psi_i}{\sqrt{|\nabla_{\mathbf{v}} U|^2 + \alpha_b \frac{\tau_m^2}{c_0^2}}} - \frac{\nabla_{\mathbf{v}} U \cdot \nabla_{\mathbf{v}} \psi_i - (\mathbf{n}^{\mathbf{v}} \cdot \nabla_{\mathbf{v}} U)(\mathbf{n}^{\mathbf{v}} \cdot \nabla_{\mathbf{v}} \psi_i)}{\sqrt{|\nabla_{\mathbf{v}} U|^2 - (\mathbf{n}^{\mathbf{v}} \cdot \nabla_{\mathbf{v}} U)^2 + \alpha_b \frac{\tau_m^2}{c_0^2}}}. \quad (5.68)$$

As with  $\alpha_{\infty}$  in Section 5.1.4, a value of  $\frac{1}{4}$  is used for  $\alpha_b$ .

This residual may be used in the boundary term (5.57) with the same expression for the coefficient  $A_b$  (5.64). Numerical solutions obtained with this scheme are shown in Figure 5.9. For  $P_e = 10$ , the solution is very similar to the solution in Figure 5.7(a) obtained without the additional boundary term. For  $P_e = 100$ , the solution adequately satisfies both the eikonal equation (2.65) and boundary condition (5.54), given the coarse discretization.

### 5.3 Summary of the Method

The numerical method developed for the simulations in Chapter 7 of excitation propagation in ventricular myocardium solves weighted residual equations that are the sum of the Petrov–Galerkin weighted residuals of Section 5.1.4 and the no-inflow weighted residual of Section 5.2.3. These are solved using the continuation method described in Section 3.5.

From Petrov–Galerkin weighted residual equations (5.48), no-inflow weighted residual equations (5.57), and governing equation continuum (3.22b), the weighted residual equations for a value of the continuation variable  $\alpha_c$  are

$$\int_{\Omega} \left( \alpha_c (c_0 \sqrt{\nabla U \cdot M \nabla U} - \tau_m) (\psi_i + \hat{w}_i) + \nabla U \cdot M \nabla \psi_i - \nabla \cdot (M \nabla U) \hat{w}_i \right) d\Omega + \int_{\Gamma_N} \left( \mathbf{n} \cdot M \nabla U \hat{w}_i + A_b r_b \frac{\partial r_b}{\partial U_i} \right) d\Gamma = 0. \quad (5.69)$$

The boundary inequality residual definition (5.67) is used for  $r_b$ .

When the value of the continuation variable is less than one, the influence of the evolution term is reduced, so the supplementary weights  $\hat{w}_i$  and the boundary integral coefficient  $A_b$  are calculated using the apparent Péclet number. The supplementary weighting functions  $\hat{w}_i$  are defined by equation (5.47) with the Péclet number defined by

$$P_e := \frac{\alpha_c c_0 \sqrt{(1 - \alpha_\infty) c_0^2 \nabla_\xi U \cdot M \xi \nabla_\xi U + \alpha_\infty \tau_m^2}}{\sqrt{(1 - \alpha_\infty) c_0^2 \nabla_\xi U \cdot M \xi M \xi \nabla_\xi U + \alpha_\infty \tau_m^2 \bar{\mu} \xi}} \quad (5.70)$$

(cf. equation (5.41)). The boundary integral coefficient  $A_b$  is defined by equation (5.64) with the Péclet number defined by

$$P_e^b := \alpha_c c_0 \left| \mathbf{n}^v \cdot \frac{\partial \mathbf{v}}{\partial \xi_n} \right| \quad (5.71)$$

(cf. equation (5.63)).

If excitation is initiated by a point stimulus, the diffusion term in the eikonal equation residual is modified as described in Section 3.3.2.

## *Chapter 6*

# **Myocardial Geometry, Structure, and Material Parameters**

The eikonal equation provides a model of the process of wavefront propagation but modelling excitation propagation in the complete ventricular myocardium still requires a description of the geometry and structure as well as material parameters for the governing equation.

## **6.1 A Model of Myocardial Geometry**

The model used here for the geometry of the ventricular myocardium is based on the work of Nielsen, Le Grice, Smaill, and Hunter (1991) and LeGrice, Hunter, and Smaill (1997), who made extensive morphological measurements in canine hearts. Nielsen *et al.* fitted to their data a 24-element mesh of the ventricular geometry, and, using similar techniques, LeGrice *et al.* fitted a 60-element mesh to similar data. In both models, the geometry was described in terms of a prolate spheroidal coordinate system. In directions tangential to the local endo- or epicardial surface, the interpolation was cubic Hermite for the radial coordinate and linear Lagrange for the angular coordinates. In the transmural direction, all coordinates were interpolated linearly.

The finite element method developed in Chapter 5 for modelling wavefront propagation

works best if the interpolation scheme for excitation time can assume  $C^1$  continuity between elements. As mentioned in Section 3.1.2, this means that  $C^1$  continuity is also required for the geometric variables. A tri-cubic Hermite interpolation is therefore used for the geometric variables.

With the flexibility of tri-cubic Hermite interpolation it is no longer necessary to describe the geometry in terms of a prolate spheroidal coordinate system. Instead, the standard rectangular Cartesian coordinate system is used so as to simplify future incorporation of the topologically more complex valves and atria.

The new tri-cubic Hermite rectangular Cartesian mesh is based on the 60-element mesh of LeGrice *et al.* (1997), which was based on a 60-element mesh that Nielsen *et al.* (1991) obtained by subdividing their 24-element mesh. The geometric parameters for the new tri-cubic mesh were fitted to the surface geometry data of LeGrice *et al.* using the positions of nodes in their mesh as initial values in the fitting process.

The method used to fit the geometric parameters was similar to that developed by Bradley, Pullan, and Hunter (1997). This method determines the location of a surface by minimizing an objective that is the sum of squares of data point projection magnitudes and smoothing terms based on  $\xi$ -space Sobolev norms of each geometric variable. The method also includes constraints on the first derivatives so that, at the nodes, the magnitude of the rate of the change in  $\boldsymbol{x}$  with respect to any  $\xi_i$  is an arithmetic mean of the lengths of adjacent element  $\xi_i$ -arcs. This keeps the magnitude of the rate of change in position with respect to each  $\xi_i$  reasonably consistent but, to improve the nature of the mesh in regions where small and large elements meet, the arithmetic mean in the method of Bradley *et al.* was changed to a harmonic mean.

In the process of fitting surfaces to data, minimizing the squares of projection magnitudes determines the movement of points in the initial surface normal to the surface, but points may drift within the surface. The Sobolev smoothing terms and the constraints on first derivatives help to control this, but sometimes it was necessary to adjust parameters manually in order to keep a reasonably regular mesh.

The fitted endo- and epicardial surfaces are shown in Figures 6.1, 6.2, and 6.3. The orientations of the diagrams presented in this thesis are described with respect to reference directions that are defined by features of the heart. A line from the apex through the middle of the base is

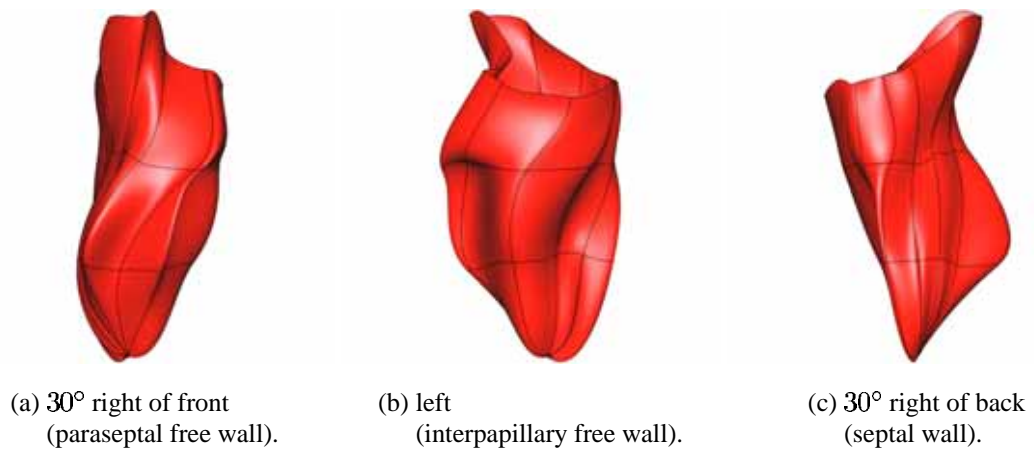


**Figure 6.1:** Fitted left ventricular endocardial surface.

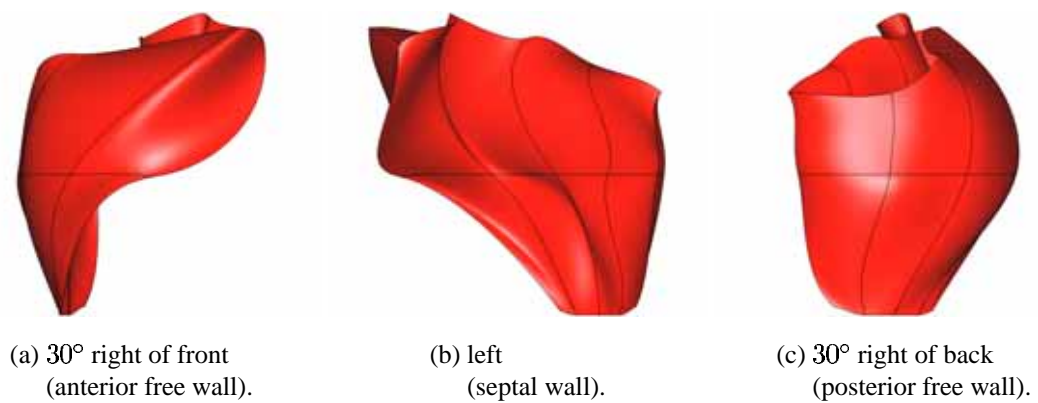


**Figure 6.2:** Fitted right ventricular endocardial surface.

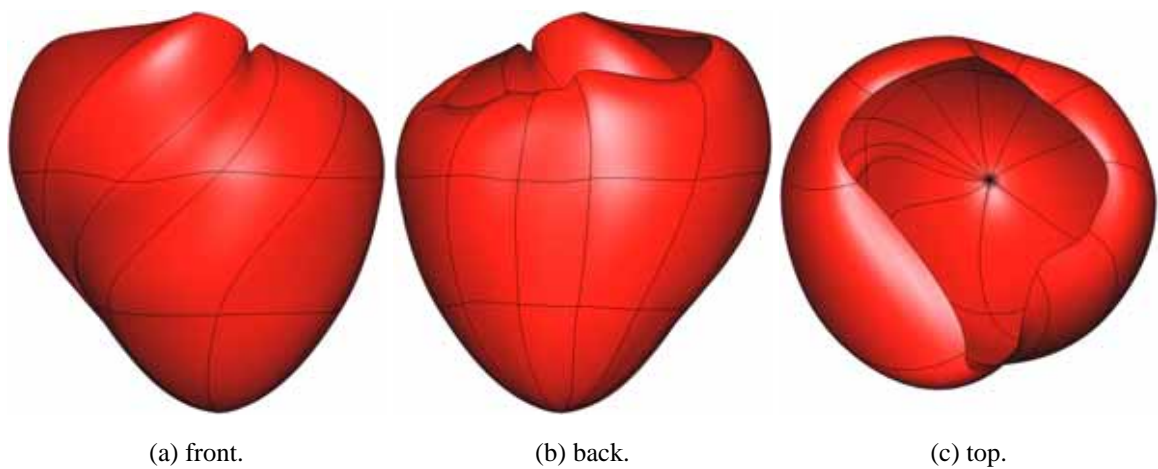


**Figure 6.3:** Fitted epicardial surface.

used for the vertical axis, and a vector from this axis through the middle of the right ventricle defines the right hand side.

Root mean square magnitudes of the data point projections are presented in Table 6.1 for the endo- and epicardial surfaces. Data for the exterior of the myocardium at the base is scarce so its location is uncertain.

Surface	Elements	Data points	RMS error
left ventricular endocardium	30	770	0.69 mm
right ventricular endocardium	16	846	0.85 mm
epicardium	30	784	0.42 mm
total	76	2400	0.68 mm

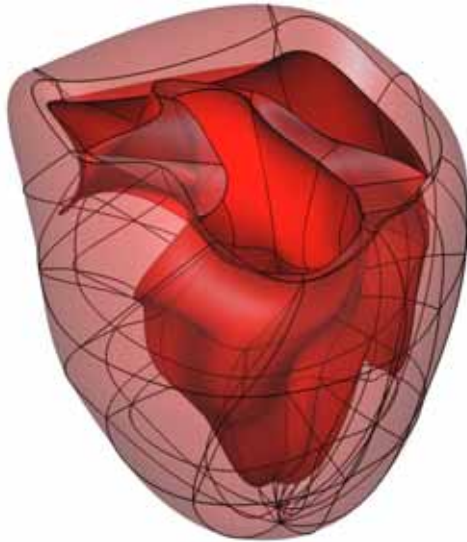
**Table 6.1:** Summary of ventricular surface fitting: number of surface elements, number of data points, and root mean square magnitudes of data point projections (RMS error).

The complete 60-element volume mesh is shown in Figure 6.4. The mesh consists of inner and outer 30-element layers, which are both centred around the left ventricular cavity. A separation in the layers forms the right ventricular cavity. Each layer is made up of 10 elements circumferentially by 3 elements from apex to base. The total volume of tissue is  $0.202 \times 10^6 \text{ mm}^3$ .

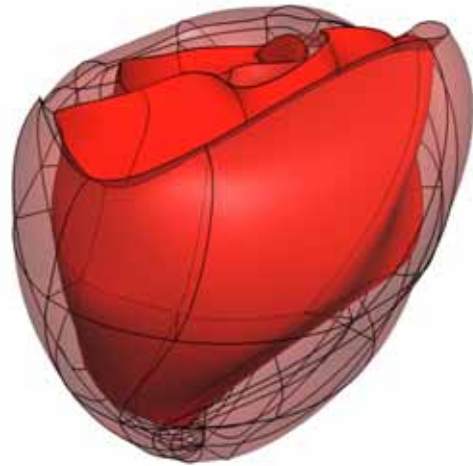
## 6.2 Myocardial Fibre and Sheet Structure

The microstructure of ventricular myocardium is both fibrous and laminar (LeGrice, Smaill, Chai, Edgar, Gavin, and Hunter, 1995). Myocytes are organised into branching and anastomosing layers, and within these layers there is a predominant orientation of the myocyte longitudinal axis. This structural anisotropy must influence the macroscopic electrical properties of the tissue.

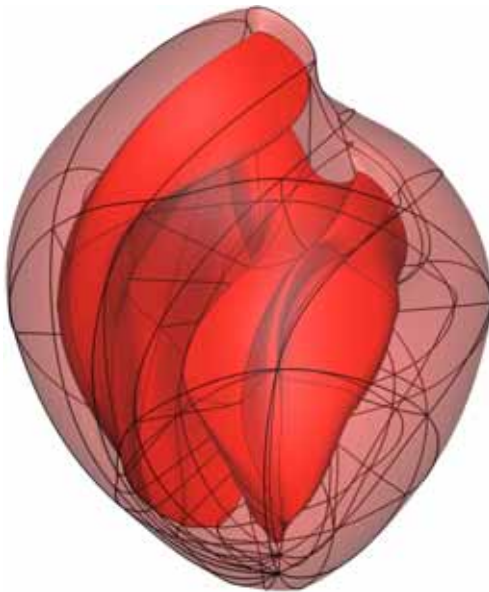
The anisotropic electrical properties are represented by the different principal effective conductivities for each principal axis  $\mathbf{a}_1$ ,  $\mathbf{a}_t$ , and  $\mathbf{a}_n$  of the effective conductivity tensors (cf. equations (2.3)). At every point in space the unit vector  $\mathbf{a}_1$  is defined to represent the predominant orientation of the longitudinal axis of the myocytes. This is called the *fibre di-*



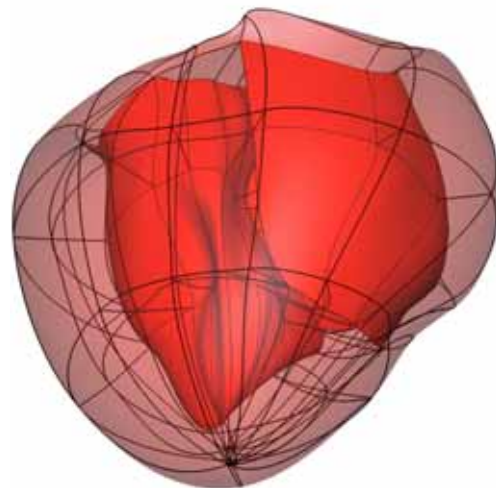
(a) left, 35° above horizontal.



(b) right, 35° above horizontal.



(c) front, 35° below horizontal.



(d) back, 35° below horizontal.

**Figure 6.4:** 60-element geometric model of the ventricular myocardium.

rection. The orthogonal unit vector  $\mathbf{a}_t$  is defined to represent the direction transverse to the fibres but still within the plane of the layers or *sheets*. The third unit vector  $\mathbf{a}_n$  is defined to represent the direction normal to these sheets, and is therefore orthogonal to  $\mathbf{a}_1$  and  $\mathbf{a}_t$ .

For a description of the principal directions at each point in the ventricular myocardial domain, the model of LeGrice *et al.* (1997) is used.

In this model, the vectors  $\mathbf{a}_1$ ,  $-\mathbf{a}_n$ , and  $\mathbf{a}_t$  are obtained from roll-pitch-yaw (or ‘*xyz*’) Euler angle rotations of orthonormal unit reference vectors  $\mathbf{h}'_1$ ,  $\mathbf{h}'_2$ , and  $\mathbf{h}_3$ , respectively. The reference vectors are defined by

$$\mathbf{h}_3 = \frac{\frac{\partial \mathbf{x}}{\partial \xi_1} \times \frac{\partial \mathbf{x}}{\partial \xi_2}}{\left| \frac{\partial \mathbf{x}}{\partial \xi_1} \times \frac{\partial \mathbf{x}}{\partial \xi_2} \right|}, \quad \mathbf{h}'_1 = \frac{\mathbf{h}_3 \times \begin{bmatrix} 1 \\ 0 \\ 0 \end{bmatrix}}{\left| \mathbf{h}_3 \times \begin{bmatrix} 1 \\ 0 \\ 0 \end{bmatrix} \right|}, \quad \text{and} \quad \mathbf{h}'_2 = \mathbf{h}_3 \times \mathbf{h}'_1, \quad (6.1)$$

so that  $\mathbf{h}'_1$  lies at the intersection of the  $\xi_1\xi_2$ -surface and the  $yz$ -plane,  $\mathbf{h}'_2$  lies in the  $\xi_1\xi_2$ -surface orthogonal to  $\mathbf{h}'_1$ , and  $\mathbf{h}_3$  is normal to the  $\xi_1\xi_2$ -surface.

The fibre and sheet orientations are therefore described by angles, and these are described by finite element interpolation schemes. The nodal positions and  $\xi_i$ -coordinate base vectors in the new tri-cubic Hermite mesh are similar to those in the mesh of LeGrice *et al.*, so the same nodal parameters were used for the Euler angles. Fibre and sheet orientations at sample points in the model are illustrated in Figure 6.5.

In the elements of both geometry meshes, the  $\xi_1$ -coordinate runs predominantly circumferentially around the heart, the  $\xi_2$ -coordinate runs from apex to base, and the  $\xi_3$ -coordinate runs transmurally from epicardium to endocardium. The plane described by  $\mathbf{h}'_1$  and  $\mathbf{h}'_2$  is therefore tangential to the local endo- or epicardial surface and the direction  $\mathbf{h}_3$  is normal to the surfaces. LeGrice *et al.* assumed that the fibre direction  $\mathbf{a}_1$  lies within this plane so the pitch or *imbrication angle* is zero. This assumption is accurate over most of the domain but inaccurate near the apex where the fibre direction has a significant transmural component.

With no pitch, the yaw is the angle from  $\mathbf{h}'_1$  to  $\mathbf{a}_1$ . The  $yz$ -plane is horizontal in the models of the geometry, so the yaw describes the angle between the fibre direction and the horizontal tangent to the local endo- or epicardial surface. The yaw is therefore called the *fibre angle*. Its interpolation is linear Lagrange in the  $\xi_1$ - and  $\xi_2$ -directions and cubic Hermite in the



(a) left, 35° above horizontal.



(b) right, 35° above horizontal.



(c) front, 35° below horizontal.



(d) back, 35° below horizontal.

**Figure 6.5:** Sample fibre and sheet orientations in the model of the ventricular myocardium showing its inhomogeneous structure. The gold ribbons in the diagrams are tangential to the sheets and run in the fibre direction.

$\xi_3$ -direction to represent the significant transmural variations. LeGrice *et al.* fitted nodal parameters for the fibre angle to 9746 measurements in a canine heart.

The roll or *sheet angle* describes the angle between the sheet normal  $\mathbf{a}_n$  and the local endo- or epicardial surface. Its interpolation is linear in the  $\xi_1$ -direction and cubic in the  $\xi_2$ - and  $\xi_3$ -directions. LeGrice *et al.* fitted nodal parameters to 16 630 measurements.

The vectors  $\mathbf{h}'_1$ ,  $\mathbf{h}'_2$ , and  $\mathbf{h}_3$  defined in (6.1) form a satisfactory set of reference vectors provided the angle between the  $\xi_1\xi_2$ -surface and the  $yz$ -plane is sufficiently large. This is the case everywhere in the model of the ventricular geometry except near the apex. If the same reference vectors are used in other geometries, however, there may be problems in regions where the  $\xi_1\xi_2$ -surface is parallel to the  $yz$ -plane. For this reason the computational implementation of the principal direction definitions uses a more general set of reference vectors defined only in terms of local element coordinate base vectors:

$$\mathbf{h}_3 = \frac{\frac{\partial \mathbf{x}}{\partial \xi_1} \times \frac{\partial \mathbf{x}}{\partial \xi_2}}{\left| \frac{\partial \mathbf{x}}{\partial \xi_1} \times \frac{\partial \mathbf{x}}{\partial \xi_2} \right|}, \quad \mathbf{h}_1 = \frac{\frac{\partial \mathbf{x}}{\partial \xi_1}}{\left| \frac{\partial \mathbf{x}}{\partial \xi_1} \right|}, \quad \text{and} \quad \mathbf{h}_2 = \mathbf{h}_3 \times \mathbf{h}_1, \quad (6.2)$$

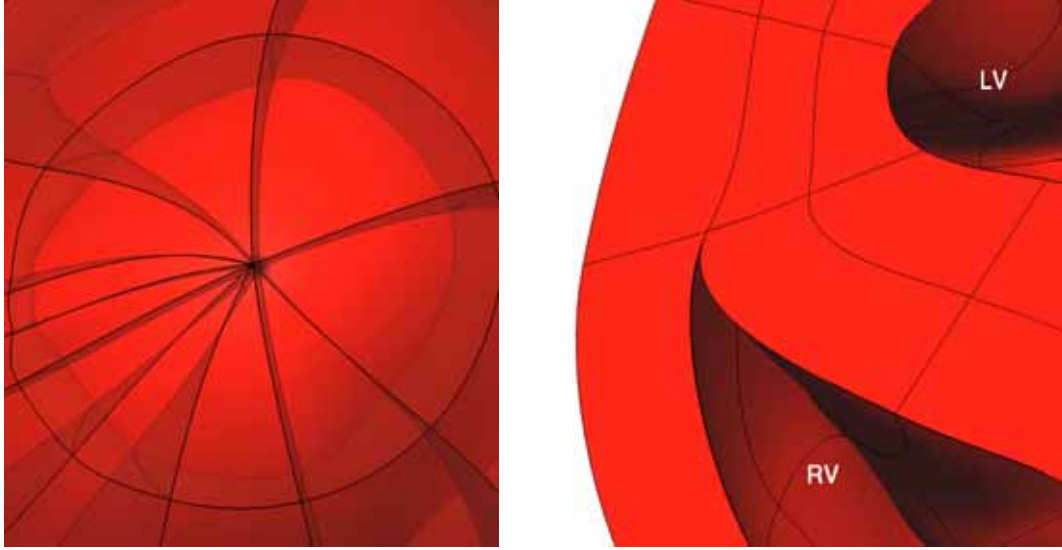
so that  $\mathbf{h}_1$  is in the direction of the  $\xi_1$ -coordinate base vector,  $\mathbf{h}_2$  is orthogonal to  $\mathbf{h}_1$  within the  $\xi_1\xi_2$ -surface, and  $\mathbf{h}_3$  is still the normal to the  $\xi_1\xi_2$ -surface.

Fibre and sheet angles have not been corrected for the change in implementation. As the  $\xi_1$ -coordinate runs predominantly circumferentially, its base vector essentially lies in the  $yz$ -plane, and so the two sets of reference vectors (6.1) and (6.2) are very similar. The discrepancy is probably small over most of the domain but may introduce more significant error near the base.

### 6.3 Dependent Variable Discretization

The dependent variable  $U$  is described by tri-cubic Hermite interpolation of nodal parameters to provide  $C^1$  continuity where possible.

In the 60-element mesh described in Section 6.1, there is only one layer of elements to



(a) Apex. The outermost layer of elements is shown with transparent faces. At the apex, the faces of the ten surrounding elements collapse into one arc. Only  $C^0$  continuity is enforced at this arc.

(b) Edge of the right ventricle. The top third of the heart is removed to show the surface of the right ventricular cavity (RV) forming a cusp where the septum joins the right free wall. Only  $C^0$  continuity is enforced at the cusp.

**Figure 6.6:** Regions of the mesh where  $C^1$  continuity in  $U$  is not enforced.

describe variations through the septal wall. The mesh is therefore refined in the  $\xi_3$ -direction (transmural) by dividing all the inner 30 elements in two. This means that the left ventricular free wall is three elements thick, the septum is two elements thick, and the right ventricular free wall is one element thick. The mesh is also refined in the  $\xi_2$ -direction by dividing all elements in two so that there are six layers of elements from apex to base. The resulting mesh has 180 elements.

At the apex of the heart, the  $\xi_2 = 0$  (apical) faces of the elements are collapsed in the  $\xi_1$ -direction (circumferential). In each layer through the wall, these faces of the ten elements nearest the apex collapse into one arc (Figure 6.6(a)).  $C^1$  continuity is not enforced at these arcs, but the necessary  $C^0$  continuity is achieved by sharing appropriate nodal parameters in surrounding elements. At each node  $j$  on these arcs, the parameters  $U_j^{000}$  and  $U_j^{001}$  are shared and  $U_j^{100}$  and  $U_j^{101}$  are zero in all elements surrounding the node. ( $U_j^{pqr}$  denotes the parameter at node  $j$  corresponding to the dependent variable differentiated  $p$ ,  $q$ , and  $r$  times

with respect to  $\xi_1$ ,  $\xi_2$ , and  $\xi_3$ , respectively. The  $\xi_3$ -coordinate runs transmurally.) For each of the remaining parameters at the node, there are 10 different *versions* each of which is shared only by adjacent elements (as if the elements were not collapsed). A similar sharing of parameters was used for the geometric variables.

At the edges of the right ventricular cavity, the left ventricular free wall splits into the septum and right ventricular free wall (Figure 6.6(b)). Enforcing  $C^1$  continuity in  $U$  would force the direction of wavefront propagation to be the same on either side of the cavity. This continuity may be reasonable if the wavefront originates in the left ventricular free wall, but, if it originates in the septum, for example, it might travel along the right ventricular septal wall around the edge of the cavity and reverse direction to travel through the free wall. For this reason, at a node  $j$  on the edge of the right ventricular cavity, the only parameters that are shared by all surrounding elements are  $U_j^{000}$  and maybe the parameter representing the first derivative with respect to the  $\xi_m$ -coordinate in the cavity edge. To ensure  $C^0$  continuity, some nodal parameters still need to be shared by some elements. The parameters that affect the value of  $U$  on a face must be shared by the elements adjacent to that face. This means that each parameter representing a derivative with respect to two variables  $\xi_m$  and  $\xi_n$  must be shared by (up to two) elements adjacent to the corresponding  $\xi_m\xi_n$ -face, each parameter representing a derivative with respect to one variable  $\xi_m$  must be shared by (up to four) elements adjacent to the corresponding  $\xi_m$ -arc, and each parameter that does not represent a derivative must be shared by (up to eight) elements surrounding the corresponding node. Parameters representing derivatives with respect to all three variables do not need to be shared at all.

In total there are 2355 nodal parameters (or degrees of freedom) in the description of the dependent variable  $U$ . If weighted residual equations are generated for all corresponding weighting functions, the Jacobian matrix for Newton's method has 358421 non-zero entries. As discussed in Section 3.3, some parameters are fixed for boundary conditions and the corresponding weighting functions are not used so the final numbers of degrees of freedom and non-zero entries may be lower than these values. Also, if excitation is initiated by a point stimulus at a node, the first derivatives are not forced to be continuous and each surrounding element has different derivative parameters, so there is a small increase the numbers of degrees of freedom and non-zero entries.

## 6.4 Material Parameters

In order to use the eikonal equation (2.65) values for the parameters,  $\mu_{ij}$ ,  $\tau_m$ , and  $c_0$  need to be specified. Each of these may be obtained from physical properties. The properties may well vary throughout the myocardium but, as there is not enough experimental data to estimate the distribution, the parameters are assumed constant here.

When rotated into fibre coordinates the coupling tensor  $M$  is diagonal with components equal to the squares of the space constants for each direction. The space constants are each related to the effective tissue resistivities in the corresponding direction and the membrane conductance per unit volume. From the definition of the space constant  $\lambda_l$  for the fibre or longitudinal direction (2.26) and (2.23), it may be expressed as

$$\lambda_l^2 = r_m \frac{g_{il}g_{el}}{g_{il} + g_{el}} = \frac{r_m}{r_{il} + r_{el}}, \quad (6.3)$$

where  $r_{il} = \frac{1}{g_{il}}$  and  $r_{el} = \frac{1}{g_{el}}$  are the effective resistivities of the intra- and extracellular spaces, and  $r_m$  is the reciprocal of the membrane conductance per unit volume. Space constants and resistivities for the direction transverse to fibres within sheets and for the direction normal to sheets may be expressed similarly.

The membrane time constant  $\tau_m$  can be related either to the membrane conductance and capacitance per unit volume or to the membrane conductance and capacitance per unit cell surface area:

$$\tau_m := r_m c_m = R_m C_m. \quad (6.4)$$

These parameters can be obtained from the passive behaviour of myocardial tissue as modelled by the passive bidomain system (2.24).

Once the time and space constants are known, the dimensionless constant  $c_0$  can be obtained from the propagation speed of a plane wave. It can be obtained from the propagation speed  $\theta_l$  for a plane wave travelling in the fibre direction using

$$c_0 = \frac{\tau_m \theta_l}{\lambda_l}. \quad (6.5)$$

This should be consistent with

$$c_0 = \frac{\tau_m \theta_t}{\lambda_t} = \frac{\tau_m \theta_n}{\lambda_n}, \quad (6.6)$$

where  $\theta_t$  is the propagation speed of plane waves travelling in the direction transverse to fibres within sheets, and  $\theta_n$  is the speed normal to sheets. The equations can only be consistent if

$$\frac{\theta_t}{\lambda_t} = \frac{\theta_n}{\lambda_n}. \quad (6.7)$$

That is

$$\theta_t \sqrt{r_{il} + r_{el}} = \theta_n \sqrt{r_{it} + r_{et}} = \theta_n \sqrt{r_{in} + r_{en}}. \quad (6.8)$$

Unfortunately, there is considerable variation in the reported values from experimental measurements of many of these material properties so selection of the appropriate parameters is somewhat uncertain. Although several investigations have been made into ventricular tissue properties in the fibre direction, reported values of tissue properties in other directions are rather scarce. Most researchers have assumed an axial symmetry in tissue properties about the fibre direction, so for now it is assumed that

$$r_{it} = r_{in}, \quad r_{et} = r_{en}, \quad \text{and} \quad \theta_t = \theta_n. \quad (6.9)$$

Before the parameters for numerical simulations are selected, the reported experimental measurements of the relevant tissue properties are first reviewed.

### 6.4.1 Resistivities

Experiments to determine the electrical resistivities have been performed both *in vitro* and *in vivo*.

*In Vitro Experiments*

Clerc (1976) investigated the longitudinal and transverse electrical properties of calf trabecular muscle using *in vitro* experiments carefully designed to confine all variations in electrical activity to just one spatial direction at a time. From microelectrode measurements of intra- and extracellular potentials due to excitation wavefronts propagating in each direction, the ratios of intra- and extracellular resistivities were found. Average values were

$$\frac{r_{il}}{r_{el}} = 3.64 \quad \text{and} \quad \frac{r_{it}}{r_{et}} = 12.7. \quad (6.10)$$

Measuring the voltage gradient due to a known current in a region where the transmembrane potential was almost constant gave bulk resistivities. (The resistivities presented here have been reverse-calculated from the specific resistivities presented by Clerc (1976).)

$$r_l = \frac{r_{il}r_{el}}{r_{il} + r_{el}} = 1.25 \Omega \text{ m} \quad \text{and} \quad r_t = \frac{r_{it}r_{et}}{r_{it} + r_{et}} = 3.91 \Omega \text{ m}. \quad (6.11)$$

Combining the two sets of measurements gave the effective resistivities. Average values were:

$$\begin{aligned} r_{il} &= 5.74 \Omega \text{ m}, & r_{it} &= 51.71 \Omega \text{ m}, \\ r_{el} &= 1.60 \Omega \text{ m}, & r_{et} &= 4.23 \Omega \text{ m}. \end{aligned} \quad (6.12)$$

These experiments were carried out at 25° C. Similar experiments were carried out by Weidmann (1970) at 37° C on trabecular muscle from sheep and calf hearts to determine the longitudinal properties,  $r_{il} = 6.27 \Omega \text{ m}$  and  $r_{el} = 1.88 \Omega \text{ m}$ . (These effective resistivities are reverse-calculated from presented results.) The consistency of the results suggests that resistivities were largely unaffected by this temperature change.

Kléber and Riegger (1987) conducted the same longitudinal measurements on arterially perfused rabbit papillary muscle surrounded by air. Microelectrode potential recordings indicated  $\frac{r_{il}}{r_{el}} = 0.83$  and  $r_l = 1.16 \Omega \text{ m}$ , which imply  $r_{il} = 2.13 \Omega \text{ m}$  and  $r_{el} = 2.55 \Omega \text{ m}$ . These values are clearly different from those obtained from Clerc and Weidmann's experiments, most notably in that the extracellular resistance is larger than the intracellular resistance. This variation seems greater than might be expected between the different species or between papillary and trabecular muscle.

When Kléber and Riegger dropped the perfusion pressure, they observed a significant immediate increase in the extracellular resistance and to a lesser extent the intracellular resistance. Buchanan, Oshita, Fujino, and Gettes (1986) observed that extracellular resistance was sensitive to changes in flow rates and total ionic content of superfusate in experiments on guinea pig papillary muscle conducted in a similar manner to those of Weidmann. These observations may explain the differences in reported values. They also suggest that values measured *in vitro* may be significantly different from *in vivo* values. The longitudinal extracellular specific resistivity calculated *in vitro* by Clerc was very close to that of the Tyrode solution which had been flowing through the preparation. Perhaps the extracellular resistivity was reduced by the Tyrode solution.

### *In Vivo Experiments*

Roberts and Scher (1982) made estimates of canine ventricular tissue resistivities *in vivo* by measuring epicardial extracellular potentials following stimulation at a point on the epicardium. They used a bidomain model for predicting tissue behaviour that assumed a semi-infinite domain and a step-function transmembrane potential generated by a prolate spheroidal wavefront. By fitting predicted potentials to measured potentials at several recording points they obtained estimates for the model parameters  $V_{el}$  and  $V_{et}$ , which correspond to the jumps in extracellular potential expected across wavefronts propagating in the fibre and transverse directions. Recording points within 1 mm of the wavefront were not included in the fit as the step-function transmembrane potential assumption is most inaccurate near the wavefront. Average values obtained were

$$V_{el} = 74 \text{ mV} \quad \text{and} \quad V_{et} = 43 \text{ mV}. \quad (6.13)$$

The same model with these parameters but assuming elliptical cylinder wavefronts gave predictions of potentials that closely matched measured potentials following line stimulations in both fibre and transverse directions.

Effective resistivity ratios were estimated from the fitted values (6.13) and an assumed transmembrane potential jump of 100 mV:

$$\frac{r_{il}}{r_{el}} = 0.35 \quad \text{and} \quad \frac{r_{it}}{r_{et}} = 1.32. \quad (6.14)$$

These ratios are clearly very different to those in equation (6.10) from the *in vitro* experiments of Clerc (1976). The extracellular potentials measured *in vivo* cannot be explained using the *in vitro* resistivity ratios.

Roberts and Scher (1982) estimated bulk resistivities using the method of Roberts, Hersh, and Scher (1979). Potentials measured during a constant current pulse at a central electrode were compared with predicted potentials from a semi-infinite monodomain model to fit the parameters,

$$r_l = 2.13 \Omega \text{ m} \quad \text{and} \quad r_t = 7.05 \Omega \text{ m}. \quad (6.15)$$

These are in a similar ratio to Clerc's *in vitro* measurements (6.11) but are larger by a factor greater than 1.7. The smaller *in vitro* values may further indicate that extracellular resistance was reduced by the Tyrode solution, but the *in vivo* estimates may not be accurate due to approximations of the monodomain model.

The model used by Roberts and Scher did not take into account fibre rotation, but the effect of this would merely be to reduce the apparent difference between  $r_l$  and  $r_t$ . The semi-infinite nature of the model meant that the effect of conductive blood beneath the myocardium was not taken into account, but, as all recording electrodes were less than 10 mm from the current injecting electrode, the effect on recorded potentials would be small.

Average effective resistivities obtained from the experiments of Roberts and Scher (1982) were:

$$\begin{aligned} r_{il} &= 2.91 \Omega \text{ m}, & r_{it} &= 16.77 \Omega \text{ m}, \\ r_{el} &= 8.52 \Omega \text{ m}, & r_{et} &= 12.47 \Omega \text{ m}. \end{aligned} \quad (6.16)$$

#### *Monodomain versus Bidomain*

When reviewing some of the reported values for resistivities Henriquez (1993) suggested that the assumption made by Roberts and Scher (1982) that myocardium behaves under current injection like a monodomain may not be appropriate. To investigate the significance of the error in this assumption consider the behaviour of the bidomain model (2.24).

For spatial scales much greater than the space constant, the membrane resistance is small so the two domains are tightly coupled together. At distances far from the current source therefore the bidomain behaves like a monodomain with resistivities equivalent to the parallel combination of intra- and extracellular resistivities. The transmembrane potential is close to its resting potential and, for a current  $I$  applied at a point on the planar boundary of a semi-infinite domain, the extracellular potential is given by

$$\phi_e = \frac{I}{2\pi} \sqrt{\frac{r_1 r_t^2}{r_1 x_1^2 + r_t (x_2^2 + x_3^2)}}, \quad (6.17)$$

where the origin of the coordinate system  $\boldsymbol{x}$  is at the current source and the  $x_1$ -axis aligned with fibres. This is the potential assumed by Roberts and Scher. Close to the electrode, however, the behaviour is more complicated. At distances from the current source much less than the space constants, the membrane resistance is large and current flows mainly through extracellular tissue.

To estimate the region in which equation (6.17) is valid, consider a bidomain with equal anisotropy. That is

$$M^i = \frac{1}{\alpha_i} M \quad \text{and} \quad M^e = \frac{1}{\alpha_e} M, \quad (6.18)$$

where

$$\alpha_i := \frac{r_{il}}{r_{il} + r_{el}} \quad \text{and} \quad \alpha_e := \frac{r_{el}}{r_{il} + r_{el}}. \quad (6.19)$$

For a step-function point current source of magnitude  $I$  on the boundary of the same domain, the solution to the bidomain equations (2.24) is

$$V_m = V_r - \frac{\phi_{\text{mono}}}{2\alpha_i} \left[ e^{-r} \operatorname{erfc} \left( \frac{r}{2} \sqrt{\frac{\tau_m}{t}} - \sqrt{\frac{t}{\tau_m}} \right) + e^r \operatorname{erfc} \left( \frac{r}{2} \sqrt{\frac{\tau_m}{t}} + \sqrt{\frac{t}{\tau_m}} \right) \right], \quad (6.20a)$$

$$\phi_e = \phi_{\text{mono}} - \alpha_e (V_m - V_r), \quad (6.20b)$$

where

$$\phi_{\text{mono}} := \frac{\alpha_i \alpha_e r_m I}{2\pi \lambda_i \lambda_t \lambda_n r} \quad (6.21)$$

is the potential predicted by the monodomain model (equivalent to  $\phi_e$  in equation (6.17)),

and

$$r := \sqrt{\mathbf{x} \cdot \mathbf{M}^{-1} \mathbf{x}} \quad (6.22)$$

is a dimensionless distance from the source. (See Appendix A for a proof.)

The transmembrane potential  $V_m$  is significantly different from its resting value at distances of up to a few space constants from the source. Therefore, unless extracellular resistivity is much smaller than intracellular resistivity, the extracellular potential differs significantly from that predicted by the monodomain model in the same region. The deviation from the monodomain prediction, however, shows transient behaviour. It should be possible to determine whether or not the monodomain model is valid from the steady or transient behaviour of recorded potentials.

Numerical simulations of steady-state current injection into a two-dimensional bidomain with nominal unequally anisotropic resistivities conducted by Sepulveda, Roth, and Wikswo (1989) showed that potential distributions were not axially symmetric and transmembrane potentials were significantly different from resting values several space constants from the source. As the largest space constant is probably almost 1 mm (see Section 6.4.2), the monodomain model is probably only valid at distances greater than a few millimetres from the current electrode.

It is not clear which electrode recordings Roberts and Scher (1982) used for their estimates of bulk resistivities. Some of the recording electrodes were only 1.5 mm from the current electrode but these may not have been used in the calculations. It seems from the description of the procedure by Roberts *et al.* (1979) that the recordings used were probably about 8 mm in the fibre direction or 4 mm in the transverse direction from the current electrode. These distances are several times the space constant and are probably just large enough for the monodomain model (6.17) to be valid. This is affirmed by the absence of significant transient behaviour in the potential recordings presented by Roberts *et al.* (1979).

### 6.4.2 Space Constants

If current is applied to tissue so as to induce a steady-state subthreshold transmembrane potential, then, for one-dimensional current flows, the bidomain model (2.24) predicts an exponential solution for the transmembrane potential in the neighbouring tissue,

$$V_m = V_r + Ae^{\pm \frac{x}{\lambda}}, \quad (6.23)$$

where  $A$  is a constant and  $\lambda$  is the space constant in the direction of current flow. This enables the space constant to be estimated from measured transmembrane potentials.

Kamiyama and Matsuda (1966) conducted experiments on canine papillary muscle. The experiments were arranged so that most of the muscle lay in a chamber filled with Tyrode solution but the severed end of the muscle was clamped by a partition and exposed to a separate chamber filled with isotonic potassium chloride solution. Using an electrode in each chamber, a constant current was passed through the muscle connecting the chambers. An exponential was fitted to the transmembrane potential distribution recorded near the partition to obtain an average space constant of 1.35 mm. Similar experiments by Sakamoto (1969) showed a similar space constant of 1.23 mm. The surrounding Tyrode bath in both of these experiments, however, would have reduced the apparent extracellular resistance. As micro-electrode measurements were probably taken near the surface of the muscle, the extracellular resistance may have been effectively zero. Assuming the longitudinal tissue resistivity ratio in (6.14) reported by Roberts and Scher (1982), the Tyrode bath may have increased the space constant by a factor of almost 2. The multi-dimensional nature of the muscular current flow in these experiments may also mean that the results do not truly reflect the longitudinal space constant  $\lambda_1$ .

Weidmann (1970) avoided the complication of a surrounding fluid bath in his experiments on sheep and calf trabeculae by exposing just the severed ends of the trabeculae to a supply of Tyrode solution. Only a small layer of Tyrode solution due to surface tension surrounded the rest of the muscle. This would have made the distribution of current in the preparation much more one-dimensional. Fitting an exponential to the transmembrane potential indicated a space constant  $\lambda_1 = 0.88$  mm. This is consistent with what might be expected from the above results but may still be a little higher than *in vivo* values if the Tyrode solution reduced the extracellular resistivity.

From experiments on arterially perfused rabbit papillary muscle, Kléber and Riegger (1987) calculated a much smaller space constant  $\lambda_1 = 0.357$  mm. Extracellular current was injected at the apex of the papillary muscle and recordings were taken for the resulting extracellular potential. The space constant was calculated by fitting an exponential to the difference between measured extracellular potentials within 1 mm of the apex and a straight line extrapolation of potentials recorded between 1 and 2 mm from the apex. Such a procedure is sensitive to the position of the straight line extrapolation. If it was fitted to recordings taken too close to the point of current injection, then the space constant would be under-estimated. The result could also be affected by the apical shape of the muscle if recordings in the exponential fit were taken too close to the apex.

### 6.4.3 Time Constant

The transient passive transmembrane potential response predicted by the bidomain model (2.24) for one dimensional current applied at  $x = 0$ ,  $t = 0$  into infinite tissue initially at rest has the form

$$V_m = V_r + Ae^{-\frac{x}{\lambda}} \operatorname{erfc} \left( \frac{x}{2\lambda} \sqrt{\frac{\tau_m}{t}} - \sqrt{\frac{t}{\tau_m}} \right) + Be^{\frac{x}{\lambda}} \operatorname{erfc} \left( \frac{x}{2\lambda} \sqrt{\frac{\tau_m}{t}} + \sqrt{\frac{t}{\tau_m}} \right), \quad (6.24)$$

where the constants A and B are determined by the boundary conditions at  $x = 0$ . For a step-function transmembrane voltage at  $x = 0$ ,  $B = A$ , and for a step-function difference in intra- and extracellular currents,  $B = -A$ . For either boundary condition the propagation speed of the point at half its maximum potential approaches  $\frac{2\lambda}{\tau_m}$  as  $x$  increases (Jack, Noble, and Tsien, 1975). The approximation is accurate for  $x \gtrsim 2\lambda$  with the voltage boundary condition and for all  $x$  with the current boundary condition. This provides a simple method for estimating the time constant  $\tau_m$  from the half times of measured potentials.

The membrane time constant may also be estimated from the time constant  $\tau_f$  of the early exponential rise in the foot of an action potential. If the action potential is of constant shape and propagating at constant velocity  $\theta$  then the transmembrane potential may be written as a function of one variable,

$$V_m(x, t) = v_m(\tau), \quad \text{where} \quad \tau := t - \frac{x}{\theta}. \quad (6.25)$$

In the foot of the action potential, where the transmembrane potential is less than threshold, the passive bidomain equation (2.24) can be applied. This reduces to (cf. equation (2.29))

$$v_m - V_r + \tau_m \frac{dv_m}{d\tau} = \frac{\lambda^2}{\theta^2} \frac{d^2v_m}{d\tau^2}, \quad (6.26)$$

which, for rising transmembrane potential, has the solution,

$$v_m = V_r + Ae^{\frac{\tau}{\tau_f}}, \quad (6.27)$$

where  $\tau_f$  is the positive root of the characteristic equation,

$$1 + \frac{\tau_m}{\tau_f} = \frac{\lambda^2}{\theta^2 \tau_f^2}. \quad (6.28)$$

The early action potential time constant  $\tau_f$  can be estimated from experimental measurements and used to calculate the membrane time constant  $\tau_m$  from

$$\tau_m = \frac{\lambda^2}{\theta^2 \tau_f} - \tau_f. \quad (6.29)$$

Kamiyama and Matsuda (1966) used the propagation speed of the half-maximum point in passive tissue and its approximation  $\frac{2\lambda}{\tau_m}$  to calculate an average membrane time constant in canine papillary muscle of  $\tau_m = 2.0$  ms. From very similar experiments, however, Sakamoto (1969) calculated a much larger time constant  $\tau_m = 4.2$  ms. Such a large difference in calculated values is not expected because the calculated space constants and the graphically presented half-maximum times are very similar. The results of Kamiyama and Matsuda are consistent, but the average space constant and half-maximum times presented by Sakamoto suggest a time constant less than 2.0 ms. In these experiments potential recordings were made within one space constant of the boundary. If it can be assumed that current enters the muscle only through extracellular space, then the step-function current boundary condition is appropriate and the approximation  $\frac{2\lambda}{\tau_m}$  for the propagation speed is accurate for (6.24). (See Section 6.4.2 for a summary of the experimental procedure.)

Sakamoto obtained another estimate,  $\tau_m = 2.5$  ms by fitting a one dimensional model similar to equation (6.24). The equation presented in the paper appears to be in error so it is unclear what boundary conditions were assumed in the model. Sakamoto also recorded action potentials and calculated a foot time constant  $\tau_f = 1.13$  ms. Using this with other results of

Sakamoto in equation (6.29) suggests  $\tau_m = 1.8$  ms.

$\tau_m$  depends only on membrane properties so the value should not have been affected if the Tyrode bath reduced the effective extracellular resistance. The accuracy of the estimates may, however, have been compromised by the assumptions of one-dimensional current flow.  $\tau_f$  is certainly affected by the non-planar shape of the excitation wavefront (Suenson, 1985).

In sheep and calf trabeculae, Weidmann (1970) calculated  $\tau_m = 4.4$  ms by comparing voltage-time records of transmembrane potential to equation (6.24) with a step-function current boundary condition. The one-dimensional current flow assumption was probably valid in these experiments. The boundary condition was based on the assumption that the ends of the fibres were sealed so all the current that passed through the tissue entered and left via the extracellular space.

Using equation (6.29) another estimate,  $\tau_m = 3.2$  ms is obtained from Weidmann's calculation of  $\tau_f = 0.38$  ms and other results. This estimate may be more appropriate for use in an eikonal model. The bidomain equations (2.24) are very much an approximation of the complex activity that occurs in reality, so the best parameters to use in a model probably depend on the purpose for which the model is to be used. If the model is to be used for excitation propagation and not for passive current flow, then parameters are probably best selected from the behaviour of the action potential.

For rabbit papillary muscle, Kléber and Riegger (1987) estimated  $\tau_m = 2.57$  ms using an (accurate) approximation based on equation (6.24) for passive response with the step-function current boundary condition (Jack *et al.*, 1975):

$$\tau_m \approx \frac{t_{0.5}(x)}{\frac{x}{2\lambda} + \frac{1}{4}}, \quad (6.30)$$

where  $t_{0.5}(x)$  is the time for the extracellular potential at  $x$  to pass half way from its initial to its steady-state value. In the experiments current was injected through an extracellular electrode, so the current boundary condition seems appropriate. However, if  $\lambda$  was underestimated (see Section 6.4.2) then  $\tau_m$  would also have been underestimated.

### 6.4.4 Propagation Speeds

In experiments on calf trabeculae at 25° C, Clerc (1976) measured the action potential propagation speeds of plane excitation waves,

$$\theta_l = 0.48 \text{ m s}^{-1} \quad \text{and} \quad \theta_t = 0.16 \text{ m s}^{-1}. \quad (6.31)$$

These were consistent with estimated resistivities (6.12) and equation (6.8) as

$$\sqrt{\frac{r_{it} + r_{et}}{r_{il} + r_{el}}} = 2.8 \quad \approx \quad \frac{\theta_l}{\theta_t} = 3.0. \quad (6.32)$$

The propagation speed is probably greater at body temperature as Weidmann (1970) measured  $\theta_l = 0.75 \text{ m s}^{-1}$  in similar experiments at 37° C. These speeds may also be significantly different from *in vivo* values if the tissue resistivities were affected by the *in vitro* preparation.

Roberts and Scher (1982) investigated canine action potential propagation near a point epicardial stimulus using *in vivo* experiments. An electrode array extending 8.25 mm in the longitudinal direction and 4.5 mm in the transverse direction was used to estimate the speeds of propagation in each direction from the stimulus,

$$\theta_l = 0.57 \text{ m s}^{-1} \quad \text{and} \quad \theta_t = 0.24 \text{ m s}^{-1}. \quad (6.33)$$

These were not, however, in the ratio expected from their estimated resistivities (6.16) and equation (6.8) as

$$\sqrt{\frac{r_{it} + r_{et}}{r_{il} + r_{el}}} = 1.6 \quad \not\approx \quad \frac{\theta_l}{\theta_t} = 2.4. \quad (6.34)$$

Le Grice (1992) also estimated propagation speeds in canine myocardium *in vivo*. These were obtained from recordings on an epicardial sock following a point epicardial stimulus. Using recordings near the stimulus gave the estimates,  $\theta_l = 0.7 \text{ m s}^{-1}$  and  $\theta_t = 0.3 \text{ m s}^{-1}$ , which are in similar ratio to those of Roberts and Scher. Using the distance between the 20 and 45 ms isochrones, however, gave the estimates,  $\theta_l = 0.67 \text{ m s}^{-1}$  and  $\theta_t = 0.5 \text{ m s}^{-1}$ , having the ratio  $\frac{\theta_l}{\theta_t} = 1.34$ . Le Grice suggested the difference might be due to transient behaviour immediately after stimulation.

The spread of excitation near an electrode stimulus is certainly more complicated than a constant rate of propagation. The eikonal model predicts slower propagation near a stimulus, but, as this approximation does not take into account applied current or variation in action potential profiles, it predicts a constant ratio  $\frac{\theta_l}{\theta_t}$ . Wikswo, Wisialowski, Altemeier, Balsler, Kopelman, and Roden (1991) observed variations in propagation speed when the stimulus current was changed. With 1 mA stimulus current applied to canine epicardium, speeds measured within 6 mm of the stimulus electrode were  $\theta_l = 0.60 \text{ m s}^{-1}$  and  $\theta_t = 0.29 \text{ m s}^{-1}$ . With 7 mA stimulus current  $\theta_l$  increased to  $0.75 \text{ m s}^{-1}$  but  $\theta_t$  essentially remained the same. This indicates that measurements near a point stimulus may not reflect the propagation speeds of plane waves. Measurements further from the stimulus may provide a better estimate, but, if they are too far away,  $\theta_t$  may be over-estimated due to the effects of fibre rotation through the wall.

### 6.4.5 Selection of Parameters

Despite the variation in the experimental estimates of parameters discussed above, they provide an indication of the appropriate parameters to use in model simulations of canine myocardium.

Simulations will be most affected by the selection of wavefront propagation speeds. The reported longitudinal speeds observed *in vivo* are reasonably consistent so the value of  $\theta_l = 0.67 \text{ m s}^{-1}$  suggested by Le Grice (1992) is selected. The transverse speed is less certain so the ratio of speeds predicted in equation (6.34) from the resistivity estimates of Roberts and Scher (1982) is used. This gives a transverse speed  $\theta_t = 0.42 \text{ m s}^{-1}$ , which is within the range of reported estimates.

The time and space constants are not so consistent and all reported estimates are based on *in vitro* experiments. Although the bidomain continuum model predicts continuous potentials, the discontinuous nature of myocardium may well cause discontinuities at small spatial scales. As micro-electrodes are likely to detect these discontinuities, their recordings may not give a good indication of larger scale bidomain properties. The recordings reported in the literature, however, do appear continuous, justifying their use in predicting bidomain continuum model parameters.

Based on the discussion (Section 6.4.2) of longitudinal space constants estimated for larger mammals, a value of  $\lambda_l = 0.8$  mm is selected. Requiring consistency with the propagation speeds in equation (6.8) determines the value for the transverse direction,  $\lambda_t = 0.5$  mm. From consideration of the time constants reported (Section 6.4.3), a value of  $\tau_m = 3$  ms is selected.

Substituting these values into (6.5) gives a value for the dimensionless coefficient  $c_0 = 2.5$ .

## *Chapter 7*

# **Simulations**

Numerical simulations of excitation propagation through the full canine ventricular myocardium were performed using the method developed in Chapter 5 to solve eikonal equation (2.65) on the mesh described in Chapter 6 with the material parameters selected in Section 6.4.5.

The method was programmed primarily in extended FORTRAN 77 as part of the CMISS (an acronym for Continuum Mechanics, Image analysis, Signal processing and System identification) software package. It was executed on one 195 MHz MIPS R10000 processor of a Silicon Graphics Octane.

## **7.1 Epicardial Point Stimulation**

In order to test the performance of the numerical method in the irregular and anisotropic geometry of the ventricular myocardium, a simulation was first performed for a point stimulus on the epicardial surface. So that results could be compared with experimental measurements, the stimulus site was chosen to match the pacing site used for epicardial activation time recordings presented by Le Grice (1992). This site is on the epicardial surface of the anterior aspect of the left ventricular free wall and located at a distance from the apex about one third of that from apex to base.

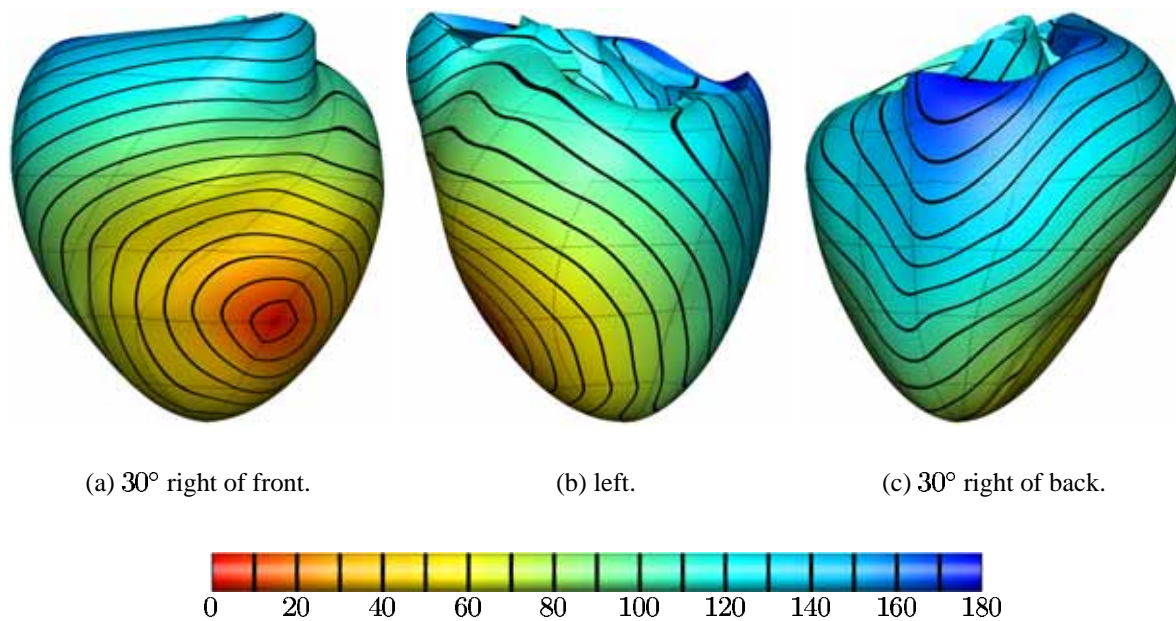


**Figure 7.1:** Simulated epicardial excitation times (ms) after epicardial point stimulus.

Epicardial isochrones from the simulation are shown in Figure 7.1 and snapshots of wavefront locations are presented in Figure 7.2. The epicardial isochrones are similar to those from experimental recordings on an epicardial sock (Le Grice, 1992) for times from about 25 ms to 65 ms after stimulation, but start to differ considerably outside this interval.

Near the stimulus site, experimental recordings showed much slower propagation in the direction transverse to the fibres. The difference in simulation results is probably due both to the inability of the eikonal model to reproduce the transient effects near a stimulus and to the coarse discretization. The distance over which slow initial transverse propagation was observed experimentally is less than one quarter of the element length in this direction.

For times greater than 65 ms after stimulation, experimental recordings showed much earlier epicardial excitation, particularly in the more basal and posterior areas on the left ventricular free wall. The region of latest recorded excitation was at the pulmonary conus, which was excited about 125 ms after stimulation. In simulations, the latest excitation occurred about 180 ms after stimulation in the basal posterior region of the right ventricular free wall. The discrepancy is most likely due to the lack of Purkinje fibre representation in the computational model. If the effects of this fast conduction network are not included in the model,

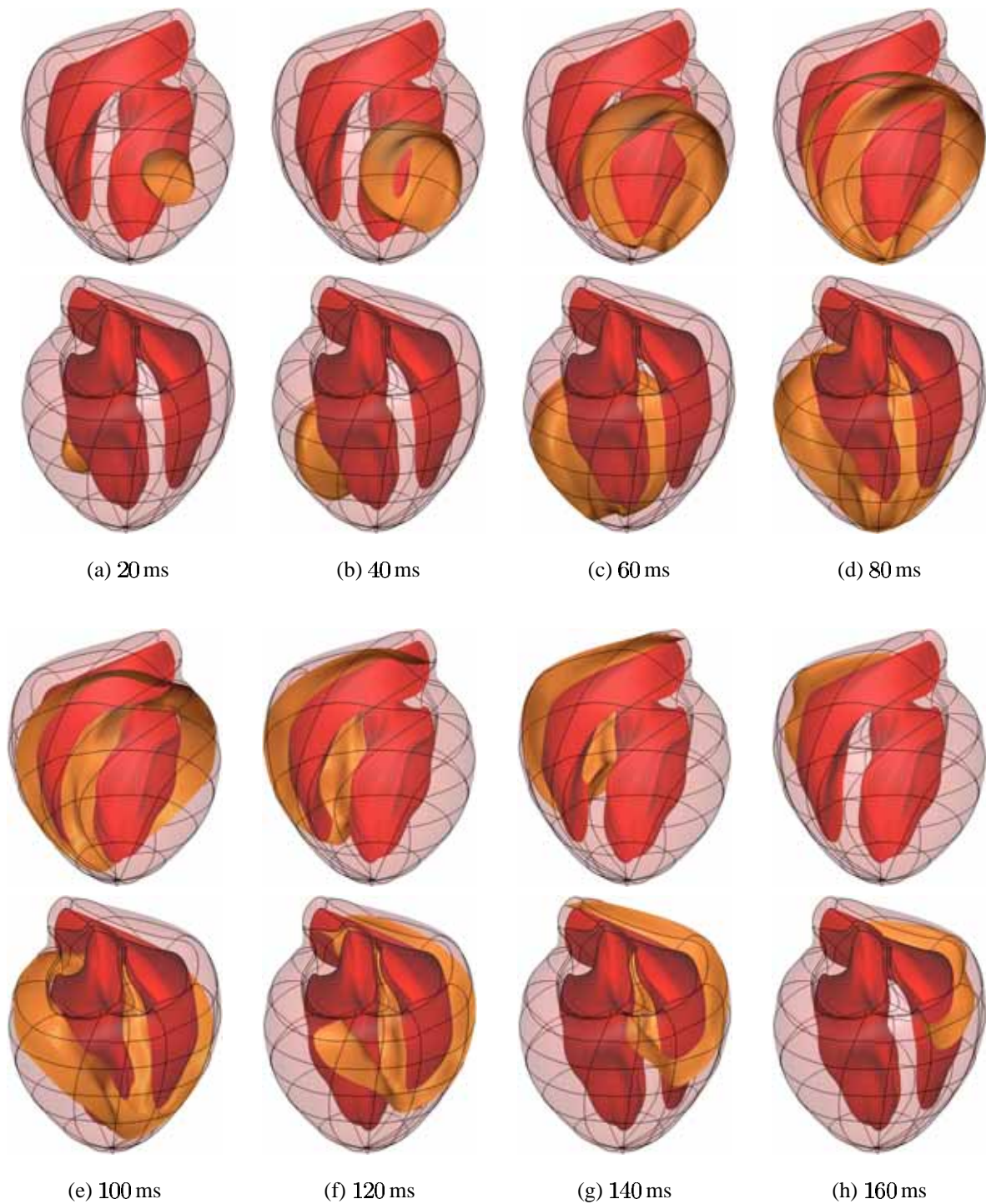


**Figure 7.2:** Wavefront locations at 20ms time intervals in simulation of propagation from an epicardial point stimulus at time 0. For each sample time, two opposing views are shown. The top view is from  $30^\circ$  below and  $30^\circ$  to the right of front.

results cannot be expected to be realistic. More realistic simulations are described in the next sections but this simulation is useful for analysing the performance of the numerical method.

It can be seen from the shape of the wavefronts (Figure 7.2) and epicardial isochrones (Figure 7.1) that, unlike the Galerkin method (Section 3.6), the Petrov–Galerkin method does not transport oscillatory errors, despite the collision occurring in the region posterior to the septum.

The solution to the discrete system of equations (5.69) was obtained after seventeen Newton iterations and required just less than four minutes of CPU time. One Newton iteration was performed for each increment of the continuation variable  $\alpha_c$  until it reached one, then four Newton iterations were required before the relative change in the solution reduced to less than  $10^{-5}$ . The time required for each iteration ranged from 10.7 s to 16.9 s. Of this, the time for calculation of the Jacobian was consistently 7.2 s, but the time for solution of the linear system of equations ranged from 3.0 s when diffusion was significant to 5.3 s when  $\alpha_c$  reached one to 9.2 s in the final iteration. Most of the remaining 0.5 s in each iteration was spent evaluating the residual in the non-linear equations.

In the solution of the linear system of equations for each Newton iteration, GMRES iterations were performed until the residual in the linear system reduced by a factor of  $10^{-3}$ . There was an increasing trend in the number of GMRES iterations required to achieve this, from 111 iterations when diffusion was significant to 170 when  $\alpha_c$  reached one to 251 in the final Newton iteration. This suggests that the condition number of the Jacobian may increase as the effect of diffusion reduces.

Although convergence in the solution to the non-linear system was achieved reasonably easily in this simulation with the material parameters selected in Section 6.4.5, when  $\alpha_c$  was increased to represent a reduction in the effects of diffusion, convergence could be achieved for  $\alpha_c = 1.06$  but not for  $\alpha_c = 1.07$ . This means that, if the material parameters were changed so that the relative magnitude of the diffusion term was reduced by more than 6 per cent, convergence could not be obtained.

Part of the reason for the inability to achieve convergence when the diffusion term is small may be related to the lack of  $C^1$  continuity in  $U$  at certain places in the mesh (see Section 6.3). A close inspection of the wavefront near the apex in Figure 7.2(c) reveals that the front is

starting to form a point as it approaches the apex. This feature of the wavefront vanishes when more diffusion is introduced into the equation.

As discussed in Section 5.2.3, when the diffusion effects become very small, the numerical method behaves as if it is solving an eikonal equation without a diffusion term. The appropriate equation to solve in this situation is the pure-evolution governing equation (5.49). Although the discrepancy between this and the eikonal equation was dealt with on boundaries in Section 5.2.3, it was assumed that inside the domain the residuals in the two equations were equivalent. The residuals are only equivalent, however, if first derivatives are continuous. The  $C^1$  constraint vanishes at the apex because the element widths vanish. Without  $C^1$  continuity the eikonal equation admits solutions where tissue is not necessarily excited by neighbouring tissue. Wavefronts can initiate at any time and spread out from any point in space where  $C^1$  continuity is not enforced. This lack of uniqueness in the solution makes the Jacobian for Newton's method singular and therefore convergence unlikely. If simulations are to be performed with less diffusion, the numerical treatment of the evolution term needs to more closely represent its form in equation (5.49). A possible approach is suggested in Chapter 8.

## 7.2 Stimulation from the Purkinje Network

It should be possible to use the model of the myocardium to produce realistic simulations of the excitation sequence for normal sinus activation if the times and locations of myocardial stimulation by the Purkinje network are known (assuming the Purkinje network excitation process is not affected by the myocardial excitation process). These stimulation times provide boundary conditions for an eikonal model of myocardial excitation.

### 7.2.1 The Purkinje Network

In this simulation, the Purkinje-fibre-to-myocardium electrical connections were modelled by specifying the myocardial stimulation times over endocardial element faces. The faces on which these boundary conditions were applied were chosen to correspond to the regions

of Purkinje-fibre-to-myocardium electrical contact as observed in canine ventricles by Myerburg, Nilsson, and Gelband (1972), Lazzara, Yeh, and Samet (1974), Nagao, Toyama, Kodama, and Yamada (1981), and Le Grice (1992). The sequences of excitation times for these faces were based on recordings made in endocardial preparations by Myerburg *et al.* and Lazzara *et al.* for the left ventricle and by Myerburg *et al.* and Nagao *et al.* for the right ventricle. Synchronization of the two ventricular surfaces was done by comparing early myocardial excitation times with those measured in a canine heart *in vivo* by Scher and Young (1956).

The regions where these boundary conditions were applied and their stimulation times are shown in Figure 7.3. Although the reported endocardial excitation sequences are reasonably consistent, there are a few differences worth noting.

In the left ventricle, Myerburg *et al.* (1972) observed earliest myocardial excitation at the junction of the middle and lower thirds of the septum while Lazzara *et al.* (1974) observed earliest excitation usually in the middle third of the septum. The time interval from earliest myocardial excitation to excitation of the apex was about 7 ms in the experiments of Myerburg *et al.* but was 10 to 15 ms in the experiments of Lazzara *et al.* Myerburg *et al.* also observed small islands of early excitation above the papillary muscles high on the paraseptal free walls on both sides of the septum at about the same time or before excitation of the apex. This feature is not mentioned by Lazzara *et al.* The excitation time observations of Myerburg *et al.* seem to be more consistent with the *in vivo* recordings of Scher and Young (1956), so the boundary conditions for this simulation more closely reflect their values.

In the right ventricle, both Myerburg *et al.* (1972) and Nagao *et al.* (1981) observed earliest excitation near the apex, but the earliest excitation detected by Scher and Young (1956) was in the upper half of the free wall. All three groups reported rapid excitation of the right ventricular free wall. If, in the experiments of Scher and Young, the recording sites on the electrodes near the apex were slightly deeper in the myocardium, it may explain the differences.

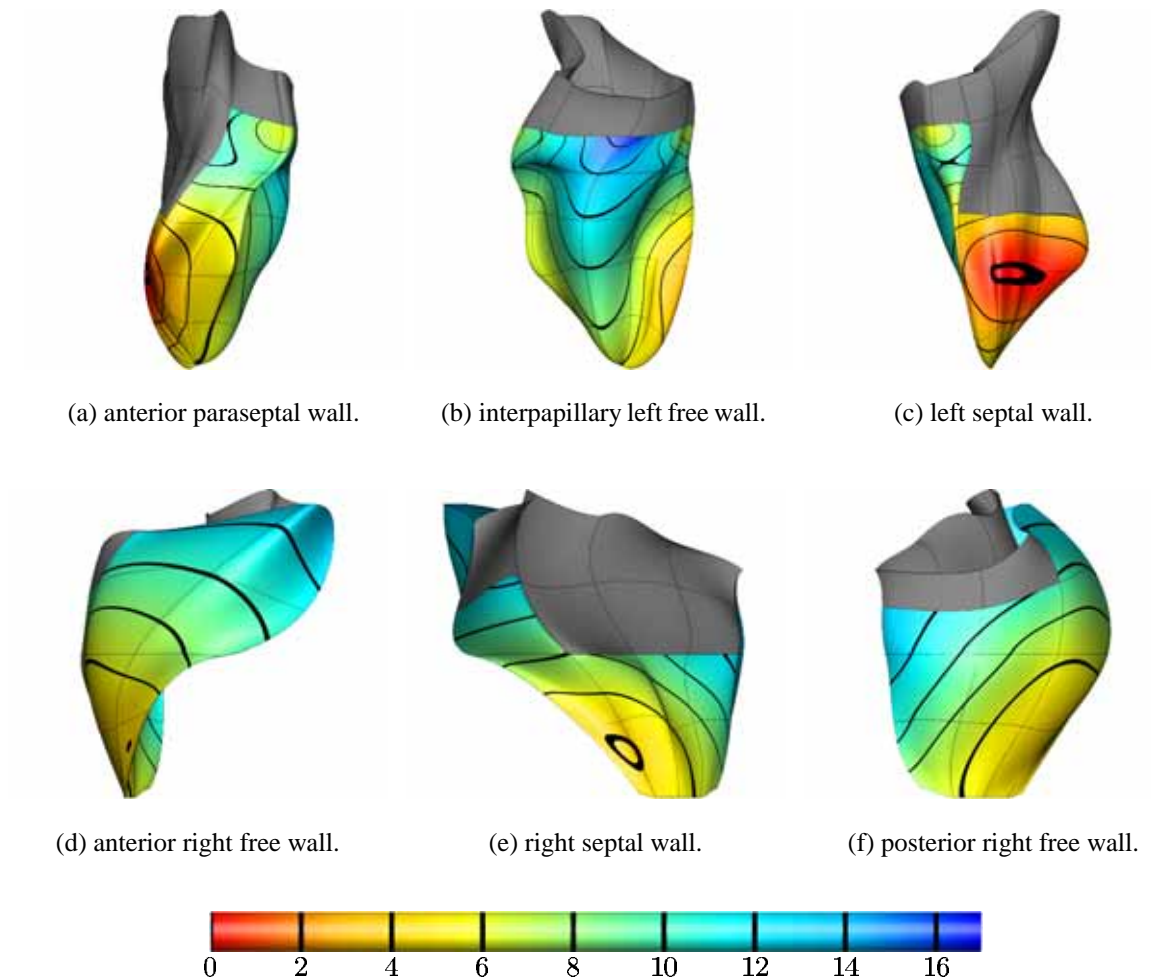


**Figure 7.3:** Stimulation times (ms) on the portions of the endocardial surfaces that are stimulated by the Purkinje network (coloured areas). These are used as boundary conditions for simulations of myocardial excitation.

## 7.2.2 Numerical Stability

The numerical solution satisfying the system of non-linear weighted residual equations (5.69) could be found when the continuation variable  $\alpha_c$  was 0.94 but not when it was increased to 0.95. Snapshots of the wavefront from the solution at  $\alpha_c = 0.94$  are shown in Figure 7.4. This value of  $\alpha_c$  corresponds to coefficients of the diffusion term that are 6 per cent greater than those obtained from estimates of material properties in Section 6.4.5.

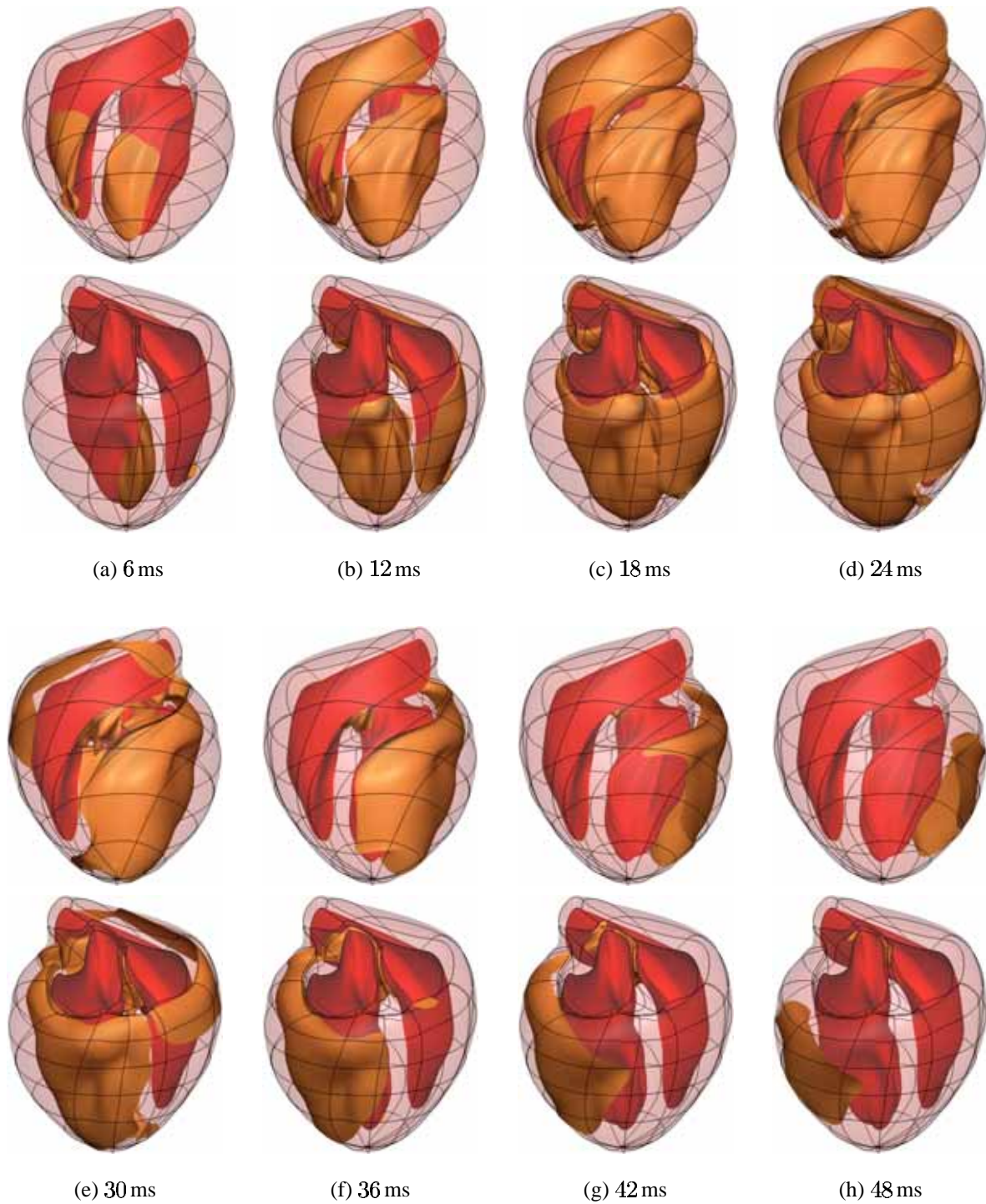


**Figure 7.4:** Wavefront propagation for excitation initiated by the Purkinje network, from a simulation with  $\alpha_c = 0.94$ .

There are two features of the solution that suggest that it is becoming unstable. The first is a region of tissue on the epicardial surface of the right free wall just below the apex of the right ventricle. The region is excited before any of the endocardium in the right free wall is excited. The effects on the solution may be seen by close examination of the top diagram of Figure 7.4(a). As well as spreading out from the right ventricular endocardium, the wavefront is also spreading out from a point below the endocardial apex. This is not physically realistic as excitation occurs in a region that is not excited by any neighbouring tissue. Spurious excitation like this suggests that the solution is not sufficiently constrained, which would prevent the convergence of Newton's method. The problem may be due to the no-inflow boundary inequality (5.54) not being enforced strongly enough and it may be related to the lack of  $C^1$  continuity around the cusp at the apex of the right ventricular endocardium (see Section 6.3).

The other feature indicating possible instability can be seen just in front of the lower half of the septum in the top diagram of Figure 7.4(b). In the wavefront spreading from the left ventricle there is a bulge that extends towards the right ventricle and has a very convex leading edge (when viewed from ahead of the wave). There are also other regions of the wavefront that are reasonably convex due to the trabeculations in the left ventricle, but this region is becoming more convex as it develops and is increasing in speed. The  $C^1$  continuity of the discretization means that, if there is a collision, there must be a point where the propagation speed is infinite, but this still does not completely explain the feature. The wave originating from the left ventricle accelerates and becomes convex before the approaching wave from the right ventricle does. The elements in the region surrounding the bulge are very contorted so as to describe the irregular neighbouring endocardial surfaces. The complex geometries of the elements may be the reason why the problem occurs in this region.

In the top diagram of Figure 7.4(e), the shape of the wavefront is irregular in the top half of the septum. This is a result of portions of the wavefronts from the two endocardial surfaces dissipating after collision. The two wavefronts merge to form one wavefront that is very concave (when viewed from ahead of the wave) near the region where the collision occurred. The descending concave regions may be larger than physically realistic due to the inability of the discretization to represent very high curvatures.

Reasonable solutions to the eikonal equation can be obtained by increasing the level of diffusion. The spurious excitation on the epicardium near the apex of the right ventricle does

not occur for values of  $\alpha_c$  up to and including 0.5. The solution at  $\alpha_c = 0.5$  is equivalent to a solution with twice the estimated physiological diffusion. The magnitude of the diffusion term is still very small and its effect is predominantly that of stabilizing rather than actually altering the nature of the solution.

Dimensional analysis of the eikonal equation leads to an estimated ratio of the effects of the evolution term to those of the diffusion term given by the global Péclet number,

$$P_g := \frac{c_0 L}{\lambda}, \quad (7.1)$$

where  $L$  is a characteristic distance based on the geometry of the domain, and  $c_0$  and  $\lambda$  are parameters in the eikonal equation.  $L$  and  $\lambda$  actually depend on direction, but the value of  $P_g$  is smallest (diffusion is most significant) when considering the transmural direction. The wall thickness is about 10 mm for the right ventricular free wall or twice that for the left free wall or septum. Selecting  $L \approx 10$  mm provides a conservative estimate of  $P_g$ . Because fibres run circumferentially, the appropriate value for  $\lambda$  is the space constant  $\lambda_t = 0.5$  mm (Section 6.4.5) for the direction transverse to fibres in the passive bidomain model.  $c_0 = 2.5$  so these values suggest  $P_g \approx 50$ . The influence of the diffusion term is therefore about 2 per cent of that of the evolution term. If the amount of diffusion is doubled the extra diffusion can be expected to make about 2 per cent difference to the solution.

The calculated wavefront locations at  $\alpha_c = 0.5$  are shown in Figure 7.5. The time for excitation of the entire myocardium was 55.86 ms which is within 0.01 per cent of the value calculated at  $\alpha_c = 0.94$ . By comparing Figures 7.4 and 7.5, it can be seen that the excitation sequences essentially only differ in the regions where the solution appeared unstable. If the solutions at  $\alpha_c = 0.5$  and  $\alpha_c = 0.94$  are so similar, the solution at  $\alpha_c = 0.5$  must provide a good estimate of the solution with physiologically realistic diffusion ( $\alpha_c = 1$ ).

If diffusion needs to be added to the equation in order to obtain a stable solution, high order convergence rates can no longer be expected, so one might ask the question as to what the advantage of high order elements is. To address this question, the cubic Hermite Petrov–Galerkin finite element scheme is compared with a simple finite difference scheme using first order upwind differences for the evolution term. A simple Taylor series analysis of first order upwind differences shows that the coefficient of numerical diffusion is half the coefficient of the evolution term multiplied by the grid point spacing, which resembles  $\frac{1}{2}c_0\lambda h$ . The

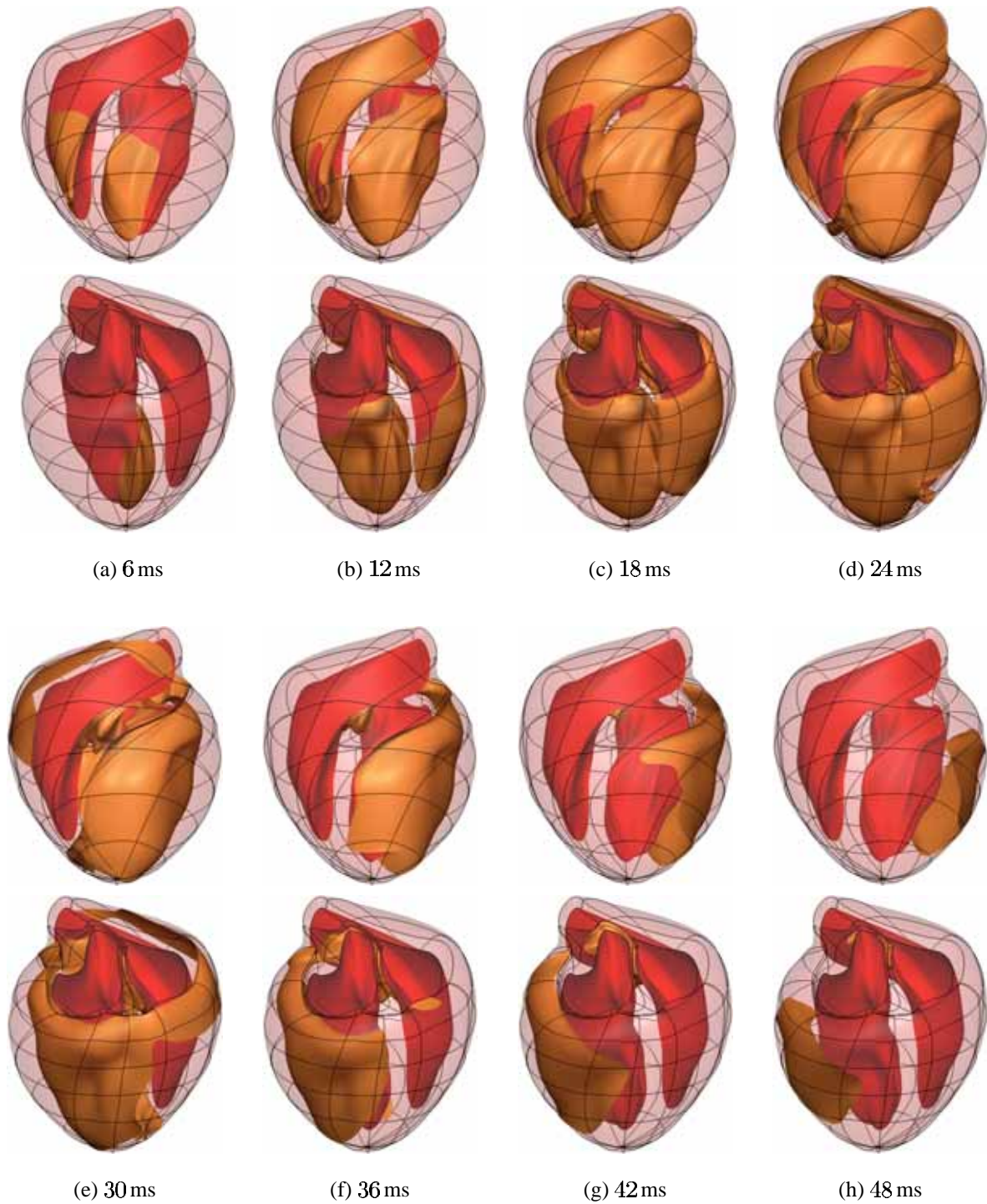


**Figure 7.5:** Wavefront propagation for excitation initiated by the Purkinje network, from a simulation with  $\alpha_c = 0.5$ .

coefficient of additional diffusion used to stabilize the cubic Hermite scheme resembles  $\lambda^2$ . In order to make the additional diffusion in the first order scheme of similar magnitude to that used in the cubic Hermite scheme, the grid point spacing must be given by

$$h = \frac{2\lambda}{c_0}. \quad (7.2)$$

(This is equivalent to requiring that the grid Péclet number  $P_e$  be equal to 2.) An optimally designed grid would therefore have grid spacings of 0.64 mm in the fibre direction and 0.4 mm in the other directions. The  $0.2 \times 10^6 \text{ mm}^3$  myocardial volume would need to be represented by about  $2 \times 10^6$  grid points. This is a factor of about  $10^3$  greater than the 2355 degrees of freedom in the cubic Hermite mesh.

A general estimate of the level of diffusion that needs to be added to stabilize the cubic Hermite Petrov–Galerkin finite element method in any geometric model may be obtained from examination of the mesh Péclet number  $P_e$  in the myocardial model when the solution is stable at  $\alpha_c = 0.5$ . As there are 180 elements in the mesh, the average element volume  $\bar{V}_e$  is  $1.12 \times 10^3 \text{ mm}^3$ . An average Péclet number may therefore be calculated using

$$P_e = \alpha_c c_0 \sqrt[3]{\frac{\bar{V}_e}{\lambda_l \lambda_t \lambda_n}}, \quad (7.3)$$

which gives a value of 22. This is effectively a volume average of the geometric mean of the Péclet numbers for each direction. The stability of the method, however, probably depends on the maximum Péclet number in the mesh rather than an average. The elements in the myocardial model are usually considerably longer in the circumferential and longitudinal directions than in the transmural direction and the dimensions also vary from one element to another, so the average Péclet number is probably not a good indicator for stability. The maximum Péclet number in any direction at any grid point in the model is 116. The stability of the method may only depend on the maximum Péclet number in the direction of propagation, which is 45 for this simulation. If a mesh has a Péclet number in the direction of propagation that is greater than this value, then diffusion probably needs to be added to reduce the Péclet number to this value. However, stability probably also depends on other variables such as the complexity of the wavefront and element geometries.

To investigate whether or not the discretization was sufficiently fine, a simulation was performed using a 1440-element mesh obtained by subdividing each element in two in each di-

rection. On the finer mesh, at  $\alpha_c = 0.5$ , excitation of the base of the septum occurred slightly later so that the time for complete excitation of the myocardium increased by 2.5 per cent to 57.23 ms. At  $\alpha_c = 1$ , the solution did not show any spurious excitation, and the shape of wavefront from the left ventricle near its collision with the wavefront from the right ventricle was much more reasonable. The excitation completion time was 56.07 ms, which is only 0.4 per cent greater than the estimate obtained from the 180-element mesh at  $\alpha_c = 0.5$ . The differences in the simulations are small compared with the uncertainties in geometry and material parameters. Convergence in the solution to the system of weighted residual equations was achieved for values of  $\alpha_c$  up to 1.46 (but not for 1.47), a factor of 1.55 higher than the maximum value for the 180-element mesh. The factor is less than the value of 2 expected from the difference in element sizes.

### 7.2.3 Comparison with Experimental Observations

Scher and Young (1956) recorded electrical activity at over 900 points throughout the canine ventricles to determine the normal sequence of ventricular excitation in a canine heart. The simulated excitation sequence illustrated in Figure 7.5 may be compared with these experimental observations.

The simulated excitation sequence shows propagation predominantly in an outward direction from the endocardial surfaces. Excitation of the right free wall occurs early, starting at the right ventricular apex, and rapidly spreading posteriorly and towards the base. The latest excitation in the right free wall occurs almost simultaneously along the entire length of the base in the epicardium. Near the apex of the heart, an epicardial breakthrough site occurs slightly posteriorly. In the left free wall, propagation is predominantly transmural but the apical regions are completely excited first. The latest excitation is in the epicardium of the mid to upper regions of the interpapillary free wall, where the wavefront splits in three before vanishing. In the septum, excitation spreads from the lower half of both endocardial surfaces, meeting approximately midway between the two, and then spreading up towards the base. The wavefronts of excitation from each surface collide in the lower third of the septum first anteriorly and second posteriorly, before the excitation of the rest of the lower third is completed. The latest excitation in the septum occurs in the middle of the base at about the same time as the latest excitation in the left free wall. Excitation is completed 56 ms after the

earliest myocardial excitation.

The model does not permit the spreading of excitation from the base of the right free wall to the base of the septum through the supraventricular crest. The basal portion of the free wall is excited well before the base of the septum, so, if this pathway was included in the model, excitation of the septum might be completed earlier and the latest excitation in the septum might occur more posteriorly.

The excitation observed experimentally by Scher and Young (1956) followed a similar sequence but occurred considerably faster. Excitation of the entire myocardium took just under 35 ms. This is consistent with the epicardial isochrones for normal excitation of the canine ventricles presented by Le Grice (1992), but Arisi, Macchi, Baruffi, Spaggiari, and Taccardi (1983) observed that some of the epicardium of the canine heart was not excited until more than 43 ms after the beginning of QRS. All observations, however, suggest that excitation in the simulation is slower than expected.

The most likely explanation for slower propagation in the simulation is that the Purkinje fibres actually penetrate a significant distance into the myocardium. This penetration has been observed in canine myocardium by Sodi Pallares, Medrano, de Micheli, Testelli, and Bisteni (1961) and Spach, Huang, and Ayers (1963). Spach *et al.* detected Purkinje fibres at a depths of 3 to 4 mm beneath the mid and lower areas of left septal surface, and 2 and 3 mm into the left free wall. On the right free wall data is less clear but penetration is probably less than 2 mm. The right septal surface was not investigated. As Purkinje fibres conduct much faster than myocardial fibres, their absence in the model would explain the slower excitation than in experimental observations.

Another possible reason for slower excitation of the model is that superficial layers of the subendocardial ventricular myocardium may in fact conduct faster than deeper myocardium. Myerburg, Gelband, Nilsson, Castellanos, Morales, and Bassett (1978) observed propagation speeds averaging  $0.98 \text{ m s}^{-1}$  for the fibre direction in endocardial tissue from the upper septal surfaces devoid of Purkinje fibre connections. Stripping the top 0.2 to 0.6 mm from the tissue significantly reduced the propagation speed. The change in speed was not observed with propagation transverse to fibres. The high conduction velocity seems consistent with observations of excitation in endocardial preparations from the left ventricle by Myerburg *et al.* (1972) and Lazzara *et al.* (1974). In preparations from the right ventricle, Nagao *et al.* (1981)

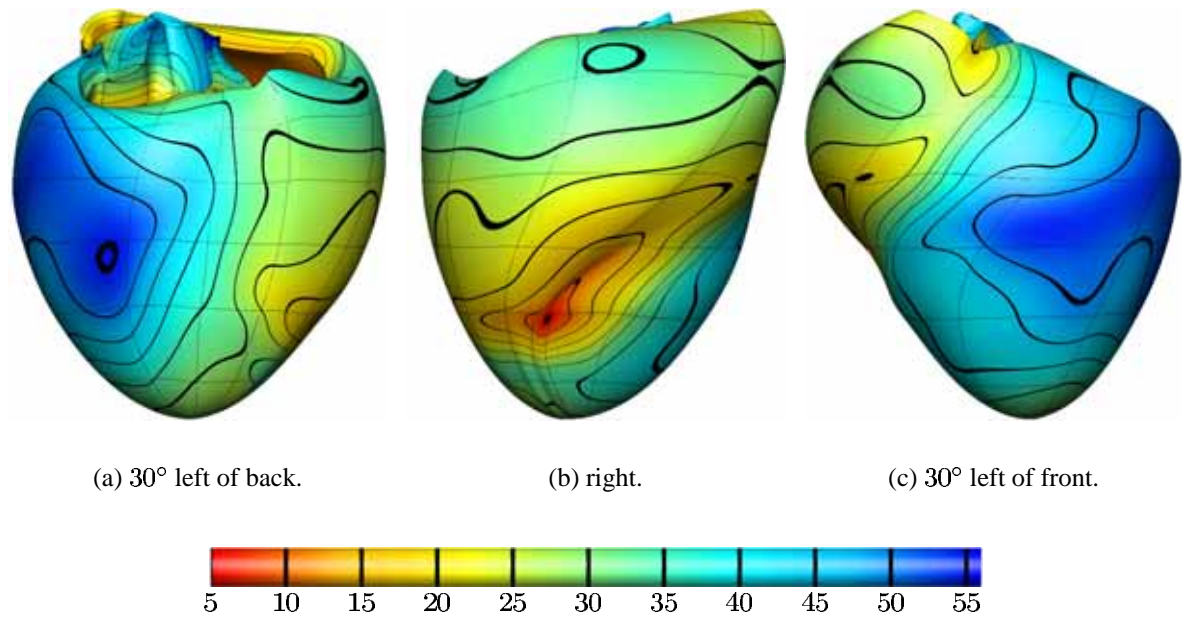


**Figure 7.6:** Simulated epicardial excitation times (ms) for Purkinje fibre stimulation. Times are with respect to the same reference time as the endocardial stimulation times in Figure 7.3

observed an average velocity of propagation from apex to base (which is essentially the fibre direction) of only 0.4 ms, but the standard deviation was 0.9 ms so in some experiments the value must have been much higher.

There are other small differences between the observations of Scher and Young (1956) and the simulation. As in the simulation, the excitation fronts from the two endocardial surfaces did meet first anteriorly in the lower third of the septum, but excitation of much of the lower third was observed before the fronts met posteriorly. Latest excitation was observed in the middle of the base of the septum and in the epicardium of interpapillary left free wall, as in the simulation, but also occurred almost simultaneously in the epicardium of the more posterior regions of the left free wall. These differences may also be due to the influence of Purkinje fibres penetrating into the myocardium.

The epicardial excitation times corresponding to the simulation in Figure 7.5 are shown in Figure 7.6. It is difficult to compare these with the experimental observations of Arisi *et al.* (1983) and Le Grice (1992) because there are considerable differences between their

observations. This is most likely due to the fact that the wavefront of excitation is predominantly tangential to the epicardium. A small difference in propagation speed or thickness of the heart wall therefore makes a large difference in the sequence of epicardial excitation. Nevertheless, the sites of earliest epicardial excitation are consistent and it is worthwhile comparing them with the simulation.

The epicardial isochrones presented by both Arisi *et al.* and Le Grice both show earliest epicardial excitation in a region adjacent to the lower half of the anterior edge of the right ventricle, as in the simulation. The experimental observations, however, did not show a distinct point of earliest excitation nearest the right ventricular apex. Instead a longer region of the epicardium was excited almost simultaneously at 10 to 11 ms after the beginning of QRS. This may indicate that the stimulation of the endocardium at the right ventricular apex may not occur as early as estimated in Section 7.2.1.

### 7.3 Penetration of Purkinje Fibres

The effects of the penetration of Purkinje fibres beneath the myocardial surface (Sodi Pallares *et al.*, 1961; Spach *et al.*, 1963) were modelled by altering the parameters of the eikonal equation in the appropriate regions to reflect the speed of propagation through Purkinje fibres.

The most important property of the Purkinje fibres is their conduction velocity. Nagao *et al.* (1981) and Myerburg *et al.* (1978) both reported average values between  $1.6 \text{ m s}^{-1}$  and  $1.7 \text{ m s}^{-1}$ , but Lazzara *et al.* (1974) reported a slightly lower average value of  $1.4 \text{ m s}^{-1}$  in the interior Purkinje network. Values for the passive space and time constants of Purkinje fibres have been reported as  $\lambda = 2 \text{ mm}$  and  $\tau_m = 20 \text{ ms}$  (Fozzard, 1966), but these may not necessarily be the appropriate values for the eikonal equation when modelling the interaction of the Purkinje fibres with the myocardium. Variation in these values for the passive properties should make little difference to the solution, provided the parameters in the eikonal equation give the appropriate propagation speed (by satisfying equation (6.5)).

The parameter values for the Purkinje fibres were specified at the same nodes on the left ventricular endocardium as where the boundary conditions were applied (cf. Figure 7.3). At all other nodes, the parameter values represented myocardium. A linear interpolation of

these nodal values was then used within the elements. This resulted in a diminishing effect of Purkinje fibres into one third of the depth of the left free wall and into the left half of the lower part of septum. Because, in this implementation, the propagation speed is only as great as the Purkinje fibre velocity at the endocardial surface, the largest reported value of  $\theta = 1.67 \text{ m s}^{-1}$ , was used for Purkinje fibre velocity. This was implemented by simply increasing the space constant  $\lambda$  to 2 mm for all directions at nodes corresponding to the Purkinje network.

The faster excitation of the superficial layers of the subendocardial ventricular myocardium (Myerburg *et al.*, 1978) was also included in this simulation by increasing the space constant in the fibre direction to  $\lambda_1 = 1.18$  at nodes on the endocardial surfaces that were not representing the Purkinje network. At all other nodes, the parameters used were the same as in the previous section.

Simulation results, which were generated with  $\alpha_c = 0.5$ , are shown in Figures 7.7 and 7.8(a). Excitation of the myocardium was completed in 48 ms, which is 14 per cent less time than in the previous simulation but completion times from experimental observations are still 9 to 27 per cent lower than this. The large difference in experimental observations suggests that there are large variations in completion times (due to sizes of the hearts, for example), but the completion time in the simulation may still be slightly higher than realistic due to the assumption in the model that myocardial excitation begins on the endocardial surface. Scher and Young (1956) and Spach *et al.* (1963) both reported regions of the left ventricular endocardium where earliest excitation of myocardial tissue occurred beneath the surface. This suggests that the myocardium on the endocardial surface may not be excited by the Purkinje network but by deeper myocardium, which is excited by the penetrating branches of the Purkinje network. The myocardial excitation times observed on the surface of endocardial preparations probably do not provide either a good indication of the earliest myocardial excitation or appropriate boundary conditions for the eikonal model. Better boundary conditions may instead be based on the excitation time of surface Purkinje fibres. The depth of earliest excitation is particularly significant under the papillary muscles (Scher and Young, 1957), which explains the late excitation of the left free wall in the simulation.

Apart from general earlier excitation of the left side of the heart and upper half of the septum, the sequence of excitation is very similar to the previous simulation. In the septum, more of the lower third is excited before the wavefronts from the endocardial surfaces collide posteriorly, which is more consistent with experimental observations. On the right free wall,

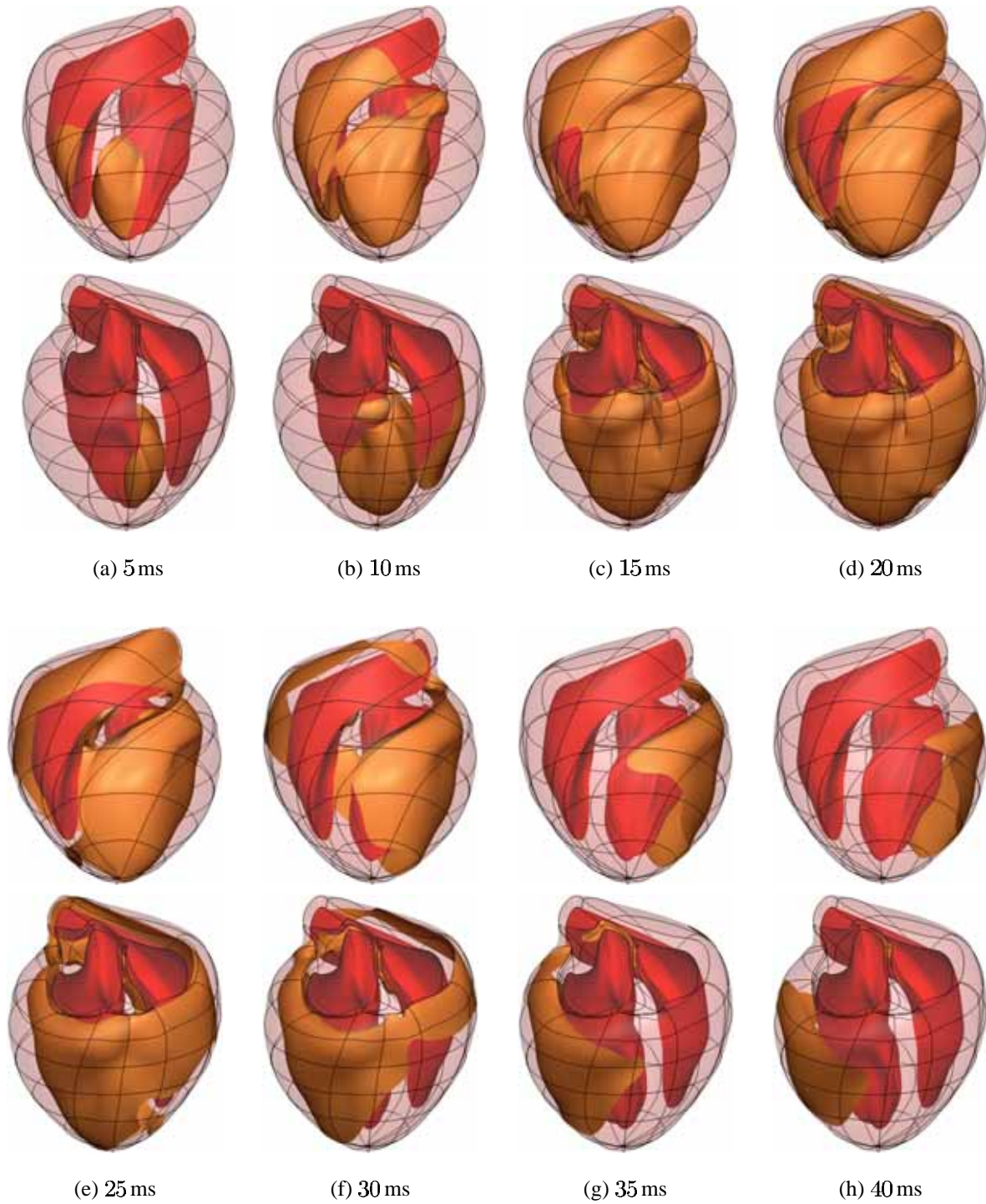


**Figure 7.7:** Wavefront propagation with the penetration of Purkinje fibres represented by faster propagation speeds in the left ventricular endocardium.

the epicardial isochrones near the breakthrough site are slightly different due to the higher fibre-direction conductivity used at the endocardium.

## 7.4 Effects of Sheet Structures

The simulations described in the first three sections of this chapter incorporate the anisotropic effects of fibres, but the electrical properties must also depend on the orientation with respect to the layers (or sheets) of myocytes (LeGrice, Smaill, Chai, Edgar, Gavin, and Hunter, 1995). In this section the effects of a different space constant in the direction normal to the sheets are investigated.

In Section 6.4.5, the parameters  $\lambda_l$  and  $\lambda_t$  were selected based on observations of properties in the fibre direction  $\mathbf{a}_l$  and the transverse direction within sheets  $\mathbf{a}_t$ . Here, an estimate of the appropriate space constant  $\lambda_n$  for the direction normal to sheets  $\mathbf{a}_n$  is based on the observations of microscopic structure by (Le Grice, 1992). Le Grice made estimates of the ratios of speeds in each direction from relative lengths of paths through the branching myocardial structure along which excitation might occur. This led to predictions that the ratio  $\frac{\theta_l}{\theta_n}$  is about 2 at the endo- and epicardial surfaces and 3 in the midwall. No attempt was made in this simulation to represent the variation through the wall, but the constant value  $\lambda_n = 0.3$  mm was selected to give a ratio of 2.67 and a propagation speed  $\theta_n = 0.25$  m s<sup>-1</sup> for the direction  $\mathbf{a}_n$ . The space constants and propagation speeds are then in the ratio  $\lambda_l:\lambda_t:\lambda_n = \theta_l:\theta_t:\theta_n = 8:5:3$ .

Simulation results (generated with  $\alpha_c = 0.5$ ) are shown in Figures 7.8(b) and 7.9. The 40 per cent reduction in velocity for the direction normal to sheets increased the total time for myocardial excitation by only 4 per cent to 50.0 ms. As propagation is largely in the transmural direction and the direction  $\mathbf{a}_t$  is predominantly transmural in the midwall, propagation is predominantly within sheets, so changing  $\lambda_n$  does not greatly affect the overall excitation time. The posterior collision in the septum is delayed by just over 1.5 ms so that it occurs within 0.1 ms of another collision in the middle of the lower third of the septum. The epicardial isochrones are perhaps less regular owing to the inhomogeneous sheet orientations, but the overall sequence of excitation is changed little. More significant differences might be observed in simulations of abnormal excitation when more propagation occurs out of the plane of the sheets.

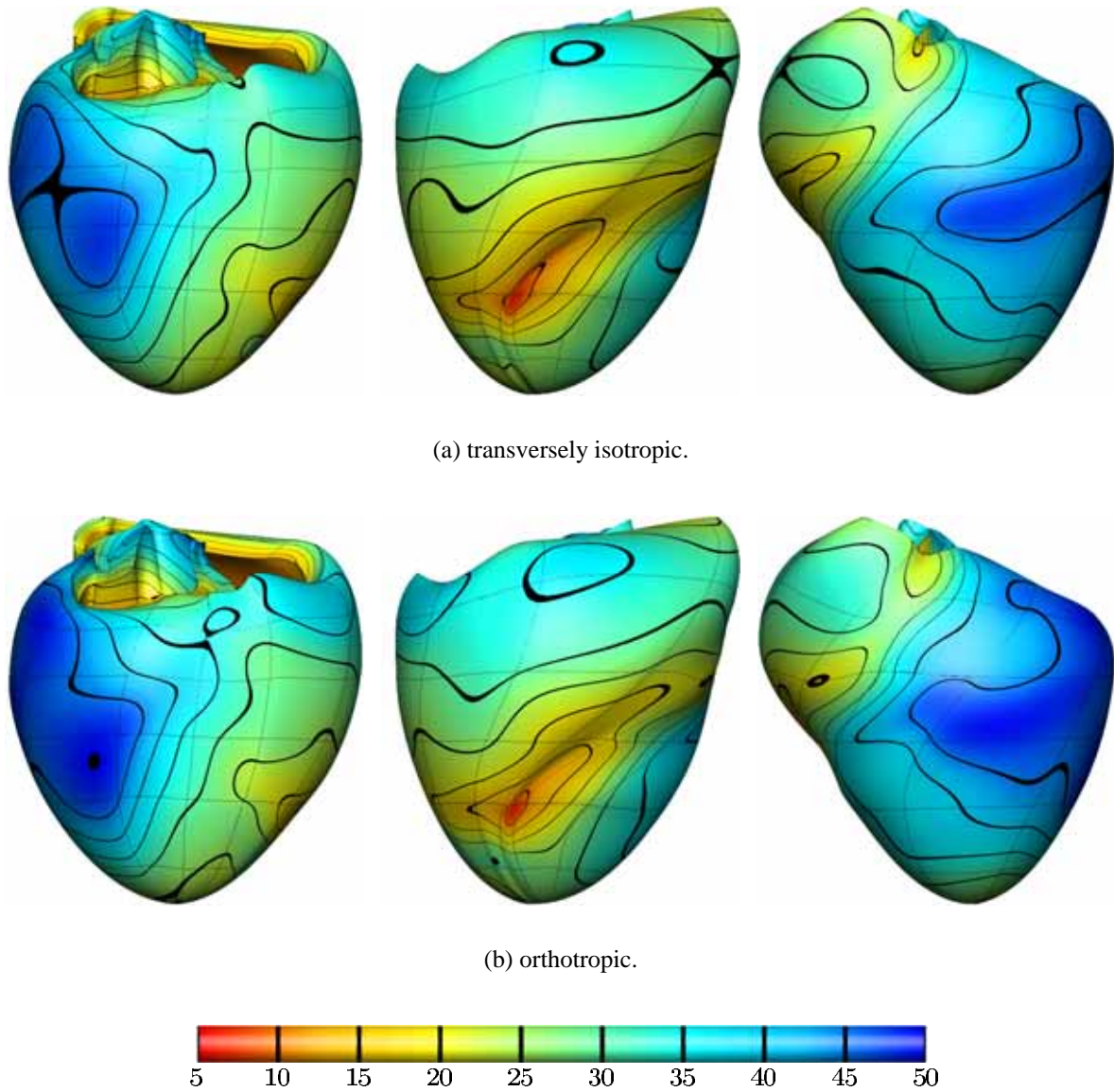


**Figure 7.8:** Epicardial excitation times (ms) with different conductivities for the direction normal to sheets. In (a),  $\lambda_n = \lambda_t$ , and in (b),  $\lambda_n = 0.6\lambda_t$ . In both simulations the propagation speed is faster on the left ventricular endocardium to represent the effects of Purkinje fibre penetration.

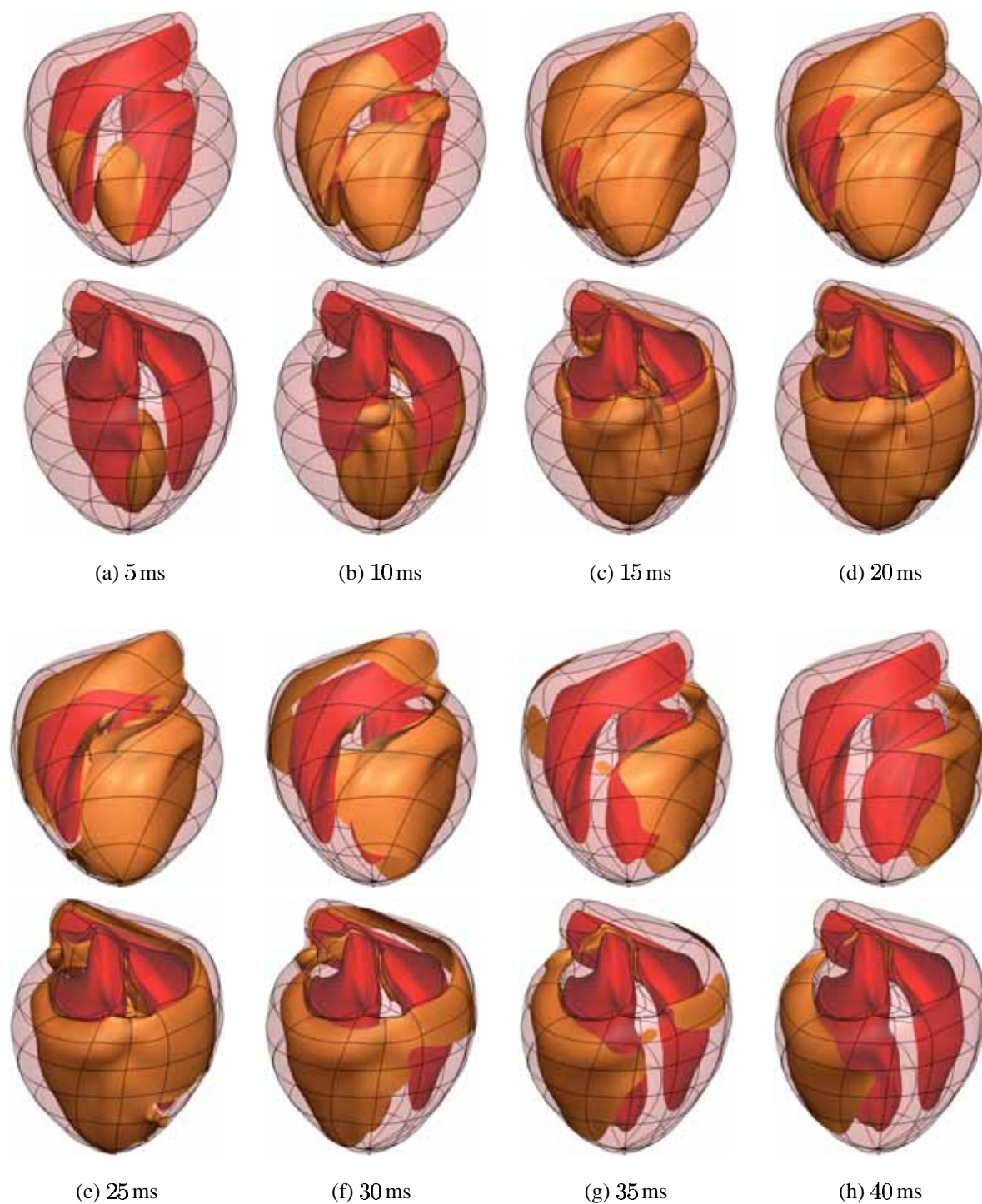


**Figure 7.9:** Wavefront propagation with reduced conductivity in the direction normal to sheets.  
 $\lambda_n = 0.6\lambda_t$ .



## *Chapter 8*

# **Further Work**

The stability of the present method is unreliable when the diffusion term is small, and the speed of the method depends to a large extent on its stability. This chapter discusses some ways to improve the speed and stability of the method as well as some extensions to the model.

Stability can be achieved by adding a small amount of artificial diffusion. It would be preferable not to add artificial diffusion at all, but, if some diffusion must be added, the amount should be minimized. Section 8.1 suggests a better method for adding diffusion.

One way to improve the speed of the method would be to design a preconditioner to take advantage of the predominantly one-directional dependence of the solution to the linear system of equation. In the myocardial model, however, less than half the computational time is spent solving the linear system, so a well designed preconditioner could not improve the speed of the method by more than a factor of two.

A greater improvement in the speed of the method would be attainable if the stability of the method could be improved. As mentioned in Section 7.1, the number of GMRES iterations required for convergence increased as the continuation variable  $\alpha_c$  increased. More significantly, the factor by which  $\alpha_c$  could be increased in each step of the continuation method without precluding convergence of Newton's method reduced rapidly as  $\alpha_c$  increased. When  $\alpha_c$  was large enough so the effects of diffusion were small,  $\alpha_c$  could only be increased by about 10 per cent in each step, despite the very small differences between the solutions for

each value of  $\alpha_c$ . If the stability of the method for low diffusion levels could be improved, it is likely that larger steps in  $\alpha_c$  could be taken and the total number of iterations would be reduced considerably.

The required computational effort increases rapidly as the mesh size is reduced, so using a smaller mesh size to obtain stability is an expensive option. Suggestions for modifying the method to improve the stability and possibly make artificial diffusion unnecessary are discussed in Section 8.2.

It would be useful if the potential on the torso surface could be calculated from the wavefront locations obtained using the myocardial excitation model, so that results could be compared with non-invasive measurements. Means for achieving this are discussed in Section 8.3.

Some additional features that should be included in the ventricular model are mentioned in Section 8.4.

## 8.1 Artificial Diffusion

When using artificial diffusion to stabilize the solution of the advection–diffusion equation, the extra diffusion is only necessary in the direction of advection, so a rank one diffusivity tensor is used (Kelly, Nakazawa, Zienkiewicz, and Heinrich, 1980). For the eikonal equation, however, the corresponding rank one tensor depends on  $\nabla U$  and produces an artificial diffusion term that has the same anisotropy structure as the physiological diffusion term (Colli Franzone, Guerri, Pennacchio, and Taccardi, 1998). There seems little point therefore in making the artificial diffusivity tensor depend on the direction of propagation.

One way to reduce the total amount of added diffusion would be to determine the level of artificial diffusion for each direction from the mesh Péclet number for that direction. Instead of increasing the diffusivity tensor by a constant factor, the diffusion would be only increased in the directions where it is required. In the myocardial model, many of the elements are reasonably short in the transmural direction and would probably not need artificial diffusion in these directions. The amount of physiological diffusion in the fibre direction is also considerably larger than in the other directions, so there would not need to be as much artificial

diffusion applied in the fibre direction.

## 8.2 Improving Numerical Stability

There are two likely reasons for the instability when diffusion is small. One is insufficient application of the constraint that propagation must be from tissue that is already excited. The other is simply that, due to non-linearity of the equation and weighting functions, there may be no solution to the weighted residual equations.

### 8.2.1 Treatment of the Evolution Term

There were features of the simulation for excitation from an epicardial point stimulus that suggested that the direction of propagation may not be sufficiently constrained in regions where  $C^1$  continuity is not enforced (Section 7.1). In such regions, the solution is certainly not sufficiently constrained when there is no diffusion, and the physiological diffusion cannot be relied on for stability when it becomes smaller than discretization errors. This problem should therefore be addressed. It seems also from the simulation for excitation from the endocardial Purkinje network that the no-inflow boundary term may not be sufficiently constraining the solution on the boundary (Section 7.2.2). These problems may be resolved by evaluating the evolution term in a way that more closely represents its form in the pure-evolution governing equation (5.49).

With conventional finite element methods, the difficulty in representing the evolution term like its supremum form in the pure-evolution equation (5.49) is a result of only evaluating the evolution term at Gauss points within each element. At these points the solution is sufficiently smooth that the supremum is equal to the evolution term in the eikonal equation. The potential problem regions, however, are the inter-element boundaries, where the solution is not sufficiently smooth, and the domain boundary. This is where the eikonal and supremum evolution terms differ.

A possible alternative finite element method that incorporates the nature of the supremum

evolution term in these problem regions is to evaluate the evolution term from an interpolation of its value at sample points. Unlike Gauss points, these sample points would be arranged so that some of them lie on the element boundaries. At each of these sample points, the evolution term could be evaluated from the supremum in (5.49). This would be equivalent to the eikonal evolution term at points within elements but would differ on the boundaries. In a cubic Hermite element, the sample points could be arranged in a  $4 \times 4 \times 4$  grid with the outermost points on the boundary of the element. The numerical residual in the governing equation would be similar to that in a conventional method when the solution is sufficiently smooth, but would be significantly affected by the constraints of the supremum when the first derivatives are discontinuous or the boundary inequality (5.54) is not satisfied.

Careful treatment of the interpolated value for evolution term may be necessary as it can be negative. It may be better to evaluate at each sample point a vector orientated in the direction of propagation  $\mathbf{a} \in A$  and having the magnitude of supremum term at that point. Over the rest of the element the value of the evolution term can then be calculated from the magnitude of the interpolation of the vectors at sample points.

The interpolation of quantities evaluated from an interpolated dependent variable may affect the expected order of convergence for the method, but it is worth a small reduction in the order if it means that artificial diffusion is not necessary.

If first derivatives are not shared between elements, the alternative evaluation of the evolution term may provide enough upwinding to prevent error transport, so Galerkin weights may be sufficient. With linear elements and Galerkin weights the method is similar to the first order upwind scheme of Colli Franzone and Guerri (1993b). With higher order elements there is the possibility of oscillations within an element. An analysis like that in Section 5.1.3 should be performed to determine the error factor. If this is not good then non-linear supplementary weights would still be required.

## 8.2.2 Existence of a Solution to the Non-Linear System

In the present model there is no guarantee that there exists a solution to the non-linear system of weighted residual equations. The exception is when the Péclet number  $P_e$  is zero because

the system is linear and positive definite so a solution must exist. It seems reasonable therefore to expect that a solution exists at least up to some finite value of  $P_e$ , but this value is unknown.

The minimum of the least squares functional (4.1) must exist (although it may not necessarily be unique). If the functional is smooth enough then the derivatives of the functional with respect to each parameter must be zero at the minimum, so a solution to the least squares weighted residual equation (4.2) must exist. The difficulty with the least squares method is the requirement of first derivative continuity. This is not a requirement, however, if there is no diffusion term because the equation is only first order.

It might be more appropriate then for the Petrov–Galerkin weights to approach the least squares weight when  $P_e$  approaches  $\infty$ . If the residual in the governing equation was reformulated into a form like expression (4.5) so that the least squares functional was smooth enough, the existence of a solution would then be guaranteed at  $P_e = \infty$ . There is still no guarantee of a solution for  $P_e \in (0, \infty)$ , but, with a solution at each end of the range, existence within the range, seems more hopeful. Such a method would require a continuous expression for the coefficient  $A_0$  of the Galerkin weight so as to retain continuity of the weighting functions (Section 5.1.4).

The existence of a numerical solution may depend on the complexity of the problem. If a lower order discretization were used for the dependent variable, its complexity would be restricted. The stability of the method might therefore be improved by reducing the order of the discretization in regions where the numerical solution appears to be becoming unstable.

### 8.3 Developing A Model of the Far-Field Potential

Colli Franzone, Guerri, and Viganotti (1983) proposed a method for modelling the far-field potential produced by an excitation wavefront. By approximating the transmembrane potential as a step-function and substituting it into the first equation of the reaction–diffusion system (2.17), the extracellular potential was shown to satisfy a generalized Laplace equation except at the wavefront where there are jumps in the potential and its normal derivative. The magnitudes of the jumps are functions of the wavefront geometry and the conductivity

tensors, and the diffusivity tensor in the Laplacian represents the bulk conductivities of the two myocardial domains. The diffusivity tensors for the myocardium and the outside volume were then approximated by a homogeneous isotropic tensor so that a boundary element method could be used for determining the extracellular and outside volume potentials.

The homogeneous isotropic approximation of the diffusion considerably simplified the method for determining the far-field potential because it meant that a discretization for the dependent variable was only required on the outermost surface where the solution was continuous. If the different conductivities of the myocardium and surrounding volumes or the inhomogeneous anisotropy of the myocardium are to be included in the model, a discretization is needed for the dependent variable on the myocardial boundary or in the myocardial domain.

Discretization of the extracellular potential on the boundary of or within the myocardium would require a method for representing the jumps in its value at the wavefront and preferably also the jumps in its normal derivative. It is possible that this could be done by using special basis functions with the appropriate jumps or by adapting the mesh for each instant in time at which the far-field potential is desired. Care would need to be taken, however, to avoid jumps in the solution when the wavefront crosses a node or when the number of elements in changed.

A simpler approach might be to first obtain the solution for the model of Colli Franzone *et al.* (1983) with the homogeneous isotropic diffusion (or possibly a similar model with an infinite domain), and then solve for the difference between this and the potential for the inhomogeneous model. The potential in the model of Colli Franzone *et al.* satisfies the required jumps across the wavefront, so, if the dependent variable is the difference in the potentials of the two models, it is much smoother and should be easier to discretize.

A derivative boundary element method was developed for use with cubic Hermite elements in the solution of the Laplace equation (Tomlinson, Bradley, and Pullan, 1996). This is being used to model the electrical field in regions of the torso where the tissue can be assumed homogeneous (Pullan and Bradley, 1996; Bradley, Pullan, and Hunter, 1997).

## 8.4 Extensions to the Ventricular Model

The present model cannot represent re-entrant wavefronts. It might be possible to approximately model this mode of excitation if the eikonal equation was solved using a marching method with a recovery time specified for each point in space. More realistic simulations, however, would probably need to model the cellular activity and would therefore need to retain the time variable of the reaction–diffusion system. A method should be sought to avoid where possible the fine discretization usually required in solving this system.

Although we cannot hope to represent every feature of the ventricles, there are some major features that should be included. In the myocardial model, the supraventricular crest should be included and the effects of tissue inhomogeneities should be investigated. The myocardial tissue in the supraventricular crest could provide an excitation pathway that significantly affects the excitation in the base of the septum (Section 7.2.3). The level of inhomogeneity through the myocardium is uncertain, but LeGrice, Smaill, Chai, Edgar, Gavin, and Hunter (1995) observed significant transmural variation in the structural coupling between adjacent muscle layers.

The Purkinje fibre network should be modelled for a more complete model of ventricular excitation. This requires both a detailed description of the network and its properties as well as an efficient numerical technique for modelling conduction and interaction with the myocardium. A better model of the effects of the Purkinje network under the papillary muscles, for example, could significantly alter the late excitation in the left ventricular free wall (Section 7.3).



## *Chapter 9*

# **Conclusions**

An efficient computational model has been developed for the excitation process in ventricular myocardium. The model solves an eikonal equation for excitation time using a new high-order Petrov–Galerkin method supplemented with a no-inflow boundary integral term. The method allows the excitation process to be modelled without the need for a fine discretization in space to represent the small-scale ionic activity and without any discretization in time.

A model of the canine ventricular geometry defined with respect to a rectangular Cartesian coordinate system has been fitted to measured surface data points. Simulations of excitation were performed in this model with 2355 degrees of freedom for the dependent variable.

The need to represent the small-scale ionic activity is eliminated by modelling the excitation process as a propagating wavefront of depolarizing tissue. Careful design of the computational method to take advantage of the reduction in complexity of the model allows reduction in the problem domain by one dimension and solution on a relatively coarse mesh.

The propagating wavefront approach permits the use of an eikonal equation to approximate the reaction–diffusion system that governs the bidomain model. Deriving a governing equation for the propagating wavefront model from satisfaction of the reaction–diffusion system at the wavefront yields an eikonal–curvature equation (Section 2.3.2), while approximate satisfaction of the reaction–diffusion system in the general vicinity of the wavefront yields an eikonal–diffusion equation (Section 2.3.3). Because the eikonal–curvature equation is derived from information only at the wavefront, the equation does not predict any effect on

wavefront propagation from boundaries or other wavefronts. The eikonal–diffusion equation, however, more accurately approximates the reaction–diffusion system near wavefront collisions or no-flux boundaries (Section 2.4.2).

A traditional Galerkin finite element method solution to the eikonal–diffusion equation shows oscillations when the mesh Péclet number is significantly greater than one (except in very simple problems) (Section 3.6). In order to obtain reasonable solutions from this method it would be necessary to use a fine spatial discretization at about the same level as that required to model the ionic activity.

A Petrov–Galerkin method using cubic Hermite elements has been developed to enable numerical solution on a reasonably coarse mesh. The method is a weighted residual method with weights that are a linear combination of Galerkin weights and  $C^0$  continuous supplementary weights based on the derivatives of the interpolation functions in the direction of propagation (Section 5.1). For one-directional propagation, the error in the solution is within a small constant factor of the optimal error achievable in the trial space. To estimate the constant factor in the error bound, it was only necessary to consider the function in the trial space with highest frequency first derivative and its corresponding weighting function. A function of the mesh Péclet number was selected for the ratio of the Galerkin and supplementary weights so that this error factor is small for all values of the Péclet number.

For high Péclet numbers, the numerical solution of the eikonal–diffusion equation behaves as if there is no diffusion term. An eikonal equation determines the speed of propagation at each point in space but provides no constraint on the direction of propagation. Without the diffusion term, there is no longer any no-flux boundary condition and spurious excitation can initiate at any point on the boundary (Section 5.2.1). A no-inflow boundary term has been designed to provide a penalty on such spurious excitation (Section 5.2.3).

The use of a continuation method to gradually introduce the non-linear term of the governing equation enables the solution to be found without any time discretization (Section 3.5). Typically, about 15 to 20 Newton iterations were required to obtain the solution for simulations in the full ventricular myocardium.

In simulations of excitation in the full ventricular myocardium, the method showed instabilities when the effect of diffusion is very small, and artificial diffusion was sometimes

necessary to obtain a solution to the non-linear discrete system of equations. Solutions were stable when the physiological diffusion term was doubled to give a maximum mesh Péclet number of 45 in the propagation direction (Section 7.2.2). This level of artificial diffusion is much less than the level of numerical diffusion that would be introduced by using a first order upwind finite difference scheme with the same number of degrees of freedom.

The model allows investigation of the effects of variation in material properties and structure on the sequence of excitation. Simulation of normal sinus excitation with the assumption that the Purkinje fibres affect excitation only on the endocardial surface showed excitation similar in sequence to reported experimental observations but slower (Section 7.2.3). Excitation in the simulation was completed in 56 ms but experimental measurements indicate completion times 23 to 38 per cent less than this. Other differences in the simulation included coalescence of the wavefronts from the endocardial surfaces in the lower third of the septum posteriorly before, instead of after, medially, and more marked late excitation on the interpapillary left free wall. Alteration of material properties to represent penetration of Purkinje fibres into one third of the depth of the left free wall and into the left half of the lower part of the septum reduced the time for complete excitation by 14 per cent to 48 ms, and also resulted in a greater spread of excitation into the medial regions of the lower third of the septum before coalescence of the wavefronts posteriorly (Section 7.3). Modelling the effects of the laminar structure of the heart by reducing the propagation speed normal to sheets by 40 per cent increased the total excitation time by only 4 per cent, but delayed the posterior coalescence of wavefronts in the septum so that it occurred almost simultaneously with coalescence in the medial regions (Section 7.4). The excitation completion time is expected to be reduced further if the supraventricular crest is included in the model and greater effort is made to model the penetration of Purkinje fibres behind the papillary muscles on the left free wall.



## Appendix A

### Step-Function Point Current Source in a Passive Bidomain with Equal Anisotropy

The following is a proof that equations (6.20) give a solution for  $V_m$  and  $\phi_e$  when a step-function point current source of magnitude  $I$  is applied to the planar boundary of a homogeneous semi-infinite passive bidomain with equally anisotropic coupling tensors  $M^i$  and  $M^e$  given by equations (6.18) and (6.19) (or equivalently (2.32)). The solution is shown to represent the correct total current flow into each domain at the source point and to satisfy the conservation of current equations (2.24) away from the source.

It is convenient to define a coordinate transformation matrix

$$X := \begin{bmatrix} \lambda_l \mathbf{a}_l & \lambda_t \mathbf{a}_t & \lambda_n \mathbf{a}_n \end{bmatrix} \quad (\text{A.1})$$

so that

$$M = XX^T. \quad (\text{A.2})$$

A natural coordinate system  $\mathbf{v}$  is defined by

$$\mathbf{v} := X^{-1}\mathbf{x}, \quad (\text{A.3})$$

where the origin of the coordinate system  $\boldsymbol{x}$  is at the current source. For any function  $z$ , then,

$$X^T \nabla z = \nabla_{\boldsymbol{v}} z, \quad (\text{A.4})$$

and, because  $X$  is constant,

$$\nabla \cdot (M \nabla z) = \nabla_{\boldsymbol{v}} \cdot (\nabla_{\boldsymbol{v}} z). \quad (\text{A.5})$$

Using equations (6.18) and (2.33), the conservation of current equations (2.24) with no applied current, in this natural coordinate system, are

$$-\frac{1}{\alpha_i} \nabla_{\boldsymbol{v}} \cdot (\nabla_{\boldsymbol{v}} V_m) = \frac{1}{\alpha_i \alpha_e} \nabla_{\boldsymbol{v}} \cdot (\nabla_{\boldsymbol{v}} \phi_e), \quad (\text{A.6a})$$

$$-V_m + V_r - \tau_m \frac{\partial V_m}{\partial t} = \frac{1}{\alpha_e} \nabla_{\boldsymbol{v}} \cdot (\nabla_{\boldsymbol{v}} \phi_e) \quad (\text{A.6b})$$

(cf. equations (2.34)). Substituting (A.6a) into (A.6b) gives the equivalent system,

$$-\frac{1}{\alpha_i} \nabla_{\boldsymbol{v}} \cdot (\nabla_{\boldsymbol{v}} V_m) = \frac{1}{\alpha_i \alpha_e} \nabla_{\boldsymbol{v}} \cdot (\nabla_{\boldsymbol{v}} \phi_e), \quad (\text{A.7a})$$

$$V_m - V_r + \tau_m \frac{\partial V_m}{\partial t} = \nabla_{\boldsymbol{v}} \cdot (\nabla_{\boldsymbol{v}} V_m). \quad (\text{A.7b})$$

Note that  $r$ , defined by equation (6.22), may be written as

$$r = |\boldsymbol{v}|, \quad (\text{A.8})$$

so, for  $r > 0$ ,

$$\nabla_{\boldsymbol{v}} r = \frac{\boldsymbol{v}}{r} \quad \text{and} \quad \nabla_{\boldsymbol{v}} \cdot (\nabla_{\boldsymbol{v}} r) = \frac{2}{r}. \quad (\text{A.9})$$

If  $z$  is a function only of  $r$  and  $t$  then, for  $r > 0$ ,

$$\nabla_{\boldsymbol{v}} z = \nabla_{\boldsymbol{v}} r \frac{\partial z}{\partial r}, \quad (\text{A.10})$$

so

$$\begin{aligned} \nabla_{\boldsymbol{v}} r \cdot \nabla_{\boldsymbol{v}} z &= \nabla_{\boldsymbol{v}} r \cdot \nabla_{\boldsymbol{v}} r \frac{\partial z}{\partial r} \\ &= \frac{\partial z}{\partial r}, \end{aligned} \quad (\text{A.11})$$

and

$$\begin{aligned}
 \nabla_{\mathbf{v}} \cdot (\nabla_{\mathbf{v}} z) &= \nabla_{\mathbf{v}} \cdot (\nabla_{\mathbf{v}} r) \frac{\partial z}{\partial r} + \nabla_{\mathbf{v}} r \cdot \nabla_{\mathbf{v}} r \frac{\partial^2 z}{\partial r^2} \\
 &= \frac{2}{r} \frac{\partial z}{\partial r} + \frac{\partial^2 z}{\partial r^2} \\
 &= \frac{1}{r^2} \frac{\partial}{\partial r} \left( r^2 \frac{\partial z}{\partial r} \right).
 \end{aligned} \tag{A.12}$$

The monodomain potential  $\phi_{\text{mono}}$  defined in (6.21) is first shown to be the solution under the assumption that the bidomain behaves like a monodomain with resistivities equivalent to the parallel combination of the intra- and extracellular resistivities. The conservation of current equation for a monodomain is

$$\nabla \cdot ((M^i + M^e) \nabla \phi_{\text{mono}}) = 0. \tag{A.13}$$

From (6.18), (2.33), and (A.5), this may be written as

$$\frac{1}{\alpha_i \alpha_e} \nabla_{\mathbf{v}} \cdot (\nabla_{\mathbf{v}} \phi_{\text{mono}}) = 0. \tag{A.14}$$

Substituting expression (6.21) for  $\phi_{\text{mono}}$  and using (A.12), the residual in this equation for  $r > 0$  is

$$\begin{aligned}
 \frac{1}{\alpha_i \alpha_e} \nabla_{\mathbf{v}} \cdot (\nabla_{\mathbf{v}} \phi_{\text{mono}}) &= \frac{r_m I}{2\pi \lambda_i \lambda_t \lambda_n} \frac{1}{r^2} \frac{\partial}{\partial r} \left( r^2 \frac{\partial}{\partial r} \left( \frac{1}{r} \right) \right) \\
 &= 0,
 \end{aligned} \tag{A.15}$$

so, away from the source point, current is conserved by the solution in (6.21).

The integral of the current through any surface  $S$  enclosing the source must equal the total current supplied by the source. That is

$$I = \int_S \mathbf{n} \cdot \mathbf{j} \, d\Gamma(\mathbf{x}), \tag{A.16}$$

where the monodomain current density  $\mathbf{j}$  is the sum of the bidomain current densities:

$$\begin{aligned}\mathbf{j} &= \mathbf{j}_i + \mathbf{j}_e \\ &= (G^i + G^e)\nabla\phi_{\text{mono}} \quad (\text{from (2.2)}) \\ &= \frac{1}{r_m}(M^i + M^e)\nabla\phi_{\text{mono}} \quad (\text{from (2.18)}).\end{aligned}\tag{A.17}$$

Substituting (A.17) into (A.16) gives

$$\begin{aligned}I &= \frac{1}{r_m} \int_S \mathbf{n} \cdot (M^i + M^e)\nabla\phi_{\text{mono}} d\Gamma(\mathbf{x}) \\ &= \frac{1}{r_m} \int_V \nabla \cdot ((M^i + M^e)\nabla\phi_{\text{mono}}) d\Omega(\mathbf{x}),\end{aligned}\tag{A.18}$$

where  $V$  is the volume enclosed by  $S$  (which includes the source). Changing to the natural coordinate system allows the current to be written as

$$\begin{aligned}I &= \frac{\det(X)}{\alpha_i\alpha_e r_m} \int_V \nabla_{\mathbf{v}} \cdot (\nabla_{\mathbf{v}}\phi_{\text{mono}}) d\Omega(\mathbf{v}) \\ &= \frac{\lambda_l\lambda_t\lambda_n}{\alpha_i\alpha_e r_m} \int_S \mathbf{n}^{\mathbf{v}} \cdot \nabla_{\mathbf{v}}\phi_{\text{mono}} d\Gamma(\mathbf{v}).\end{aligned}\tag{A.19}$$

$S$  is selected to be a surface of constant  $r$ , so the normal to  $S$  in the natural coordinate system is given by  $\mathbf{n}^{\mathbf{v}} = \nabla_{\mathbf{v}}r$ , and

$$I = \frac{\lambda_l\lambda_t\lambda_n}{\alpha_i\alpha_e r_m} \int_S \nabla_{\mathbf{v}}r \cdot \nabla_{\mathbf{v}}\phi_{\text{mono}} d\Gamma(\mathbf{v}).\tag{A.20}$$

Substituting expression (6.21) for  $\phi_{\text{mono}}$  into the right hand side and using equation (A.11) gives

$$\begin{aligned}\frac{\lambda_l\lambda_t\lambda_n}{\alpha_i\alpha_e r_m} \int_S \nabla_{\mathbf{v}}r \cdot \nabla_{\mathbf{v}}\phi_{\text{mono}} d\Gamma(\mathbf{v}) &= \frac{I}{2\pi} \int_S \frac{\partial}{\partial r} \left( \frac{1}{r} \right) d\Gamma(\mathbf{v}) \\ &= I,\end{aligned}\tag{A.21}$$

so the monodomain solution in (6.21) represents the correct current at the source.

For a bidomain, equation (A.7a) represents conservation of total current in the two domains. Substituting expression (6.20b) for  $\phi_e$ , the residual in this equation for  $r > 0$  is

$$\begin{aligned} \frac{1}{\alpha_i} \nabla_{\mathbf{v}} \cdot (\nabla_{\mathbf{v}} V_m) + \frac{1}{\alpha_i \alpha_e} \nabla_{\mathbf{v}} \cdot (\nabla_{\mathbf{v}} \phi_e) &= \frac{1}{\alpha_i \alpha_e} \nabla_{\mathbf{v}} \cdot (\nabla_{\mathbf{v}} \phi_{\text{mono}}) \\ &= 0 \quad (\text{from (A.15)}), \end{aligned} \quad (\text{A.22})$$

so, away from the source point, total current is conserved.

Equation (A.7b) describes the behaviour of currents between the two domains. Each of the terms in this equation are first evaluated with  $V_m$  given by expression (6.20a), before evaluating the residual in the equation. It is convenient to define the functions

$$\eta_1 := \frac{r}{2} \sqrt{\frac{\tau_m}{t}} - \sqrt{\frac{t}{\tau_m}} \quad \text{and} \quad \eta_2 := \frac{r}{2} \sqrt{\frac{\tau_m}{t}} + \sqrt{\frac{t}{\tau_m}}, \quad (\text{A.23})$$

and the constant

$$A := \frac{\alpha_e r_m \mathbf{I}}{4\pi \lambda_l \lambda_t \lambda_n}, \quad (\text{A.24})$$

so that expression (6.20a) can be written as

$$V_m = V_r - \frac{A}{r} (e^{-r} \operatorname{erfc}(\eta_1) + e^r \operatorname{erfc}(\eta_2)). \quad (\text{A.25})$$

Note that

$$\begin{aligned} \frac{\partial \eta_1}{\partial t} &= \frac{1}{2t} \left( -\frac{r}{2} \sqrt{\frac{\tau_m}{t}} - \sqrt{\frac{t}{\tau_m}} \right) = -\frac{\eta_2}{2t} \\ \text{and} \quad \frac{\partial \eta_2}{\partial t} &= \frac{1}{2t} \left( -\frac{r}{2} \sqrt{\frac{\tau_m}{t}} + \sqrt{\frac{t}{\tau_m}} \right) = -\frac{\eta_1}{2t}, \end{aligned}$$

so

$$\begin{aligned} \frac{\partial}{\partial t}(\operatorname{erfc}(\eta_1)) &= -\frac{2}{\sqrt{\pi}} \frac{\partial \eta_1}{\partial t} e^{-\eta_1^2} = \frac{1}{\sqrt{\pi}} \frac{\eta_2}{t} e^{-\eta_1^2} \\ \text{and} \quad \frac{\partial}{\partial t}(\operatorname{erfc}(\eta_2)) &= -\frac{2}{\sqrt{\pi}} \frac{\partial \eta_2}{\partial t} e^{-\eta_2^2} = \frac{1}{\sqrt{\pi}} \frac{\eta_1}{t} e^{-\eta_2^2}. \end{aligned}$$

With  $V_m$  defined by (A.25), the time derivative term in (A.7b) is therefore

$$\tau_m \frac{\partial V_m}{\partial t} = -\frac{A}{\sqrt{\pi}} \frac{\tau_m}{rt} \left( \eta_2 e^{-r} e^{-\eta_1^2} + \eta_1 e^r e^{-\eta_2^2} \right). \quad (\text{A.26})$$

The  $r$ -derivatives of  $\eta_1$  and  $\eta_2$  are

$$\frac{\partial \eta_1}{\partial r} = \frac{\partial \eta_2}{\partial r} = \frac{1}{2} \sqrt{\frac{\tau_m}{t}},$$

so

$$\begin{aligned} \frac{\partial}{\partial r}(\operatorname{erfc}(\eta_1)) &= -\frac{2}{\sqrt{\pi}} \frac{\partial \eta_1}{\partial r} e^{-\eta_1^2} = -\frac{1}{\sqrt{\pi}} \sqrt{\frac{\tau_m}{t}} e^{-\eta_1^2}, \\ \frac{\partial}{\partial r}(\operatorname{erfc}(\eta_2)) &= -\frac{2}{\sqrt{\pi}} \frac{\partial \eta_2}{\partial r} e^{-\eta_2^2} = -\frac{1}{\sqrt{\pi}} \sqrt{\frac{\tau_m}{t}} e^{-\eta_2^2}, \\ \frac{\partial}{\partial r}(e^{-\eta_1^2}) &= -2 \frac{\partial \eta_1}{\partial r} \eta_1 e^{-\eta_1^2} = -\sqrt{\frac{\tau_m}{t}} \eta_1 e^{-\eta_1^2}, \\ \text{and } \frac{\partial}{\partial r}(e^{-\eta_2^2}) &= -2 \frac{\partial \eta_2}{\partial r} \eta_2 e^{-\eta_2^2} = -\sqrt{\frac{\tau_m}{t}} \eta_2 e^{-\eta_2^2}. \end{aligned}$$

Using these results to differentiate  $V_m$  from (A.25) with respect to  $r$  gives

$$\begin{aligned} \frac{\partial V_m}{\partial r} &= \frac{A}{r^2} (e^{-r} \operatorname{erfc}(\eta_1) + e^r \operatorname{erfc}(\eta_2)) \\ &\quad + \frac{A}{r} (e^{-r} \operatorname{erfc}(\eta_1) - e^r \operatorname{erfc}(\eta_2)) + \frac{A}{r\sqrt{\pi}} \sqrt{\frac{\tau_m}{t}} (e^{-r} e^{-\eta_1^2} + e^r e^{-\eta_2^2}), \quad (\text{A.27}) \end{aligned}$$

$$\begin{aligned} r^2 \frac{\partial V_m}{\partial r} &= A (e^{-r} \operatorname{erfc}(\eta_1) + e^r \operatorname{erfc}(\eta_2)) \\ &\quad + Ar (e^{-r} \operatorname{erfc}(\eta_1) - e^r \operatorname{erfc}(\eta_2)) + \frac{Ar}{\sqrt{\pi}} \sqrt{\frac{\tau_m}{t}} (e^{-r} e^{-\eta_1^2} + e^r e^{-\eta_2^2}), \quad (\text{A.28}) \end{aligned}$$

$$\begin{aligned}
\frac{\partial}{\partial r} \left( r^2 \frac{\partial V_m}{\partial r} \right) &= -A (e^{-r} \operatorname{erfc}(\eta_1) - e^r \operatorname{erfc}(\eta_2)) - \frac{A}{\sqrt{\pi}} \sqrt{\frac{\tau_m}{t}} (e^{-r} e^{-\eta_1^2} + e^r e^{-\eta_2^2}) \\
&\quad + A (e^{-r} \operatorname{erfc}(\eta_1) - e^r \operatorname{erfc}(\eta_2)) - Ar (e^{-r} \operatorname{erfc}(\eta_1) + e^r \operatorname{erfc}(\eta_2)) \\
&\quad - \frac{Ar}{\sqrt{\pi}} \sqrt{\frac{\tau_m}{t}} (e^{-r} e^{-\eta_1^2} - e^r e^{-\eta_2^2}) + \frac{A}{\sqrt{\pi}} \sqrt{\frac{\tau_m}{t}} (e^{-r} e^{-\eta_1^2} + e^r e^{-\eta_2^2}) \\
&\quad - \frac{Ar}{\sqrt{\pi}} \sqrt{\frac{\tau_m}{t}} (e^{-r} e^{-\eta_1^2} - e^r e^{-\eta_2^2}) - \frac{A}{\sqrt{\pi}} \frac{r\tau_m}{t} (\eta_1 e^{-r} e^{-\eta_1^2} + \eta_2 e^r e^{-\eta_2^2}) \\
&= -Ar (e^{-r} \operatorname{erfc}(\eta_1) + e^r \operatorname{erfc}(\eta_2)) \\
&\quad - \frac{Ar}{\sqrt{\pi}} \frac{\tau_m}{t} \left[ \left( \eta_1 + 2\sqrt{\frac{t}{\tau_m}} \right) e^{-r} e^{-\eta_1^2} + \left( \eta_2 - 2\sqrt{\frac{t}{\tau_m}} \right) e^r e^{-\eta_2^2} \right] \\
&= -Ar (e^{-r} \operatorname{erfc}(\eta_1) + e^r \operatorname{erfc}(\eta_2)) - \frac{Ar}{\sqrt{\pi}} \frac{\tau_m}{t} (\eta_2 e^{-r} e^{-\eta_1^2} + \eta_1 e^r e^{-\eta_2^2}).
\end{aligned} \tag{A.29}$$

For  $r > 0$ , the Laplacian term in (A.7b) with  $V_m$  given by (A.25) may be expressed using (A.12) and (A.29) as

$$\begin{aligned}
\nabla_{\mathbf{v}} \cdot (\nabla_{\mathbf{v}} V_m) &= \frac{1}{r^2} \frac{\partial}{\partial r} \left( r^2 \frac{\partial V_m}{\partial r} \right) \\
&= -\frac{A}{r} (e^{-r} \operatorname{erfc}(\eta_1) + e^r \operatorname{erfc}(\eta_2)) - \frac{A}{\sqrt{\pi}} \frac{\tau_m}{rt} (\eta_2 e^{-r} e^{-\eta_1^2} + \eta_1 e^r e^{-\eta_2^2}) \\
&= V_m - V_r + \tau_m \frac{\partial V_m}{\partial t} \quad (\text{from (A.25) and (A.26)}),
\end{aligned} \tag{A.30}$$

so equation (A.7b) is satisfied and the behaviour of currents between the two domains is correct away from the source point.

For the total current at the source to be correct, equation (A.16) must be satisfied. Following the same process as for equation (A.17), the total current density  $\mathbf{j}$  in a bidomain is given by

$$\begin{aligned}
\mathbf{j} &= \frac{1}{r_m} (M^i \nabla \phi_i + M^e \nabla \phi_e) \\
&= \frac{1}{r_m} (M^i \nabla V_m + (M^i + M^e) \nabla \phi_e) \quad (\text{from (2.5)}).
\end{aligned} \tag{A.31}$$

Following the same process as for (A.20), equation (A.16) becomes

$$I = \frac{\lambda_l \lambda_t \lambda_n}{\alpha_i \alpha_e \Gamma_m} \int_S \nabla_{\mathbf{v}} r \cdot \nabla_{\mathbf{v}} (\alpha_e V_m + \phi_e) d\Gamma(\mathbf{v}). \quad (\text{A.32})$$

Substituting expression (6.20b) for  $\phi_e$  into the right hand side gives

$$\begin{aligned} \frac{\lambda_l \lambda_t \lambda_n}{\alpha_i \alpha_e \Gamma_m} \int_S \nabla_{\mathbf{v}} r \cdot \nabla_{\mathbf{v}} (\alpha_e V_m + \phi_e) d\Gamma(\mathbf{v}) &= \frac{\lambda_l \lambda_t \lambda_n}{\alpha_i \alpha_e \Gamma_m} \int_S \nabla_{\mathbf{v}} r \cdot \nabla_{\mathbf{v}} \phi_{\text{mono}} d\Gamma(\mathbf{v}) \\ &= I \quad (\text{from (A.21)}), \end{aligned} \quad (\text{A.33})$$

so the total current applied at the source point is correct.

It remains only to show that all the current applied at the source is applied to the extracellular domain. Equivalently, the integral of extracellular current through an infinitesimal volume containing the source must equal the total current:

$$I = \lim_{r \rightarrow 0} \int_{S(r)} \mathbf{n} \cdot \mathbf{j}_e d\Gamma(\mathbf{x}), \quad (\text{A.34})$$

where  $S(r)$  is the surface of constant  $r$ . The integral may be expressed in terms of  $\phi_e$  using (2.2) and (2.18):

$$\begin{aligned} \int_{S(r)} \mathbf{n} \cdot \mathbf{j}_e d\Gamma(\mathbf{x}) &= \frac{1}{\Gamma_m} \int_{S(r)} \mathbf{n} \cdot M^e \nabla \phi_e d\Gamma(\mathbf{x}) \\ &= \frac{\lambda_l \lambda_t \lambda_n}{\alpha_e \Gamma_m} \int_{S(r)} \nabla_{\mathbf{v}} r \cdot \nabla_{\mathbf{v}} \phi_e d\Gamma(\mathbf{v}). \end{aligned} \quad (\text{A.35})$$

Substituting expression (6.20b) for  $\phi_e$  gives

$$\begin{aligned}
\int_{S(r)} \mathbf{n} \cdot \mathbf{j}_e d\Gamma(\mathbf{x}) &= \frac{\lambda_l \lambda_t \lambda_n}{\alpha_e \Gamma_m} \int_{S(r)} \nabla_{\mathbf{v}} r \cdot \nabla_{\mathbf{v}} (\phi_{\text{mono}} - \alpha_e V_m) d\Gamma(\mathbf{v}) \\
&= \alpha_i I + \frac{\lambda_l \lambda_t \lambda_n}{r_m} \int_{S(r)} \nabla_{\mathbf{v}} r \cdot \nabla_{\mathbf{v}} V_m d\Gamma(\mathbf{v}) \quad (\text{from (A.21)}) \\
&= \alpha_i I + \frac{\lambda_l \lambda_t \lambda_n}{r_m} \int_{S(r)} \frac{\partial V_m}{\partial r} d\Gamma(\mathbf{v}) \quad (\text{from (A.11)}) \\
&= \alpha_i I + \frac{2\pi \lambda_l \lambda_t \lambda_n}{r_m} r^2 \frac{\partial V_m}{\partial r} \\
&= \alpha_i I + \frac{\alpha_e I}{2A} r^2 \frac{\partial V_m}{\partial r} \quad (\text{from (A.24)}). \quad (\text{A.36})
\end{aligned}$$

The total current entering the extracellular domain is therefore

$$\lim_{r \rightarrow 0} \int_{S(r)} \mathbf{n} \cdot \mathbf{j}_e d\Gamma(\mathbf{x}) = \alpha_i I + \frac{\alpha_e I}{2A} \lim_{r \rightarrow 0} \left\{ r^2 \frac{\partial V_m}{\partial r} \right\}. \quad (\text{A.37})$$

Using expression (A.28) for  $r^2 \frac{\partial V_m}{\partial r}$  when  $V_m$  is given by expression (6.20a), and noting that, at  $r = 0$ ,

$$\begin{aligned}
e^{-r} &= e^r = 1, \\
\eta_2 &= -\eta_1 = \sqrt{\frac{t}{\tau_m}}, \\
\text{and} \quad \text{erfc}(\eta_1) + \text{erfc}(-\eta_1) &= 2,
\end{aligned}$$

the limit in the right hand side of equation (A.37) is

$$\lim_{r \rightarrow 0} \left\{ r^2 \frac{\partial V_m}{\partial r} \right\} = 2A. \quad (\text{A.38})$$

Substituting this into (A.37) gives a total extracellular source current

$$\lim_{r \rightarrow 0} \int_{S(r)} \mathbf{n} \cdot \mathbf{j}_e \, d\Gamma(\mathbf{x}) = \alpha_i I + \alpha_e I \quad (\text{A.39})$$

$$= I \quad (\text{from (2.33)}), \quad (\text{A.40})$$

which is what was required by equation (A.34).

# References

- Allgower, E. L. and Georg, K. (1990), *Numerical Continuation Methods: An Introduction*, Springer-Verlag, Berlin.
- Anyukhovskiy, E. P., Sosunov, E. A., and Rosen, M. R. (1996), 'Regional differences in electrophysiological properties of epicardium, midmyocardium, and endocardium. In vitro and in vivo correlations.', *Circulation*, **94**(8), 1981–1988.
- Arisi, G., Macchi, E., Baruffi, S., Spaggiari, S., and Taccardi, B. (1983), 'Potential fields on the ventricular surface of the exposed dog heart during normal excitation', *Circ. Res.*, **52**(6), 706–715.
- Barrett, J. W. and Morton, K. W. (1984), 'Approximate symmetrization and Petrov–Galerkin methods for diffusion–convection problems', *Comput. Methods Appl. Mech. Engrg.*, **45**, 97–122.
- Bradley, C. P., Pullan, A. J., and Hunter, P. J. (1997), 'Geometric modelling of the human torso using cubic Hermite elements', *Ann. Biomed. Eng.*, **25**(1), 96–111.
- Brooks, A. N. and Hughes, T. J. R. (1982), 'Streamline upwind/Petrov–Galerkin formulations for convection dominated flows with particular emphasis on the incompressible Navier–Stokes equations', *Comput. Methods Appl. Mech. Engrg.*, **32**, 199–259.
- Broyden, C. G. (1965), 'A class of methods for solving nonlinear simultaneous equations', *Math. Comp.*, **19**, 577–593.
- Buchanan, Jr., J. W., Oshita, S., Fujino, T., and Gettes, L. S. (1986), 'A method for measurement of internal longitudinal resistance in papillary muscle', *Am. J. Physiol.*, **251**(1 Pt 2), H210–217.

- Christie, I., Griffiths, D. F., Mitchell, A. R., and Zienkiewicz, O. C. (1976), 'Finite element methods for second order differential equations with significant first derivatives', *Int. J. Numer. Meth. Eng.*, **10**, 1389–1396.
- Clerc, L. (1976), 'Directional differences of impulse spread in trabecular muscle from mammalian heart', *J. Physiol.*, **255**, 335–346.
- Colli Franzone, P. and Guerri, L. (1993a), 'Models of the spreading of excitation in myocardial tissue', in T. C. Pilkington, B. Loftis, J. F. Thompson, S. L.-Y. Woo, T. C. Palmer, and T. F. Budinger, eds, *High-Performance Computing in Biomedical Research*, CRC Press Inc., Ch. 13, pp. 359–401.
- Colli Franzone, P. and Guerri, L. (1993b), 'Spreading of excitation in 3-D models of the anisotropic cardiac tissue. I. Validation of the eikonal model', *Math. Biosci.*, **113**, 145–209.
- Colli Franzone, P., Guerri, L., Pennacchio, M., and Taccardi, B. (1998), 'Spread of excitation in 3-D models of the anisotropic cardiac tissue. II. Effects of fiber architecture and ventricular geometry', *Math. Biosci.*, **147**, 131–171.
- Colli Franzone, P., Guerri, L., and Rovida, S. (1990), 'Wavefront propagation in an activation model of the anisotropic cardiac tissue: Asymptotic analysis and numerical simulations', *J. Math. Biol.*, **28**(2), 121–176.
- Colli Franzone, P., Guerri, L., and Tentoni, S. (1990), 'Mathematical modelling of the excitation process in the myocardial tissue: Influence of the fibre rotation on the wavefront propagation and the potential field', *Math. Biosci.*, **101**, 155–235.
- Colli Franzone, P., Guerri, L., and Viganotti, C. (1983), 'Oblique dipole layer potentials applied to electrocardiology', *J. Math. Biol.*, **17**(1), 93–114.
- Davis, T. A. and Duff, I. S. (1997), 'An unsymmetric-pattern multifrontal method for sparse  $LU$  factorization', *SIAM J. Matrix Anal. Appl.*, **18**(1), 140–158.
- Donea, J., Belytschko, T., and Smolinski, P. (1985), 'A generalized Galerkin method for steady convection–diffusion problems with application to quadratic shape function elements', *Comput. Methods Appl. Mech. Engrg.*, **48**, 25–43.
- Eisenstat, S. C. and Walker, H. F. (1994), 'Globally convergent inexact Newton methods', *SIAM J. Optim.*, **4**(2), 393–422.

- Falcone, M., Giorgi, T., and Loreti, P. (1994), 'Level sets of viscosity solutions: Some applications to fronts and rendez-vous problems', *SIAM J. Appl. Math.*, **54**(5), 1335–1354.
- Fozzard, H. A. (1966), 'Membrane capacity of the cardiac Purkinje fibre', *J. Physiol.*, **182**, 255–267.
- Green, L. S., Taccardi, B., Ershler, P. R., and Lux, R. L. (1991), 'Epicardial potential mapping. Effects of conducting media on isopotential and isochrone distributions', *Circulation*, **84**(6), 2513–2521.
- Gulrajani, R. M., Roberge, F. A., and Savard, P. (1989), 'The inverse problem of electrocardiography', in P. W. Macfarlane and T. F. V. Lawrie, eds, *Comprehensive Electrocardiography*, Permagon Press, Ch. 9, pp. 237–288.
- Heinrich, J. C., Huyakorn, P. S., and Zienkiewicz, O. C. (1977), 'An 'upwind' finite element scheme for two-dimensional convective transport equation', *Int. J. Numer. Meth. Eng.*, **11**, 131–43.
- Henriquez, C. S. (1993), 'Simulating the electrical behaviour of cardiac tissue using the bidomain model', *Crit. Rev. Biomed. Eng.*, **21**(1), 1–77.
- Hunter, P. J., McNaughton, P. A., and Noble, D. (1975), 'Analytical models of propagation in excitable cells', *Prog. Biophys. Mol. Biol.*, **30**(2/3), 99–144.
- Jack, J. J. B., Noble, D., and Tsien, R. W. (1975), *Electric current flow in excitable cells*, Clarendon Press, Oxford, Ch. 3.
- Kamiyama, A. and Matsuda, K. (1966), 'Electrophysiological properties of the canine ventricular fiber', *Jpn. J. Physiol.*, **16**, 407–420.
- Keener, J. P. (1991), 'An eikonal-curvature equation for action potential propagation in myocardium', *J. Math. Biol.*, **29**, 629–651.
- Keener, J. P. and Panfilov, A. V. (1995), 'Three-dimensional propagation in the heart: The effects of geometry and fiber orientation on propagation in myocardium', in D. P. Zipes and J. Jalife, eds, *Cardiac Electrophysiology: From Cell to Bedside*, 2nd edn, Saunders, Philadelphia, Ch. 32, pp. 335–347.
- Kelly, D. W., Nakazawa, S., Zienkiewicz, O. C., and Heinrich, J. C. (1980), 'A note on upwinding and anisotropic balancing dissipation in finite element approximations to convective diffusion problems', *Int. J. Numer. Meth. Eng.*, **15**, 1705–1711.

- Kléber, A. G. and Riegger, C. B. (1987), 'Electrical constants of arterially perfused rabbit papillary muscle', *J. Physiol.*, **385**, 307–324.
- Klein, M. V. (1970), *Optics*, Wiley, New York.
- Krassowska, W. and Neu, J. C. (1994), 'Effective boundary conditions for syncytial tissues', *IEEE Trans. Biomed. Eng.*, **41**(2), 143–150.
- Lazzara, R., Yeh, B. K., and Samet, P. (1974), 'Functional anatomy of the canine left bundle branch', *Am. J. Cardiol.*, **33**, 623–632.
- Le Grice, I. J. (1992), 'A finite element model of myocardial structure: Implications for electrical activation in the heart', PhD thesis, The University of Auckland, New Zealand.
- LeGrice, I. J., Hunter, P. J., and Smaill, B. H. (1997), 'Laminar structure of the heart: A mathematical model', *Am. J. Physiol.*, **272**(5 Pt 2), H2466–2476.
- LeGrice, I. J., Smaill, B. H., Chai, L. Z., Edgar, S. G., Gavin, J. B., and Hunter, P. J. (1995), 'Laminar structure of the heart: Ventricular myocyte arrangement and connective tissue architecture in the dog', *Am. J. Physiol.*, **269**(2 Pt 2), H571–582.
- Morton, K. W. (1996), *Numerical Solution of Convection–Diffusion Problems*, Vol. 12 of Applied Mathematics and Mathematical Computation, Chapman & Hall, London.
- Myerburg, R. J., Gelband, H., Nilsson, K., Castellanos, A., Morales, A. R., and Bassett, A. L. (1978), 'The role of canine superficial ventricular muscle fibers in endocardial impulse distribution', *Circ. Res.*, **42**(1), 27–35.
- Myerburg, R. J., Nilsson, K., and Gelband, H. (1972), 'Physiology of canine intraventricular conduction and endocardial excitation', *Circ. Res.*, **30**, 217–243.
- Nagao, K., Toyama, J., Kodama, I., and Yamada, K. (1981), 'Role of the conduction system in the endocardial excitation spread in the right ventricle', *Am. J. Cardiol.*, **48**, 865–870.
- Neu, J. C. and Krassowska, W. (1993), 'Homogenization of syncytial tissues', *Crit. Rev. Biomed. Eng.*, **21**(2), 137–199.
- Nielsen, P. M. F., Le Grice, I. J., Smaill, B. H., and Hunter, P. J. (1991), 'Mathematical model of geometry and fibrous structure of the heart', *Am. J. Physiol.*, **260**(4 Pt 2), H1365–1378.

- Osher, S. and Sethian, J. A. (1988), 'Fronts propagating with curvature-dependent speed: algorithms based on Hamilton–Jacobi formulations', *J. Comput. Phys.*, **79**, 12–49.
- Plonsey, R. and Barr, R. C. (1987), 'Mathematical modeling of electrical activity of the heart', *J. Electrocardiol.*, **20**(3), 219–226.
- Pullan, A. J. and Bradley, C. P. (1996), 'A coupled cubic hermite finite element/boundary element procedure for electrocardiographic problems', *Computational Mechanics*, **18**(5), 356–368.
- Roberts, D. E., Hersh, L. T., and Scher, A. M. (1979), 'Influence of cardiac fiber orientation on wavefront voltage, conduction velocity, and tissue resistivity in the dog', *Circ. Res.*, **44**, 701–712.
- Roberts, D. E. and Scher, A. M. (1982), 'Effect of tissue anisotropy on extracellular potential fields in canine myocardium in situ', *Circ. Res.*, **50**, 342–351.
- Rodriguez-Sinovas, A., Cinca, J., Tapias, A., Armadans, L., Tresanchez, M., and Soler-Soler, J. (1997), 'Lack of evidence of M-cells in porcine left ventricular myocardium', *Cardiovasc. Res.*, **33**(2), 307–313.
- Saad, Y. and Schultz, M. H. (1986), 'GMRES: A generalized minimal residual algorithm for solving nonsymmetric linear systems.', *SIAM J. Sci. Statist. Comput.*, **7**(3), 856–869.
- Sakamoto, Y. (1969), 'Membrane characteristics of the canine papillary muscle fiber', *J. Gen. Physiol.*, **54**, 765–781.
- Scher, A. M. and Young, A. C. (1956), 'The pathway of ventricular depolarization in the dog', *Circ. Res.*, **4**, 461–469.
- Scher, A. M. and Young, A. C. (1957), 'Ventricular depolarization and the genesis of QRS', *Ann. N. Y. Acad. Sci.*, **65**, 768–778.
- Schmitt, O. H. (1969), 'Biological information processing using the concept of interpenetrating domains', in K. N. Leibovic, ed., *Information Processing in the Nervous System*, Springer-Verlag, New York, Ch. 18, pp. 325–331.
- Sepulveda, N. G., Roth, B. J., and Wikswa, Jr., J. P. (1989), 'Current injection into a two-dimensional anisotropic bidomain', *Biophys. J.*, **55**, 987–999.

- Sethian, J. A. (1996), 'Theory, algorithms, and applications of level set methods for propagating interfaces', *Acta Numerica*, **1996**, 309–395.
- Sodi Pallares, D., Medrano, G. A., de Micheli, A., Testelli, M. R., and Bisteni, A. (1961), 'Unipolar QS morphology and Purkinje potential of the free left ventricular wall', *Cir*, **23**, 836–846.
- Spach, M. S., Huang, S., and Ayers, C. R. (1963), 'Electrical and anatomic study of the Purkinje system of the canine heart', *Am. Heart J.*, **65**(5), 664–673.
- Suenson, M. (1985), 'Interaction between ventricular cells during the early part of excitation in the ferret heart', *Acta Physio. Scand.*, **125**, 81–90.
- Tomlinson, K. A., Bradley, C. P., and Pullan, A. J. (1996), 'On the choice of a derivative boundary element formulation using Hermite interpolation', *Int. J. Numer. Meth. Eng.*, **39**, 451–468.
- Trayanova, N. (1996a), 'Discrete versus syncytial tissue behavior in a model of cardiac stimulation—I: Mathematical formulation', *IEEE Trans. Biomed. Eng.*, **43**(12), 1129–1140.
- Trayanova, N. (1996b), 'Discrete versus syncytial tissue behavior in a model of cardiac stimulation—II: Results of simulation', *IEEE Trans. Biomed. Eng.*, **43**(12), 1141–1150.
- Weidmann, S. (1970), 'Electrical constants of trabecular muscle from mammalian heart', *J. Physiol.*, **210**, 1041–1054.
- Wikswa, Jr., J. P., Wisialowski, T. A., Altemeier, W. A., Balsler, J. R., Kopelman, H. A., and Roden, D. M. (1991), 'Virtual effects during stimulation of cardiac muscle. Two-dimensional in vivo experiments', *Circ. Res.*, **68**(2), 513–530.
- World Health Organization (1999), *The World Health Report 1999*.  
<http://www.who.org/whr/>
- Yan, G. X., Shimizu, W., and Antzelevitch, C. (1998), 'Characteristics and distribution of M cells in arterially perfused canine left ventricular wedge preparations', *Circulation*, **98**(18), 1921–1927.
- Zienkiewicz, O. C. and Taylor, R. L. (1994), *The Finite Element Method*, 4th edn, McGraw-Hill, Berkshire.